AD-A179 506 SURFACE ROUGHNESS: ITS EFFECTS ON THE PERFORMANCE OF A TWO-DIMENSIONAL CO (U) AIR FORCE INST OF TECH WRIGHT-PATTERSON AFB OH SCHOOL OF ENGI J R POULIN 1/3

UNCLASSIFIED DEC 86 AFIT/GAE/AA/86D-13 F/G 20/4 NN

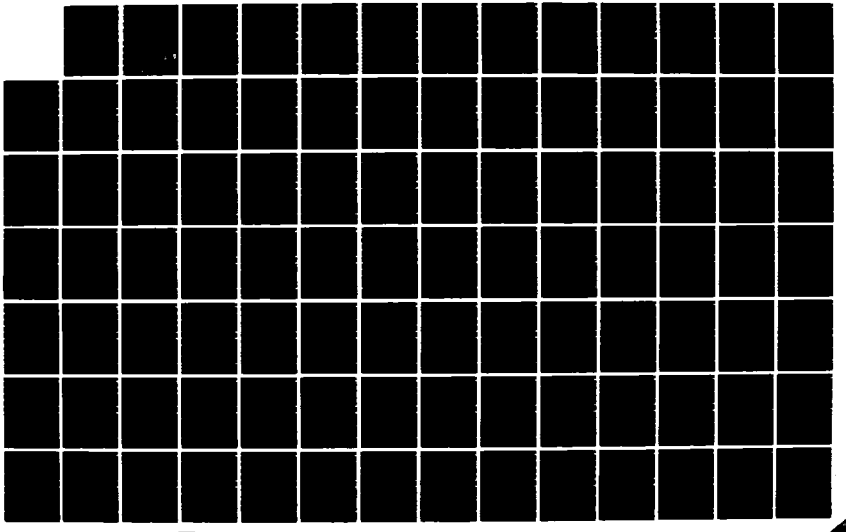

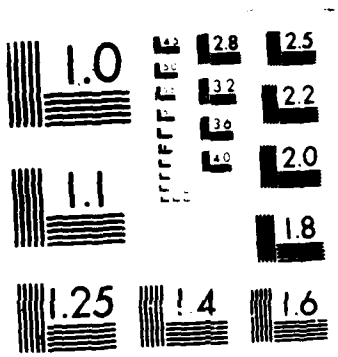

SURFACE ROUGHNESS: ITS EFFECTS ON THE PERFORMANCE OF A TWO-DIMENSIONAL COMPRESSOR CASCADE

THESIS

J. Rémy Poulin, BEng
Captain, Canadian Armed Forces

AFIT/GAE/AA/86D-13

DEPARTMENT OF THE AIR FORCE
AIR UNIVERSITY
AIR FORCE INSTITUTE OF TECHNOLOGY

Wright-Patterson Air Force Base, Ohio

AFIT/GAE/AA/86D-13

SURFACE ROUGHNESS: ITS EFFECTS ON THE PERFORMANCE OF A TWO-DIMENSIONAL COMPRESSOR CASCADE

THESIS

Presented to the Faculty of the School of Engineering

of the Air Force Institute of Technology

Air University

In Partial Fulfillment of the

Requirements for the Degree of

Master of Science in Aeronautical Engineering

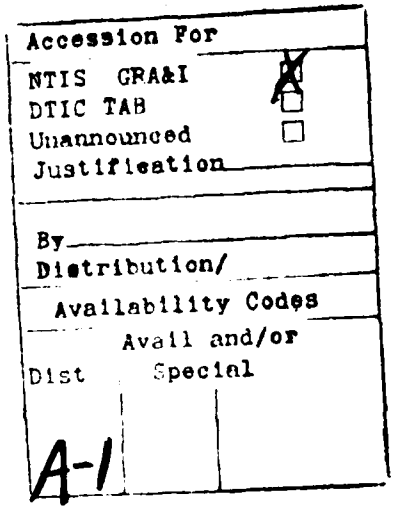

J. Rémy Poulin, BEng

Captain, Canadian Armed Forces

December 1986

Approved for public release; distribution unlimited

Acknowledgments

I would like to thank the members of my thesis committee, Dr. Milton E. Franke and Dr. James E. Hitchcock, for the assistance and suggestions they offered during the course of this study. I am especially grateful to my principal advisor, Dr. William C. Elrod, for his help, support, and guidance.

The support received from both the laboratory staff and fabrication shop was first rate. Special thanks go to John Brohas for his efforts in preparing the instrumented airfoils and suggestions on modifying the test facility. I would also like to thank Dr. Rivir from the propulsion lab for his assistance in calibrating the hot wires.

Finally, I wish to thank my wife, Lynn, and children, Eric and NIcole, for their patience and understanding during the past year and a half. Their encouragement kept me going through many long hours.

This report was prepared with the Timeworks Word Writer 128 word processing software package operated on a Commodore 128 computer. The printer was a Panasonic KX-P1091.

J. Rémy Poulin

Table of Contents

List of Figures

Page

List of Tables

List of Symbols

Symbol	Name	Units
a,b	Constants in equation for minimum wake velocity	
A	Area	in^2
c	Chord length	in
c_p	Specific heat at constant pressure	Btu/lbm-^oR
C_F	Skin friction coefficient	
C_p	Pressure coefficient	
d	diameter	in_2
dA	Incremental area	in^2
E	Voltage	volts
^oF	Degrees Fahrenheit	
h	Convection heat transfer coefficient	Btu/sec-ft^2-^oR
H	Form factor	
I	Current	amperes
k	Technical roughness	micrometers
k_s	Equivalent sand roughness	micrometers
k_T	Thermal conductivity	Btu/sec-ft-^oR
K	Pseudoenergy factor	
L	Length	in
N	Number of data points	
Nu	Nusselt number	
P	Static pressure	lbf/in^2
P_T	Total pressure	lbf/in^2
r_c	Recovery factor	
R	Resistance	ohms
^oR	Degrees Rankine	
Ra	Arithmetic average roughness	micrometers
Re	Reynolds number	
T	Static temperature	^oR
T_{AW}	Adiabactic wall temperature	^oR
T_T	Total tempereature	^oR
Tu	Turbulence intensity	percent
U	Velocity within cascade blade row	ft/sec
V	Velocity outside of cascade blade row	ft/sec
V'	Corrected velocity	ft/sec
x	Downstream distance	in
X	Streamwise direction	
y	Displacement from blade surface	in
Y	Vertical direction	
Z	Lateral direction	
β	Angle between flow direction and cascade axial direction	degrees

Symbol	Name	Units
γ	Ratio of specific heats	
δ	Thickness	in
δ_1	Displacement thickness	in
δ_2	Momentum thickness	in
δ_3	Pseudoenergy thickness	in
θ	Wake momentum thickness parameter	in
μ	Dynamic viscosity	lbm/ft-sec
μm	Micrometer	
ν	Kinematic viscosity	ft^2/sec
ρ	Density	lbm/ft^3
σ	Solidity	in
ϖ	Total pressure loss coefficient	

Subscripts

BL	Boundary layer
C	Calibrator
E	Edge
INV	Inviscid
L	Local
M	Mean
MEAS	Measured
MIN	Minimum
RMS	Root mean square
TE	Trailing Edge
W	Wire
X	Arbitrary measuring station downstream of trailing edge
τ	Shear
∞	Measuring station far downstream of trailing edge
o	Free-stream
1	Inlet
2	Exit

Acronyms

AFIT	Air Force Institute of Technology
CTF	Cascade Test Facility
HP	Hewlett Packard
NACA	National Advisory Committee on Aeronautics
TSI	Thermal Systems International

Abstract

An experimental investigation was conducted into the effects of surface roughness on the losses in the flow through a two-dimensional compressor cascade. The cascade consisted of seven NACA 65-A506 airfoils with two inch chords and aspect ratios of one. The blades were mounted with a stagger angle of 16 degrees, an angle of attack of 15 degrees and a solidity of 1.5. The Reynolds number per foot was in excess of two million. Three blade configurations were evaluated: one smooth and two with different degrees of roughness applied to the first quarter chord. Hot wire/film anemometers were used to measure velocities and turbulence intensities both in the wake and along the suction surface of the center blade. Pressure distributions were obtained from taps drilled along the suction surface.

Surface roughness is shown to increase both boundary layer edge velocities and boundary layer thickness towards the trailing edge while advancing the transition point towards the leading edge. It is also shown to increase wake full thickness, momentum thickness, form factor, and total pressure loss coefficient while decreasing the velocity recovery immediately downstream of the trailing edge. The wake characteristics are most sensitive to an initial increase in roughness, but, regardless of the roughness level, the majority of the changes occur within the first half a chord length distance downstream.

SURFACE ROUGHNESS: ITS EFFECTS ON THE PERFORMANCE OF A TWO-DIMENSIONAL COMPRESSOR CASCADE

I. Introduction

The nature of the flow through a rotating compressor blade row is a complicated one. Factors including viscosity, unsteadiness, and three-dimensionality make it difficult to obtain purely theoretical solutions. Therefore, in order to obtain the necessary blade design data, the "...prevailing approach has been to treat the flow across individual compressor blade sections as a two-dimensional flow" (13:183). This lends itself to experimental investigations using two-dimensional cascades. Though some recent studies have questioned the reliability of using cascade data in predicting turbomachine blade performance (8:292), it is "...nevertheless felt that the calculation and understanding of the flow through two-dimensional cascades will remain the corner-stone of turbomachinery-aerodynamics for a long time to come" (24:496).

The Air Force Institute of Technology (AFIT), in conjunction with the Air Force Wright Aeronautical Laboratories, has, over the past few years, made use of a cascade

to study the effects of surface roughness on the performance of a compressor. Interest in this area is based on the knowledge that compressor efficiency is influenced a great deal by the surface quality of the blading (3:283). A number of examples exist in the literature (Refs 3 and 22) where full scale testing of compressors were used to collect data. Acknowledging that this is the preferred method of analysing component performance, it is still felt that examination of the flow through a two-dimensional cascade can contribute to this study.

Research began in 1981 with the design and construction of the AFIT cascade facility. Since then, successive investigations (Refs 17,25,30) have improved the facility, examined the variation of total pressure loss with roughness, and initiated surveys of the cascade blade pressure profile and boundary layer.

Objectives and Scope

The objectives of this investigation were: (1) to concentrate on the suction surface of the center blade in the cascade and obtain more detailed information on the effects of surface roughness on its pressure profile and boundary layer growth; (2) examine the flow in the center blade's wake to determine trends in the variation of certain wake parameters with roughness; and (3) quantify the losses due to roughness experienced by the cascade in terms of a total pressure loss coefficient.

Hot wire/film anemometers were used to measure velocities and turbulence intensities, and the center blade suction surface was instrumented with pressure taps to obtain the pressure profile. A secondary goal of this study was to fully automate the control and movement of the probe around the suction surface contour and integrate that feature into the data acquisition system. Surface roughness was measured by a profilometer and characterized in terms of an arithmetic average roughness, Ra , an equivalent sand roughness, k_s , and a so-called technical roughness k . The latter was formulated by Schäffler (22:10) in an attempt to better quantify the roughness produced by different kinds of manufacturing processes. It is presented as a comparison and not used in describing the results of this study.

II. Theory

Evaluating the losses of a flow through a cascade requires a knowledge of the boundary layer around the blades, the pressure distribution about the contour of the blades, and the effects of mixing in the wake of the cascade (23:771).

Boundary Layer

"Although...the blade surface boundary layer constitutes a small portion of the flow field, it plays a decisive part in the determination of the actual flow characteristics of the cascade" (21:153). This is particularly true in the case of the suction surface of a blade where the presence of an adverse pressure gradient is conducive to flow separation.

When analyzing boundary layer velocity profiles, one must take into account the effects of the normal pressure gradient that exists between the suction surface of one blade and the pressure surface of the next. With the static pressure remaining nearly constant across a boundary layer (21:152), Bernoulli's equation yields a velocity at the edge of the pressure surface boundary layer that is less than that at the corresponding suction surface location. Measuring the velocities between the two blades would therefore yield a profile similar to that depicted in Fig. 1(a). As a result of this effect, the boundary layer edge velocity and

thickness are difficult to determine. One way to approach the problem is to assume that the measured profile is actually a composite profile consisting of three regions. These are: (1) an inner region close to the surface where viscosity acts; (2) an outer inviscid region in the channel where the normal pressure gradient acts; and (3) a region between the two where the conditions match (7:8). This can be represented mathematically through the use of "The Method of Matched Asymptotic Expansions" detailed by Van Dyke (28:77-97). Essentially, the matching principle used is that the inner limit of the outer region is equal to the outer limit of the inner region. The composite profile can then be obtained by summing the inner and outer expansions minus the part they have in common so as not to count it twice. Mellor and Wood (16:307), in their study of axial compressor end-wall boundary layer theory, expressed this as follows:

$$U_{MEAS} = U_{BL} + U_{INV} - U_E \qquad (1)$$

where U_{MEAS} is the measured velocity of the composite profile, U_{BL} the boundary layer velocity, U_{INV} the velocity in the inviscid region, and U_E the boundary layer edge velocity. The three regions of the composite profile are shown in Fig. 1(b). As a result of this procedure, the edge velocity can be determined as well as the boundary layer thickness.

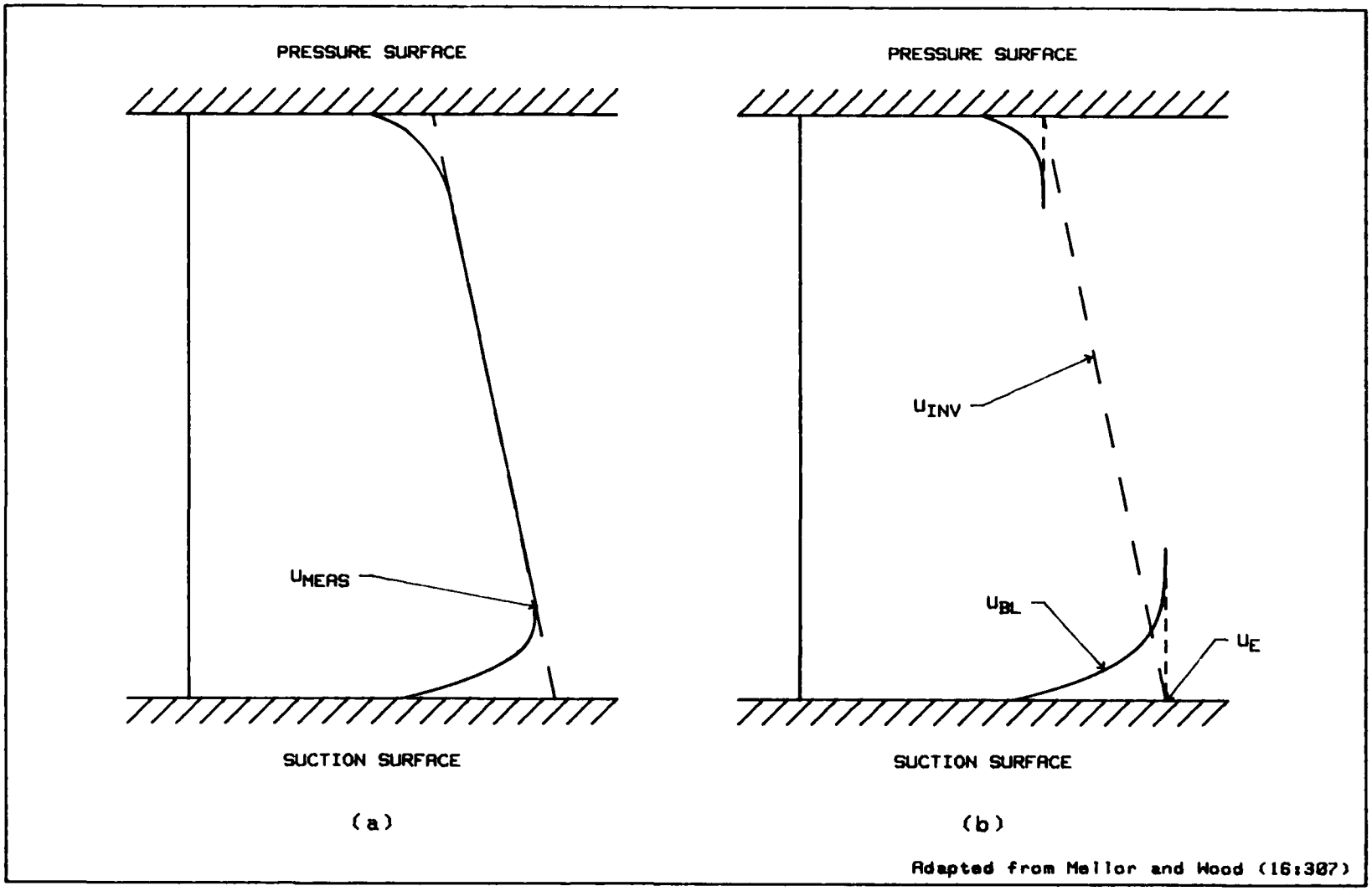

Fig. 1. Matching Channel and Boundary Layer Profiles

Pressure Distribution

The variation in local static pressure around the contour of a blade is usually presented as a dimensionless pressure coefficient, C_p. It is defined as

$$C_p = (P_L - P_1)/(1/2\ \rho V_1^2) \qquad (2)$$

where P_L is the local static pressure, and P_1, ρ, and V_1 the static pressure, density, and velocity, respectively, at the inlet to the cascade.

Information obtained from the pressure distribution include the detection of flow separation, observed as a flattening of the pressure profile. In certain cases, a separated laminar boundary layer may become turbulent and reattach itself to the surface. This forms a region of recirculating flow known as a laminar separation bubble (23:220). Roberts, as reported by Scholz (24:475-476), described the formation of these bubbles by first distinguishing between two regions in the flow. The first lies between the separation streamline and the surface and actually makes up the bubble. The other is the free shear layer itself extending from the same streamline out to the inviscid flow. While this shear layer remains laminar, the flow is separated and represented by a constant pressure plateau in the pressure profile. If the shear layer becomes turbulent, the entrainment of high energy free-stream fluid allows the boundary layer to reattach itself to the surface. Mueller (18:3), in his investigation of separated flow near

the leading edge of airfoils, interpreted sharp discontinuities in the pressure profile following the plateau as the location of the onset of transition and the point of reattachment.

Flow in the Wake

The boundary layers that form on the suction and pressure surfaces of a blade in a cascade meet at the trailing edge and form a wake. As this wake moves downstream, the retarded flow is mixed with the free-stream until, at some distance behind the blade trailing edge, the flow is once again uniform (21:153). This is pictured in Fig. 2.

The velocity defect in the wake also manifests itself as a local defect in total pressure. The mixing that occurs downstream represents an additional loss of energy so that the total pressure in the plane of uniform flow is less than that at the trailing edge (15:4).

Total Pressure Loss Coefficient. Though the effects of the cascade on the flow can be expressed in many ways, including the various force coefficients such as drag, it is best described in terms of the loss in total pressure. In this form, it is "...especially adapted to the practical demands of turbomachine design" (24:34). This loss parameter, known as the total pressure loss coefficient ϖ, is defined to be the ratio of the mass-averaged loss in total pressure across the blade row to a reference free-stream dynamic pressure (13:201). In this investigation, it was

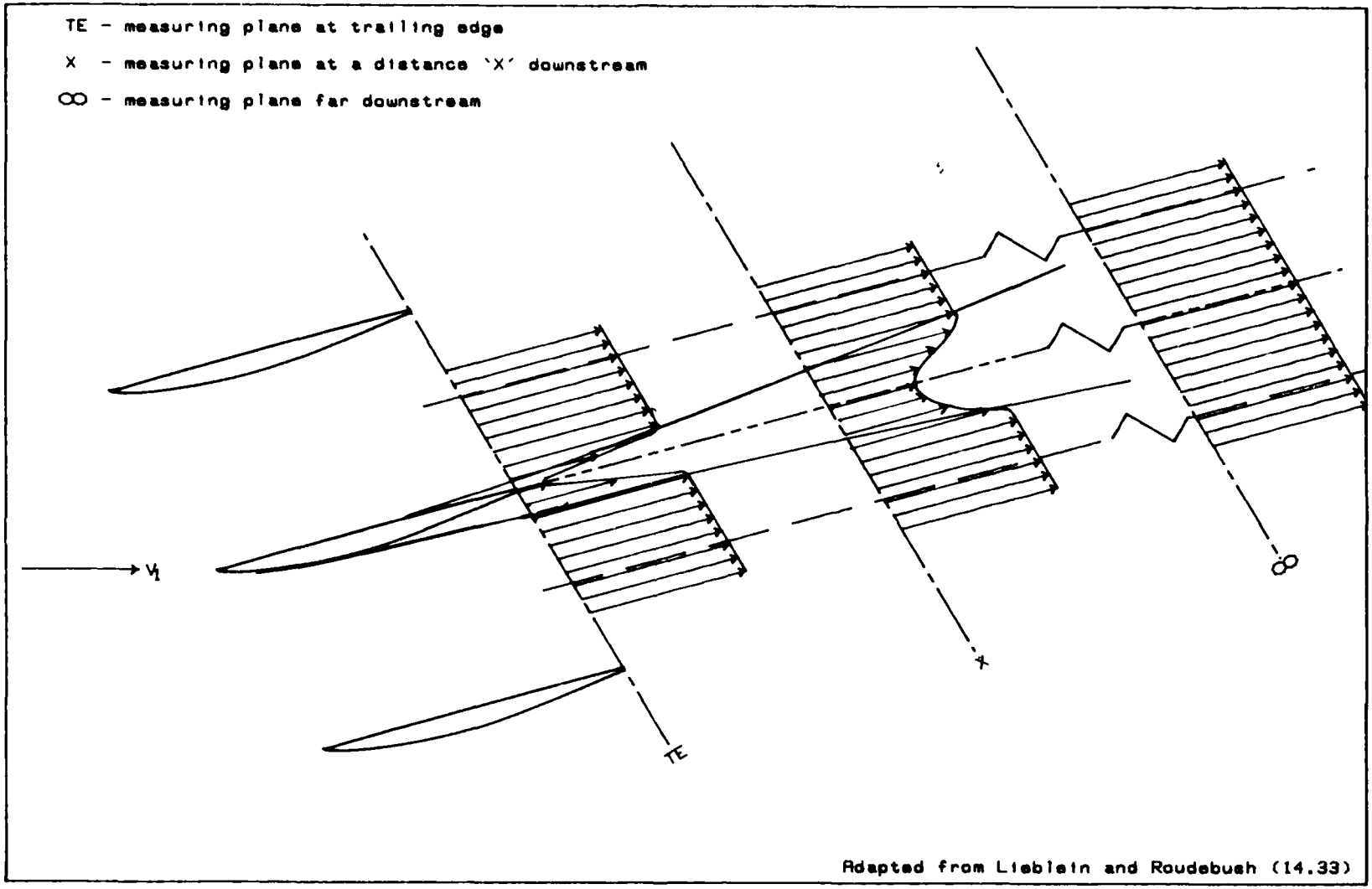

Fig. 2. Schematic Representation of Boundary Layer and Wake Development

obtained from the following:

$$\bar{\omega} = \frac{P_{T_1} - \bar{P}_{T_2}}{1/2\ \rho V_1^2} \qquad (3)$$

where P_{T_1} is the total pressure upstream of the cascade, $\bar{P}_{T_2}$ the mass-averaged total pressure across a blade spacing downstream, and $1/2\ \rho\ V_1^2$ the dynamic head at the inlet.

Unlike some parameters such as the drag coefficient, $\bar{\omega}$ will vary with distance downstream of the trailing edge due to the effects of viscosity and turbulent mixing. Consequently, the complete loss in total pressure through the cascade is one based on the properties of the flow at a station far enough downstream so that the flow is once again uniform across the blade spacing (21:156).

Wake Thicknesses and Parameters. As can be seen from Fig. 2, the flow field for some distance downstream of the trailing edge of a blade can be separated into a wake region and a free-stream region. It would therefore be of interest to express the total pressure loss in terms of the wake characteristics (15:5).

Like a boundary layer over a surface, various wake thicknesses can be calculated from the velocity distribution normal to the outlet flow. The actual wake thickness δ is arbitrarily defined to be the width of the wake as established by the points where V/V_o are equal to 0.99 (14:15). Making reference to Fig. 3, the displacement thickness δ_1, momentum thickness δ_2, and pseudoenergy

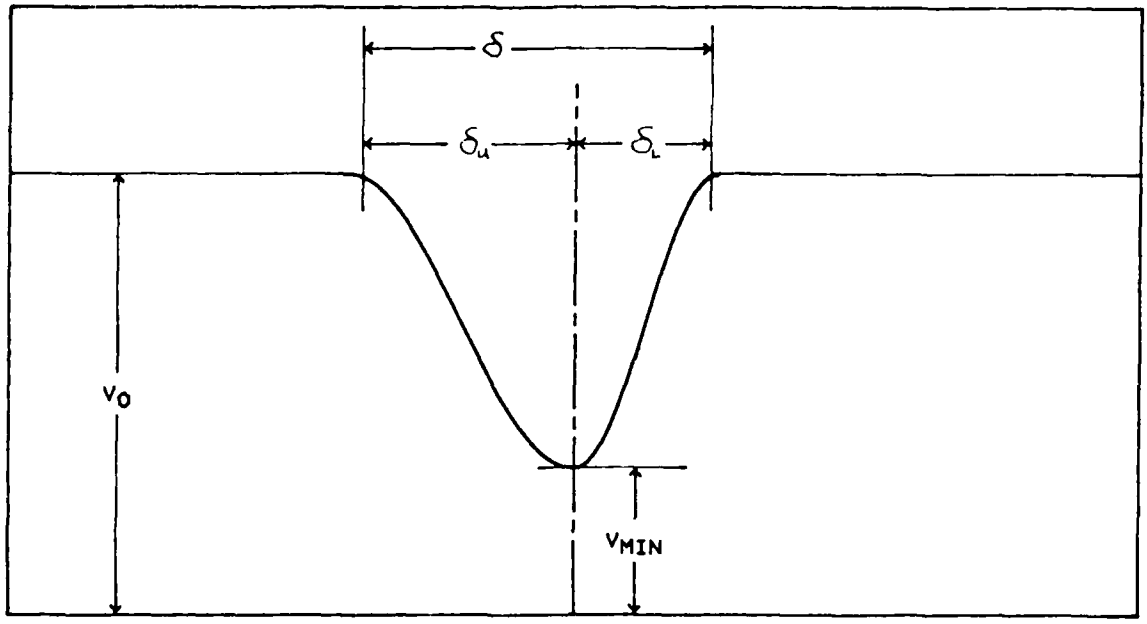

Fig. 3. Velocity Variation in Wake

thickness δ_3 are defined as follows:

$$\delta_1 = \int_{-\delta_L}^{\delta_u} \left[1 - \frac{V}{V_0}\right] dy \qquad (4)$$

$$\delta_2 = \int_{-\delta_L}^{\delta_u} \left[1 - \frac{V}{V_0}\right] \frac{V}{V_0} \, dy \qquad (5)$$

$$\delta_3 = \int_{-\delta_L}^{\delta_u} \left[1 - \frac{V}{V_0}\right] \left[\frac{V}{V_0}\right]^2 dy \qquad (6)$$

The velocity profile in the wake can also be characterized by so-called shape factors. These are dimensionless quantities formed by taking the ratio of the thicknesses discussed above (23:673). Two of particular use in analyzing the wake are the form factor H and the pseudoenergy factor K defined as follows (15:10):

$$H = \delta_1/\delta_2 \tag{7}$$

$$K = \delta_3/\delta_2 \tag{8}$$

Wake Minimum Velocity. The downstream variation of the wake minimum velocity is one way of measuring the intensity of the velocity defect in the wake. Lieblein and Roudebush (14:6-7) postulate that this variation is in the form

$$V_{MIN}/V_0 = 1 - a(x/c + b)^{-1/2} \tag{9}$$

where V_{MIN} is the minimum velocity in the wake, V_0 the free-stream velocity, x the distance downstream from the trailing edge, and c the chordlength of the cascade airfoil. They found the value of the constants a and b to be 0.13 and 0.025, respectively. They arrived at this conclusion by comparing actual turbulent-wake cascade data to theoretical studies done on laminar-wake profiles behind solid bodies.

Wake Form Factor. Lieblein and Roudebush (14:8) also determined that an empirical variation of form factor with downstream distance, obtained previously for isolated airfoils, is also applicable for the turbulent wakes of cascade

airfoils. The relationship is

$$1 - \frac{1}{H} = \left[1 - \frac{1}{H_{TE}}\right]\left[\frac{x/c + b}{b}\right]^{-1/2} \qquad (10)$$

where H_{TE} is the form factor at the trailing edge of the blade and b the same empirical constant found in Eq (9)

Wake Full Thickness. The downstream variation of the wake full thickness ratio, δ/c , for isolated airfoils, as derived from empirical data, is given by

$$(\delta/c)_x = (\delta/c)_{TE} + 0.052(x/c)^{0.75} \qquad (11)$$

where $(\delta/c)_{TE}$ is the full thickness ratio at the blade trailing edge. Lieblein and Roudebush (14:11-12) believe that this relationship also holds for cascades due to the similarities observed between the mixing processes in the wakes of cascade and isolated airfoils.

Total Pressure Loss. A theoretical analysis of total pressure loss in low-speed two-dimensional cascade flow was carried out by Lieblein and Roudebush (15). In it, they formulate the following equation for the total pressure loss coefficient at an arbitrary distance x downstream of the trailing edge:

$$\bar{\omega}_x = \left[\frac{\cos \beta_1}{\cos \beta_x}\right]^2 2\theta_x \left[\frac{2H_x}{3H_x - 1}\right] (1 - \theta_x H_x)^{-3} \qquad (12)$$

where β_1 and β_X are the angles between the flow direction and the cascade axial direction at the inlet and particular outlet plane, respectively. The wake momentum thickness parameter θ_X included in the equation is given

by

$$\theta_x = (\delta_2/c)_x \, \sigma/\cos \beta_x \tag{13}$$

where σ is the solidity of the cascade.

In order to obtain the theoretical loss equation in its presented form, an approximate relationship between the pseudoenergy factor K and the form factor H was used. Values for K were obtained for different analytical representations of wake velocity, and it was determined that the K-H relationship based on a power velocity profile was both simple and accurate (15:11-12). It was

$$K = (H + 1)/(3H - 1) \tag{14}$$

As discussed previously, the complete loss in total pressure is measured at a station far enough downstream so that the velocity is uniform across the blade spacing. The total pressure loss coefficient at this station, $\bar{\omega}_\infty$, can be expressed in terms of the wake characteristics at an arbitrary measuring plane downstream of the trailing edge by

$$\bar{\omega}_\infty = \left[\frac{\cos \beta_1}{\cos \beta_x}\right]^2 2\theta_x \frac{1 + 1/2 \, \theta_x H_x^2}{(1 - \theta_x H_x)^2} \tag{15}$$

This equation, developed by Lieblein and Roudebush (15:22), incorporates the analytical observation that for values of H_x less than 1.2, the air outlet angle β_x has very little effect on the loss for complete mixing.

III. Experimental Apparatus

Cascade Test Facility

The experimental work for this thesis was conducted on the Cascade Test Facility (CTF) located in the Air Force Institute of Technology School of Engineering. The CTF consisted of a 40 horsepower centrifugal blower with a discharge rating of 3000 ft^3/min at 26 oz of head. Outside air was drawn into a sealed containment room where the option existed to mix it with recirculated warmer room air in order to stabilize the discharge temperature. Upstream of the blower itself were screen wire filters and an electrostatic air cleaner assembly for trapping particles. The outlet flow from the blower was directed through a nine foot long diffuser section into a stilling tank where it was radially diffused by a center body plug. Before exiting the tank, the flow was filtered once more by a 40 mesh wire screen and then straightened by a four inch thick honeycomb grid. It then entered a two by eight inch test section with a Reynolds Number per foot in excess of two million and inlet turbulence intensities generally less than two percent as measured by a hot film sensor.

A more detailed description of the CTF is given by Allison (1). A general schematic of the hardware is shown in Fig. 4.

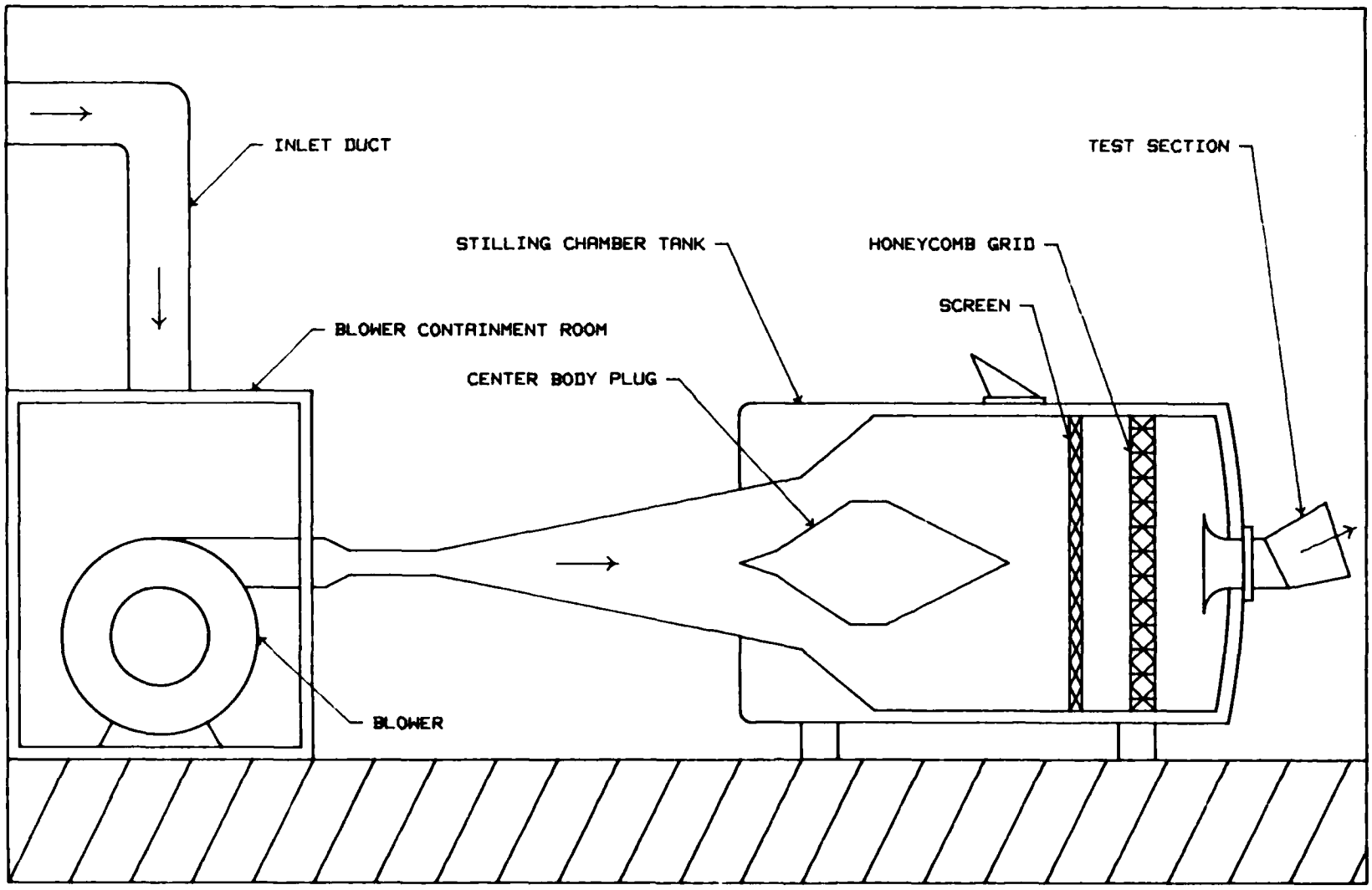

Fig. 4. General Schematic of the AFIT Cascade Test Facility

Test Section

The CTF test section, shown in Fig. 5, consisted of seven NACA-A506 airfoils. According to Moe (17:5), the profile of these blades was similar to that found in the latter stages of a high pressure compressor. The blades were set at a row angle of 31 degrees, a stagger angle of 16 degrees, and an angle of attack of 15 degrees. This resulted in a flow turning angle of 19 degrees. The individual blades had a chord and span of two inches for an aspect ratio of one. The solidity was 1.5 based on a blade spacing of 1.333 in. In addition, the two outside blades were half imbedded into the end walls in order for the test section to simulate an infinite cascade (30:8).

Seven static pressure taps were located on one side of the inlet duct to the test section and were used to verify the uniformity of the upstream flow and determine its velocity. The exit channel was made up of two 13 in long plexiglass sides with adjustable endwalls. Four static pressure taps were distributed along the length of each endwall to aid in setting the channel to the desired configuration. Additional pressure taps were placed along one sidewall to coincide with the four exit plane traverse locations.

Sidewall Suction System

As described by Moe (17:8), a boundary layer control mechanism was incorporated into the CTF test section. The sidewalls immediately around the blades were made of a

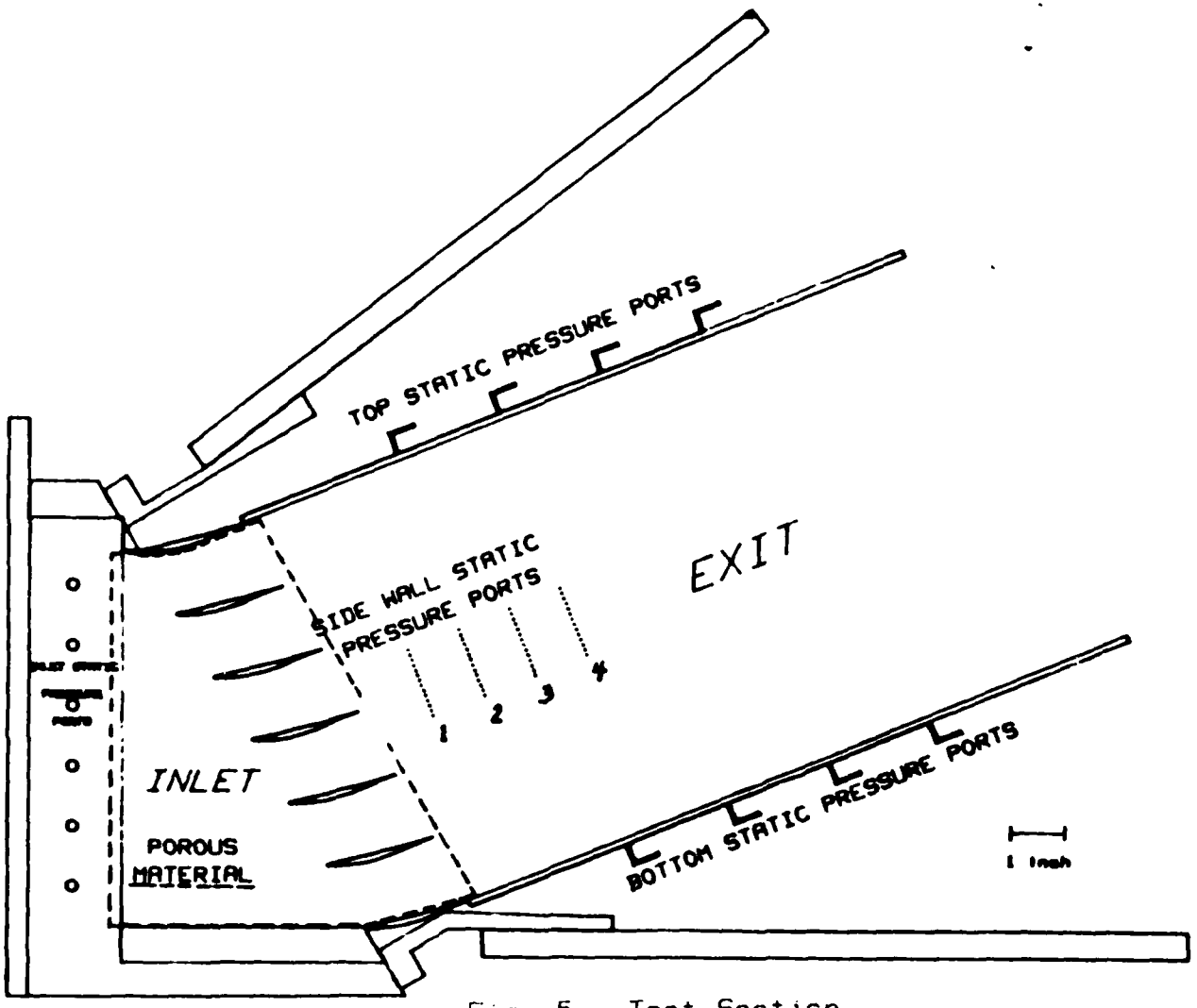

Fig. 5. Test Section

porous stainless steel through which the boundary layer can be continuously drawn off. Suction was provided by an industrial vacuum cleaner connected to the test section by two aluminium manifolds. Moe (17:47) determined that with the suction applied, two dimensional flow was established over the center span of the airfoils in the cascade extending for approximately two thirds the width of the blade.

Instrumentation

Monitoring of the flow conditions in the CTF required the use of a variety of pressure, temperature, and velocity measuring devices. A complete listing of the components that make up these systems is attached as Appendix A. Measurements made include the stilling tank total pressure and temperature, test section inlet and exit static pressures, and ambient temperature and pressure. Eighteen 30-in U-tube water manometers were also integrated into the system to monitor the test section inlet, exit, and endwall pressure taps as well as the tank total pressure and sidewall suction. In addition, a 48 channel Scanivalve pressure measuring system was used to obtain the pressure distribution about the suction surface of the center blade of the cascade.

The pressure transducers were calibrated over their operating ranges with a linear curve fit used to convert the output voltages to pressures. The two "T-type" copper/constantan thermocouple voltage outputs were converted into

temperatures through the use of software provided with the data acquisition system (10:8.78,8.85).

Velocity and turbulence data in the blade boundary layer and wake regions were obtained using three Thermal Systems International (TSI) Model 1050 Constant Temperature Anemometers. Two were used with a TSI model 1241-10 "X" configuration hot film probe to survey the center blade's wake region. The remaining one was connected to a TSI model 1218-T1.5 hot wire boundary layer probe. Since the temperature of the air going through the CTF is increased by 30 to 40 ° F above ambient, the hot wire/film probes were calibrated using a scheme that takes into account the effects of elevated temperatures (29). The complete procedure is detailed in Appendix B. The final result is a single calibration curve for each sensor that is applicable over the range of expected test conditions. Figures 6 and 7 are examples of such curves for the wake and boundary layer probes, respectively.

The calibration procedure required the use of an air supply whose velocity and temperature could be measured and varied as needed. This was accomplished using a modified TSI Model 1125 Calibrator system instrumented to measure the total temperatures at the interior chamber inlet and exit as well as the total pressure. A portion of the source air, provided by the shop compressor, was diverted through a quartz heater assembly powered by an adjustable 20 amp transformer. This "hot" air was then mixed with "cool" air

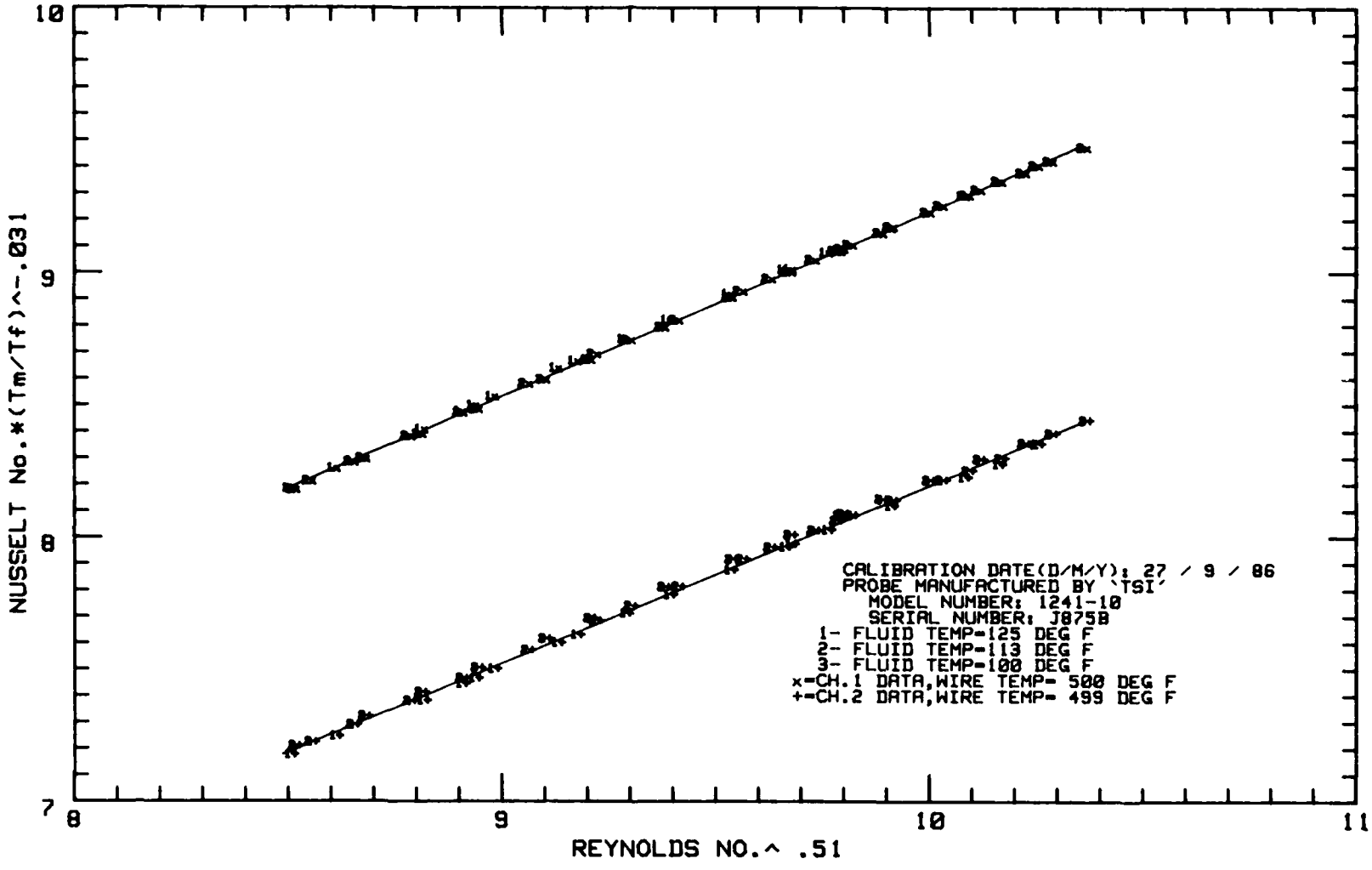

Fig. 6. Wake Probe Calibration Curve

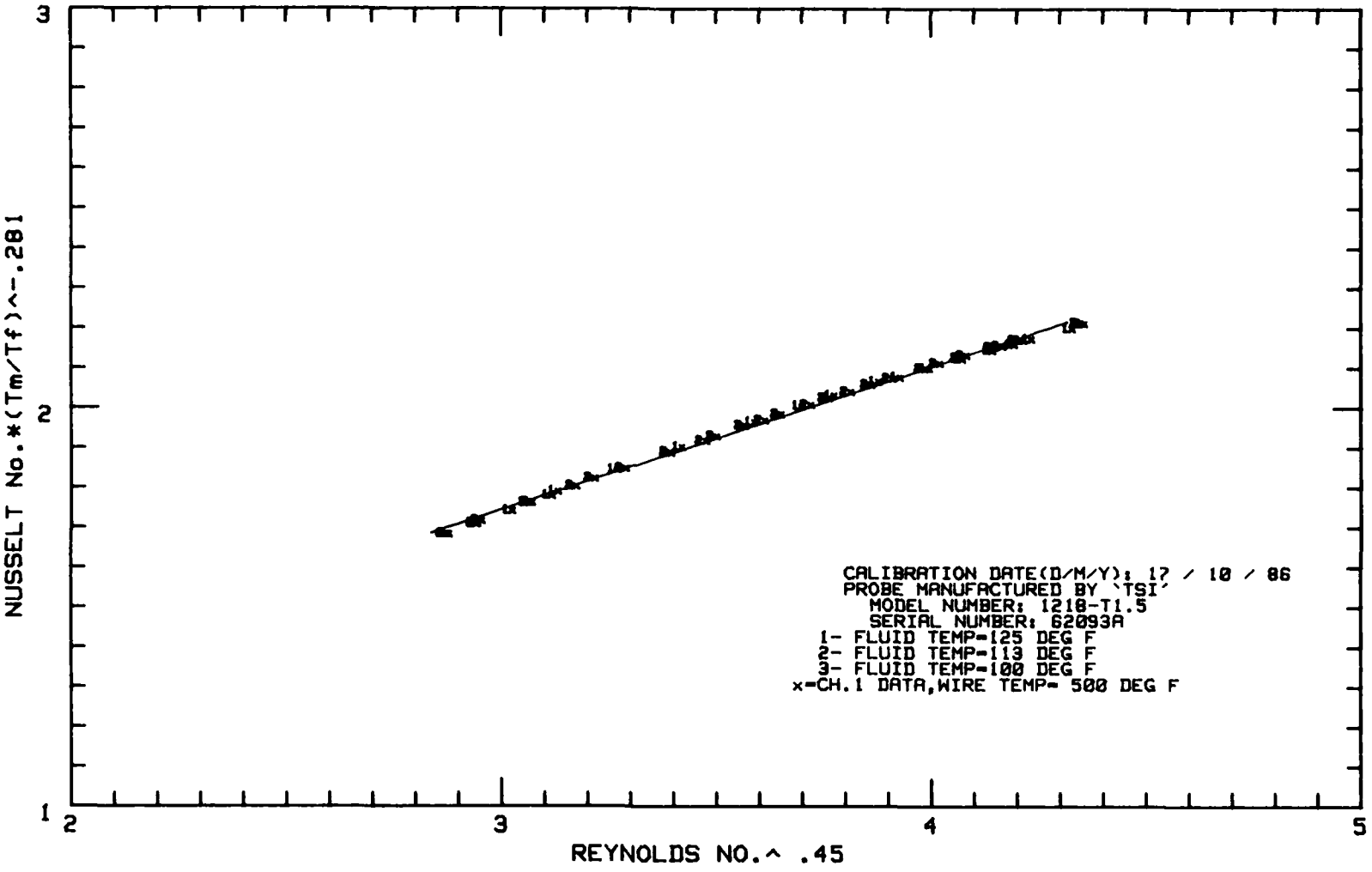

Fig. 7. Boundary Layer Probe Calibration Curve

directly from the compressor before being directed into the calibrator. By varying the amount of "hot" and "cool" air mixed upstream, the velocity and temperature of the air exiting the calibrator could be adjusted. A specified temperature was reached when the two thermocouples agreed to within a tenth of a degree Fahrenheit.

Traversing System

The hot wire/film sensors used to probe the flow about the cascade were connected to an 18 in probe support, the opposite end of which was fitted in an airfoil shaped mount. The complete sensor/support assembly was attached to a traversing mechanism capable of motor driven movements in both the X and Y directions. Spanwise movement was possible by manually adjusting a thumbscrew. The traversing system as a whole could be rotated about the Z axis in order to align the probe to the desired angle in relation to the cascade.

Though the sensor could be positioned manually, the traversing mechanism was integrated into the data acquisition system to allow automatic control of probe movement. In this mode, the accuracy of sensor positioning was estimated at +/- 0.002 in in both the X and Y directions. The actual resolution of the stepper motors in the X and Y directions were 0.002 and 0.001 in, respectively.

Blade Roughness Configurations

The NACA 65-A506 airfoils used in this investigation

were cast in sets of six blades each using Fiber-Resin Corporation FR44 resin and 5595 hardener. The mixture was poured into an aluminium casting mould and cured at room temperature for ten hours. To further increase the stiffness of the blades, the castings were then heat treated in two hour increments at 150, 200, and 250 ^{o}F.

It can be deduced that roughness would have the greatest effect on the performance of a cascade if it were applied on the suction surface, near the leading edge of the blade. In this region, the boundary layer is subjected to an adverse pressure gradient and the relative magnitude of the roughness elements to the boundary layer thickness is largest. Tanis (25:50) demonstrated this experimentally by varying the location of surface roughness and measuring the effect on the pressure loss coefficient.

In previous investigations using the AFIT CTF (17;25;30) the primary method of adding roughness to a blade was by applying different grades of carborundum grit to the surface and sealing them in place with an acrylic adhesive. This procedure had a number of drawbacks, the most serious of which was the possibility of altering the blade profile, particularly when applying the larger-sized grit. To alleviate this problem, the application of surface roughness in this study was incorporated into the actual casting process. This was done by tacking a strip of emery paper to the suction side of the casting mould, beginning a sixteenth of an inch back from the leading edge and extending to the 25 per-

cent chord point. Two grades of emery paper were used: 280 and 180. In addition, one set of blades were cast without added roughness to serve as a baseline smooth configuration for comparison.

The surface roughness of each blade was measured with a Rank Taylor Hobson Surtronic 3 profilometer. A cut-off distance of 0.8 mm was used with the standard pickup 112/1503. A total of 36 readings were taken about the center blade's midspan and averaged. The output of the profilometer was the arithmetic average roughness, Ra , in micrometers. This roughness parameter is described in Appendix C along with two empirical correlations to convert Ra to the equivalent sand roughness, k_s , and Schäffler's technical roughness, k . The results are tabulated below.

TABLE I

Blade Roughness Data

Conf. #	Ra, μm	k_s, μm	k, μm
1	0.45	2.79	4.01
2	12.1	75.0	107.7
3	18.3	113.5	162.9

For comparison, Koch and Smith (12:423-424) report an Ra value of 18 micrometers for 180 grade sandpaper. For the remainder of this investigation, roughness will be characterized in terms of Ra or k_s .

Suction Surface Pressure Distribution

Information on the suction surface pressure profile was obtained by instrumenting the center blade of each roughness configuration with 38 static pressure taps. Due to the small size of the blade, the taps were offset a sixteenth of an inch on either side of the midspan and alternated left and right. The use of a staggered layout for the taps was possible due to the two-dimensionality of the flow. In addition, Williams (30:24) demonstrated that a profile obtained with a staggered arrangement did not differ significantly from one obtained with all the taps aligned along the blade's centerline.

Holes were drilled from either end of the blade to join with the taps. Small (0.022 in OD) metal tubes were inserted into the holes and connected to the Scanivalve system with pressure lines. The actual pressure tap arrangement is depicted in Fig. 8. A complete profile was not possible due to the thin trailing edge, and the need to accommodate holes for the blade's four mounting pins.

Data Acquisition and Analysis System

The CTF was monitored and controlled from an air conditioned room located alongside which housed a Hewlett-Packard (HP) 9845B computer integrated with an HP 3052A Automatic Data Acquisition System. Again the various components of the system are listed in Appendix A.

Software controlled the movement of the traversing mech-

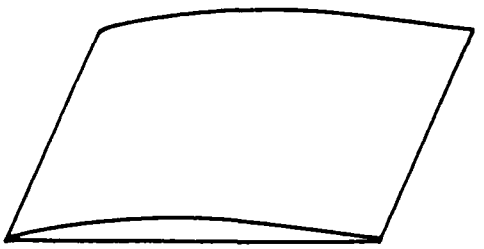

NACA 65-A506 Profile

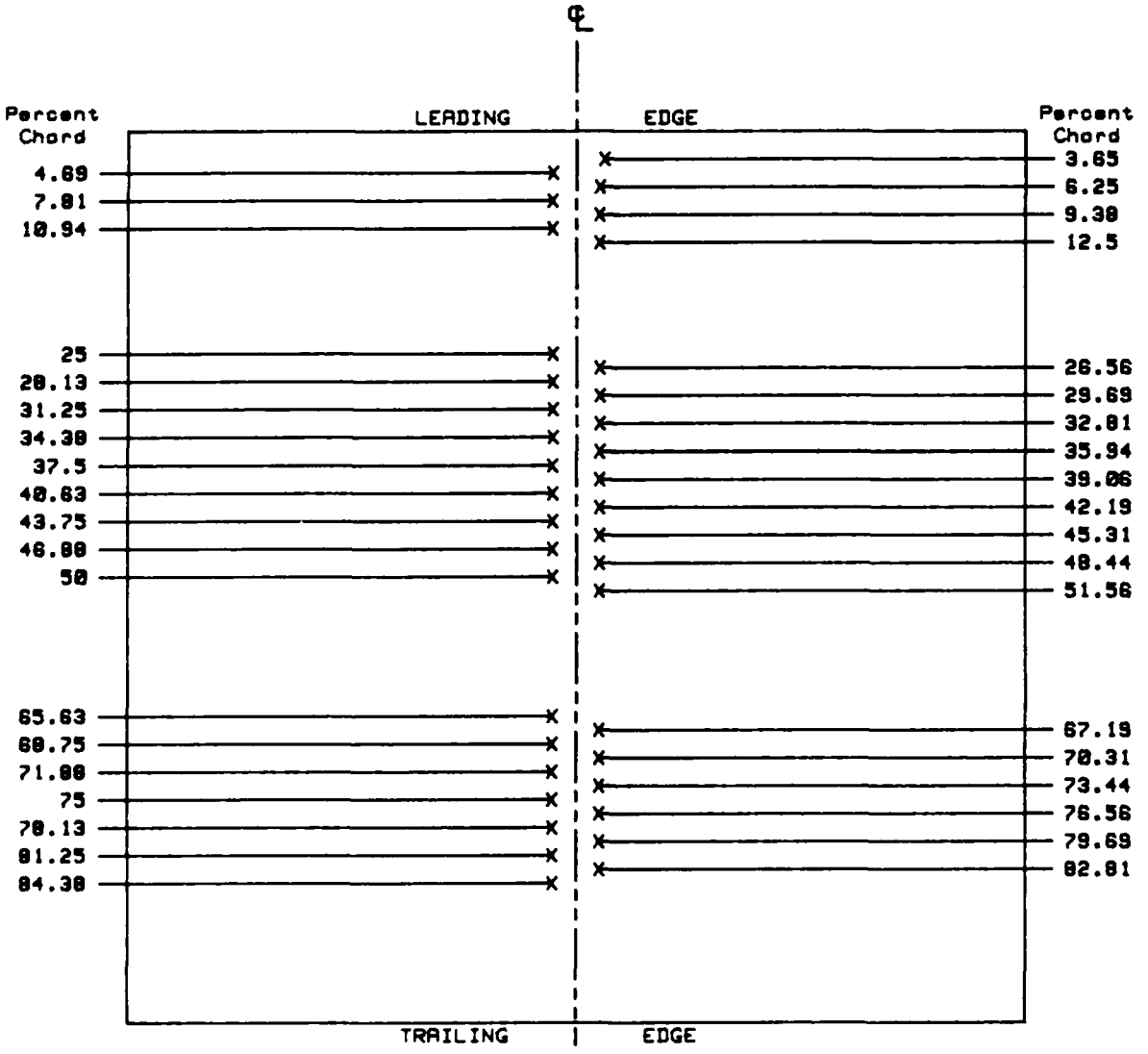

Top view of center blade, looking down at the suction surface, showing pressure tap locations (X) and tube arrangement.

Fig. 8. Blade Profile and Pressure Tap Arrangement

anism and read the voltage outputs from the various measuring devices. Though, in certain cases, data were reduced on-line, the standard procedure used was to store the voltage readings on magnetic disks. These were later converted and stored as engineering units making them available to additional programs used to calculate the performance parameters of interest.

IV. Experimental Procedure and Data Reduction

Testing Procedure

The testing procedure for this study was divided into three stages. The first stage consisted of a survey of the center blade's wake with a 1241-10 hot film probe. This was followed by the measurement of the pressure distribution about the suction surface of the center blade. The third and final stage made use of a 1218-T1.5 boundary layer probe to survey the flow field around the suction surface of that same blade. This three part procedure was repeated for each configuration of roughness.

Prior to taking any measurements, the CTF was allowed to warm up and the flow to reach a stabilized operating temperature. The exit endwalls and the boundary layer suction were then adjusted to balance the test section. The balanced condition was reached when the static pressure taps along both endwalls read approximately ambient pressure, and the inlet pressure to the test section was uniform. Moe (17) demonstrated that balancing the test section in this manner established two dimensional flow through the cascade.

Wake Survey

With the test section balanced, the traversing mechanism was rotated about the Z axis so as to align the probe support with the exit flow direction. This direction was de-

termined from the position of the endwalls. Wake surveys were then conducted at 1.25, 2.25, 3.25, and 4.25 in downstream of the center blade's trailing edge. Each traverse consisted of 133 data points located at 0.01 in intervals in the Y direction as shown in Fig. 9.

Velocity Correction. The voltage outputs of the two sensors were converted into X and Y components of velocity through the use of the probe's calibration curve. As was found in previous work with this cascade facility (25:16;17:12;30:23), the measured velocity was five to ten percent higher than theoretically possible. This was apparent when the exit total pressure calculated from the measured velocity was higher than the pressure measured in the stilling tank. This discrepancy was thought to be related to the variation in heat transfer rate with varying humidity as well as the variation of the probe support resistance with changing flow temperature (25:14-15). Note that during the calibration procedure, the probe support is not exposed to the different temperatures of the flow to the extent that it is during an actual run. The problem was corrected using a procedure outlined by Tanis (25:15-16) and Moe (17:12) in which continuity between two centerline planes located upstream and downstream of the cascade is used.

Local Turbulence Intensity. The ratio of the root mean square velocity to the streamwise velocity at a particular data point was used as the definition of the local turbu-

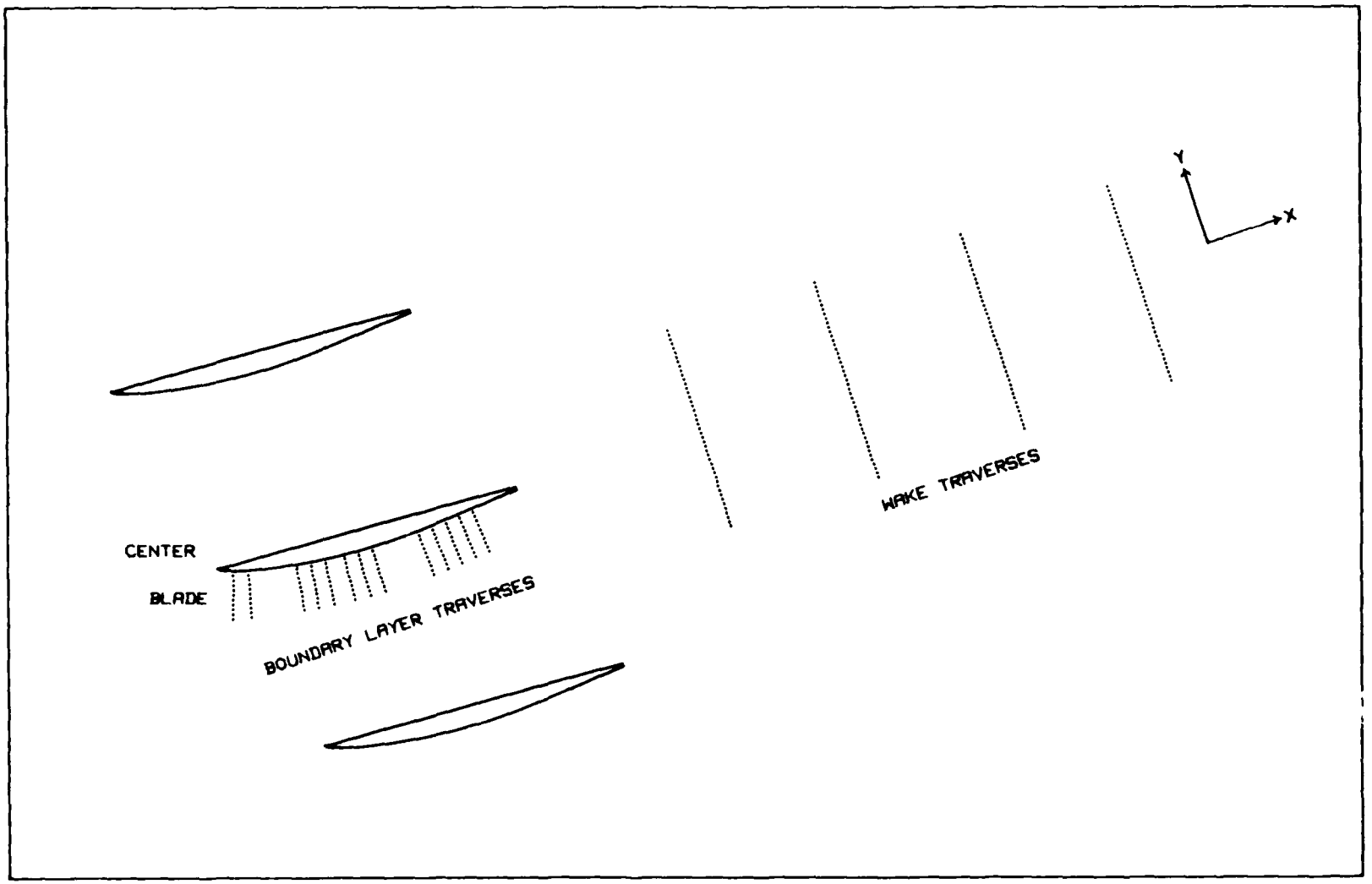

Fig. 9. Representation of Wake and Boundary Layer Traverses

lence intensity, Tu , in this investigation. That is

$$Tu = V_{rms}/V_2 \tag{16}$$

where V_{RMS} is the local time varying velocity, measured as the RMS voltage output of the anemometer, and V_2 is the local axial velocity, measured as the DC output.

Due to the configuration of the two sensors on the probe, Tu in the wake could be resolved into X and Y components, thereby giving an orientation to the fluctuations.

Total Pressure Loss. The total amount of losses through a cascade was quantified by the nondimensional total pressure loss coefficient, defined earlier in Eq (3). The total pressure upstream of the cascade was measured by the pressure transducer situated in the stilling tank. The total pressure at a particular traverse location downstream was calculated by first determining the total pressure P at each data point as follows:

$$P_{T_2} = P_{s_2}\left[1 - \frac{(V_2')^2}{2c_pT_T}\right]^{\gamma/(1-\gamma)} \tag{17}$$

where

P_{s_2} = exit static pressure
V_2' = corrected exit velocity
T_T = tank total temperature
γ = ratio of specific heats

The exit total pressure could then be determined by mass averaging these individually calculated total pressures:

$$\overline{P_{T_2}} = \frac{\int_A P_{T_2} \rho V_2' dA}{\int_A \rho V_2' dA} \qquad (18)$$

where P_{T_2} is the mass-averaged exit total pressure, ρ the local density evaluated using the perfect gas law, and dA the incremental area.

As pointed out by Moe (17:16), the area integrals above can be reduced to single integrals with respect to Y since the flow is two-dimensional and spanwise uniform at the blade centerline. The integrals were solved numerically using the trapezoidal rule.

Suction Surface Pressure Distribution

The Scanivalve pressure measurement system was used to measure the static pressure at each of the 38 tap locations on the suction surface of the center blade. This was repeated up to five times for each run, and the results stored on magnetic disks. The pressure coefficients were calculated using Eq (2).

This measurement was carried out immediately prior to any boundary layer run. This allowed for the calculation of a local velocity, U_L at each tap location based on the local static pressure. Applying Bernoulli's equation along a streamline from the inlet of the test section to a particular tap location yields

$$U_L = V_1(1 - C_p)^{1/2} \qquad (19)$$

This local velocity was used as a check against the results obtained with the boundary layer probe during the next phase of the investigation. In addition, it was used to calculate the mean reference temperature at which the fluid properties would be evaluated (see Appendix B).

Suction Surface Boundary Layer Survey

The boundary layer along the midspan of the center blade's suction surface was surveyed at thirteen chord locations. These corresponded to pressure taps and were located at the 4.69, 9.38, 25, 29.69, 34.38, 40.63, 45.31, 50, 65.63, 70.31, 75, 79.69, and 84.38 percent chord positions.

In the previous investigation (30:17), limitations in the axial movement of the traversing mechanism prohibited measurements forward of the 42.75 percent chord location. This limitation was resolved in this study by modifying the probe support mount fairing to allow an additional 2.25 in of movement in the axial direction. This modification also alleviated the blockage problem experienced by Williams (30:17), negating the requirement to rebalance the test section for each traverse.

Probe Positioning and Control. One of the objectives of this thesis was to fully automate the acquisition of boundary layer data. This required that the movement of the probe around the suction surface be computer controlled.

The profile coordinates, used by a computerized milling machine to manufacture the blade moulds, were entered into

the HP 9845B computer and referenced to an arbitrary point. With the probe support aligned with the center blade's chord line, the wire was manually moved to a known location in the test section. The traversing system's X and Y position encoders were then adjusted to reflect this position relative to the same arbitrary point. By knowing the location of the probe and the blade surface, the computer could now control the movement of the former in relation to the latter.

Accuracy of the traverse was very much dependent on the accuracy of the initial setting of the probe at the known location in the test section. This was estimated to be +/- 0.005 in in both the X and Y directions. The orientation of the probe in relation to the cascade during the traverses is depicted in Fig. 10.

A traverse at a particular chord location would begin with the computer positioning the probe wire at a point 0.03 in away from the surface of the blade. Some vibrations were present when the probe was moved from one data point to the next. Though these vibrations dampened out quickly, moving the probe no closer than 0.03 in from the blade reduced the chances of the wire contacting the surface.

A secondary reason for the offset starting position was to avoid any possible influence of the cooler blade surface on the heat transfer characteristics of the probe. Oka and Kostic (19:31,33) found that when a probe was in close proximity to a colder wall, the additional cooling effects

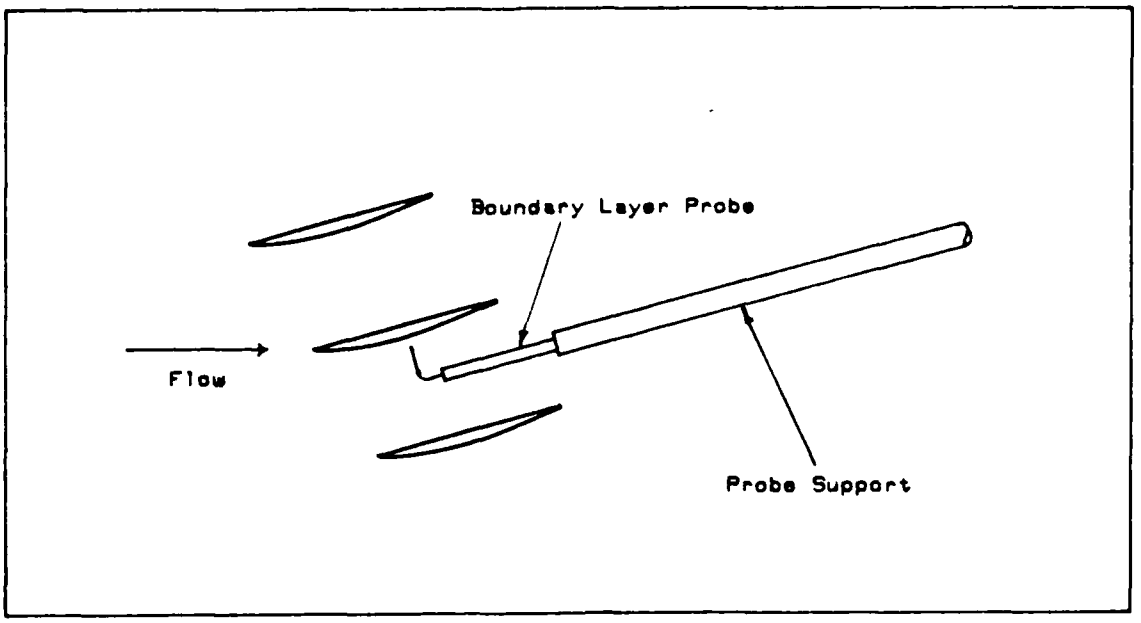

Fig. 10. Boundary Layer Probe Orientation

gave rise to higher apparent velocities. In their investigation, velocities measured in this region were on the order of five to six times greater than the true value. The maximum distance from the wall at which this influence was detected was 0.04 in for the condition of zero velocity flow. In addition, the region of influence decreased with increased Reynolds number. Consequently, an offset distance of 0.03 in, for the Reynolds number range of this study, was felt to be well clear of any influence of the wall.

From its starting position, the computer would automatically move the probe away from the blade in increments of 0.005 in for a total of 60 data points per traverse. At the same time, the axial position would be adjusted so as to maintain a traverse normal to the blade surface. The tra-

verses were depicted in Fig. 9. Once a particular traverse was completed, the probe would automatically be moved to the next chordwise location and the sequence repeated.

Unlike the wake survey, it was found that consecutive readings of the DC and, particularly, the AC voltage output varied considerably at each data point close to the blade. This was thought to be due, at least in part, to the higher frequency response of a hot wire compared to a hot film probe, requiring that some sort of mean reading be used. Therefore, at each data point in the boundary layer survey, ten readings of the AC and DC voltage outputs were taken and averaged. From a number of trial runs, it was found that the arithmetic mean of 10 readings did not differ considerably from that of 30 readings but that the data-taking time was significantly decreased.

Edge Velocities. Outside of the actual boundary layer, the measured velocity profile decreased with distance from the blade due to the presence of a blade to blade normal pressure gradient. This complicated the determination of the edge velocity and hence the boundary layer thickness.

As discussed previously in Section II, the measured velocity profile can be assumed to be a composite profile made up of three regions. This was mathematically represented by Eq (1) repeated below:

$$U_{MEAS} = U_{BL} + U_{INV} - U_e \qquad (1)$$

Looking specifically at the case right at the wall, the no-

slip condition dictates that both the measured velocity and boundary layer velocity equal zero. From the above equation, U_E must then be equal to U_{INV} at the wall. Therefore, in order to determine the edge velocity and subsequently the boundary layer velocity profile, one must first find a way to extrapolate the inviscid velocity profile to the surface of the blade. Deutsch and Zierke point out that a "... rigorous approach does not appear possible so one must settle for a self consistent attack which produces plausible results" (7:8).

Ball, Reid, and Schmidt (2:11-13), in their investigation into the end-wall boundary layer in a two-stage fan, addressed the problem by using an iterative approach. They began by curve fitting the outer inviscid velocity profile to an assumed value for U_E . The boundary layer velocity profile could then be calculated using Eq (1). Boundary layer integrations were carried out to obtain the momentum and displacement thicknesses which in turn were used to calculate the skin friction coefficient based on Ludwieg and Tillman's relationship (2:11). A subsequent iteration of Cole's law of the wake (2:11) resulted in a value for the shear velocity, U_τ . A new value for the edge velocity could then be obtained from the relationship

$$U_E = \frac{U_\tau}{(C_f/2)^{1/2}}$$

This value was compared to the value assumed for U_E at the start of the loop. If it was different, the process was re-

peated with the new value until such time the new and old U 's were approximately equal.

This approach was not possible in this investigation due to the unknown nature of the flow field at distances closer than 0.03 in from the blade surface. The lack of data in this region precluded the determination of the momentum and displacement thicknesses.

The scheme that was employed in this study was one adapted from Deutsch and Zierke (7:8-9). They found that a range of points existed in the inviscid region through which a quadratic curve fit extrapolated to the wall would yield an edge velocity that was essentially invariant. This range was represented by $N_{INV}/2$ +/- $N_{INV}/4$ where N_{INV} is the number of data points from the maximum velocity position to the measured point furthest from the blade. Williams (30:32), in his measurements of the boundary layer over the aft region of the blade, curve fitted $N_{INV}/2$ of the outermost points of the measured velocity profile. He carried out both a first and second order least squares fit and chose the one with the least variance.

Initially, the problem was approached in the same manner as Williams. Difficulties arose, however, when attempting to duplicate results from one run to the next. This was particularly true for traverses located near the leading edge. In this region, the inviscid profile exhibits some curvature as compared to the linear decay of velocity for traverses further aft on the blade (7:6). The procedure was

therefore modified as follows. First, both linear and quadratic least squares fits were carried out for three ranges of outermost points: $N_{INV}/4$, $N_{INV}/2$, and $3N_{INV}/4$. All of these were extrapolated to the wall to yield a maximum of six values for edge velocity. Some second order fits gave complex conjugate roots when extrapolated and were ignored. The remaining values for U_E were reviewed, and any that were significantly different from the rest were deleted. What was left was averaged to give a mean value for U_E for that particular traverse location.

Boundary Layer Thickness. Using Eq (1), the boundary layer velocity profile was calculated for each value of edge velocity remaining from the curve fits. In each case, the boundary layer thickness δ_{BL} was found by determining the distance from the blade where

$$U_{BL} = 0.99\ U_e \qquad (20)$$

Note that the particular edge velocity corresponding to that curve fit was used and not the mean value. The separate values for δ_{BL} were then averaged to give a mean boundary layer thickness for that chordwise location.

Local Turbulence Intensity. In a manner similar to the wake survey, the local turbulence intensity in the boundary layer, Tu_{BL} was calculated using

$$Tu_{BL} = U_{RMS}/U_{MEAN} \qquad (21)$$

where U_{RMS} is the local time varying velocity measured as

the true RMS output of the anemometer and U_{MEAS} the local streamwise measured velocity determined from the DC output.

Deutsch and Zierke (7:9) point out that turbulence intensities in a classical equilibrium boundary layer will show a higher than freestream value for distances $y \leq 1.25\delta$. This relationship was used to obtain a rough value for the boundary layer thickness to compare with the hot wire results.

V. Results and Discussion

Suction Surface Pressure Distribution

The static pressure measured at each of the 38 pressure tap locations on the suction surface was reduced to pressure coefficients using Eq (2). For each blade configuration, the pressure coefficients obtained from three runs were averaged to give a mean pressure profile. These profiles are shown in Figures 11 through 13. Though these plots are based on an average of the results, it was found that the profiles for a particular configuration were very similar from run to run. This is an indication of the consistency of the flow through the CTF.

The profile for configuration 1, Fig. 11, is very similar to that obtained by Williams (30:27) for his smooth baseline blade. The additional pressure taps used in this investigation provide for greater definition of the profile particularly in the forward region of the blade (seven taps versus two used by Williams). The profile between the 25 and 50 percent chord locations is relatively flat suggesting that the flow has separated. It has not, however, completely separated since the pressure coefficient begins to increase again aft of the 65 percent chord point. Rather, the flat region marks the presence of a laminar separation bubble. The exact locations of the points of separation, transition, and turbulent reattachment are difficult to

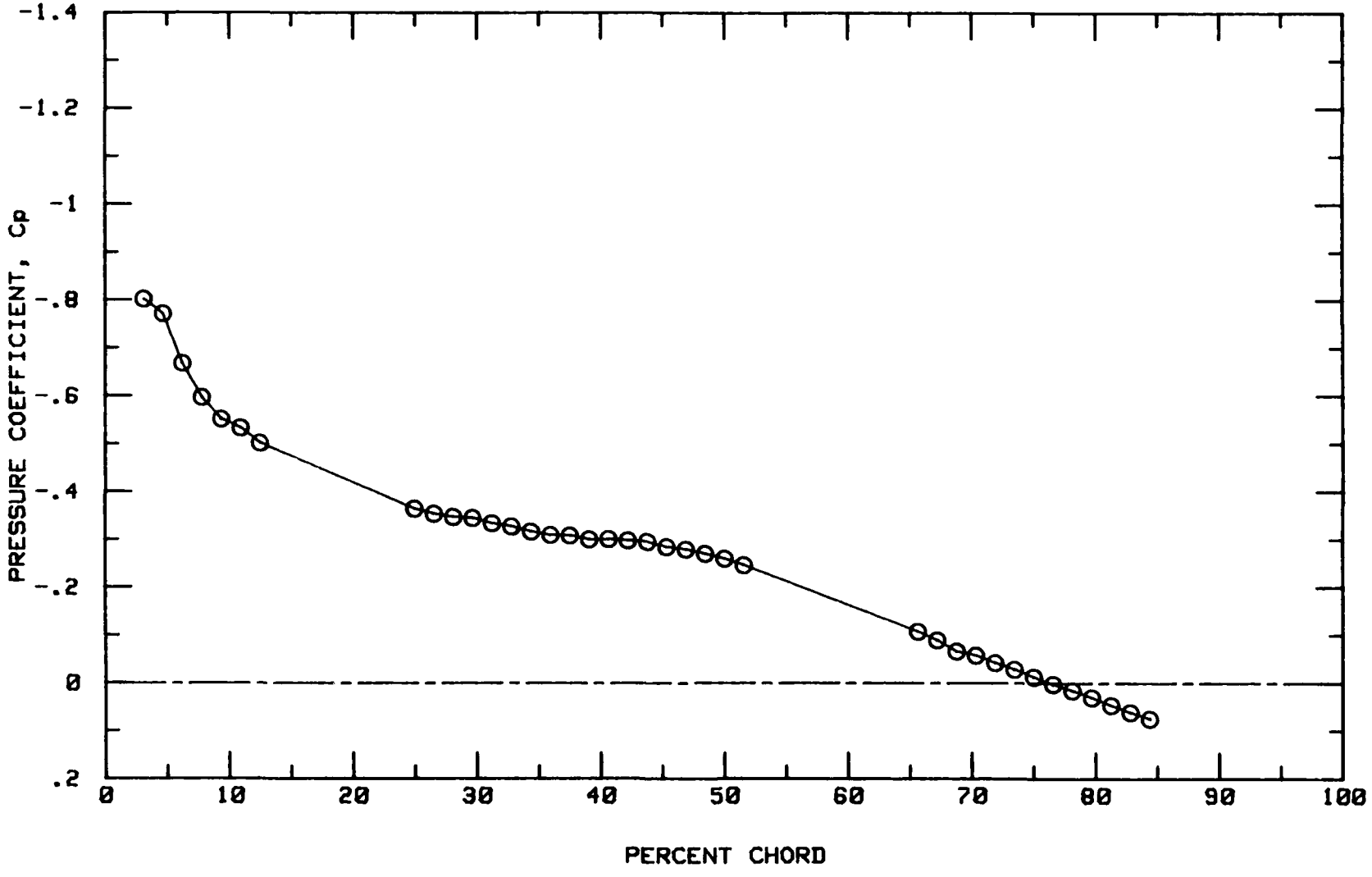

Fig. 11. Pressure Profile, Conf. #1, Ra = 0.45 micrometers

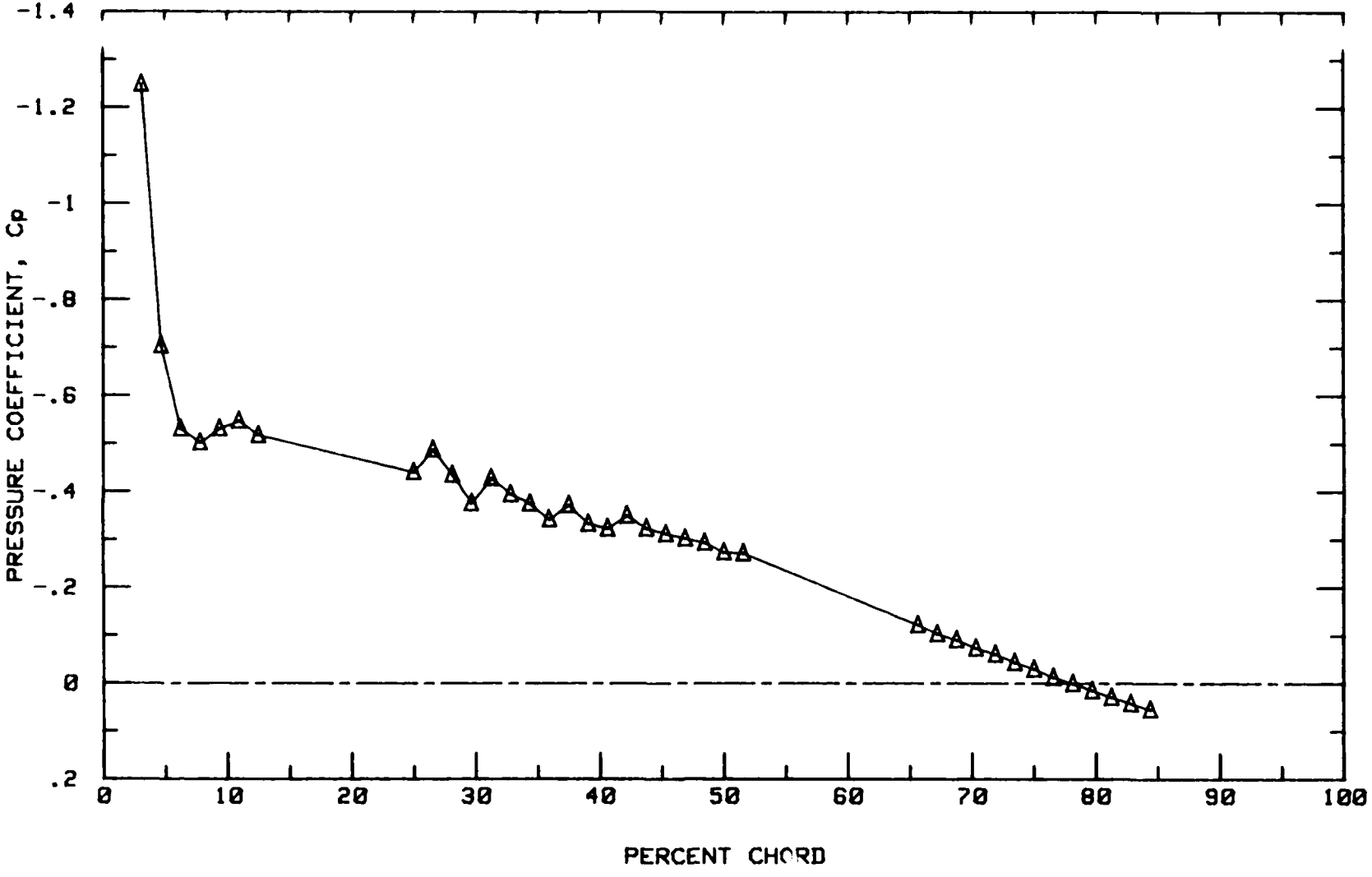

Fig. 12. Pressure Profile, Conf. #2, Ra = 12.1 micrometers

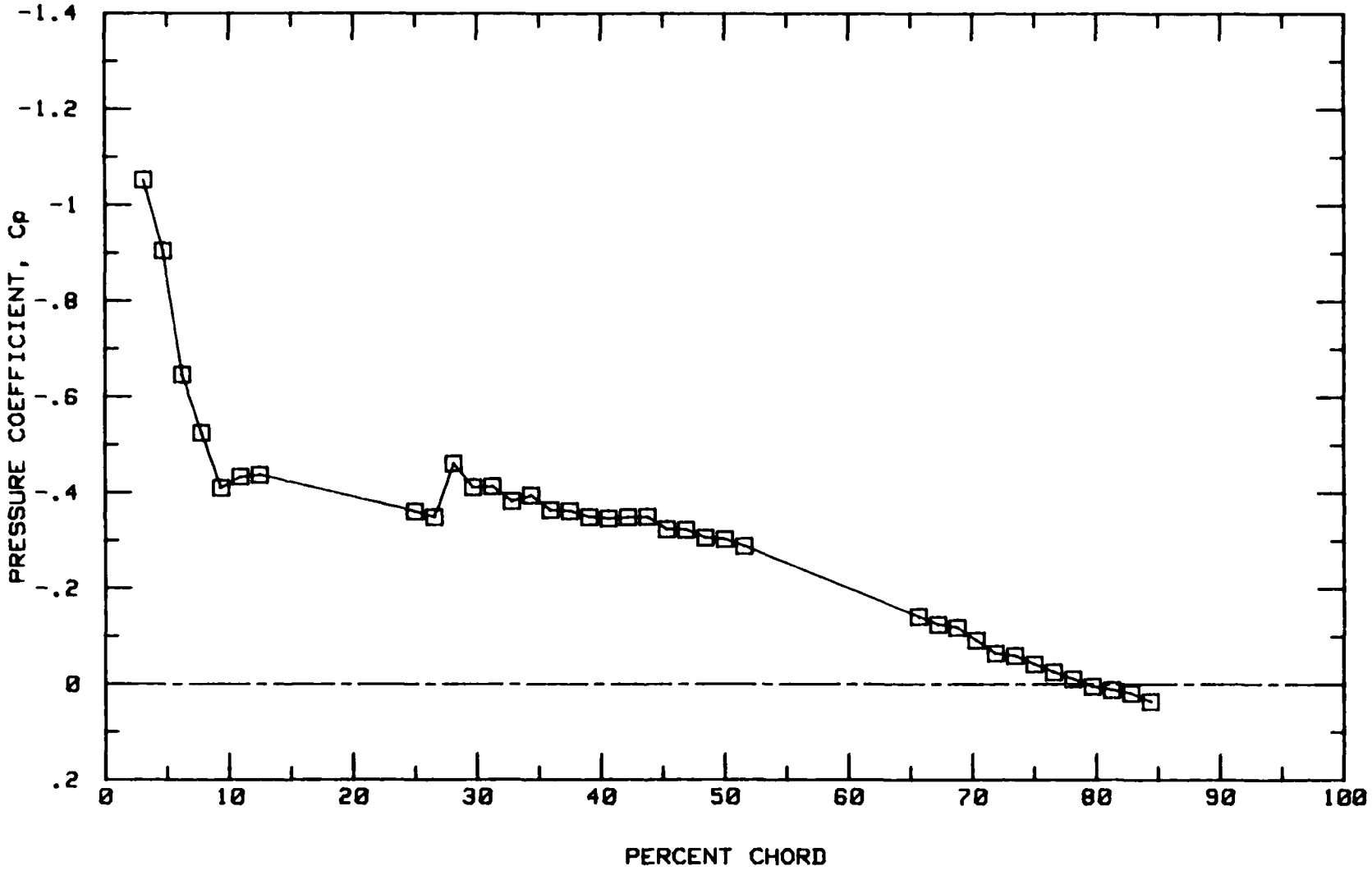

Fig. 13. Pressure Profile, Conf. #3, Ra = 18.3 micrometers

pinpoint due to the lack of the associated sharp discontinuities. It does appear though that the flow reattaches by about the 50 percent chord point.

Analyzing the pressure profiles for the two roughened blades, Figs. 12 and 13, a definite fluctuation exists in the pressure coefficient between the 25 and 42 percent chord locations. This was not apparent in Williams (30:28-30) results. Though not definite, it is felt that the cause of this anomaly lies in the method of applying the roughness. By incorporating the roughness in the actual casting process, it was anticipated that the profile of the blade could be maintained without adding a joint or other discontinuity to mark the edge of the emery paper. This, unfortunately, was not the case as a distinct though small ridge was apparent at about the 25 percent chord point. This is where the roughness ends, and the regular surface of the blade continues. The fluctuations do dampen out, however, and the profiles aft of the 45 percent chord location follow the same trend as for configuration 1.

Another distinct change in the pressure profile with the addition of roughness occurred in the forward part of the blade. The pressure coefficient at the forwardmost tap, 3.125 percent chord, is significantly less than the corresponding baseline value. For configuration 2, there is approximately a 58 percent decrease, while configuration 3 experiences about a 34 percent decrease. The magnitude of these jumps may have been influenced, to a certain extent,

by the location of the forwardmost tap which coincides with the transition from smooth to roughened surface. In both cases, over a short distance downstream, the pressure increases to values greater than that of configuration 1. This, of course, means that the adverse pressure gradient is much more severe for the roughened blades than for the smooth one. This can be seen by the steep slope of the pressure profile in the forward region of the blade.

Due to the fluctuations present, it is difficult to identify a distinct constant pressure plateau for configurations 2 and 3 although one is possible for the latter from about the 38 to 44 percent chord points. Nevertheless, it appears unlikely that the initial laminar boundary layer, with its limited momentum influx, could advance that far against such an adverse pressure gradient before separating (21:154). A more plausible interpretation of the results is that laminar separation occurs shortly aft of the pressure minimum, where both profiles exhibit a local pressure maximum. These points are at the 7.8 and 9.4 percent chord locations, respectively, for configurations 2 and 3. Due to the finite spacing between pressure taps, a short constant pressure plateau may exist here. At the very least, the distinct variations in the profiles about these points suggest that the boundary layer is undergoing some sort of change, if not a laminar separation bubble, then possibly just a natural transition from a laminar to a turbulent state without separation. For either to occur, however, re-

quires the transition point to move forward as compared to configuration 1. The likelihood of this occurring can be evaluated by examining the influence of surface roughness on transition.

When a laminar boundary layer becomes unstable with respect to small velocity disturbances, it will begin the transition to the more stable turbulent mode (24:334). The distance over which this transition takes place is small and often thought of as a point, specifically, the transition point (21:159). The disturbances that affect the boundary layer in this manner include those produced by surface irregularities such as roughness. If the disturbances are large enough, the laminar boundary layer will become unstable earlier, and the transition point will move forward. The larger the roughness elements, the farther forward the transition point moves until, eventually, its location coincides with the roughness itself (23:536).

The above suggests that a limit exists for surface roughness below which no effect is felt by the transition point. This limit is expressed as (24:335)

$$\frac{V_1 k_e}{\nu} \leq 120 \qquad (22)$$

where ν is the kinematic viscosity of the flow. For a typical inlet velocity of 480 ft/sec and a total temperature of 113 ° F, Eq (22) gives a critical roughness height of 13.61 μ m. Comparing this value to those in Table I, both configurations 2 and 3 have equivalent sand roughness values

that are substantially greater. Therefore, it is expected that transition will occur sooner for those two blade configurations as compared to the smooth blade whose k_s value is less than the critical height.

Except for a slight decrease with roughness, the profiles aft of the 45 percent chord for configurations 2 and 3 are essentially the same as the baseline case. This reinforces the idea that the flow in this region is also turbulent. It is possible for the flow to be completely separated aft of the 84.375 percent chord, but there were no pressure taps located there to verify that condition. It is unfortunate that, due to the blade mounting pins, two of these gaps exist in the pressure data. This is particularly true for the forward one which is close to the leading edge of the blade and could possibly mask significant information.

Boundary Layer

Three series of boundary layer traverses were carried out for each configuration over a period of two to three days. Representative plots from one of those runs are attached as Appendices D, E, and F for configurations 1, 2, and 3 respectively. Each figure consists of: (1) the measured velocity profile showing the influence of the normal pressure gradient; (2) the better of a first or second order least squares fit of $N_{INV}/2$ of the outermost points; and (3) the resultant boundary layer velocity profile as calculated from Eq (1). The inviscid curve fit is shown extrapo-

lated to the wall, giving the value for the edge velocity for the particular run presented. For comparison, the mean value for the edge velocity, based on an average of as many as six different curve fits per location, over three separate runs, is marked as an E on the velocity axis.

Edge Velocity. The mean edge velocities for each configuration are tabulated in Table II. Included, for comparison, are the corresponding velocities, U_L , determined from the pressure profiles using Eq (19). The other parameters listed will be discussed later.

The relatively good agreement between the values of U_E and U_L indicates that the method of obtaining edge velocities from the hot wire data is a reasonable one. The best agreement was obtained for those regions with a flatter pressure profile. An example is configuration 1 between the 25 and 50 percent chord locations. The largest differences were at the forwardmost points which coincide with the larger pressure gradients. Data obtained by Deutsch and Zierke (7:16) and Williams (30:33) behave in a similar fashion.

The variation of the edge velocity along the suction surface can be seen in Fig. 14. For this plot, the edge velocity is non-dimensionalized with respect to the inlet velocity. With the exception of the forward region, there is little difference between the three configurations, and particularly between the two roughened ones. This is understandable given the closeness of the pressure profiles. As expected, the edge velocity decreases with distance along

TABLE II

Boundary Layer Parameters

Conf. #	% Chord	U_e (ft/sec)	U_t (ft/sec)	δ_{BL} (in)	Tu δ_{BL} (in)
1	4.688	603.30	656.61	0.032	0.032
	9.375	592.44	614.93	0.038	0.039
	25.000	575.94	577.23	0.046	0.048
	29.688	574.17	573.27	0.046	0.052
	34.375	570.83	567.46	0.046	0.052
	40.625	568.37	564.23	0.048	0.048
	45.313	566.24	560.45	0.047	0.043
	50.000	562.11	555.32	0.048	0.044
	65.625	540.01	520.64	0.054	0.055
	70.313	533.13	508.93	0.058	0.056
	75.000	528.52	498.07	0.066	0.060
	79.688	519.72	487.31	0.070	0.062
	84.375	508.80	476.27	0.076	0.068
2	4.688	580.48	637.16	--	--
	9.375	573.47	603.33	--	0.031
	25.000	564.16	585.68	0.033	0.036
	29.688	559.89	572.43	0.033	0.031
	34.375	558.59	572.16	0.034	0.039
	40.625	553.49	561.47	0.040	0.048
	45.313	551.67	559.04	0.043	0.051
	50.000	547.64	550.93	0.046	0.056
	65.625	525.08	517.38	0.055	0.058
	70.313	517.81	505.74	0.059	0.064
	75.000	512.05	495.77	0.068	0.060
	79.688	503.14	484.57	0.073	0.067
	84.375	495.17	474.92	0.079	0.072
3	4.688	589.81	667.46	--	--
	9.375	567.71	574.19	--	0.030
	25.000	560.16	564.70	0.037	0.036
	29.688	560.43	575.09	0.039	0.045
	34.375	557.72	571.67	0.044	0.047
	40.625	553.07	561.94	0.050	0.059
	45.313	550.19	557.25	0.051	0.063
	50.000	546.42	552.69	0.051	0.064
	65.625	523.61	517.35	0.062	0.067
	70.313	516.92	506.11	0.070	0.068
	75.000	508.55	494.46	0.075	0.073
	79.688	500.22	483.30	0.080	0.075
	84.375	490.32	475.67	0.086	0.080

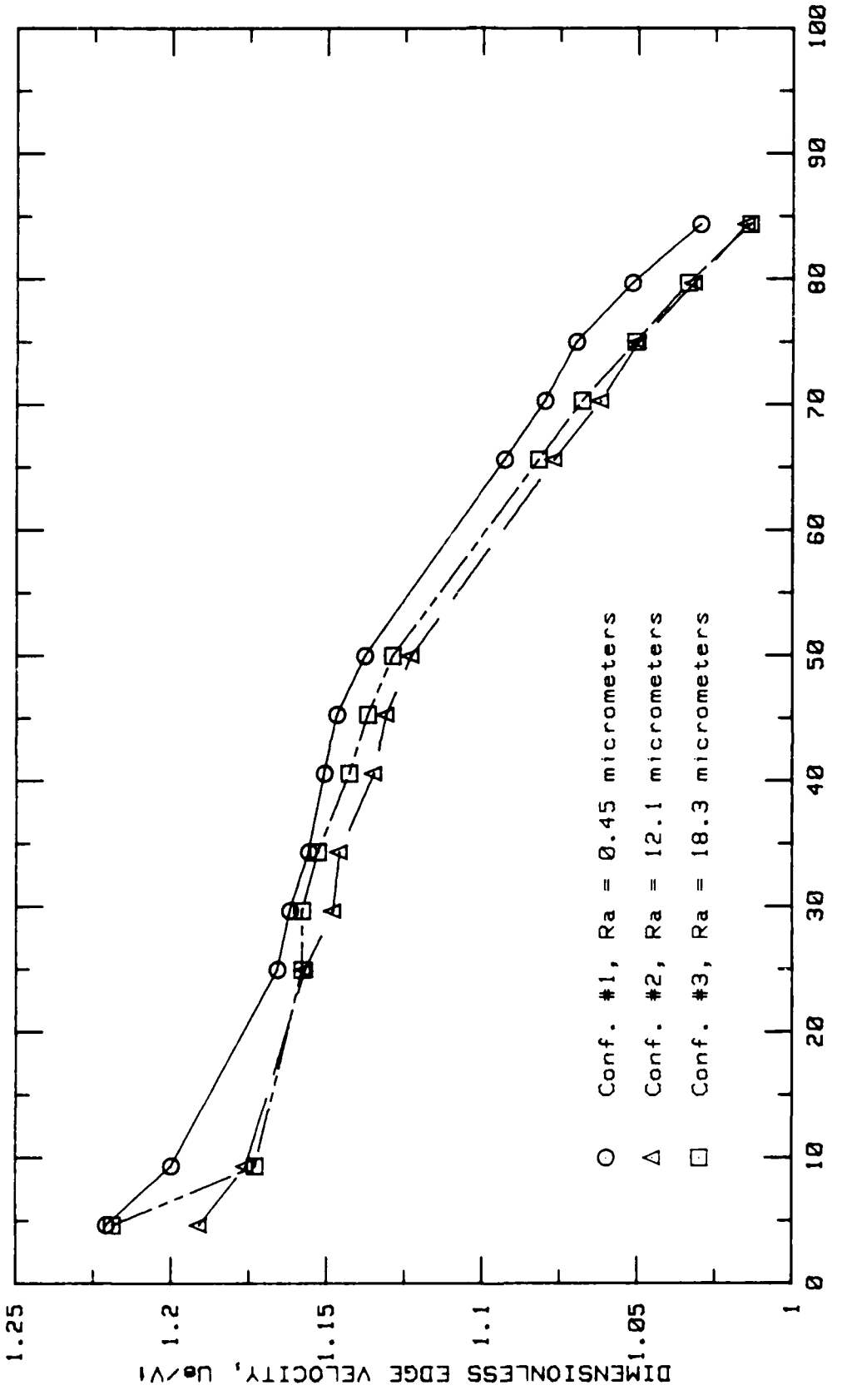

Fig. 14. Boundary Layer Edge Velocity Along the Suction Surface

the blade. It also appears that edge velocity increases with the addition of roughness since the plot shows configuration 3 with slightly higher velocities than configuration 2. This is in keeping with the pressure profiles which show configuration 3 having slightly less pressure over most of the surface. The increase in velocity is due to the thickening of the boundary layer with roughness which constricts the inviscid region between the blades. In order to maintain the mass flow rate, the velocities in that region must increase. Note, however, that edge velocities for both rough blades are lower than that for the smooth blade. This contradiction is more than the likely a result of the uncertainty in the traversing mechanism.

Boundary Layer Thickness. The boundary layer thickness, δ_{BL}, was calculated using Eq (20). Fig. 15 shows the variation in boundary layer growth with roughness. The results are also listed in Table II. The boundary layer for configuration 1 appears to confirm the previous analysis that the flow is turbulent over the back half of the blade. This can be seen by the distinct thickening of the boundary layer in this region. It is interesting to note that the constant pressure plateau, associated with a laminar separation bubble, in the pressure profile corresponds to a relatively flat boundary layer in Fig. 15.

The lack of data points in the forward region of the blade for configurations 2 and 3 indicates local boundary layer thicknesses that are less than 0.03 in, the minimum

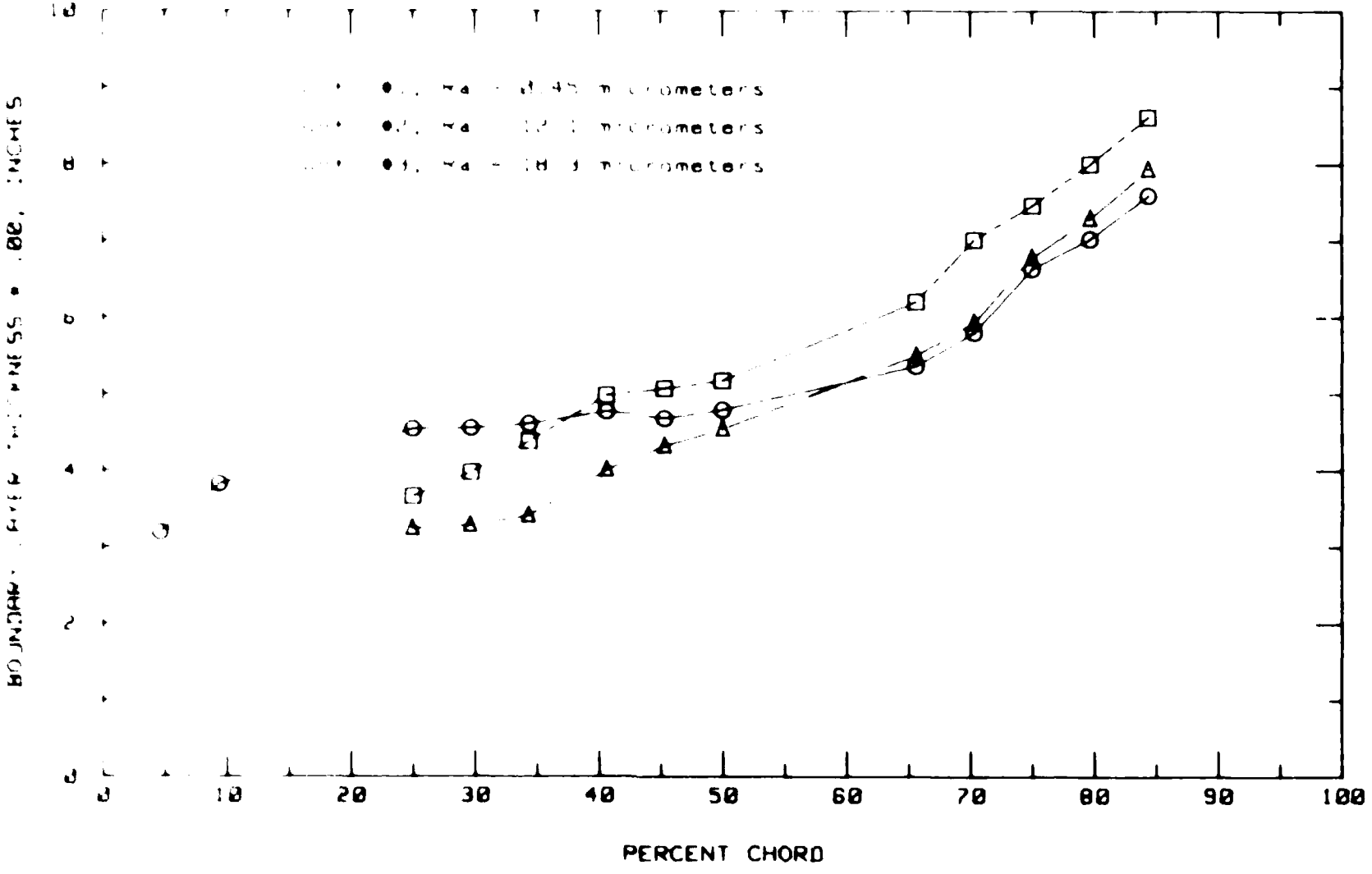

Fig. 15. Boundary Layer Growth Along the Suction Surface

distance the probe is brought from the surface. In view of the inherent errors involved in positioning the probe, however, it is entirely possible for the boundary layer to be thicker than 0.03 in in this area. In comparison with configuration 1, the boundary layer growth shown for the two rough configurations appears to be that of a developing turbulent boundary layer. This would be in keeping with the interpretation of the corresponding pressure profiles discussed earlier. As expected, configuration 3, with its greater roughness, has a thicker boundary layer than configuration 2. However, measurements indicate that both rough blades have thinner boundary layers than configuration 1 over the first portion of the blade. This region extends back to about the 37 and 58 percent chord points for configurations 3 and 2 respectively. The reason for this anomaly is unclear but may be a result of one or more of the following: (1) initial probe positioning accuracy estimated to be [illegible] inches in both the X and Y directions; (2) an apparent increase in boundary layer thickness for configura[illegible] due to the laminar separation bubble; and (3) an apparent decrease in a rough blade's thickness due to diffi[illegible] the point where the velocity is [illegible] boundary layers. [illegible] boundary

sity in the boundary layer, as calculated by Eq (21), is shown plotted as a function of distance from the surface in Appendices G, H, and I, corresponding to configurations 1, 2, and 3, respectively. As mentioned in section IV, the turbulence intensity will increase from its free-stream value as the distance to the blade surface decreases. This increase is first felt at a distance of $y_1 = 1.25\ \delta_{BL}$. The boundary layer thicknesses obtained from this relationship are tabulated for each configuration in Table II. The agreement between thickness predicted in this manner and that determined from the velocity profile is inconsistent. In some cases, the two agree exactly while in others, the difference can be as high as 30 percent. The range is not surprising when one considers that the above relationship for the increase in turbulence intensity assumes a classical equilibrium boundary layer, i.e., one with no pressure gradient along the surface. Clearly the pressure profiles indicate that the suction surface boundary layer cannot be considered to be in equilibrium (7:5,9). In addition, the measured turbulence intensities continue to decrease somewhat outside of the boundary layer. Therefore, unlike Deutsch and Zierke's results (7), the lack of a constant free stream value for turbulence makes it difficult to pinpoint the location where turbulence intensity first increases near the boundary layer.

Wake Surveys

As detailed previously, the flow exiting the cascade was probed by a two-dimensional hot film sensor at four distances downstream of the center blade's trailing edge. Both velocity and turbulence intensity measurements were resolved into their respective X and Y components, and the resultant vectors plotted. The results are collected in Appendices J, K, and L corresponding to configurations 1, 2, and 3, respectively. Each figure contains both velocity and turbulence intensity vectors: the lighter lines for velocity and the darker ones for turbulence intensity. The origin of each vector is the actual surveyed position, and their magnitudes can be converted to their respective units with the scale factors indicated. These are 150 ft/sec/in for velocity and 5 percent/in for turbulence intensity.

The wake produced by the boundary layers along the blade is clearly discernible. By numerically integrating the velocity profiles, the displacement, momentum, and pseudoenergy thicknesses can be obtained as defined by Eqs (4) through (6). These, along with other wake characteristics, can then be analyzed, and the effects of surface roughness determined.

Wake Minimum Velocity. The plot of the downstream variation in the velocity ratio, V_{MIN}/V_O, is shown in Fig. 16 for all three roughness configurations. For comparison, two of Moe's (17) configurations are also plotted. His data is for the same blade type and flow conditions, but with a

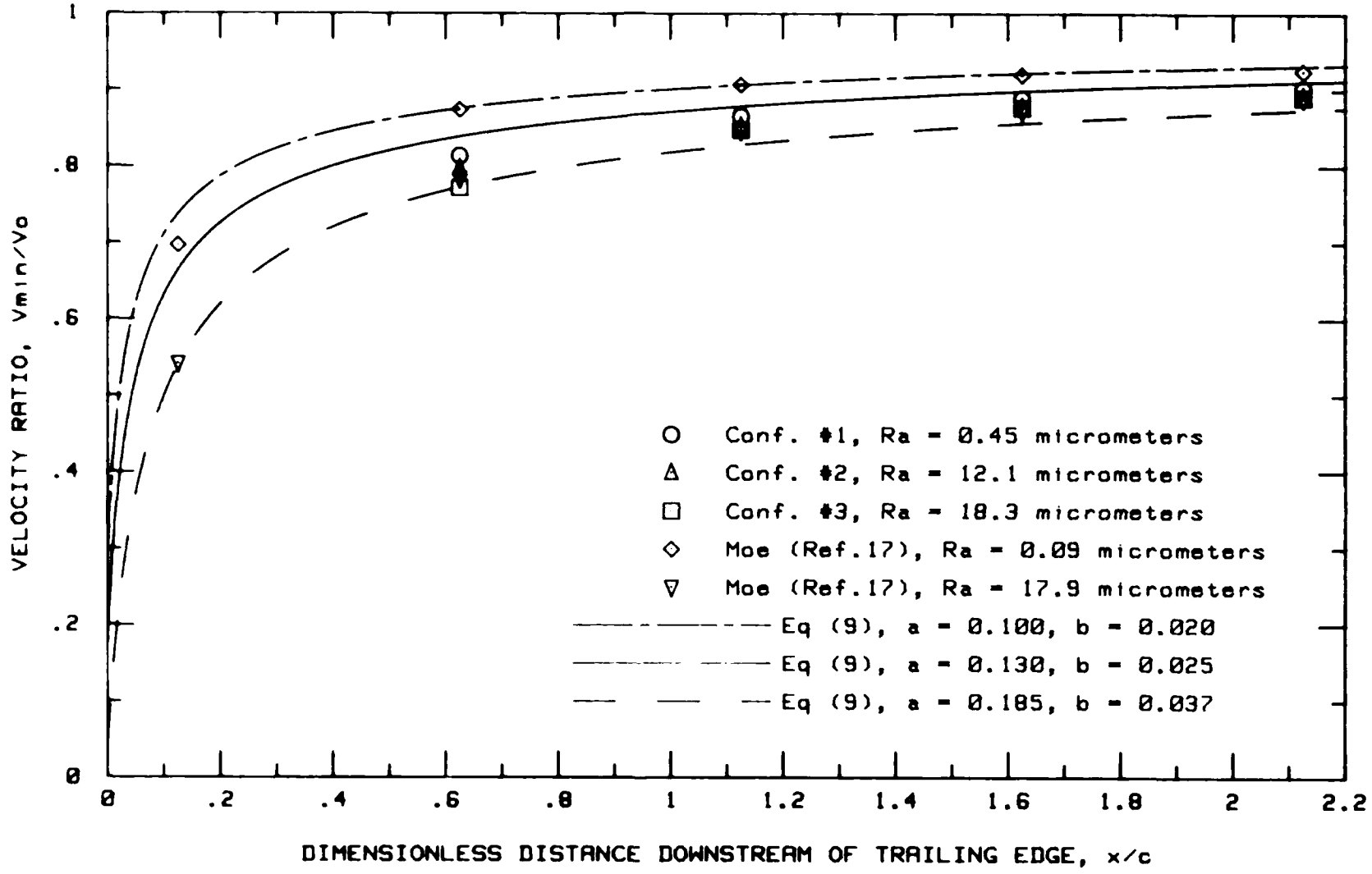

Fig. 16. Wake Velocity Recovery

pressure taps on the surface. One is his smooth baseline configuration with a measured arithmetic average roughness of 0.09 micrometers (compared to 0.45 micrometers in this study), and the other has roughness applied giving an Ra value of 17.9 micrometers. The latter is comparable to configuration 3 in this study which has an Ra value of 18.3 micrometers. As well, Moe had some results for a measuring plane closer to the trailing edge.

In addition to the data points, three lines are shown in the figure. The solid line is a plot of Eq (9) with Lieblein and Roudebush's constants of 0.13 and 0.025 for a and b , respectively. As can be seen, it does, in fact, give a good representation of the velocity recovery in the wake for a cascade. A definite trend for the effects of roughness is also apparent. It seems that increasing surface roughness also increases, to a certain extent, the distance downstream required to recover the velocity. This is not to say that the mixing process is slower. Rather, with a thicker boundary layer and corresponding greater velocity defect at the trailing edge, the mixing process behind a rougher blade takes a little longer to equalize the velocity. It is interesting to note, however, that, regardless of the roughness, approximately 80 percent of the boundary layer's edge velocity is recovered within the first half length downstream of the trailing edge. Additional gains in the velocity defect after that distance are much slower. This reinforces the point made by Lieblein and Roudebush

(14:1) that the wake is reenergized very quickly with the majority of the mixing losses occurring within 1/4 to 1/2 chord length downstream of the trailing edge.

The other two lines on the figure are the bounding curves in the form of Eq (9) for the data presented. Constants for the upper curve are a = 0.1 and b = 0.02, and for the lower curve a = 0.185 and b = 0.037. In addition, note the excellent agreement between configuration 3 and Moe's blade of similar roughness.

Wake Form Factor. Fig. 17 is a plot of the downstream variation of the wake form factor. Again, the results from Moe's study are included for comparison. The results can be related to the variation of the velocity ratio through Eq (10). These are plotted for the same three cases presented in Fig. 16. The form factor at the trailing edge for the solid line was determined by Lieblein and Roudebush (14:8) to be 2.8. The corresponding values for the two limiting curves were calculated from the data presented in this study. Since the upper curve in Fig. 16 closely approximates Moe's results, each of those data points were substituted into Eq (10) to solve for H_{TE}. The average of those results gave a value of 2.19 for the trailing edge form factor. Similarly, the data points for configuration 3 were used to obtain a mean value of 2.86 for the lower curve's trailing edge form factor.

The applicability of using Eq (10) to solve for the variation of the form factor can now be analyzed from Fig. 17.

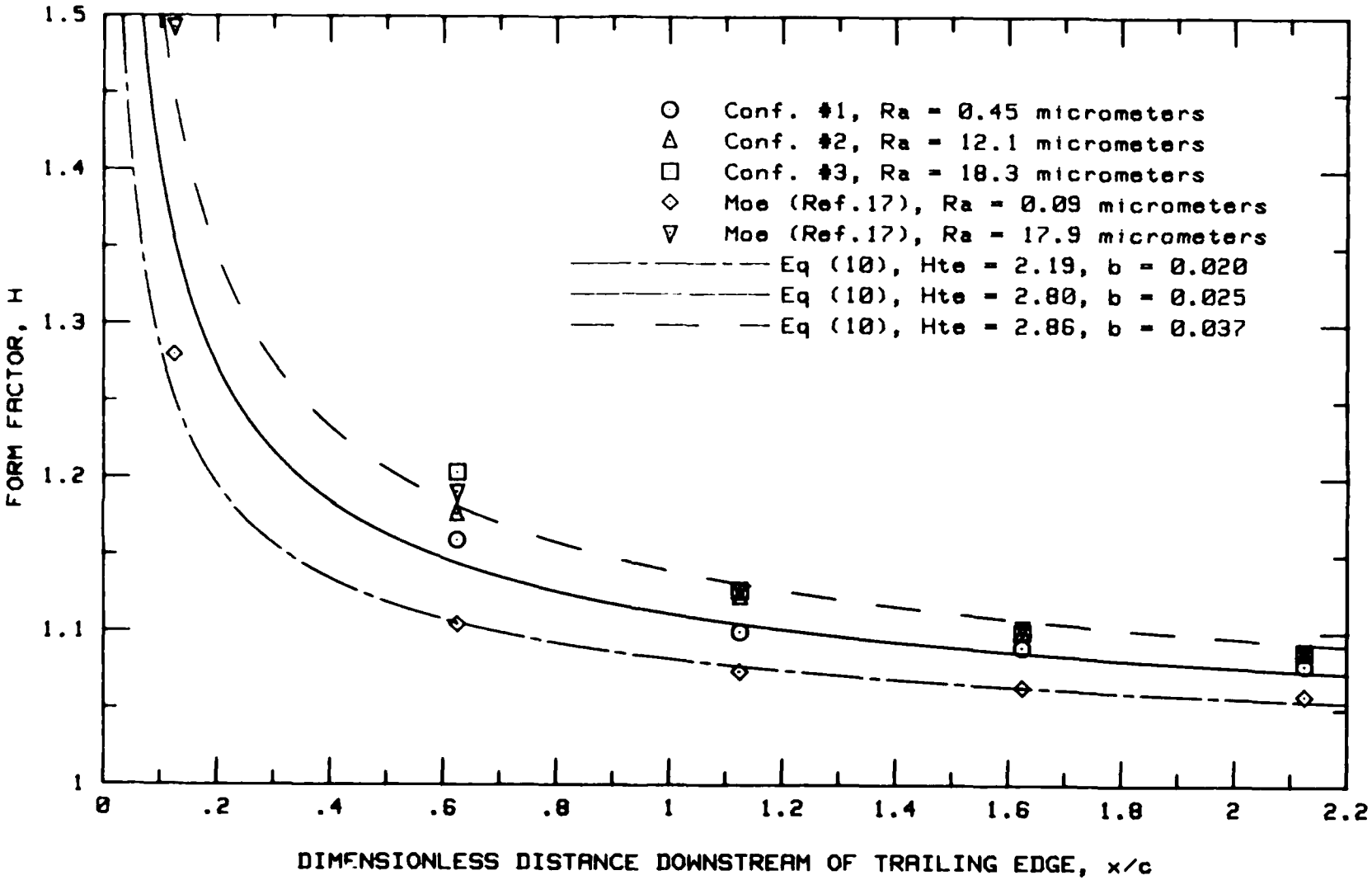

Fig. 17. Downstream Variation of the Wake Form Factor

The equation does appear to predict the variation in form factor quite well for Moe's smooth blade. Its accuracy diminishes, however, with roughness added, particularly in predicting values for the first chord length downstream.

Lieblein and Roudebush (14:9) observed that for chord length distances greater than 0.4, the values of form factor are less than 1.2, regardless of the value at the trailing edge. This does not appear to hold, however, beyond a certain roughness level since the form factor for configuration 3 is greater than 1.2 at a chord length distance of 0.6. In all cases though, the wake form factor decreases rapidly just aft of the trailing edge and appears to approach a value of 1 asymptotically far downstream as predicted by Eq (10).

Wake Full Thickness. The full thickness ratio, δ/c , is shown plotted against downstream distance in Fig. 18. As expected, blades with greater roughness have thicker wakes. The mixing process that occurs in the wake is shown by the increase in the full thickness ratio with downstream distance. Once again, note the excellent agreement between the two curves representing configuration 3 and Moe's blade of comparable roughness.

The increase in the wake full thickness ratio, defined to be $(\delta/c)_x - (\delta/c)_{TE}$, with distance downstream is shown in Fig. 19. Since no measurements were made at the blade trailing edge proper, the full thickness ratio there was determined from Eq (11). As was the case with the form

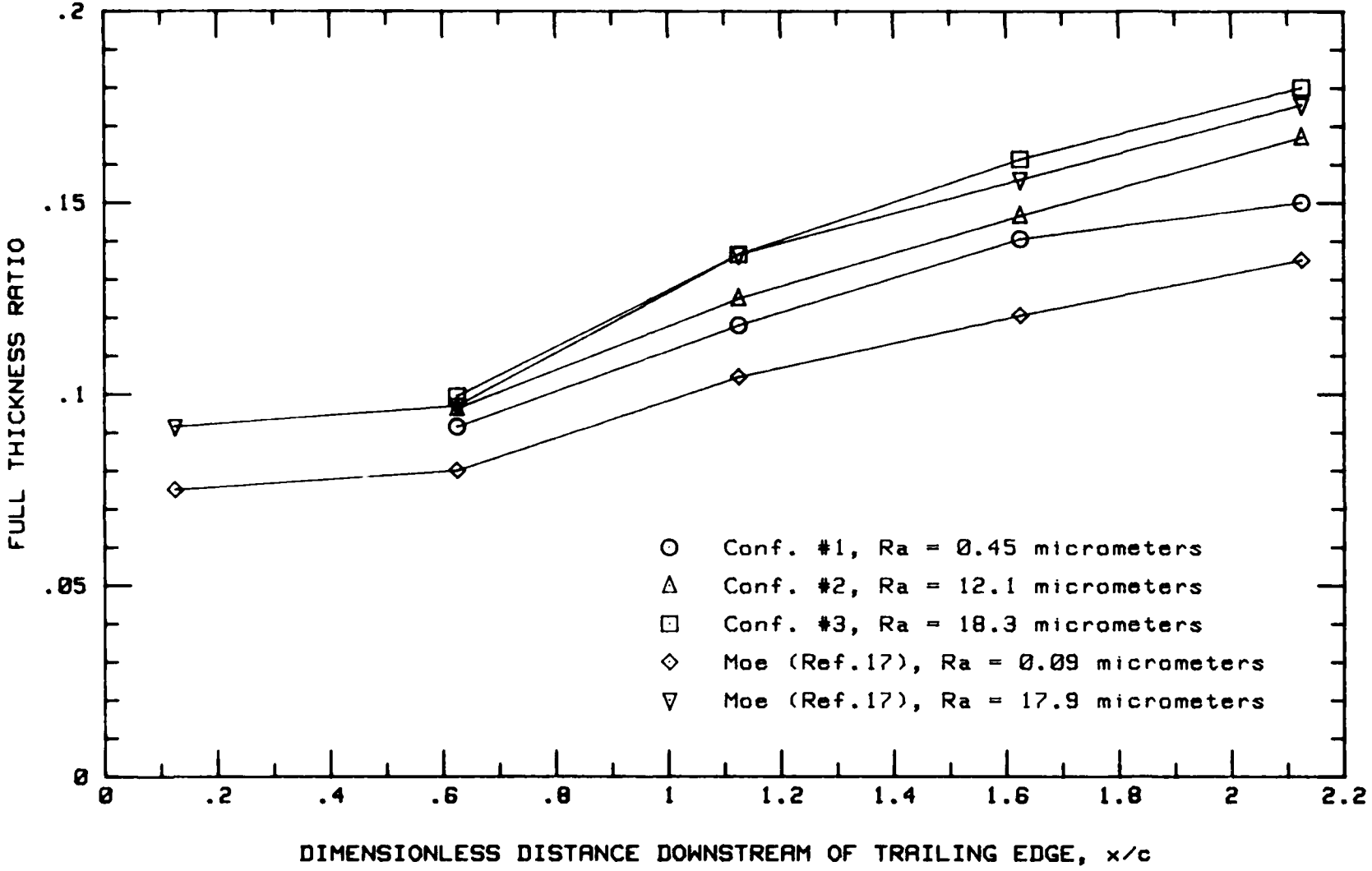

Fig. 18. Downstream Variation of Full Thickness Ratio

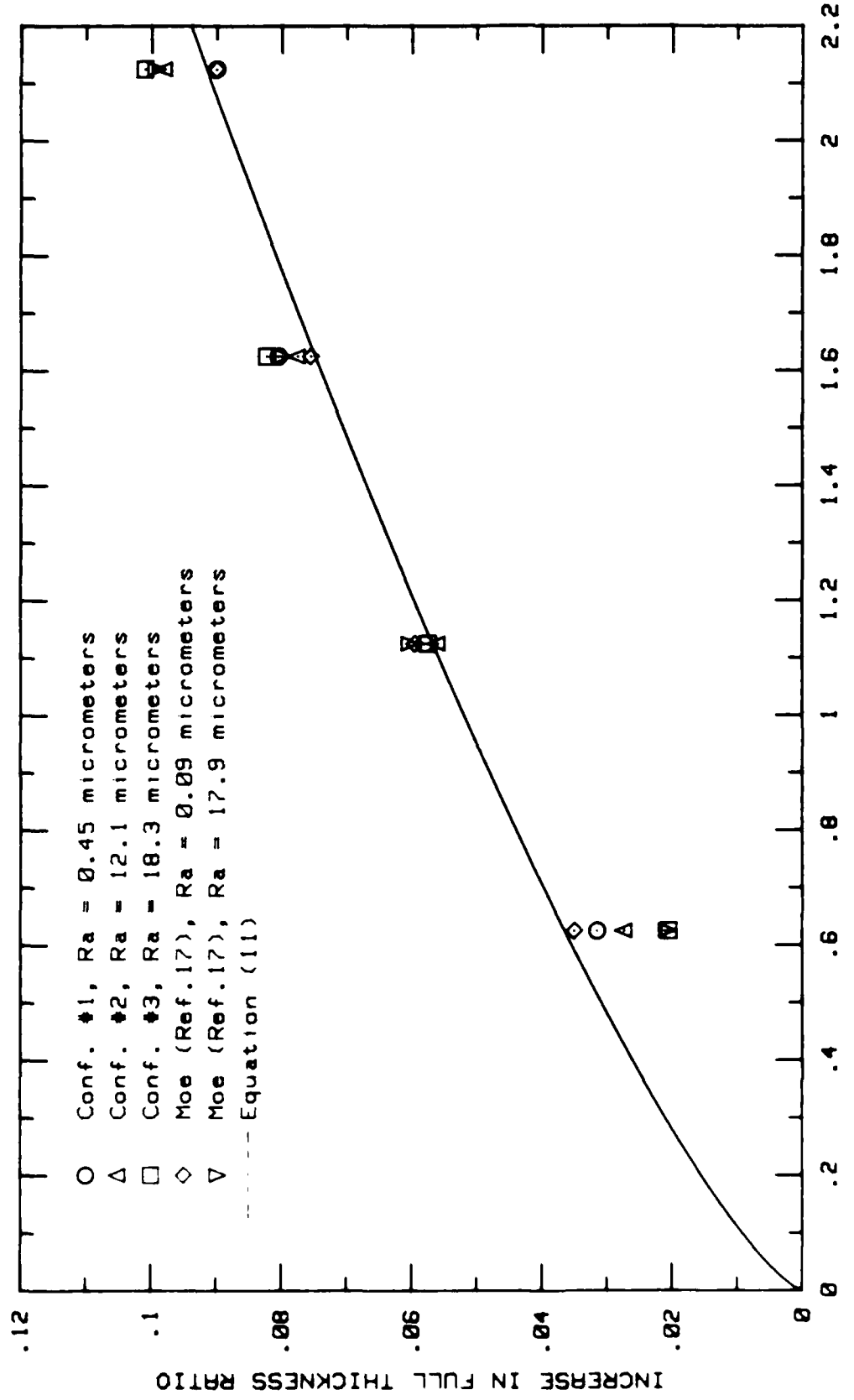

Fig. 19. Increase in Wake Full Thickness

factor, data for each configuration was used to calculate a mean value of $(\delta/c)_{TE}$ for that particular roughness configuration. The line shown is a plot of Eq (11) directly.

The relation, based on isolated airfoil data, does indeed apply to cascades of smooth blades. This is shown by the excellent agreement with Moe's smooth blade and, to certain extent, configuration 1's data. The agreement gets progressively worse, however, with increased values of roughness with one exception. At a chord length distance of 1.125, the full thickness ratio for all five configurations presented falls very close to the line.

Wake Momentum Thickness. The plot of the momentum thickness ratio, δ_2/c, versus downstream distance is shown in Fig. 20. For the most part, the momentum thickness is essentially constant for each configuration. This agrees with Lieblein and Roudebush [14:10-11] who theoretically showed that for $x/c > 0.2$, little change occurs in δ_2, regardless of the trailing edge condition. However, their study also indicated that a slightly increasing trend in momentum thickness with downstream distance is to be expected at distances close to the trailing edge. This observation was based on limited experimental data. The two data points from Moe's data at a chord length distance of 1.125 appear to contradict this. In fact, the data for Moe's blades indicate that the downstream variation of momentum thickness is small and may be of the order of measured in the wake [illegible]

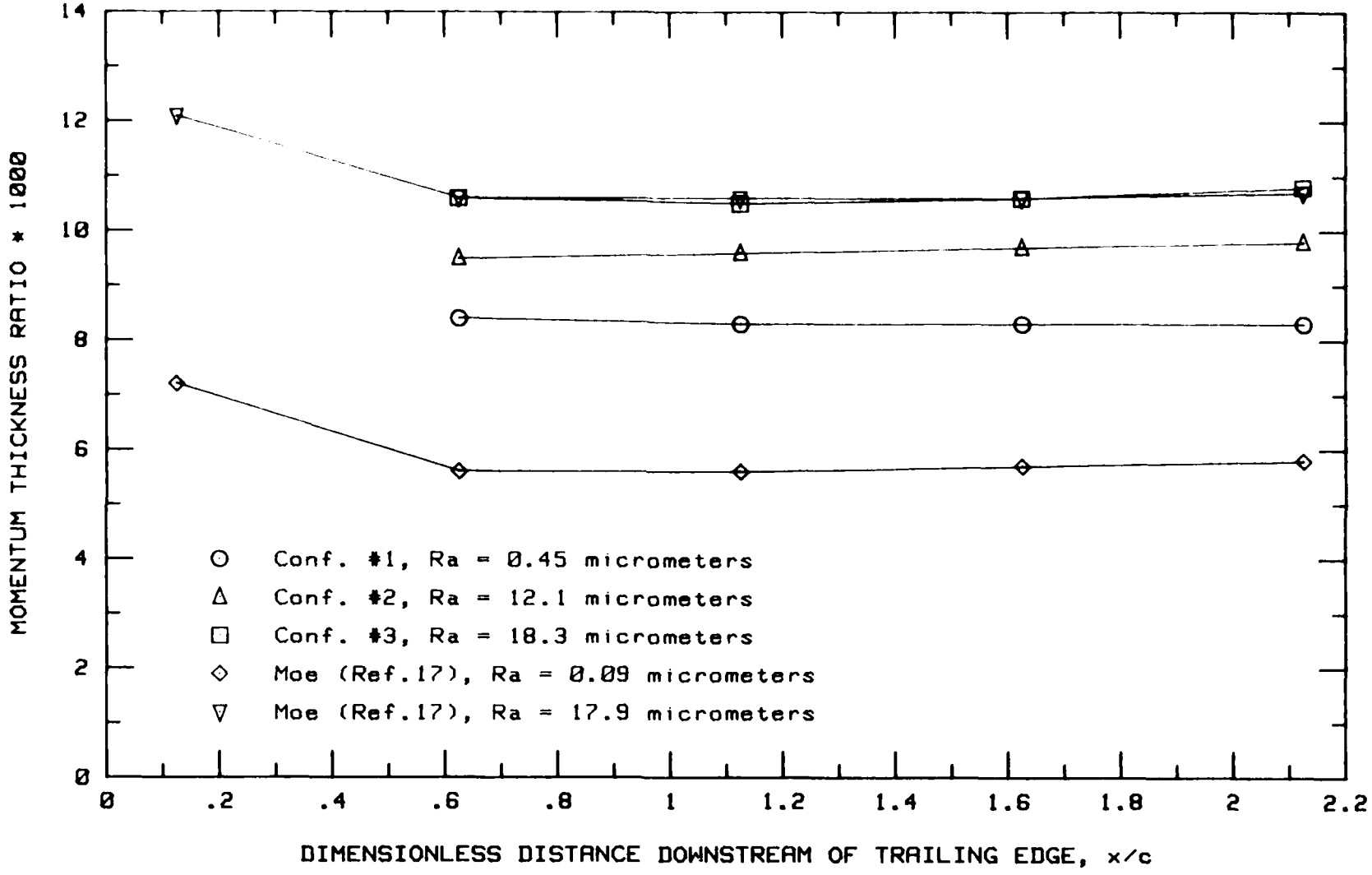

Fig. 20. Downstream Variation of Wake Momentum Thickness

From Fig. 20, it is clear that surface roughness increases momentum thickness in the wake with the largest jump occurring between Moe's smooth blade and configuration 1. This same kind of jump is detectable in all the wake parameters examined previously, leading one to conclude that an initial increase in roughness produces the greatest change in wake characteristics. Moe (17:47) reported similar observations in his study with regards to the effects of roughness on the total pressure loss coefficient.

Total Pressure Loss. Using the procedure outlined in Section IV, the total pressure loss coefficient, ϖ, was determined for each downstream measuring station from Eq (3). The results are tabulated in Table III. Included in the listing are total pressure loss coefficients calculated from data obtained by Moe (17) and Williams (30). The latter was added since that blade's roughness level was also similar to configuration 3.

Significant discrepancies are evident in the results presented. One example is the variation in ϖ among the three configurations of similar roughness, i.e., configuration 3, Moe's configuration number 13, and Williams' configuration number 3. Values of ϖ calculated in this study are, on average, approximately 92 and 73 percent of those of Moe and Williams, respectively. The coefficients for configuration 1, however, are greater than Moe's [illegible] differences

TABLE III

Summary of Total Pressure Loss Coefficients

Investigator	Conf. #	Ra, μm	x/c				
			0.125	0.625	1.125	1.625	2.125
Poulin	1	0.45	--	0.0641	0.0780	0.0659	0.0663
Poulin	2	12.1	--	0.0729	0.0770	0.0750	0.0770
Poulin	3	18.3	--	0.0808	0.0895	0.0877	0.0896
Moe	11	0.09	0.0403	0.0423	0.0398	0.0409	0.0381
Moe	13	17.9	0.0329	0.0455	0.0457	0.0461	0.0435
Williams	3	19.5	--	0.0559	0.0516	0.0484	0.0465
Poulin (THEORY)	1	0.45	--	0.0211	0.0212	0.0213	0.0214
Poulin (THEORY)	2	12.1	--	0.0235	0.0241	0.0246	0.0250
Poulin (THEORY)	3	18.3	--	0.0265	0.0268	0.0274	0.0280

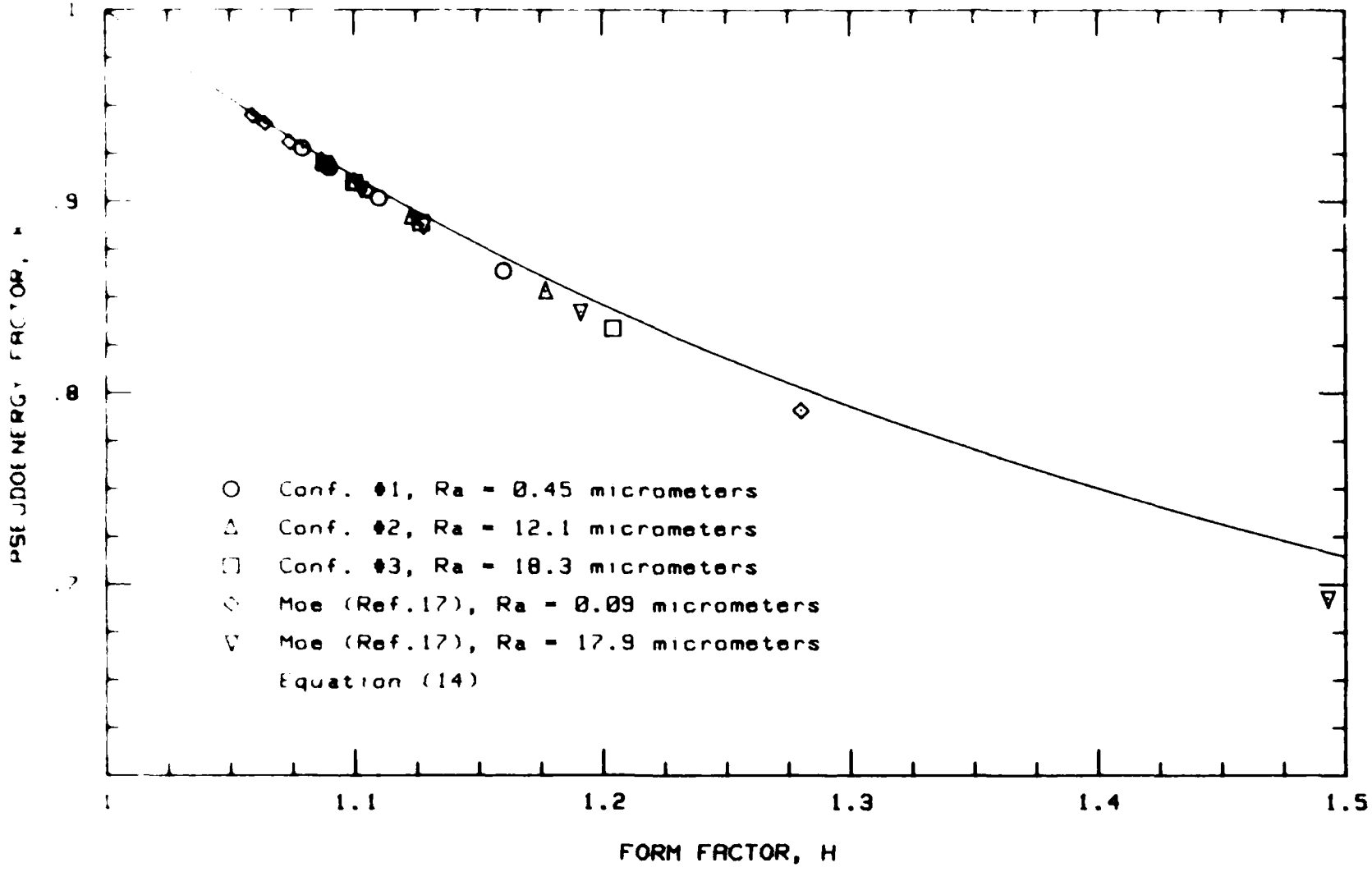

Fig. 21. Variation of Wake Pseudoenergy Factor with Wake Form Factor

the power velocity assumption and Eq (14) are considered to be valid.

The theoretical total pressure loss coefficients, calculated from Eq (12) for the three blade configurations used in this investigation, are listed in Table III. It appears that discrepancies also exist between these theoretical results and actual values obtained experimentally. The significant spread between the two can be appreciated from Fig. 22. Nevertheless, a number of qualitative observations can be made. Firstly, loss in total pressure increases with downstream distance from the trailing edge. This can be seen as an increase in $\bar{\omega}$ for the theoretical curves in Fig. 22. The increase is very slight indicating that the majority of the mixing losses occurred at distances closer to the trailing edge. This is in keeping with the analysis of the wake velocity recovery made earlier. It can also be verified by calculating $\bar{\omega}$ for the case of complete mixing using Eq (15). The equation was applied at the four measuring stations for each configuration and the results averaged. It yielded values for $\bar{\omega}_m$ of 0.0215, 0.0246, and 0.0274, respectively, for configurations 1, 2, and 3. These are not much different than the corresponding values for $\bar{\omega}$ obtained at each measuring station. Except for a sudden and unexplained jump at a chord length distance of 1.125, an [illegible] for all three configurations, the experimental [illegible]

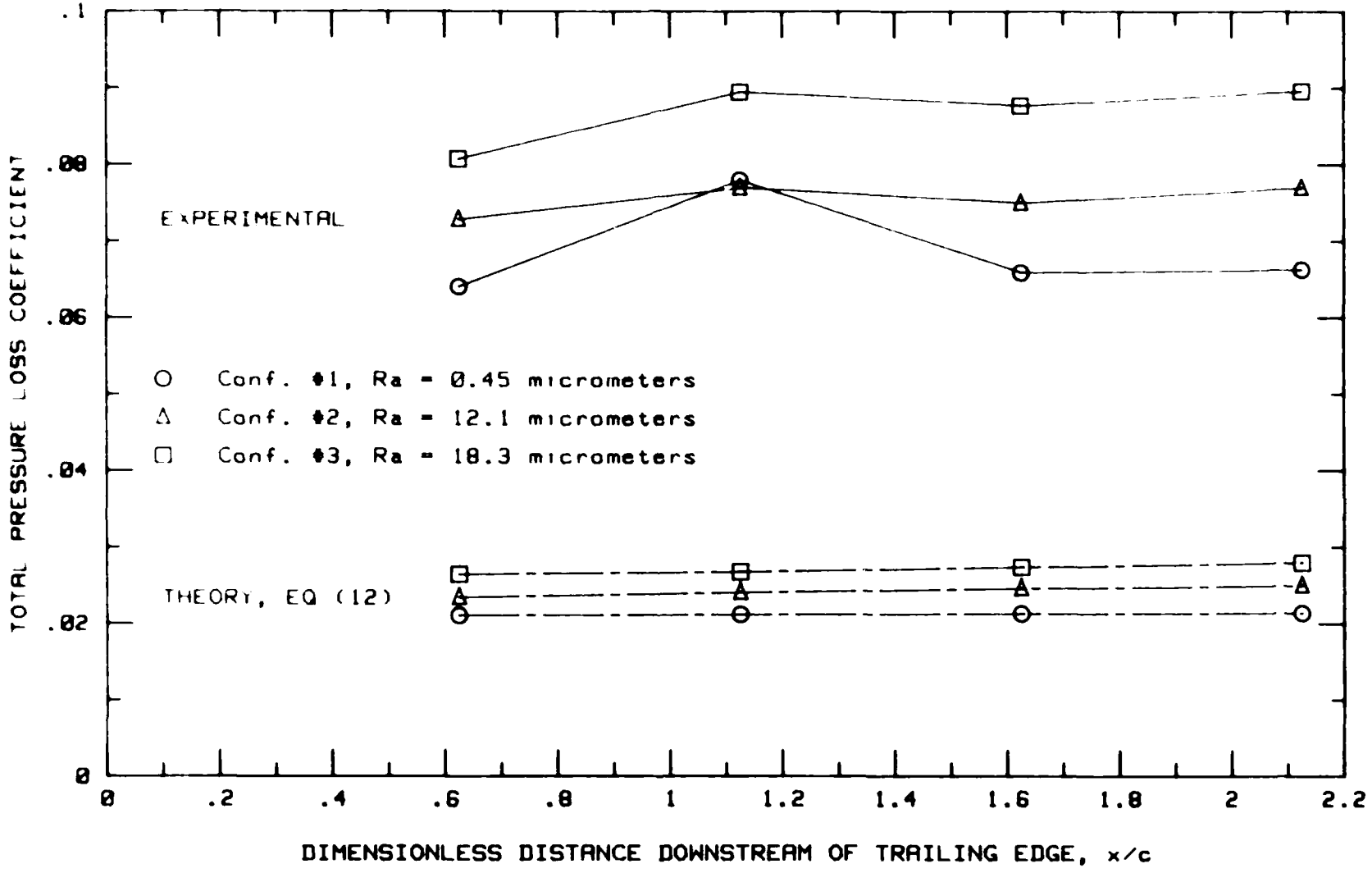

Fig. 22. Change in the Total Pressure Loss Coefficient (Theory and Actual)

Both the theoretical and experimental curves indicate that an increase in surface roughness leads to an increase in total pressure loss. This is not surprising in view of the thicker boundary layer near the trailing edge and greater velocity defects in the wake associated with greater roughness levels. It is interesting to note that, except for the anomaly at x/c = 1.125, the percentage increase in $\bar{\omega}$ is comparable between theory and experiment. For example, at a chord length distance of 0.625, there is approximately a 25 percent increase in total pressure loss between configurations 1 and 3, measured experimentally or theoretically. Farther downstream at x/c = 2.125, the increase is 35 percent experimental and 31 percent theoretical. This agreement indicates that even though some questions exist with the quantitative results, the method does provide reasonably good qualitative information.

Local Turbulence Intensity. The effects of surface roughness on the local turbulence intensity, Tu , in the wake can be surmised from the plots in Appendices J through L. It appears that the initial application of roughness, configuration 2, causes the freestream turbulenc to approximately double compared to configuration 1. No further increase in freestream turbulence is discernable with additional roughness, as represented by configuration 3. In fact, a very slight decrease in Tu , on the order of one or two tenths of a percent, is observed from configuration 2 to 3. Other effects of increasing roughness include an in

crease in the affected wake area and a larger spread of peak fluctuations. These general trends were also observed by Moe (17).

The most distinguishing features of the wake turbulence intensity profiles are the large fluctuations emanating primarily from the suction surface of the blade (lower cross stream location). The pressure surface, on the other hand, though still contributing to the affected wake area, has fluctuations that are smaller in magnitude and essentially streamwise in orientation. Referring to Fig. 105, the wake profiles for configuration 1, it is interesting to note the magnitude and orientation of the turbulence intensity fluctuations from the suction surface of a blade that has no added roughness. The cause of the peaks could be interpreted to be the 38 pressure taps drilled in the suction surface except that the same trend can be found in Moe's profile (17:78) for his smooth blade with no pressure taps. It appears, therefore, that Fig. 105 is representative of the turbulence intensities found over a smooth blade of this type under these conditions. The same Tu "footprint" is observed in the profiles of configurations 2 and 3 at the same downstream distance, Figs. 109 and 113, respectively. Superimposed on this "footprint" are the effects attributable to the addition of surface roughness. For configuration 2, the Tu vectors show a larger spread in orientation but no increase in peak values. Configuration 3, on the other hand, has both a larger spread and greater magnitudes.

It would be of interest to see if the trends observed in the wake turbulence intensity profiles could be traced back to the turbulence intensity profiles along the suction surface. Reference is made to Figs. 78, 91, and 104 which depict these profiles at the 84.375 percent chord location for configurations 1, 2, and 3, respectively. It appears from these figures that the peak value of turbulence intensity does indeed remain fairly constant from configurations 1 to 2 before increasing with configuration 3. In addition, the variation of freestream turbulence with roughness, observed in the wake, can also be seen on the suction surface. That is, the value for freestream turbulence increases from configuration 1 to 2 before decreasing slightly with configuration 3. Note that these are qualitative observations only. Turbulence intensities measured along the suction surface are significantly larger than what was found in the wake. One reason for this may be that a hot wire was used for the boundary layer measurements while a hot film was used in the wake. Another contributing factor could be that the large fluctuations dampen out somewhat prior to the first measuring station in the wake, located 1.25 in downstream of the trailing edge. Note the large amount of damping that occurs between that station and the next one at 2.25 in. Similar damping would, therefore, be anticipated immediately aft of the trailing edge. This premise is reinforced by reviewing Moe's (17) plots at a downstream location of 0.25 in. Each of his configurations show significant damping of the peak

values of Tu from that station to the next one at 1.25 in.

A final note on the wake turbulence intensity profiles has to do with the downstream variation. Regardless of surface roughness, the large peaks are found to be completely damped out by a chord length distance of 2.125. Over the same distance, however, the affected area in the wake undergoes little change as compared to the velocity profile. This suggests that the turbulence generated by the blade will still be felt at a distance downstream where the velocity distribution is once again uniform.

VI. Conclusions and Recommendations

Conclusions

The major conclusions of this investigation are:

1. The transition point of the boundary layer along the suction surface of the blade moves forward with the addition of roughness.
2. The boundary layer edge velocity as well as the boundary layer thickness near the trailing edge increase with roughness.
3. The addition of roughness increases wake full thickness, momentum thickness, and form factor while decreasing the velocity recovery immediately downstream of the trailing edge.
4. The total pressure loss coefficient increases with roughness as well as distance downstream.
5. Wake characteristics are most sensitive to an initial increase in roughness.
6. Roughness effects on wake turbulence intensity include an increase in free-stream turbulence, affected wake area, and peak fluctuations. These trends can be predicted from suction surface turbulence intensity profiles near the trailing edge.

In addition to the above noted roughness effects, the following general observations are made:

1. Laminar separation with turbulent reattachment

appears to occur on the suction surface of the smooth blade.

2. The method used to determine the boundary layer edge velocity is a reasonable one, giving results comparable to that obtained from the pressure profile.
3. A reasonable qualitative assessment of the boundary layer growth can be interpreted from the corresponding turbulence intensity profiles.
4. The relationship between pseudoenergy thickness and wake form factor, developed by assuming a power profile for the wake velocity profile, is a satisfactory one, regardless of roughness levels, for form factors up to 1.2.
5. Downstream variation of wake momentum thickness ratio and increase in full thickness ratio for cascade flow have similar trends to that of flow over an isolated airfoil.
6. Majority of the changes in the wake characteristics and mixing losses occur within half a chord length distance downstream of the trailing edge.
7. Turbulence generated by the blade will continue to be felt in the wake even after the velocity distribution is once again uniform.

Recommendations

As previously suggested by Moe (17) and Williams (30), the effects of varying inlet turbulence on the performance of the cascade would be of interest. One objective should

be to determine if the effects of surface roughness are still discernible in a flow of relatively high free-stream turbulence such as would be found in an actual turbomachine. In addition, this and previous investigations have been restricted to one particular blade angle setting. Thought should be given to modifying the test section to allow for simple variations in angle of attack and incidence angle.

Though the boundary layer along the suction surface of the blade was investigated, and the procedure successfully automated, the information obtained was deficient in that no data were available closer than 0.03 in from the surface. The primary reason for this was concern in contacting the blade surface with the probe. This would be alleviated by switching from a hot wire to a laser anemometer system. Of course, any benefits gained would have to be weighed against the increased complexity of the system and required modifications to the test section.

Finally, discrepancies in the total pressure loss coefficients obtained in this and the previous two investigations suggest that a problem exists in the data reduction procedure. The difficulty is further emphasised by the disparity between theoretical and experimental loss coefficients calculated in this study from the same wake velocity profiles. Consequently, the procedures and software used should be reviewed in an attempt to either confirm the results or identify the problem.

APPENDIX A: Component Listing

Component	Type/Model #
Pressure Transducers	
Tank Total Pressure	Statham PM60TC
Test Section Inlet Static	Statham P6TC
Test Section Exit Static	Statham P6TC
Ambient Pressure	CEC 4-326
Bridge Balance	CEC type 8-108
DC Power Supply	HP 6205C
Scanivalve System	
Pressure Transducer	PDCR 23D
Scanivalve	48S9-3003
Controller	CTLR 2/S2-S6
Scanner Position Display	J102/J104
Thermocouples	
Four copper-constantan types to measure ambient temperature, tank total temperature, and calibrator chamber top and bottom total temperature	Omega T-type
Traversing Mechanism	
Motors (2)	North American P[illegible] Controls K8[illegible]
Encoder Transducers (2)	Astrosystems MT[illegible]
Hot Wire/Film Anemometer System	
Anemometers (3)	TSI Model [illegible]
Monitor and Power Supply	TSI Model [illegible]
Oscilloscope	B&K Model [illegible]
Boundary Layer Hot Wire	TSI Model [illegible]
X-configuration Hot Film	TSI Model [illegible]
Boundary Layer Probe Support	TSI Model [illegible]
X-configuration Probe Support	TSI Model [illegible]
Calibrator (modified)	TSI Model [illegible]
Transformer (to heat air for calibrator)	[illegible]
Data Acquisition System	
Computer	
Disk Drives (2)	
Channel Scanner	
Digital Voltmeter	
Printer	
Plotter	

AD-A179 586 SURFACE ROUGHNESS: ITS EFFECTS ON THE PERFORMANCE OF A TWO-DIMENSIONAL CO (U) AIR FORCE INST OF TECH WRIGHT-PATTERSON AFB OH SCHOOL OF ENGI J R POULIN

UNCLASSIFIED DEC 86 AFIT/GAE/AA/86D-13 F/G 20/4 NN

2/3

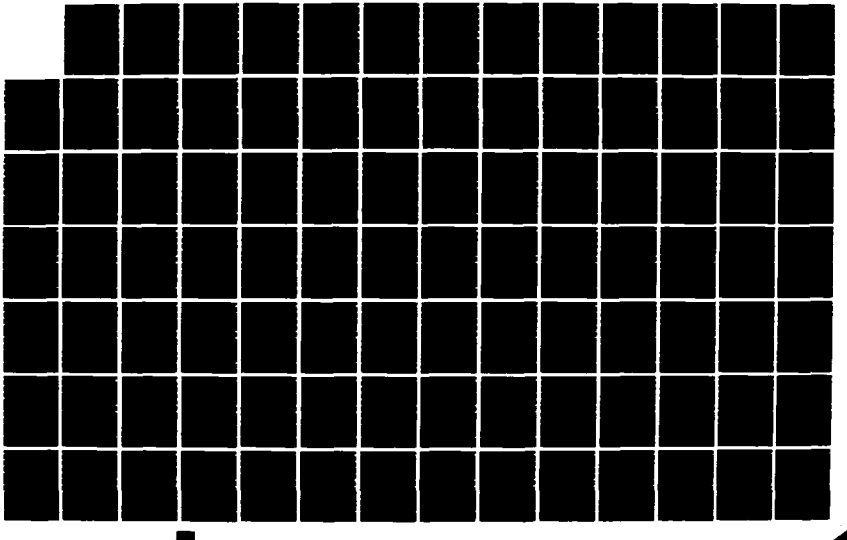

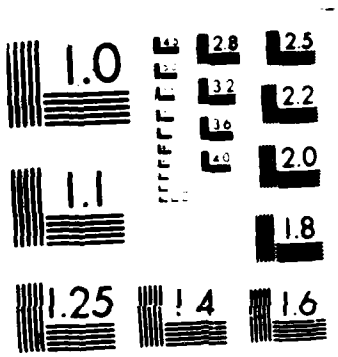

APPENDIX B: Hot Wire/Film Calibration

The procedure used to calibrate the hot wires and films in this investigation was one developed by Rivir and Vonada (29) to take into account elevated temperatures. This was necessary since the flow exiting the CTF did so at temperatures typically 30 to 40 ^{o}F above ambient. In addition, the temperature at which the system stabilized for a particular run would vary from day to day depending on weather conditions. For the remainder of this appendix, the term "wire" will be used to denote both the hot wire and hot film sensors used in the study.

Hot wire anemometry is basically a heat transfer problem. Therefore, of primary interest in the calibration is the variation of Nusselt number with Reynolds number. King was one of the first to study this and developed the following semi-empirical equation known as King's law:

$$Nu = A + BRe^{n} \qquad (23)$$

where Nu is the Nusselt number, A and B the intercept and slope of the calibration curve respectively, Re the Reynolds number, and n an exponent applicable for a particular range of Reynolds number. King used a value of 0.5 for n (5:114).

Heat is transferred out of the wire by radiation, buoyant convection, conduction to the end supports, and forced convection by the fluid flow. Of these, the first two are

neglected since radiation heat loss amounts to only about about 0.1 percent of the electrical input to the wire while buoyant convection is significant only at very low speeds (5:109). The effect of end losses due to conduction to the supports and convection at zero velocity are contained in the quantity A in Eq (23) (9:177).

Referring to King's law Eq (23), Bradshaw points out that correlations of this type "... are applicable only over a limited range of Reynolds number and there is no physical reason why a single exponent should do for an indefinitely large range" (5:114). For this reason, the calibration scheme employed the following values for n chosen by Collis and Williams (6:370)

$$n = 0.45 \text{ for the range } 0.02 < Re < 44$$

$$n = 0.51 \text{ for the range } 44 < Re < 140$$

"The temperature difference between the wire and the fluid is usually large enough for the choice of reference temperature for the fluid properties to be in doubt" (5:115). Collis and Williams (6:370) recognized this problem and chose to evaluate fluid properties at a mean temperature defined to be $T_M = (T_W + T_O)/2$ where T_W is the temperature of the wire and T_O the temperature of the free stream. Their final form of the King's law equation, which includes a so-called "temperature loading" factor applied to the Nusselt number, reads as follows:

$$Nu(T_w/T_e)^n = A + BRe^n \qquad (24)$$

with the exponent m having a value of -0.17 (6:369). The final result of the calibration procedure outlined below is a curve of this form.

Calibration Procedure

The first step in calibrating a wire was to determine how its resistance varied with temperature. This was accomplished by placing the sensor in a low velocity flow maintained at a particular temperature and measuring its cold resistance. This was repeated for different temperature settings in the range of interest which for this study was 100 to 125 ° F. By extrapolating this data, the required operating resistance needed to yield a wire temperature of 500 °F was calculated.

An important parameter in the calculation of heat transfer is the adiabatic wall temperature T_{AW}, also known as the recovery temperature. It is the equilibrium temperature attained by a surface exposed to a flow when there is no heat transfer at the surface. The adiabatic wall temperature for the wire was determined by setting it in the calibrator flow at the expected test velocity and temperature and measuring its cold resistance. The expected test velocities, based on previous investigations, were 450 ft/sec for the wake survey and 500 ft/sec for the boundary layer survey, both at temperatures of 113 °F. Since the wire was not being heated by the anemometer, it was assumed that it would quickly reach a temperature at equilibrium with the flow, and the condition

of no heat transfer at the wall would be attained. The equation for the adiabatic wall temperature is given by

$$T_{aw} = T_e + (V_e^2/2c_p)r_c \qquad (25)$$

where r_c is a nondimensional fluid temperature known as the recovery factor (11:297).

Applying the isentropic relationship between total and static temperatures yields the following equation for the recovery factor:

$$r_c = (T_{aw}-T_e)/(T_{T_e}-T_e) \qquad (26)$$

where T_{T_0} is the total temperature of the flow. This value for the recovery factor was assumed to be constant and was used repeatedly in the calibration as well as data reduction to calculate the adiabatic wall temperature.

The question is again raised as to what temperature should the fluid properties be evaluated at. Due to the relatively high velocities to be measured, the reference temperature was calculated as follows:

$$T_R = (T_w-T_e)/2 + 0.22(T_{aw}-T_e) \qquad (27)$$

This equation, formulated by Eckert assuming constant specific heat, yields solutions for high velocity, laminar boundary layers that are applicable over a wide range of free-stream and surface temperatures (11:304). Note that in Collis and Williams investigation (6:361), the maximum velocity used was 140 ft/sec. Applying Eq. (25) at this speed yields

a difference of only 1.63 °F between the adiabatic wall and free-stream flow temperatures, assuming a Prandtl number of unity. Consequently, for the range of velocities studied by Collis and Williams, $T_{AW} \approx T_O$ and Eq (27) reduces to the relationship that they employed for calculating the reference mean temperature.

The data points for the actual calibration curves were obtained by measuring the output voltage of the anemometer for 15 to 20 velocities in the range expected. These were measured at three fluid temperatures: 100, 113, and 125 °F. In addition to the voltage, the acquisition system sampled the calibrator chamber total pressure, inlet and exit total temperatures, and the ambient pressure at each data point. With these values, the velocity of the flow was determined along with the adiabatic wall temperature using Eq (25).

The Reynolds number plotted on the calibration curves was based on the diameter of the wire:

$$Re = (\rho V_c d)/\mu \qquad (28)$$

where V_c is the calibrator velocity, d the diameter of the wire, and μ the dynamic viscosity. The fluid properties were evaluated at the reference temperature calculated from Eq (27). The Reynolds number based on the data taken at the expected test velocity determined the value of the exponent n from Collis and Williams criteria.

The final parameter to be determined is the Nusselt number. In a constant temperature anemometer system, the wire

is maintained at a specific temperature by a feedback controlled bridge circuit. At equilibrium, an energy balance of the wire dictates that the electrical power generated by the anemometer to maintain the constant temperature must equal the heat dissipated by the wire to the fluid over time. This can be expressed as

$$R_w I^2 = hA(T_w - T_e) \tag{29}$$

where R_W is the resistance of the wire, I the current through the wire, h the convection heat transfer coefficient, and A the surface area of the wire.

Substituting E_W / R_W for the current, where E_W is the voltage across the wire, and rewriting the heat transfer area as the product of the wire's circumference and its length L, yields

$$E_w^2/R_w = h\pi dL(T_w - T_e) \tag{30}$$

Dividing through by the thermal conductivity of the flow and rearranging

$$\frac{E_w^2}{k_f R_w \pi L(T_w - T_e)} = \frac{hd}{k_f} \tag{31}$$

The expression hd/k is termed the Nusselt number, based on the diameter of the wire.

From the schematic of the bridge circuit, Fig. 23, it can be shown that

$$E_o = E_{o_b} + E_w$$

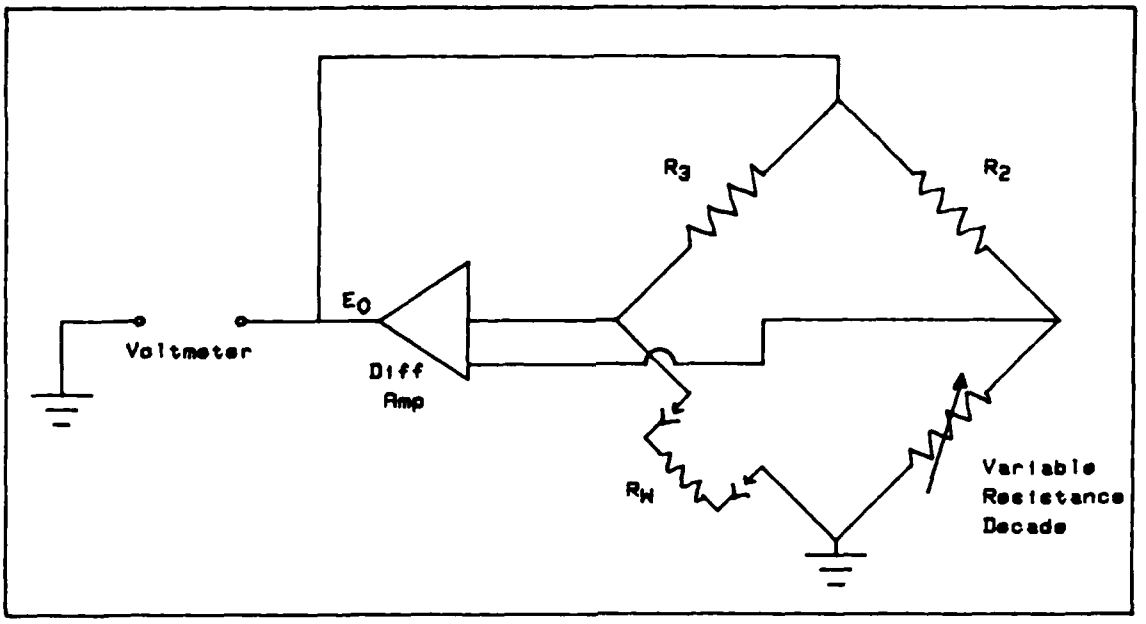

Fig. 23. Simplified Schematic of the Anemometer Bridge Circuit

where E_0 is the voltage output of the anemometer system and E_{R_3} the voltage drop across the resistor R_3. Replacing E_{R_3} with IR_3 and introducing $I = E_0/(R_3 + R_W)$ yields

$$E_w = E_0[R_w/(R_s+R_w)] \qquad (32)$$

Substituting Eq (32) into Eq (31) results in the final form for the Nusselt number as a function of the anemometer output voltage:

$$Nu = \frac{E_0^2 R_w}{k\pi L(R_T L(R_s+R_w)^2(T_w-T_0)} \qquad (33)$$

The calibration curves themselves are plots of the Nusselt number times a temperature loading factor raised to an exponent m versus Reynolds number raised to the exponent n.

An example is depicted in Fig. 24. In this case, the three separate curves, corresponding to the three temperatures at which the calibrations were carried out, are clearly discernible.

The final step of the calibration procedure is for the computer to iterate to determine the value of the exponent m for which a linear regression of all the data points yields the smallest variance. The slope and intercept of that curve fit, which correspond to the quantities B and A in Eq (24), are saved on magnetic disks for subsequent use in reducing anemometer output voltages, obtained in experimental runs, into velocities.

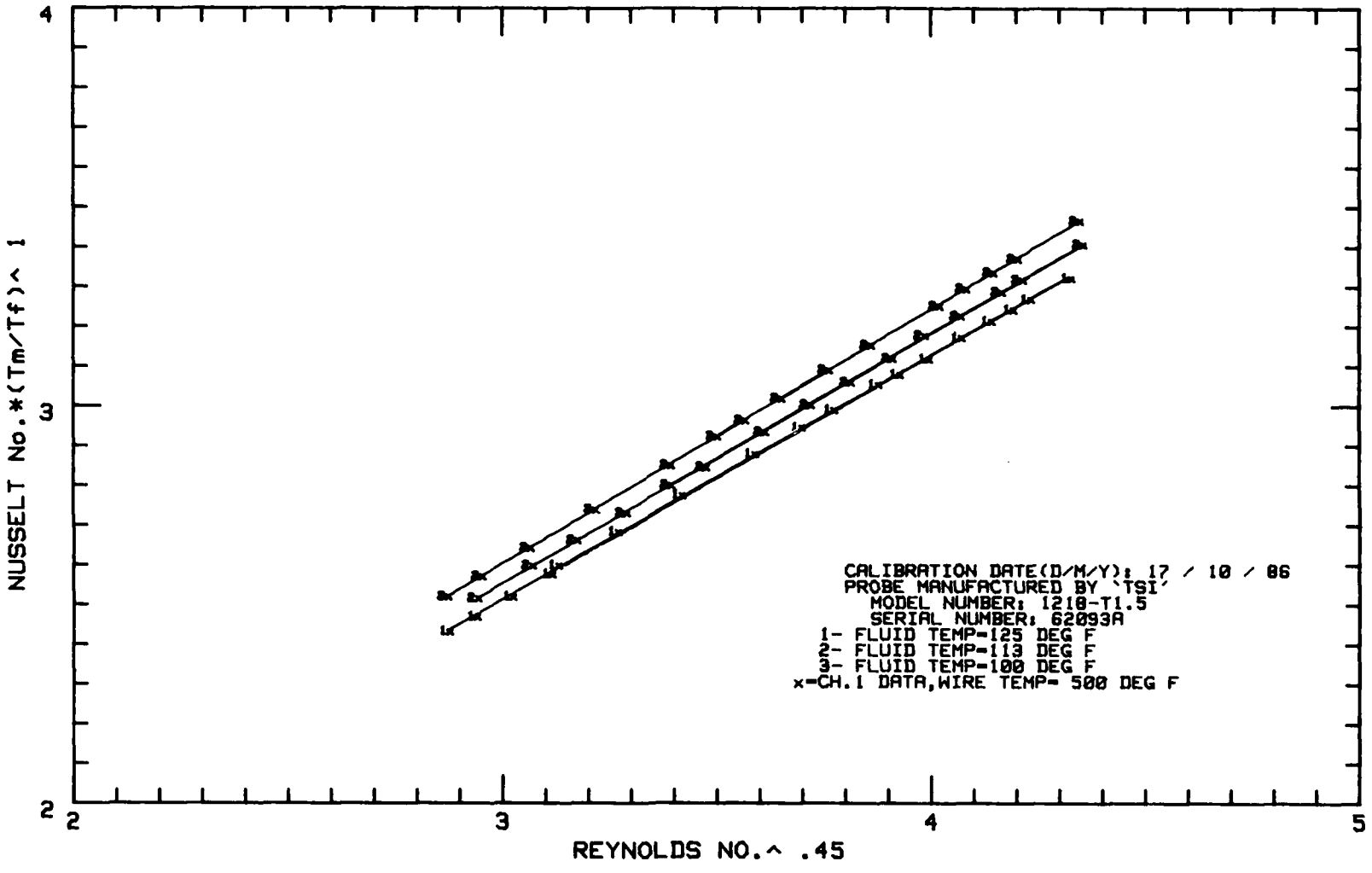

Fig. 24. Sample Probe Calibration Curves at Three Temperatures

APPENDIX C: Roughness Definitions

"The quality of the surface is defined as the height of the peaks, the structure of the roughness and the waviness. In workshop practice, however, only a roughness value is prescribed" (4:30). The most common of these roughness parameters is the arithmetic average roughness, Ra, defined to be the average value of the deviations from the center-line over a particular sampling length (20:5). Schäffler (22:10) expressed this mathematically as

$$Ra = \frac{1}{L}\int_0^L |y|\, dx \qquad (34)$$

where L is the roughness sample length, and x and y the roughness length and height coordinates, respectively, as shown below:

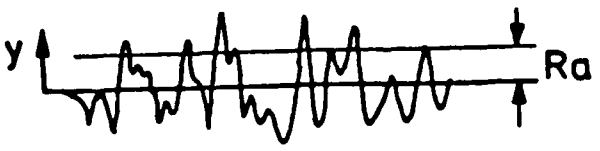

Fig. 25. Average Roughness, Ra

The traditional way of specifying roughness in fluid mechanics is in terms of an equivalent sand roughness, k_s. By correlating the results of two previous studies, Koch and Smith (12:424) arrived at the following equation to relate

equivalent sand roughness to profilometer readings:

$$k_s = 6.2\ Ra \qquad (35)$$

Schäffler (22:10) points out, however, that there are some problems in using Ra or k_s to quantify the technical roughness associated with various manufacturing processes. For example, equivalent sand roughness is based on tightly packed grains of equal size while technical roughness consists of a large range of peak heights and surface waviness. The calculation of the arithmetic average value of roughness, on the other hand, includes small roughness elements, the effects of which are insignificant in defining the hydrodynamic characteristic of the surface. Consequently, Schäffler proposes a different roughness parameter, k , which describes the peaks rather than the average value of roughness. "Roughness k is defined as the difference between the arithmetic averages of the ten highest peaks and the ten deepest grooves which exist per millimeter length" (22:10) or

$$k = \bar{y}_{PEAK} - \bar{y}_{GROOVE}$$

Figure 26 is an example of a roughness trace with the roughness height k depicted. By measuring the surface roughness of a large number of blades, he obtained the following simple correlation between k and Ra:

$$k = 8.9\ Ra \qquad (36)$$

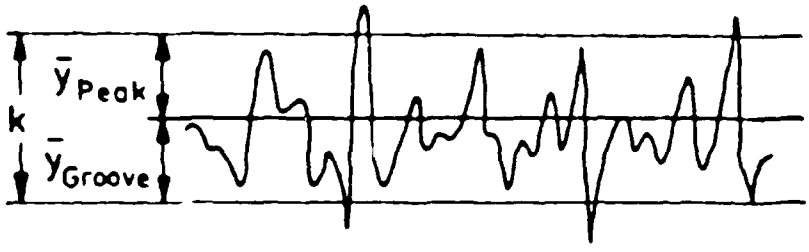

Fig. 26. Schäffler's Technical Roughness

APPENDIX D

Boundary Layer Velocity Profiles, Configuration #1

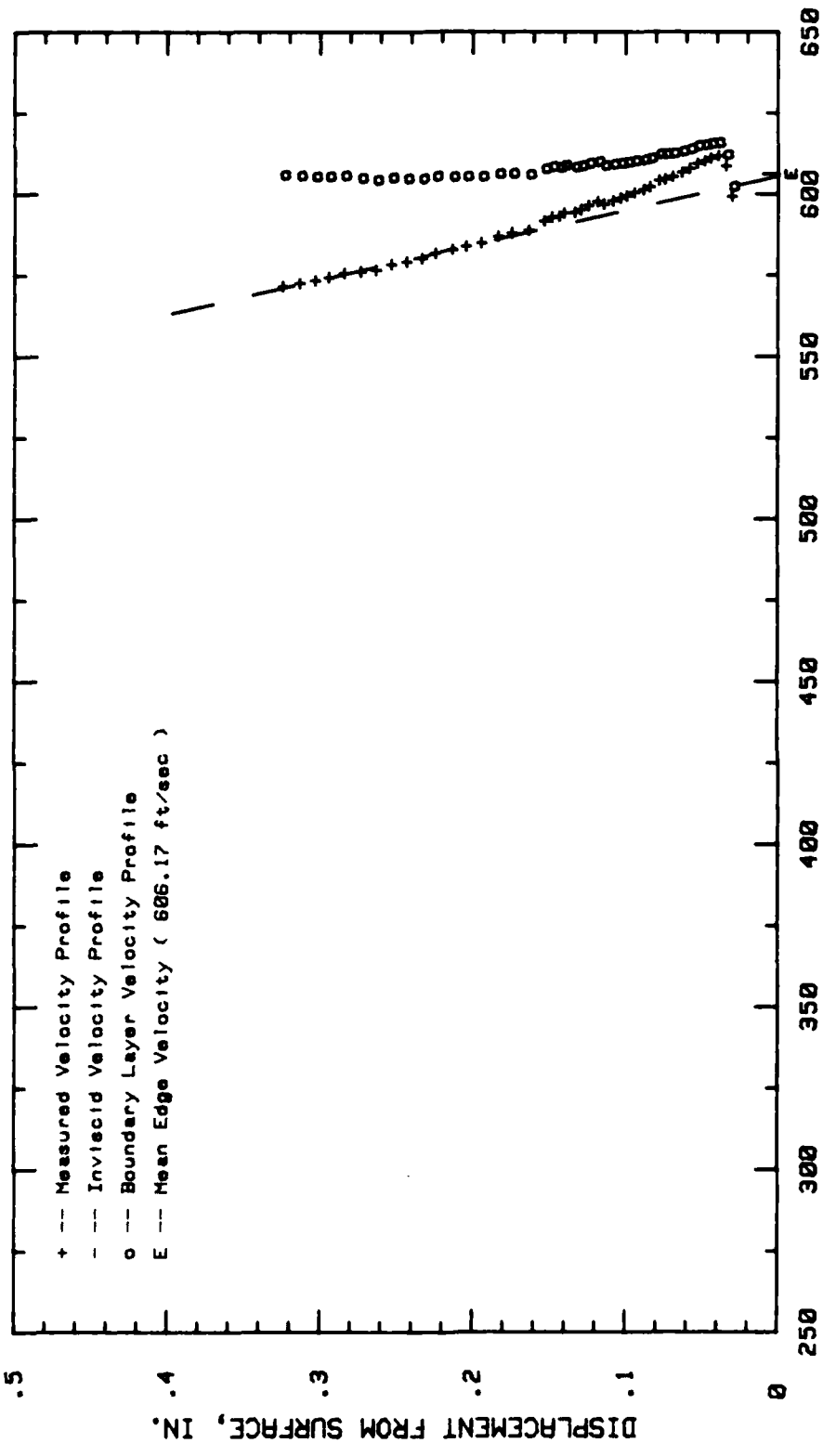

Fig. 27. Boundary Layer Velocity Profiles, Conf.#1 at 4.68 % Chord

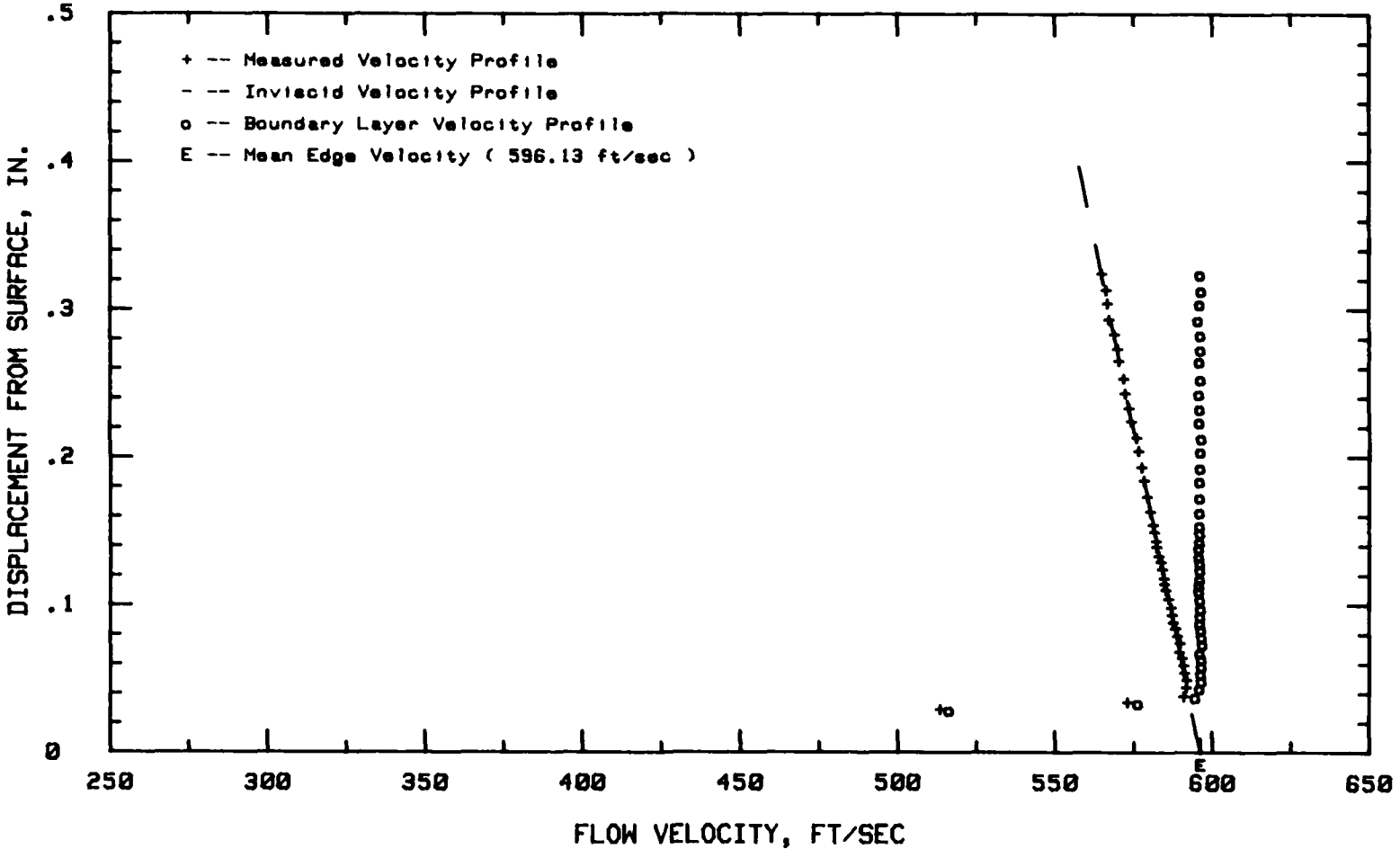

Fig. 28. Boundary Layer Velocity Profiles, Conf.#1 at 9.37 % Chord

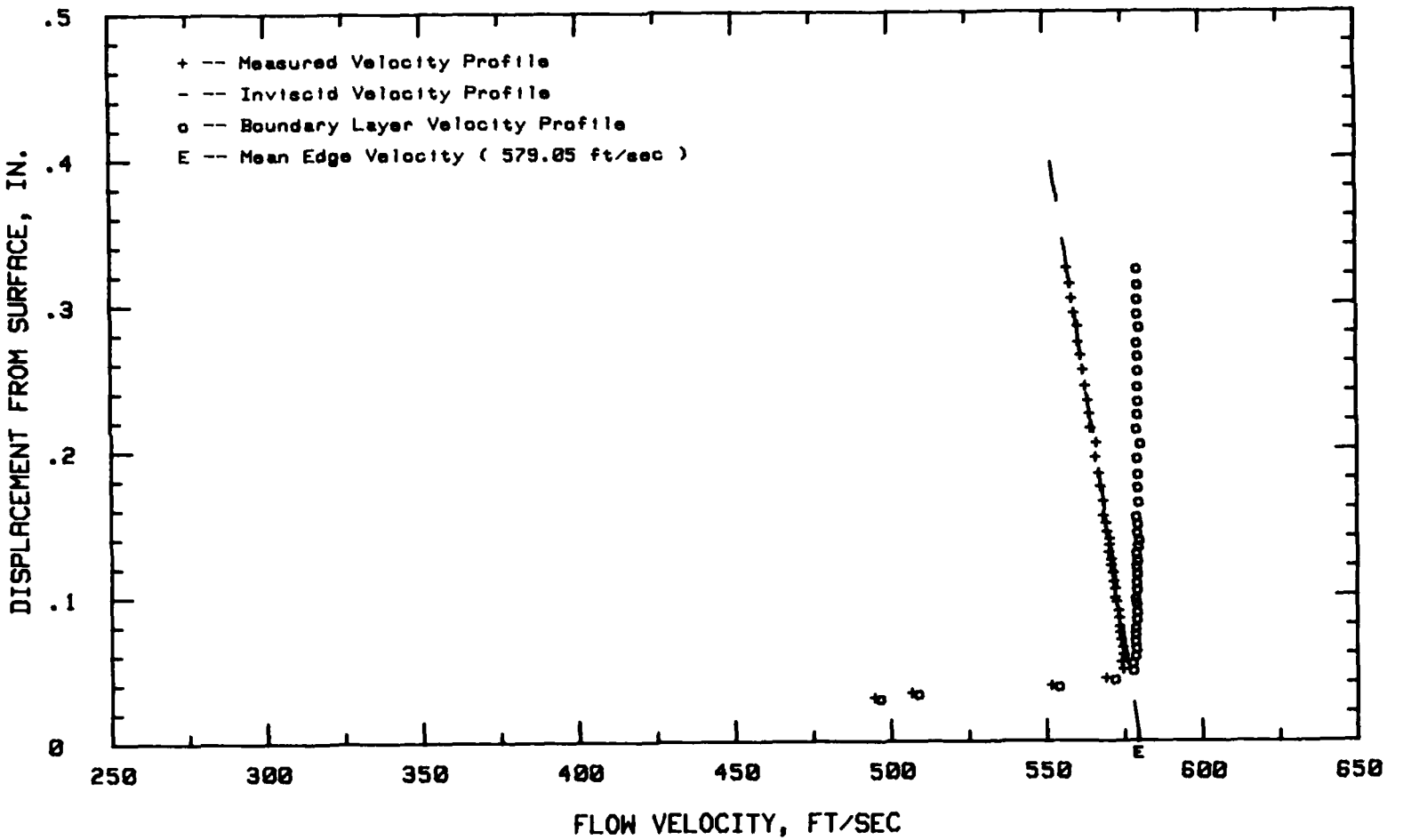

Fig. 29. Boundary Layer Velocity Profiles, Conf.#1 at 25 % Chord

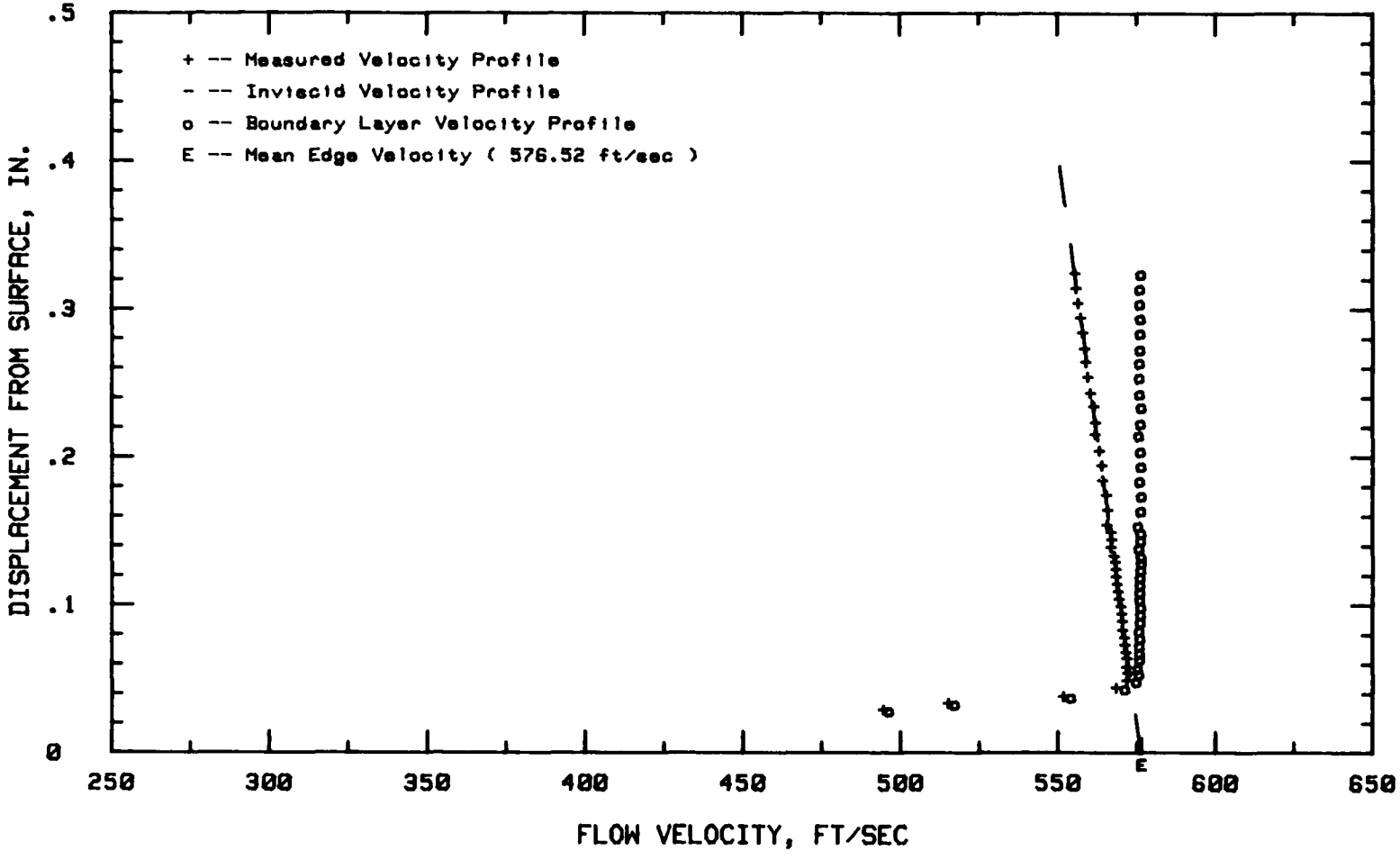

Fig. 30. Boundary Layer Velocity Profiles, Conf.#1 at 29.68 % Chord

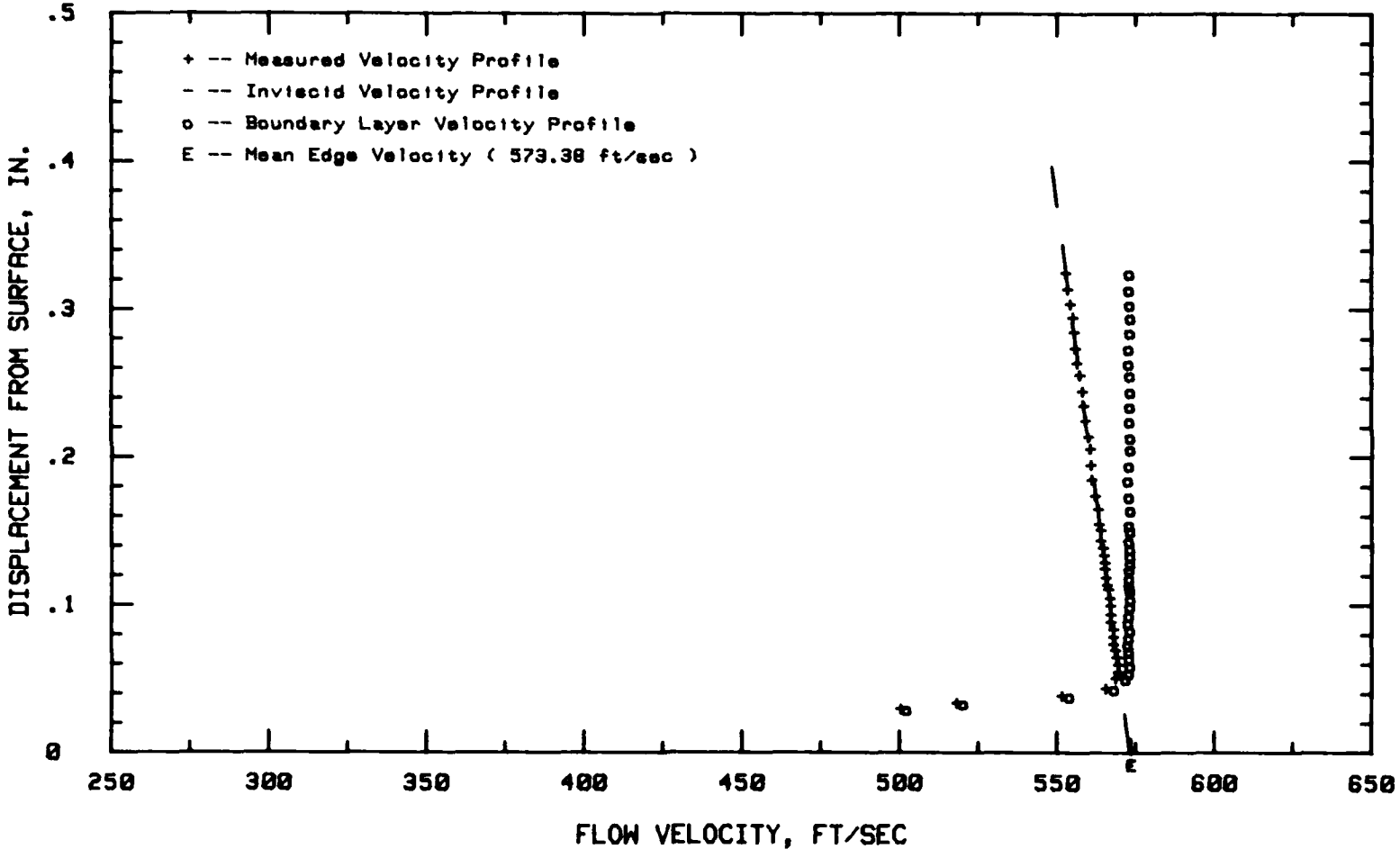

Fig. 31. Boundary Layer Velocity Profiles, Conf.#1 at 34.37 % Chord

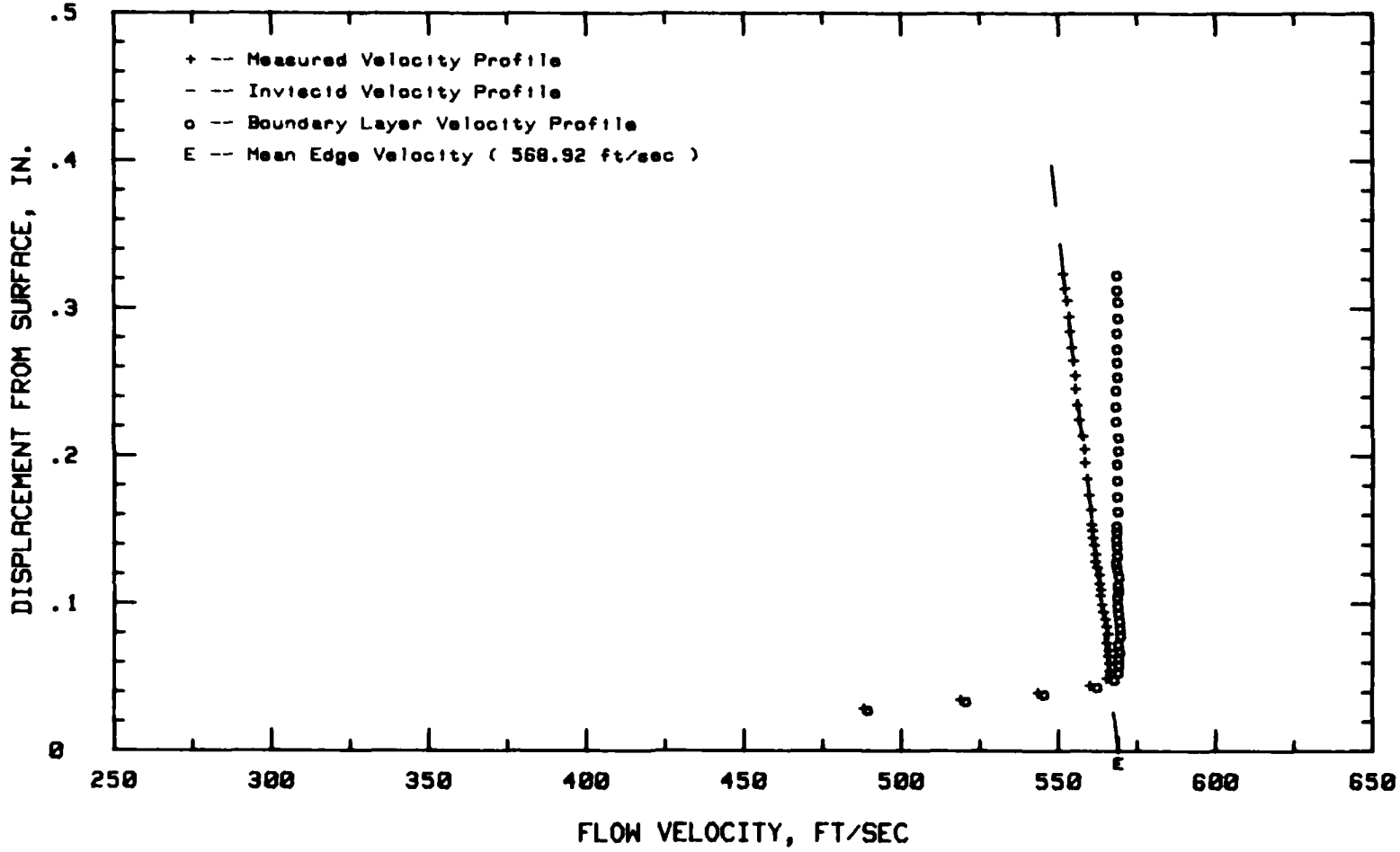

Fig. 32. Boundary Layer Velocity Profiles, Conf.#1 at 40.62 % Chord

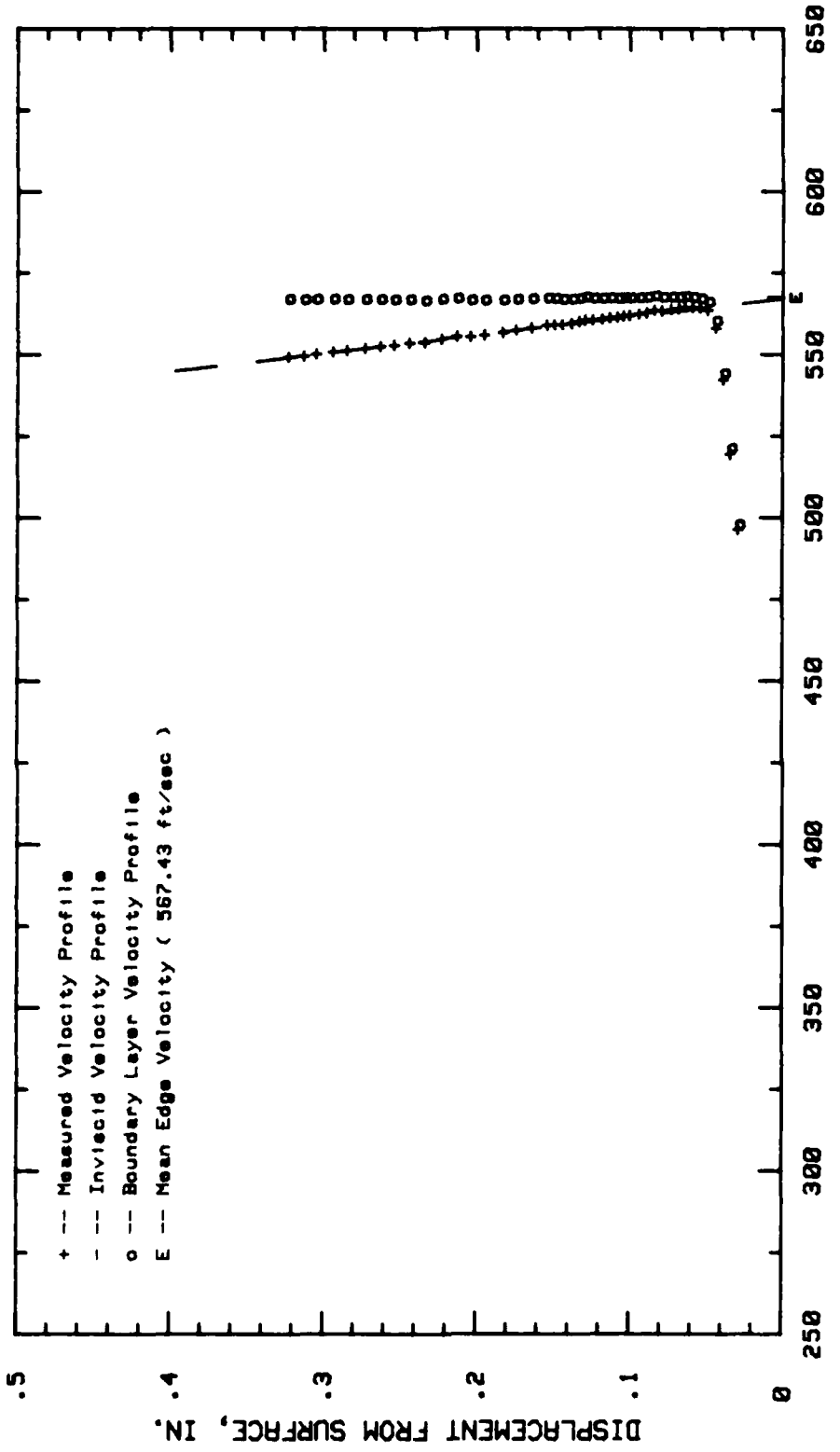

Fig. 33. Boundary Layer Velocity Profiles, Conf.#1 at 45.31 % Chord

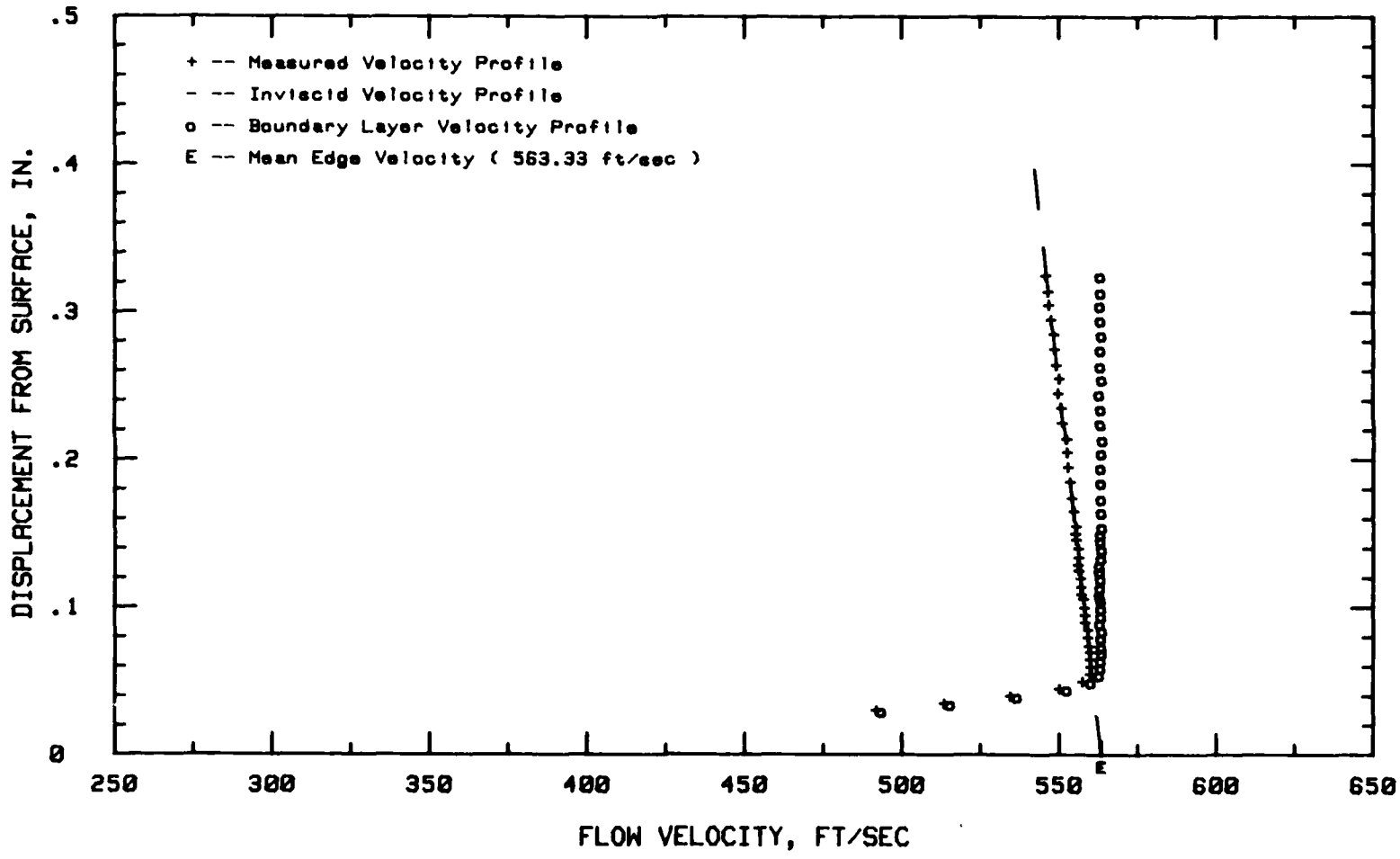

Fig. 34. Boundary Layer Velocity Profiles, Conf.#1 at 50 % Chord

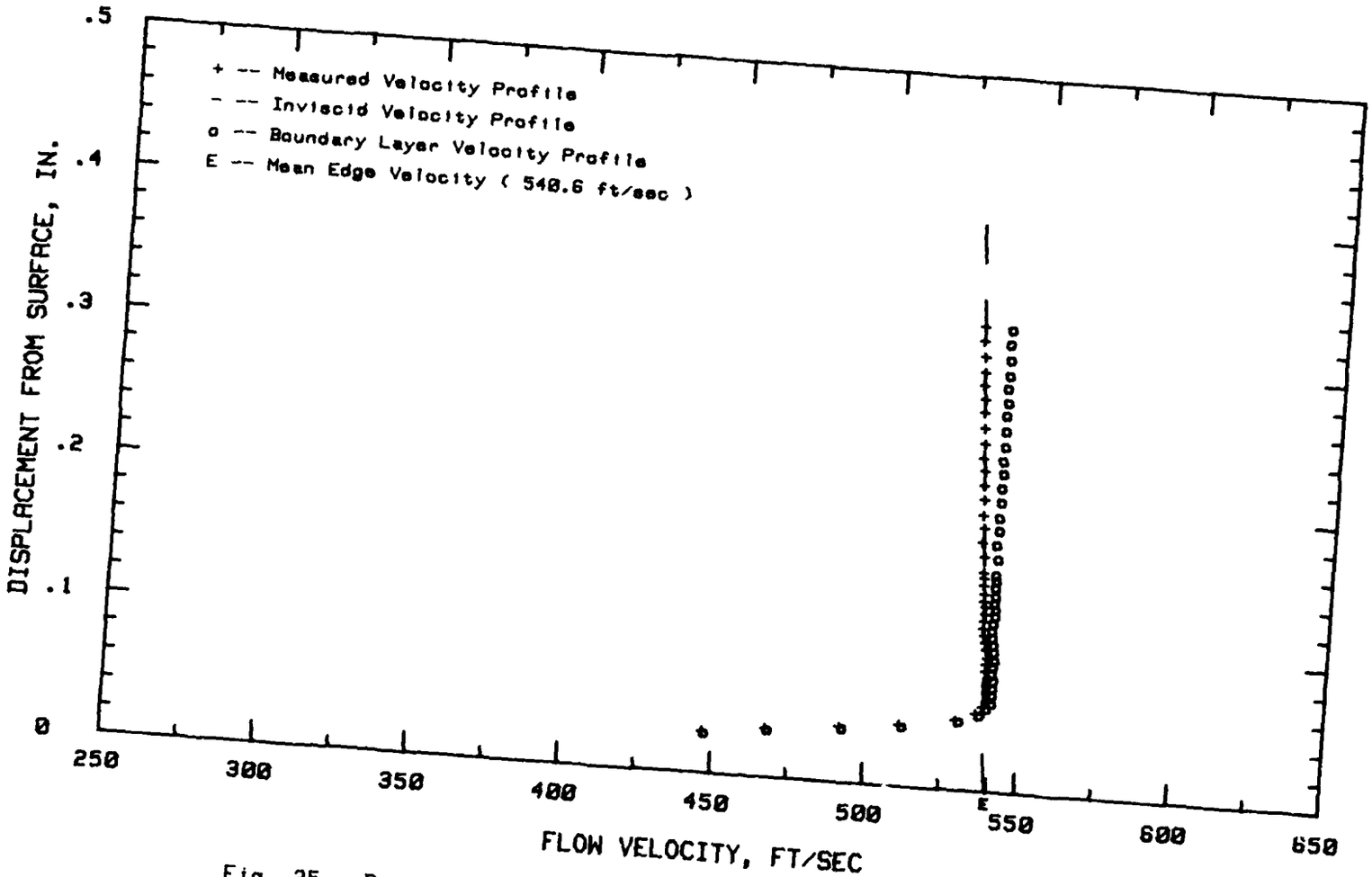

Fig. 35. Boundary Layer Velocity Profiles, Conf.#1 at 65.62 % Chord

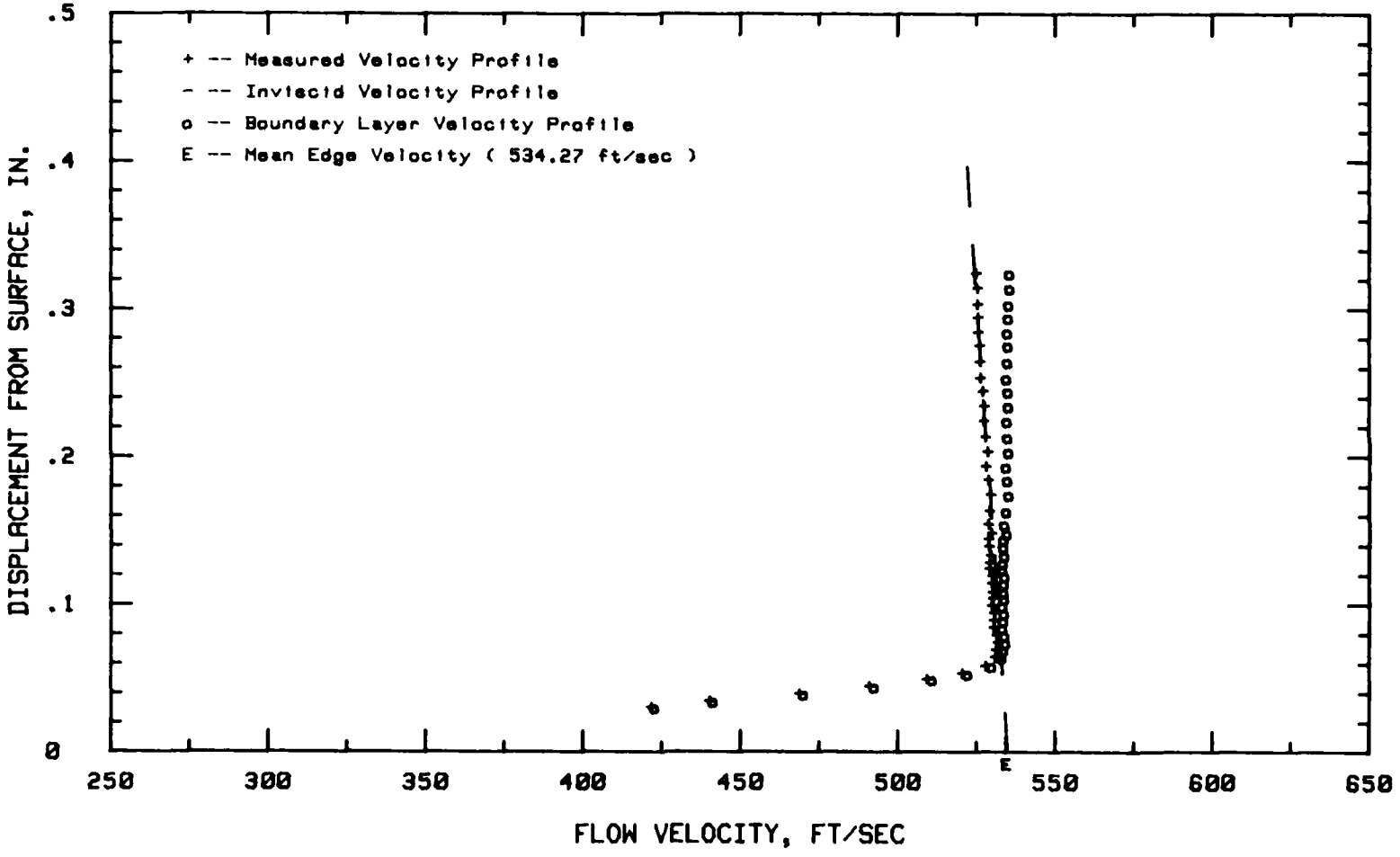

Fig. 36. Boundary Layer Velocity Profiles, Conf.#1 at 70.31 % Chord

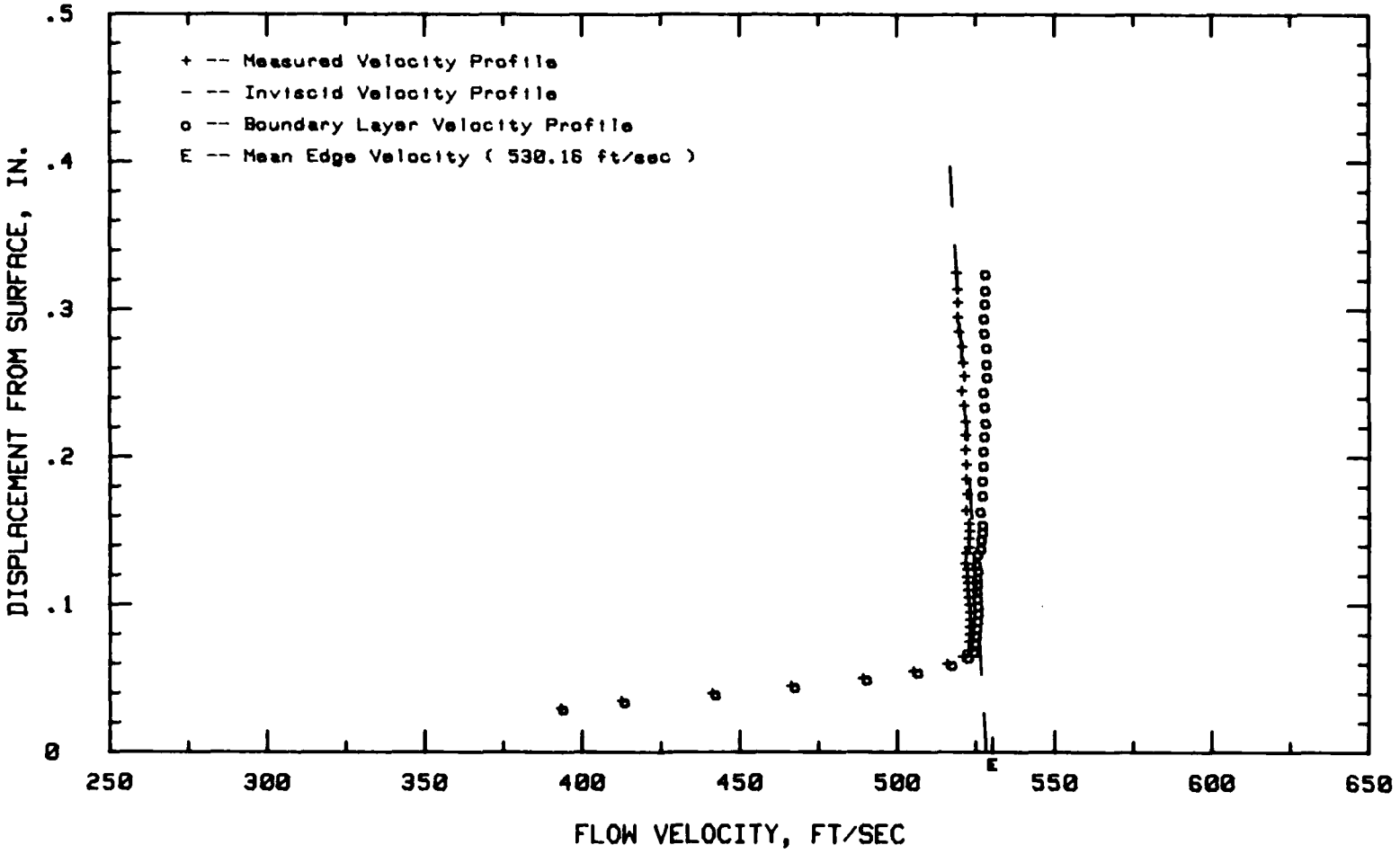

Fig. 37. Boundary Layer Velocity Profiles, Conf.#1 at 75 % Chord

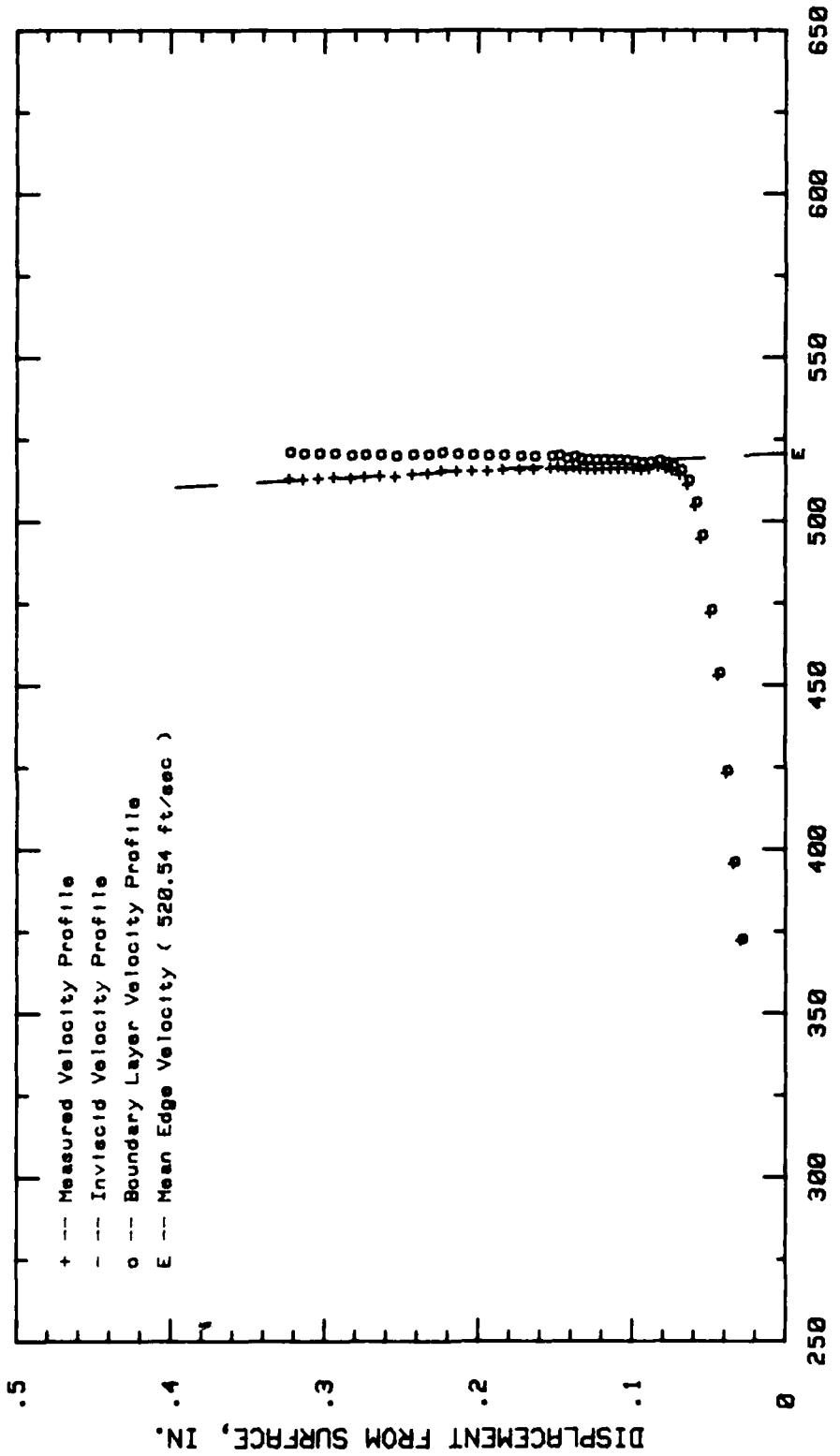

Fig. 38. Boundary Layer Velocity Profiles, Conf.#1 at 79.68 % Chord

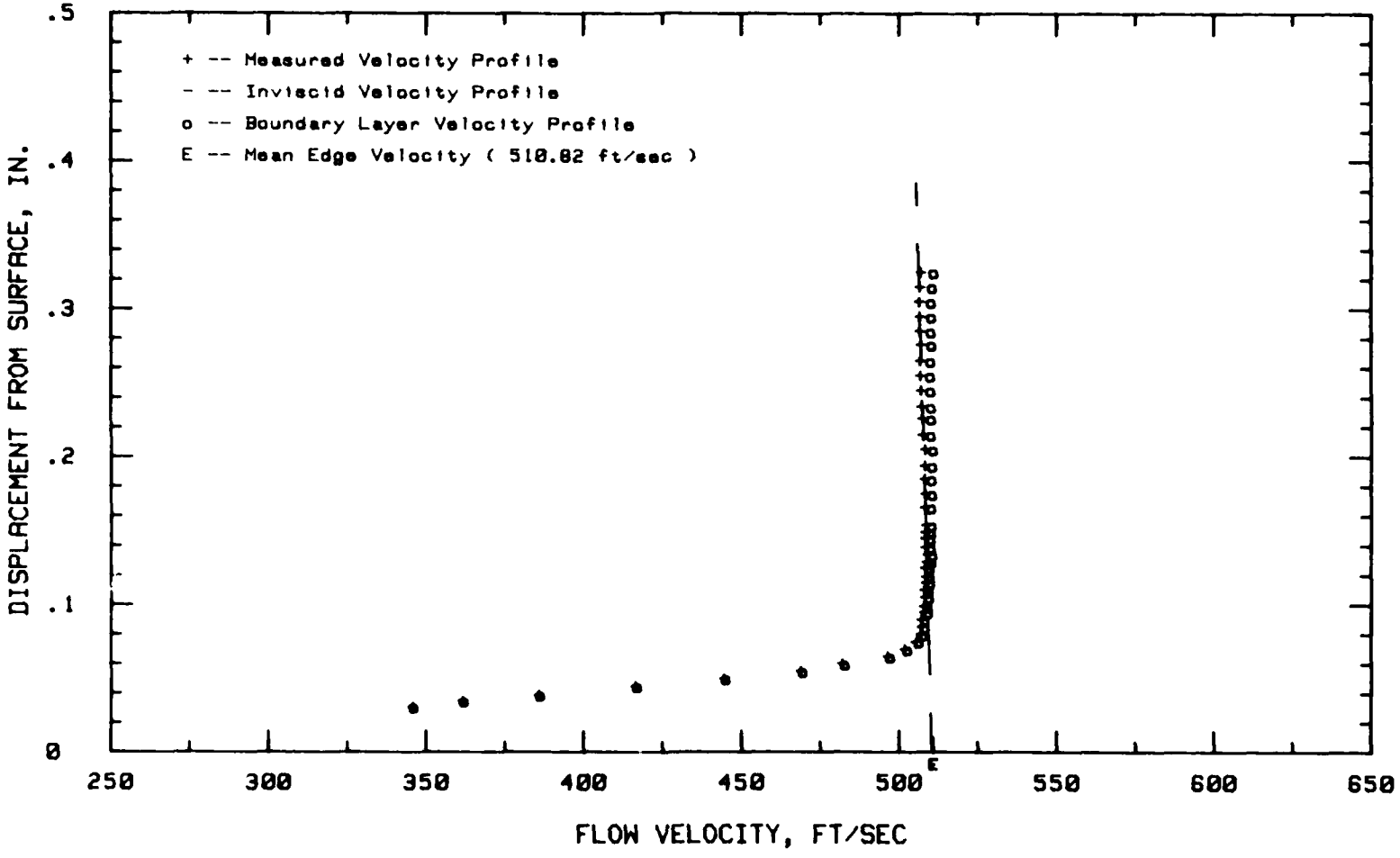

Fig. 39. Boundary Layer Velocity Profiles, Conf.#1 at 84.37 % Chord

APPENDIX E

Boundary Layer Velocity Profiles, Configuration #2

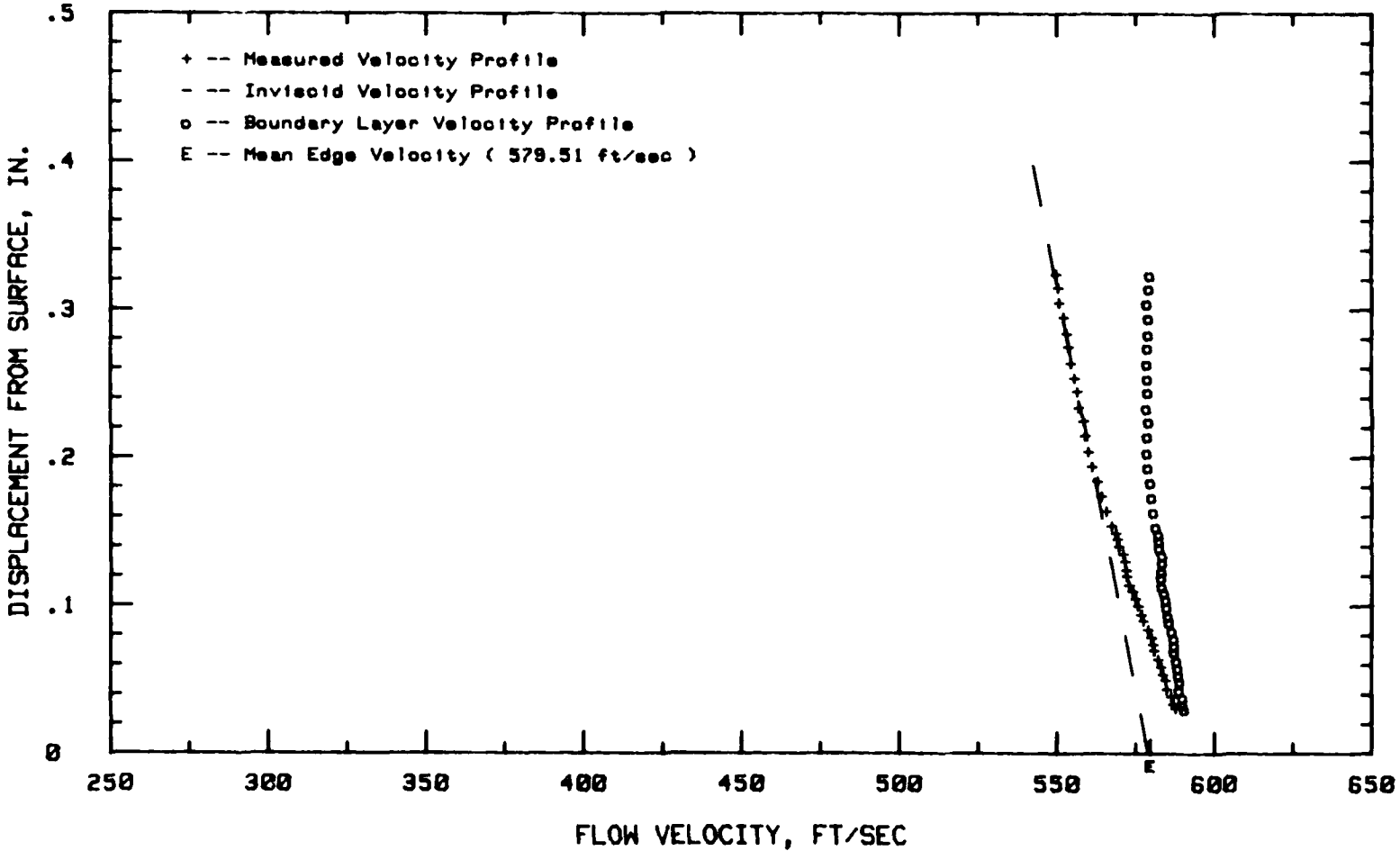

Fig. 40. Boundary Layer Velocity Profiles, Conf.#2 at 4.68 % Chord

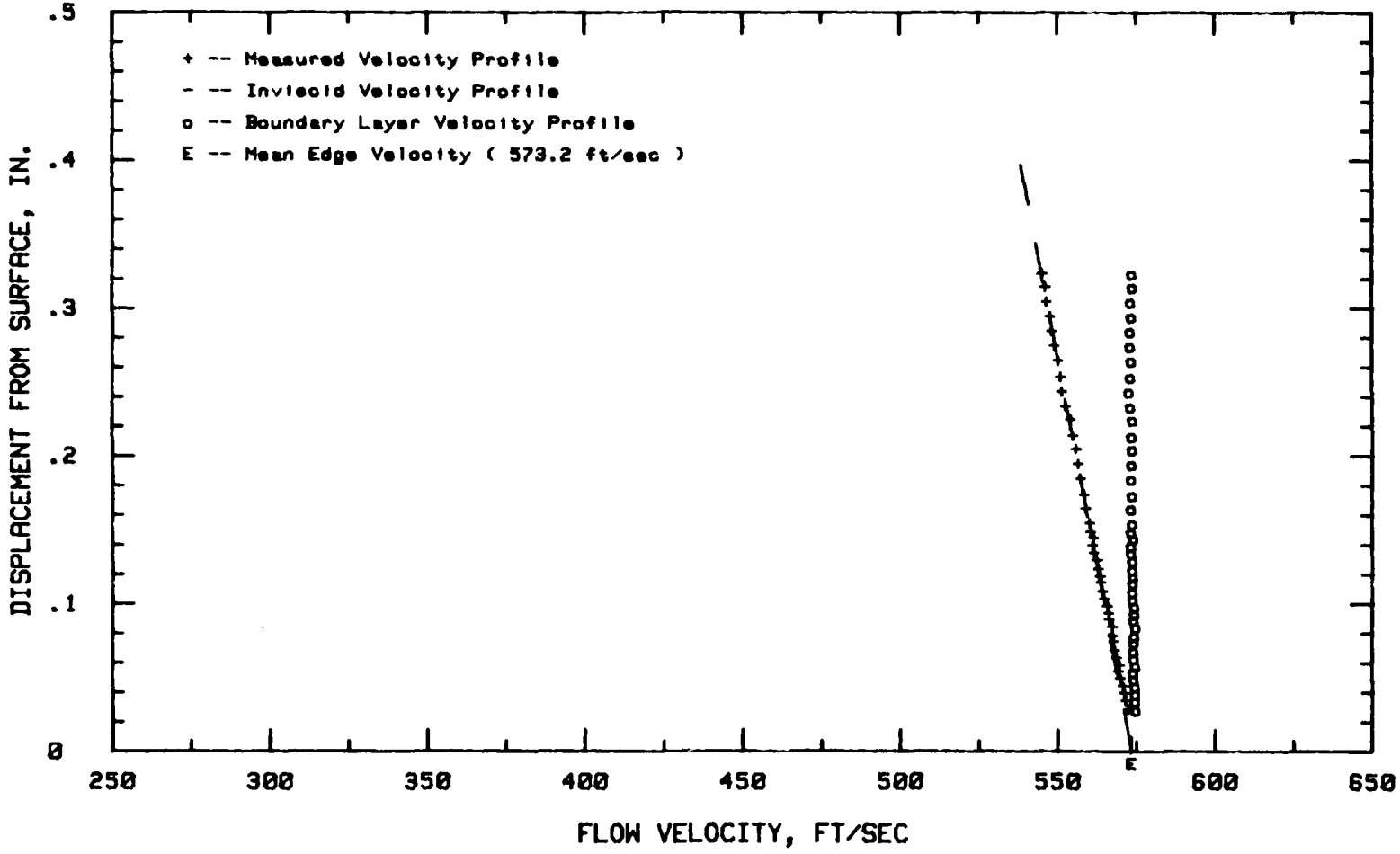

Fig. 41. Boundary Layer Velocity Profiles, Conf.#2 at 9.37 % Chord

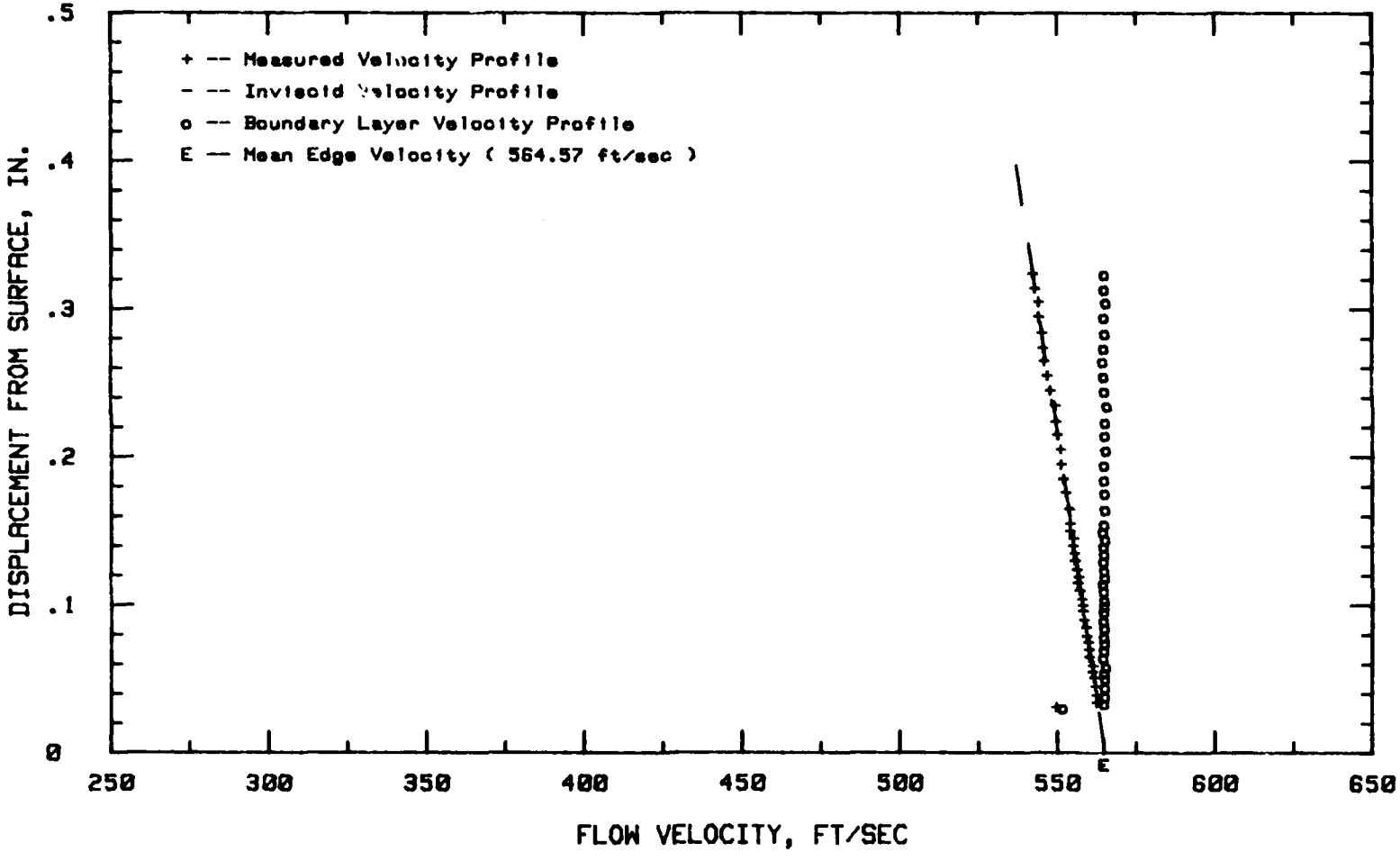

Fig. 42. Boundary Layer Velocity Profiles, Conf.#2 at 25 % Chord

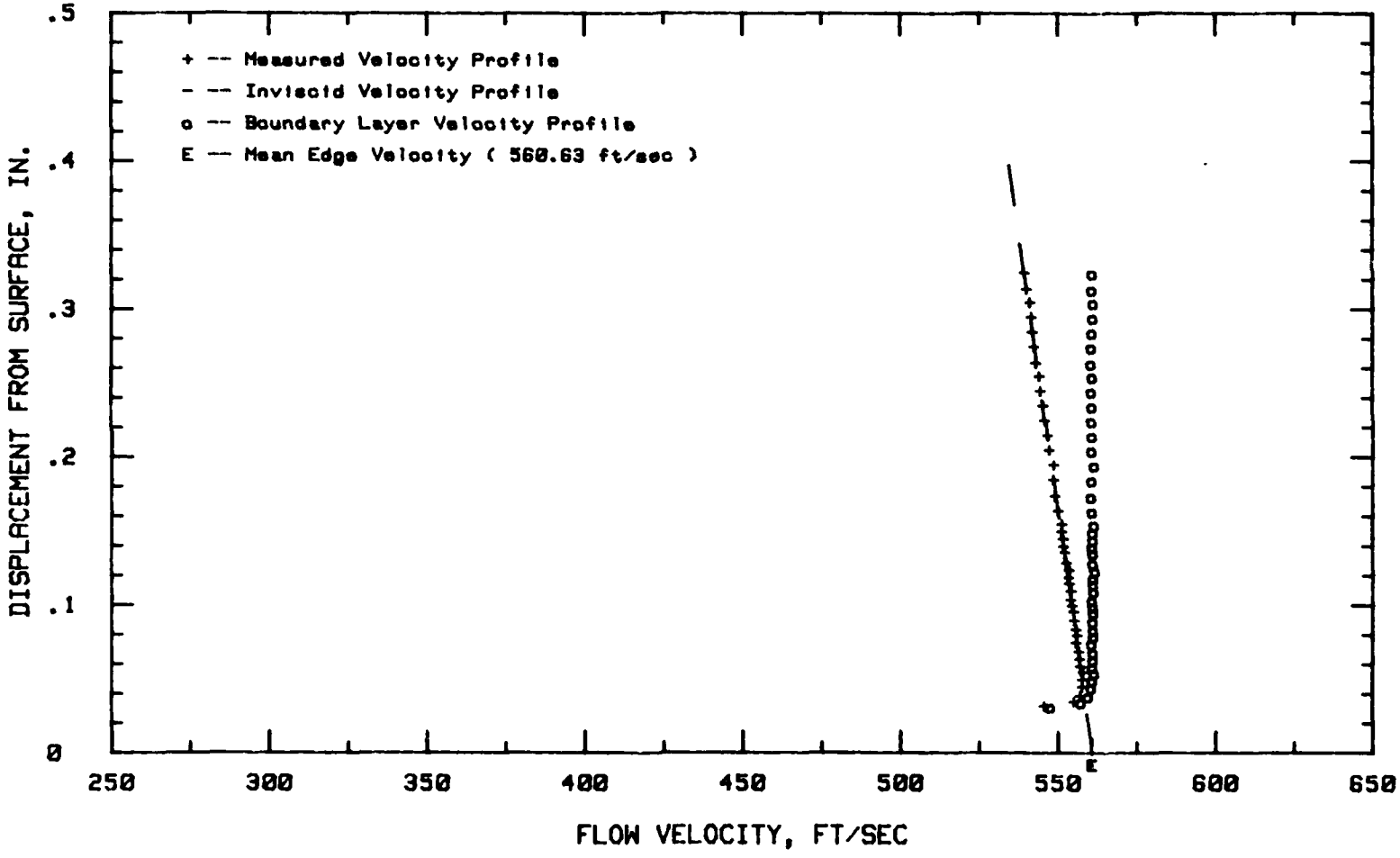

Fig. 43. Boundary Layer Velocity Profiles, Conf.#2 at 29.68 % Chord

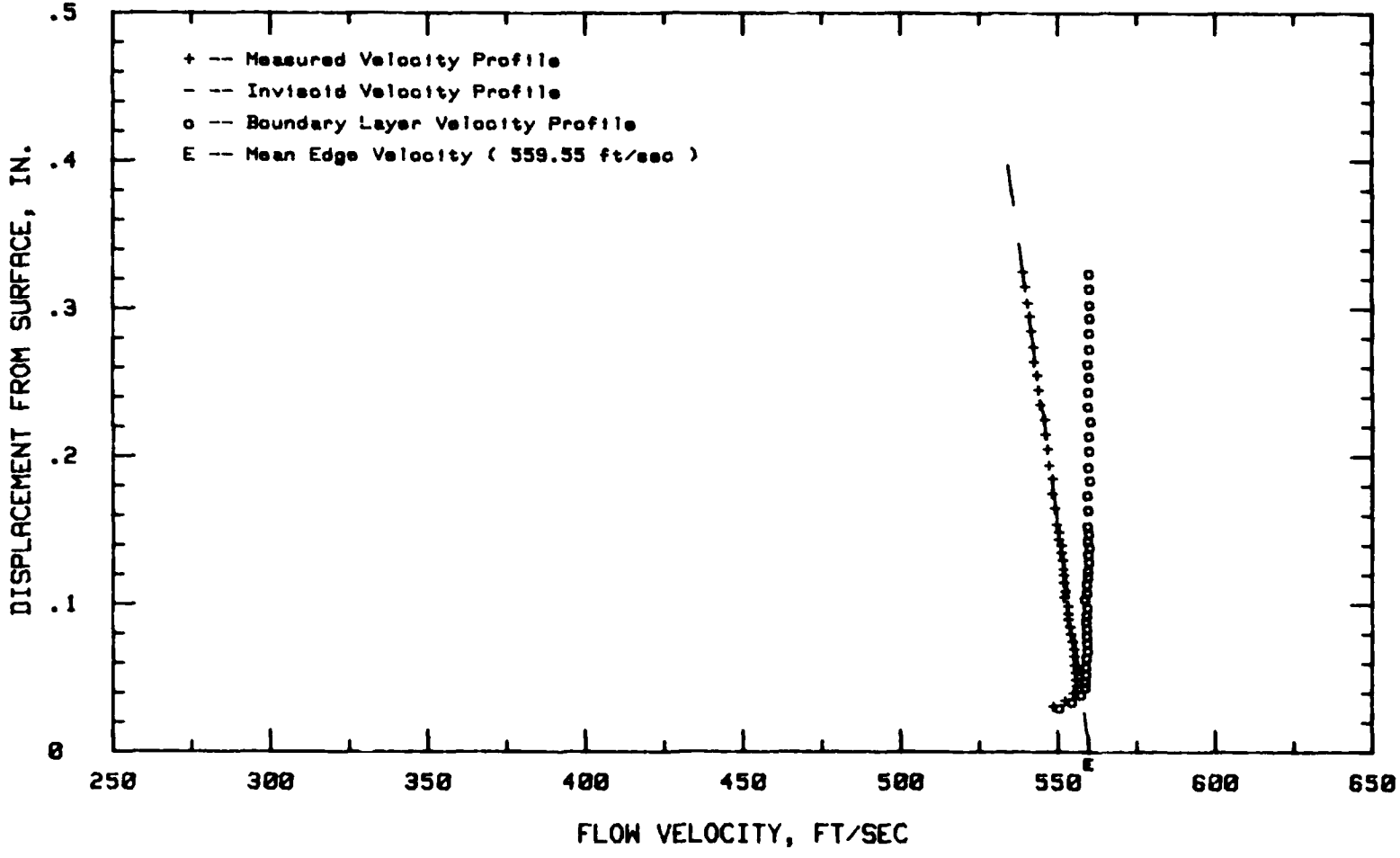

Fig. 44. Boundary Layer Velocity Profiles, Conf.#2 at 34.37 % Chord

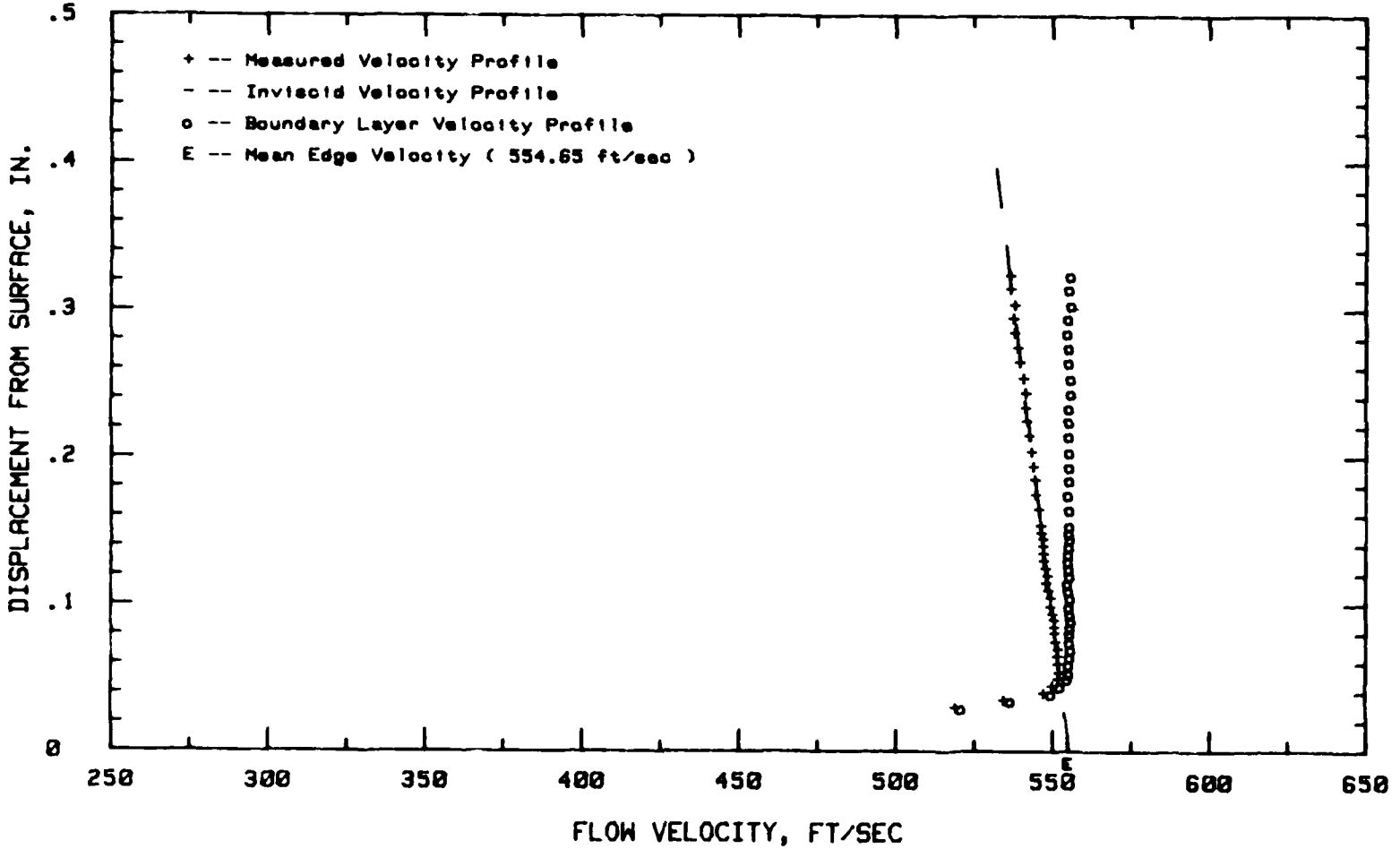

Fig. 45. Boundary Layer Velocity Profiles, Conf.#2 at 40.62 % Chord

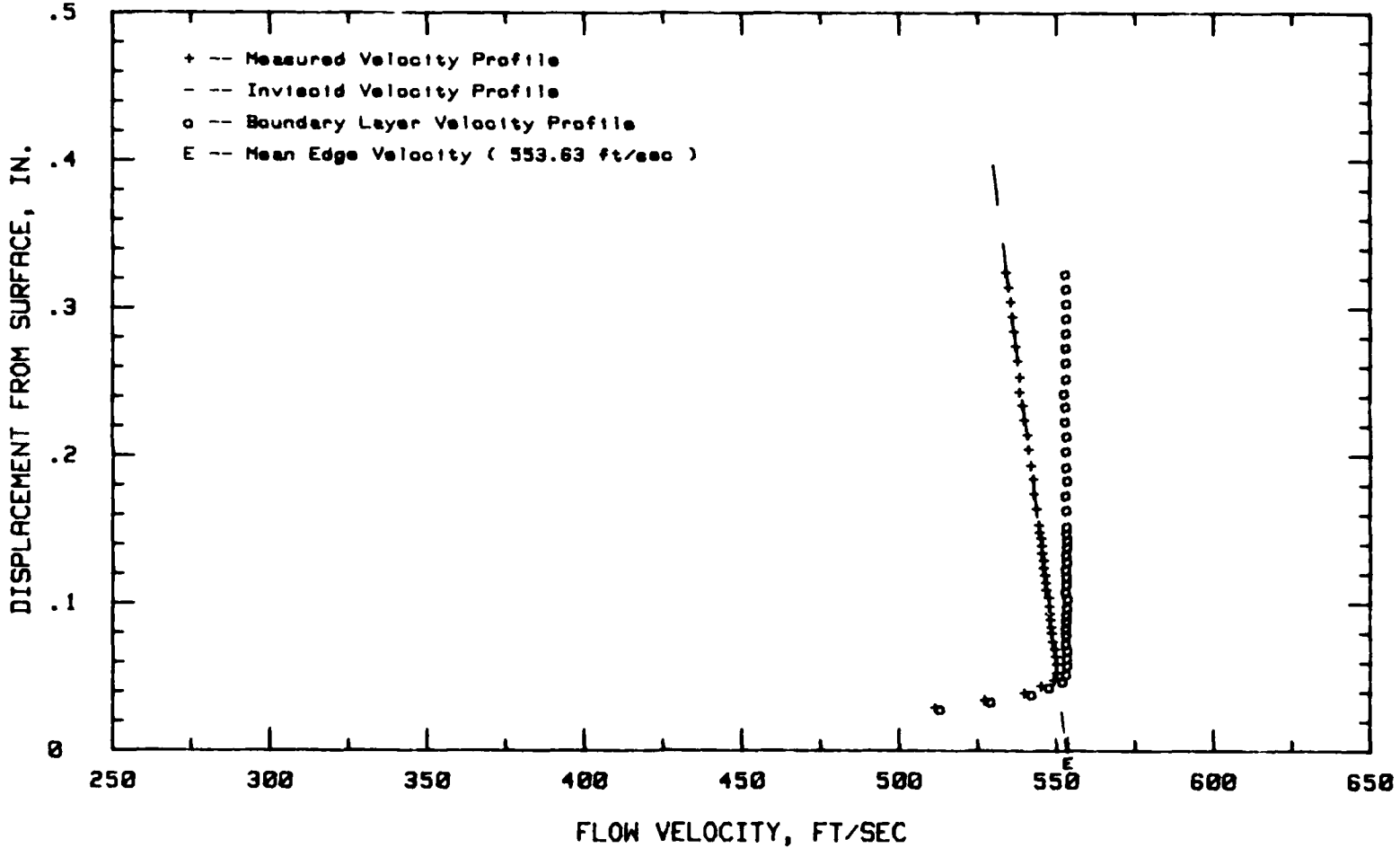

Fig. 46. Boundary Layer Velocity Profiles, Conf.#2 at 45.31 % Chord

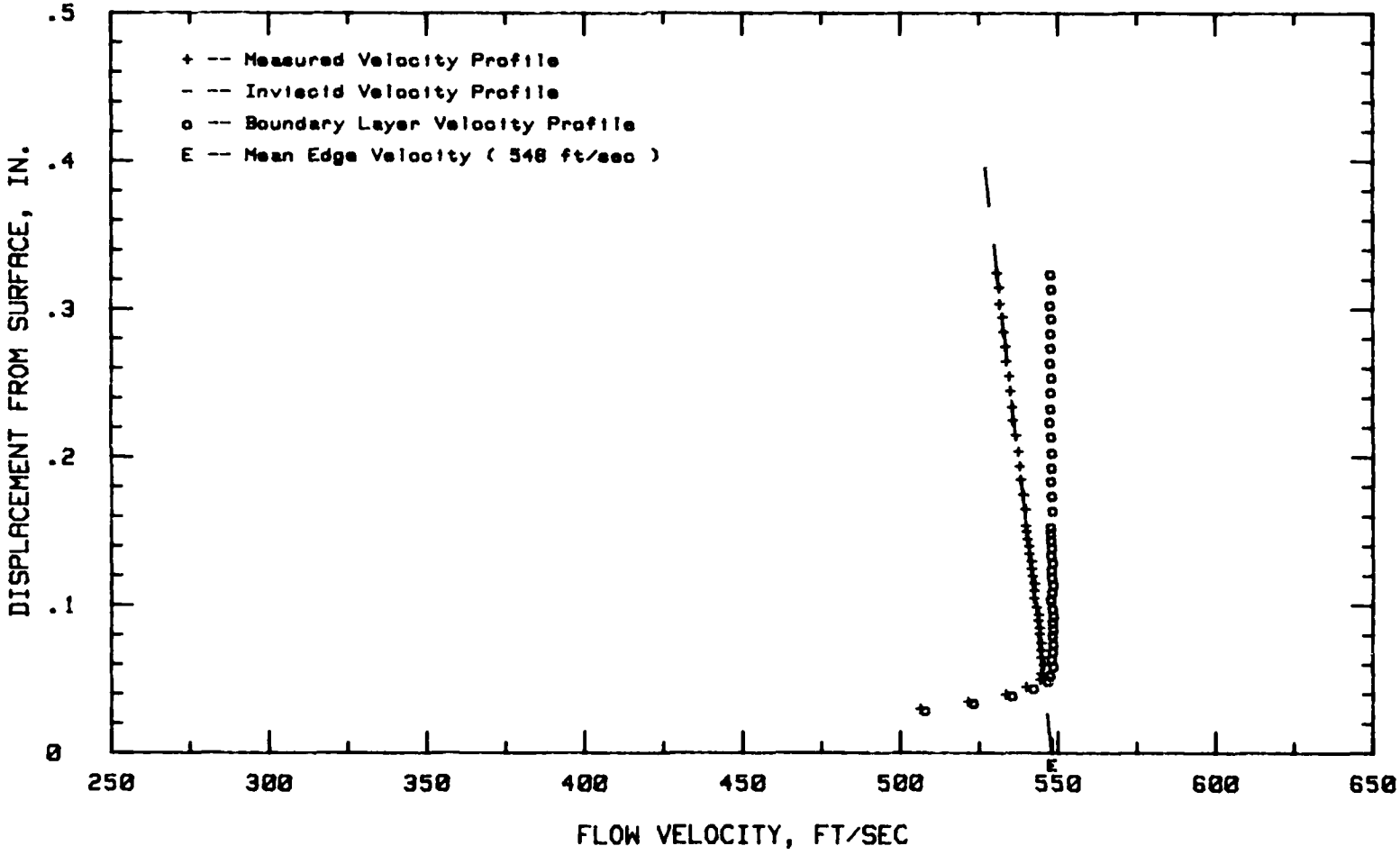

Fig. 47. Boundary Layer Velocity Profiles, Conf.#2 at 50 % Chord

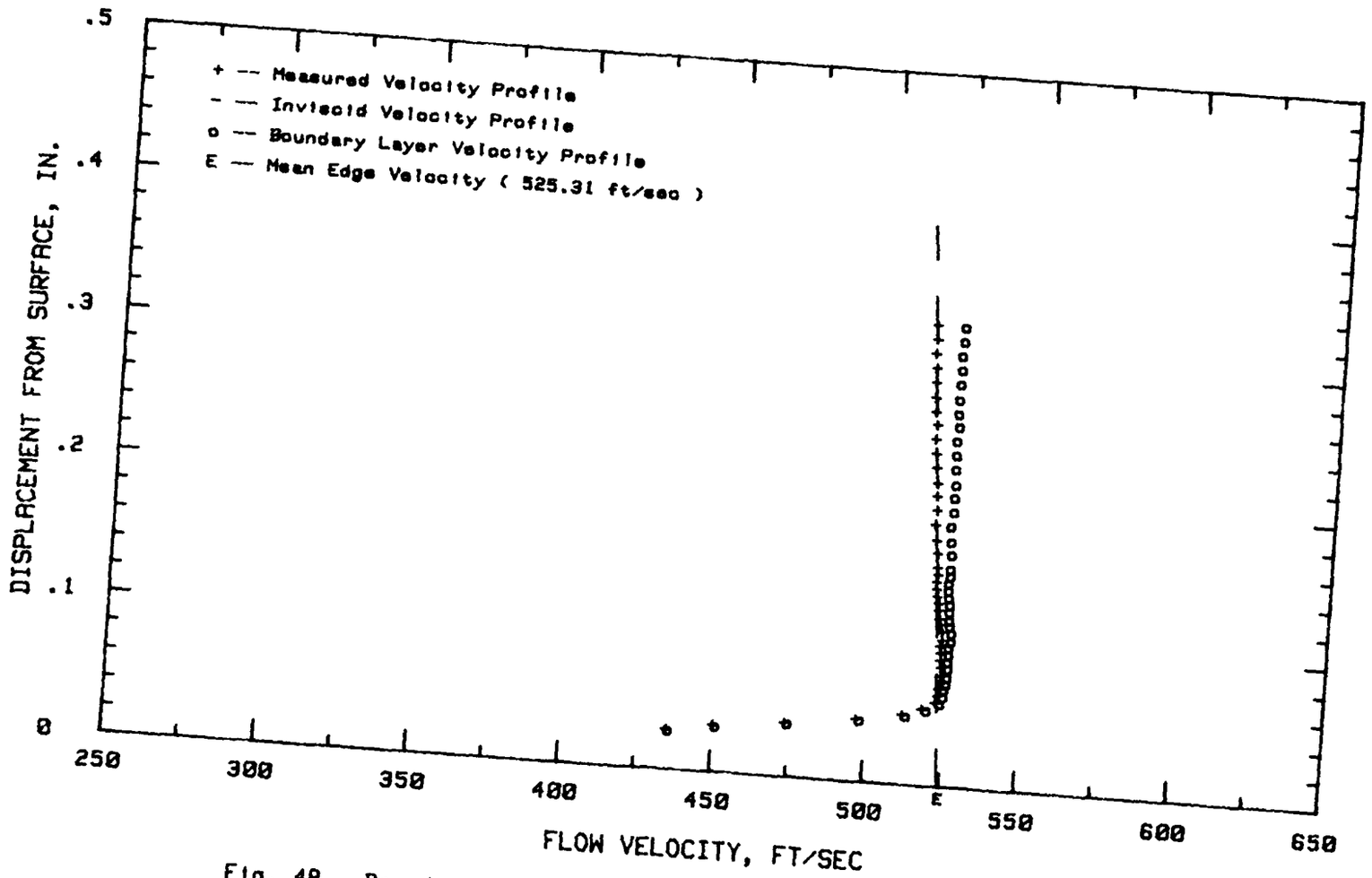

Fig. 48. Boundary Layer Velocity Profiles, Conf.#2 at 65.62 % Chord

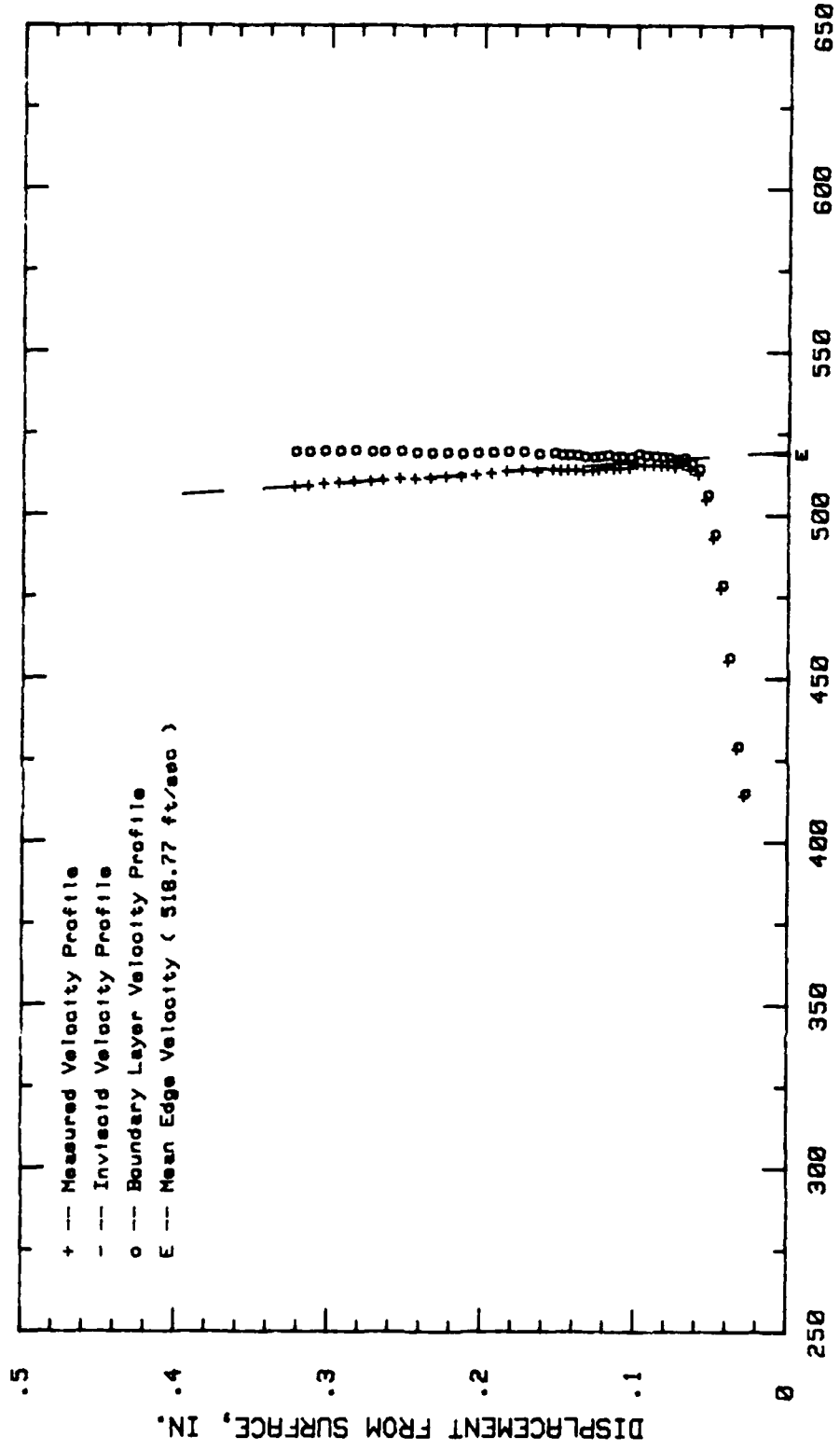

Fig. 49. Boundary Layer Velocity Profiles, Conf.#2 at 70.31 % Chord

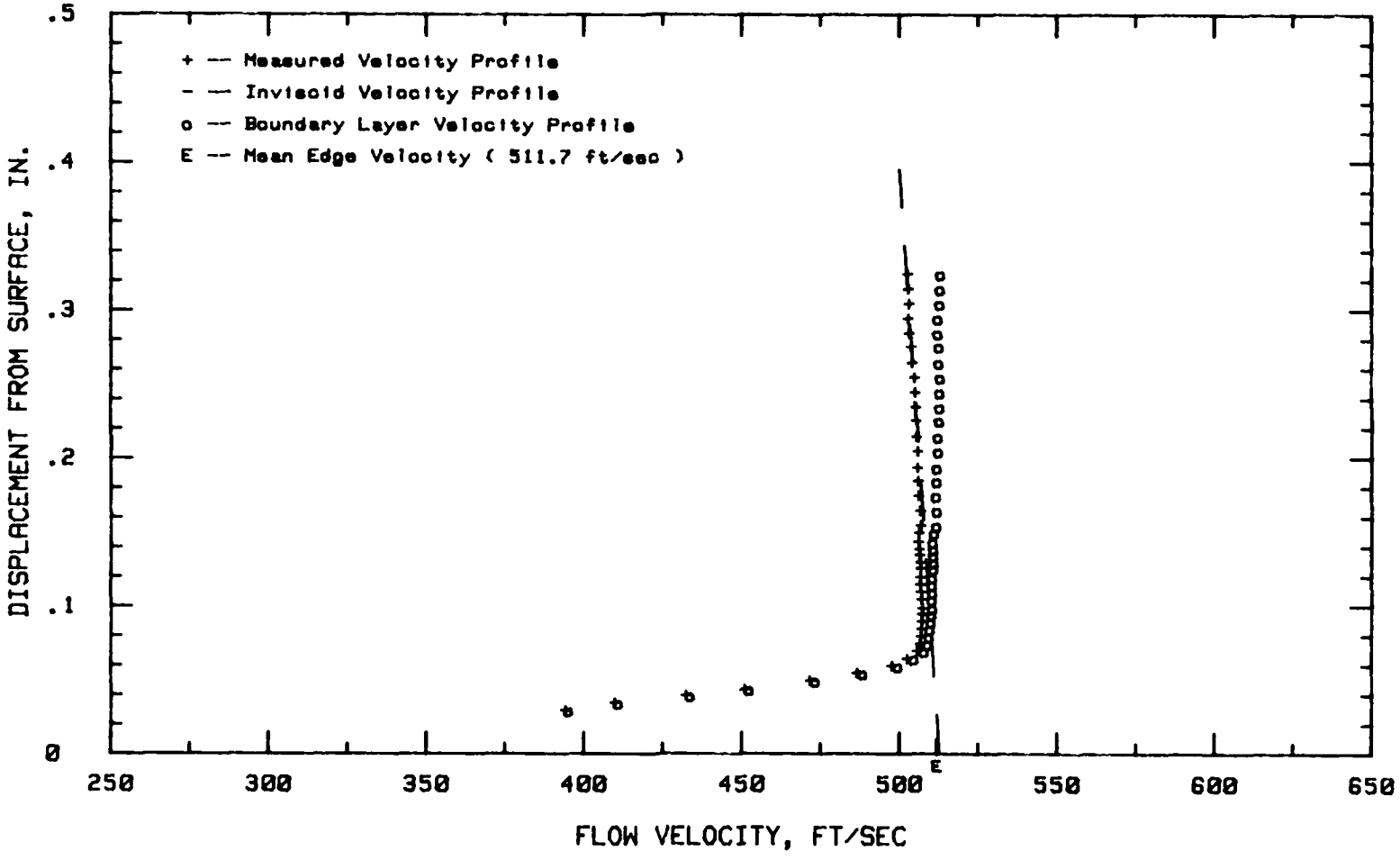

Fig. 50. Boundary Layer Velocity Profiles, Conf.#2 at 75 % Chord

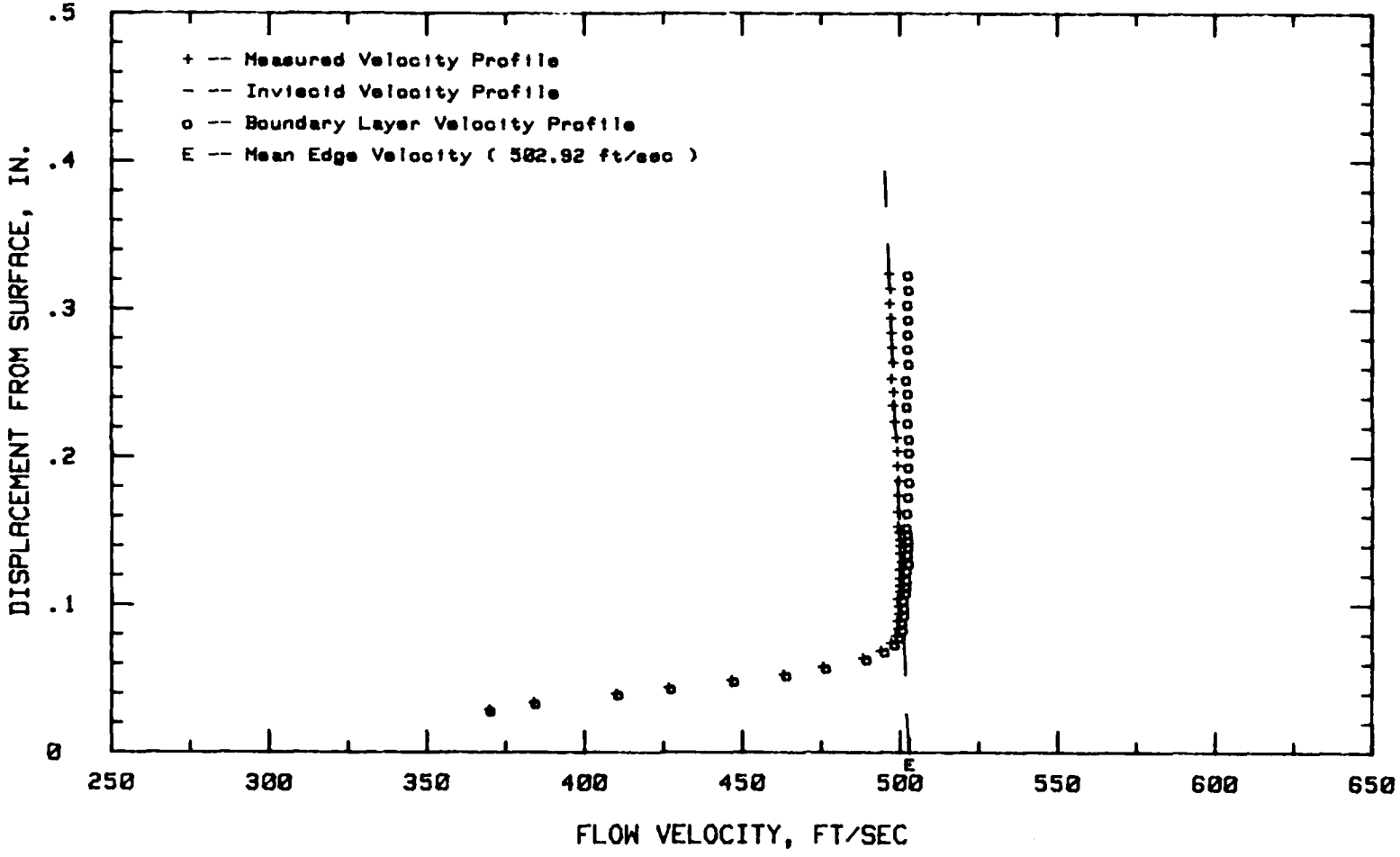

Fig. 51. Boundary Layer Velocity Profiles, Conf.#2 at 79.68 % Chord

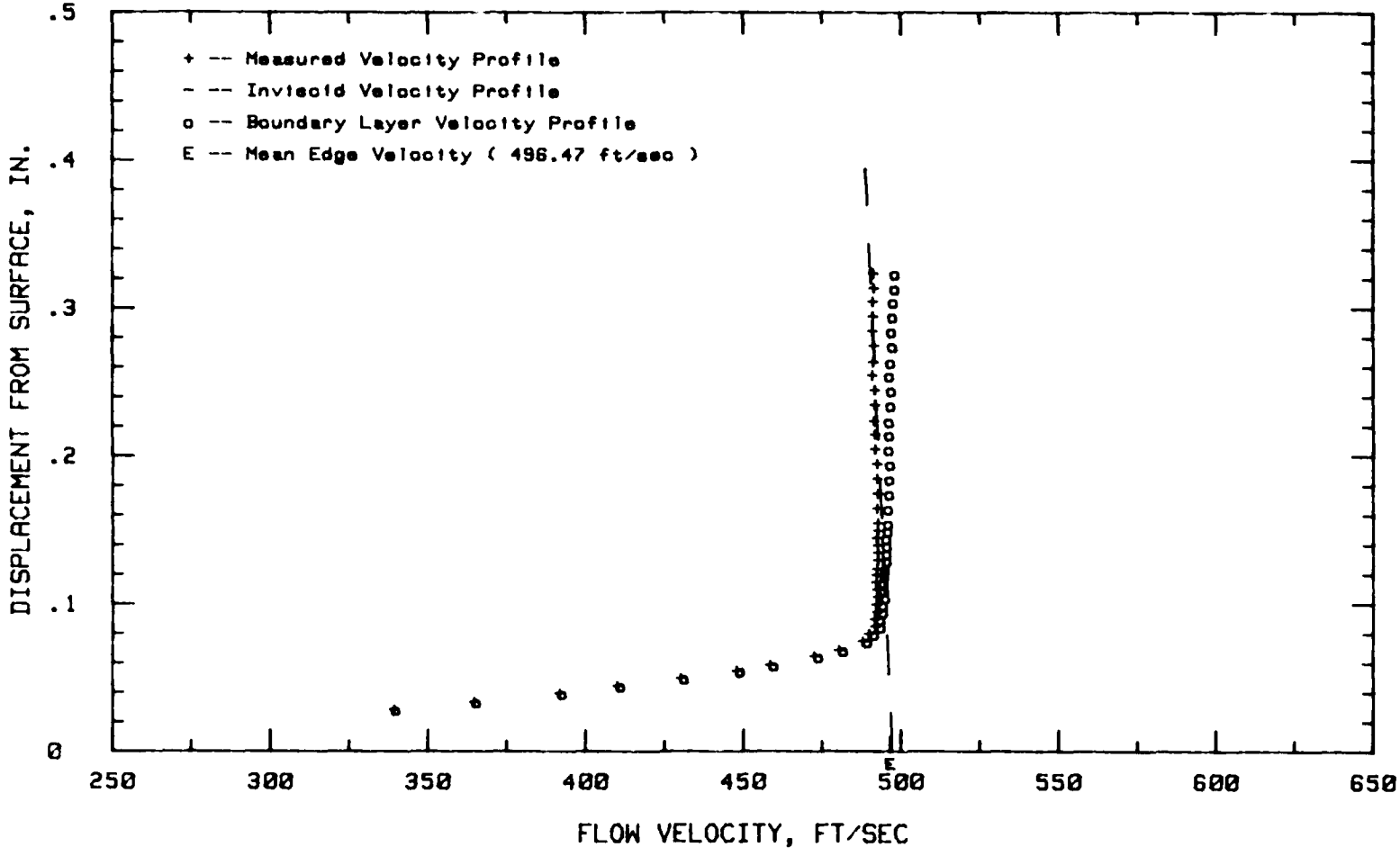

Fig. 52. Boundary Layer Velocity Profiles, Conf.#2 at 84.37 % Chord

APPENDIX F

Boundary Layer Velocity Profiles, Configuration #3

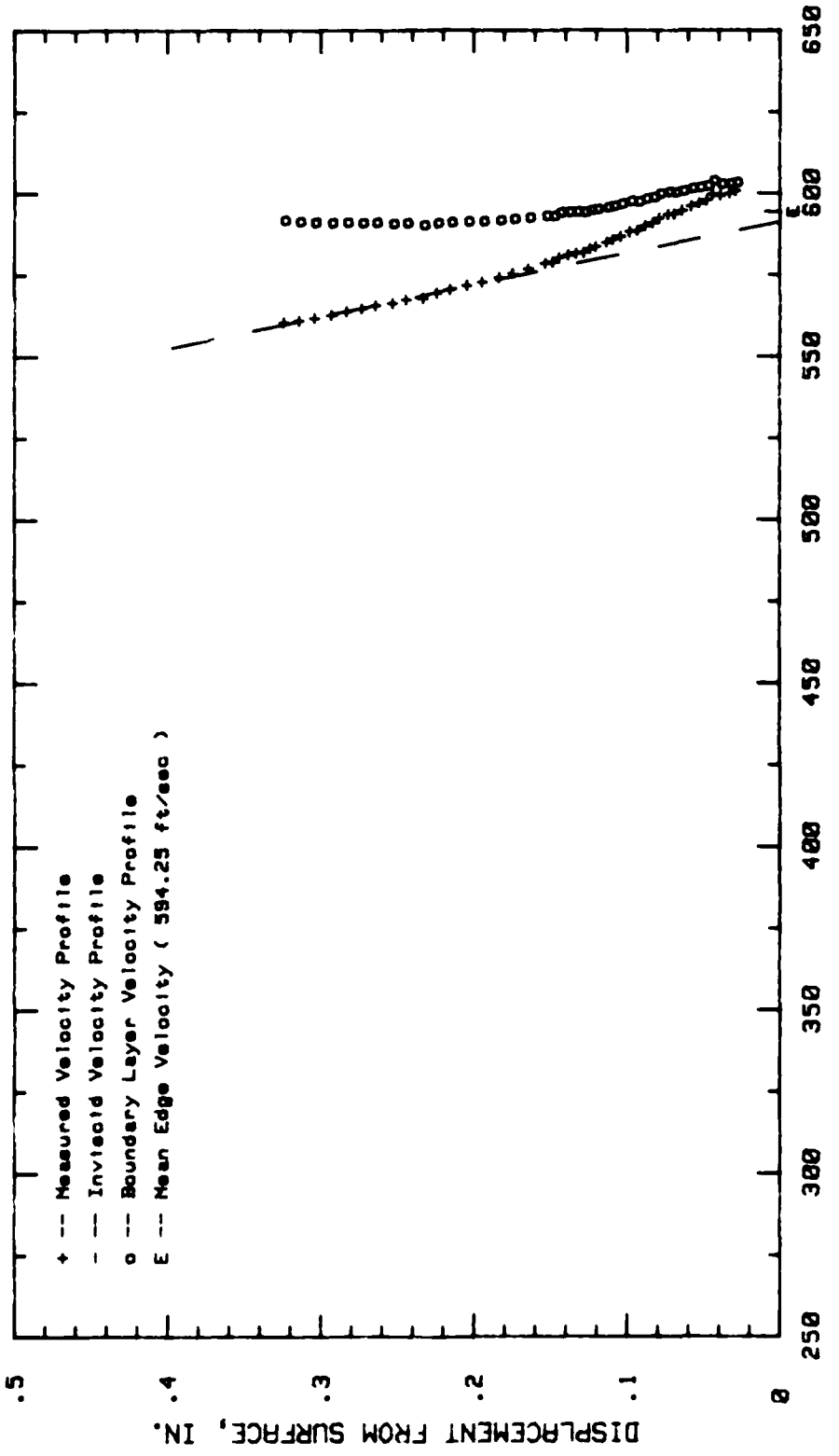

Fig. 53. Boundary Layer Velocity Profiles, Conf.#3 at 4.68 % Chord

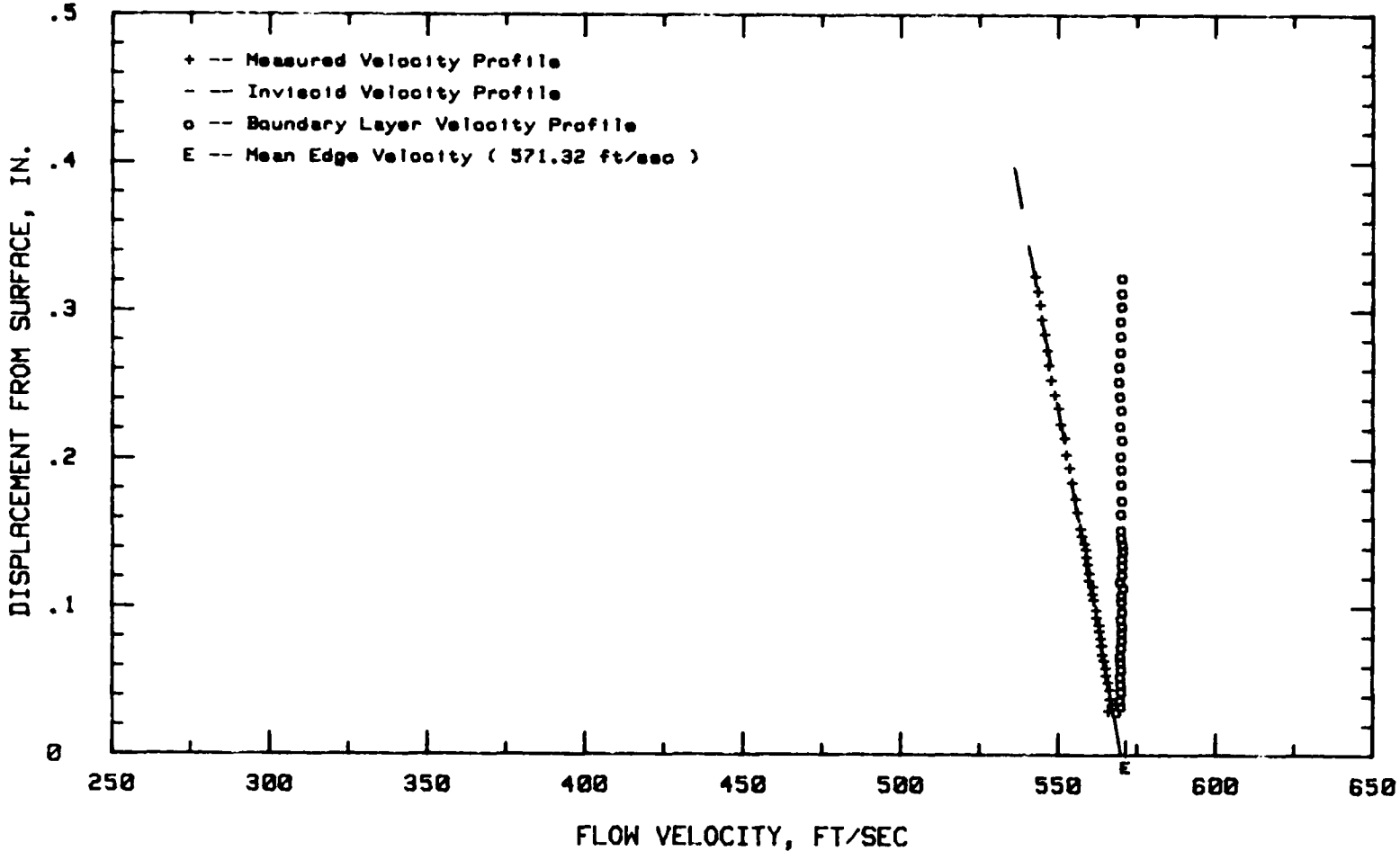

Fig. 54. Boundary Layer Velocity Profiles, Conf.#3 at 9.37 % Chord

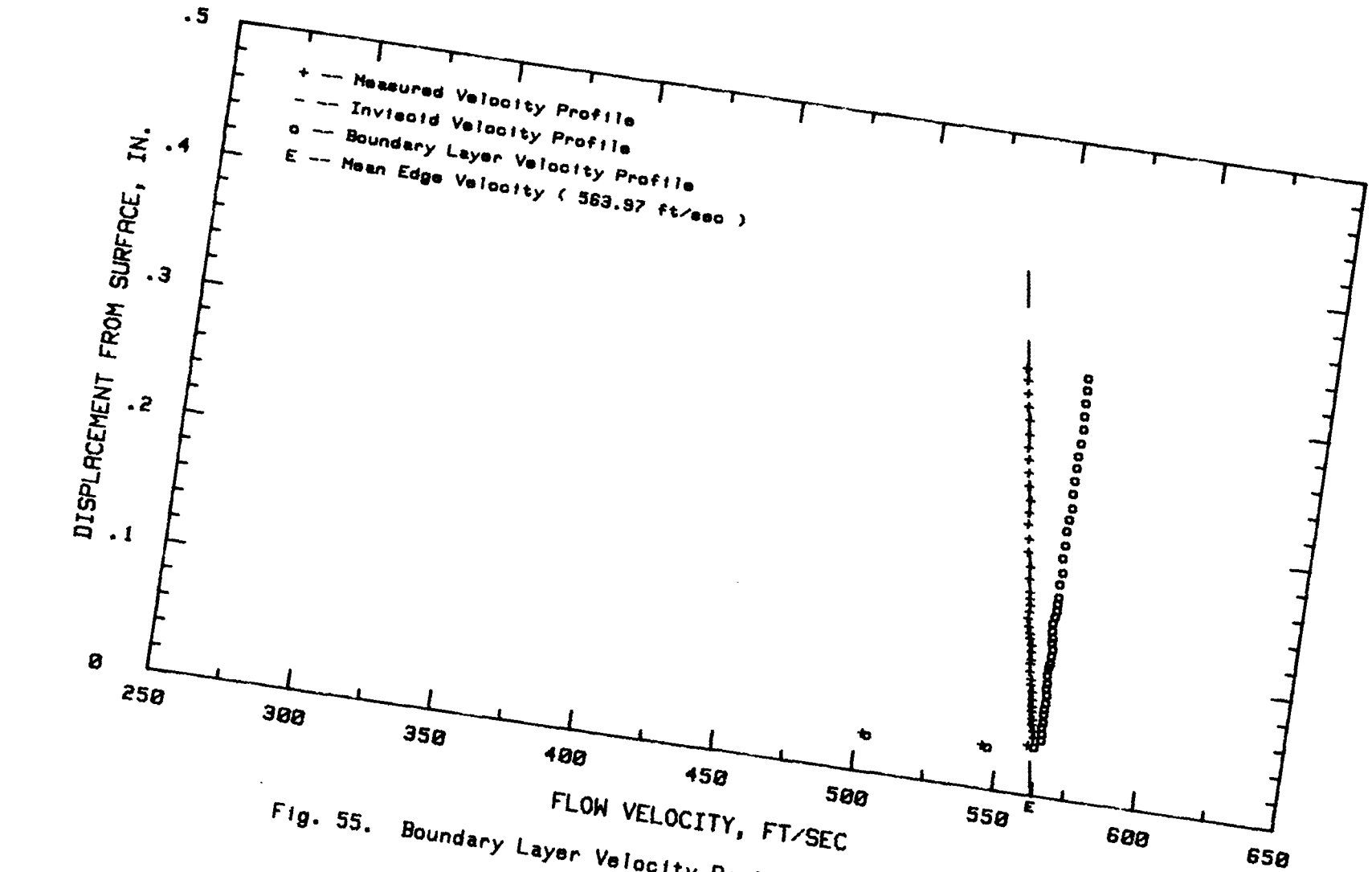

Fig. 55. Boundary Layer Velocity Profiles, Conf.#3 at 25 % Chord

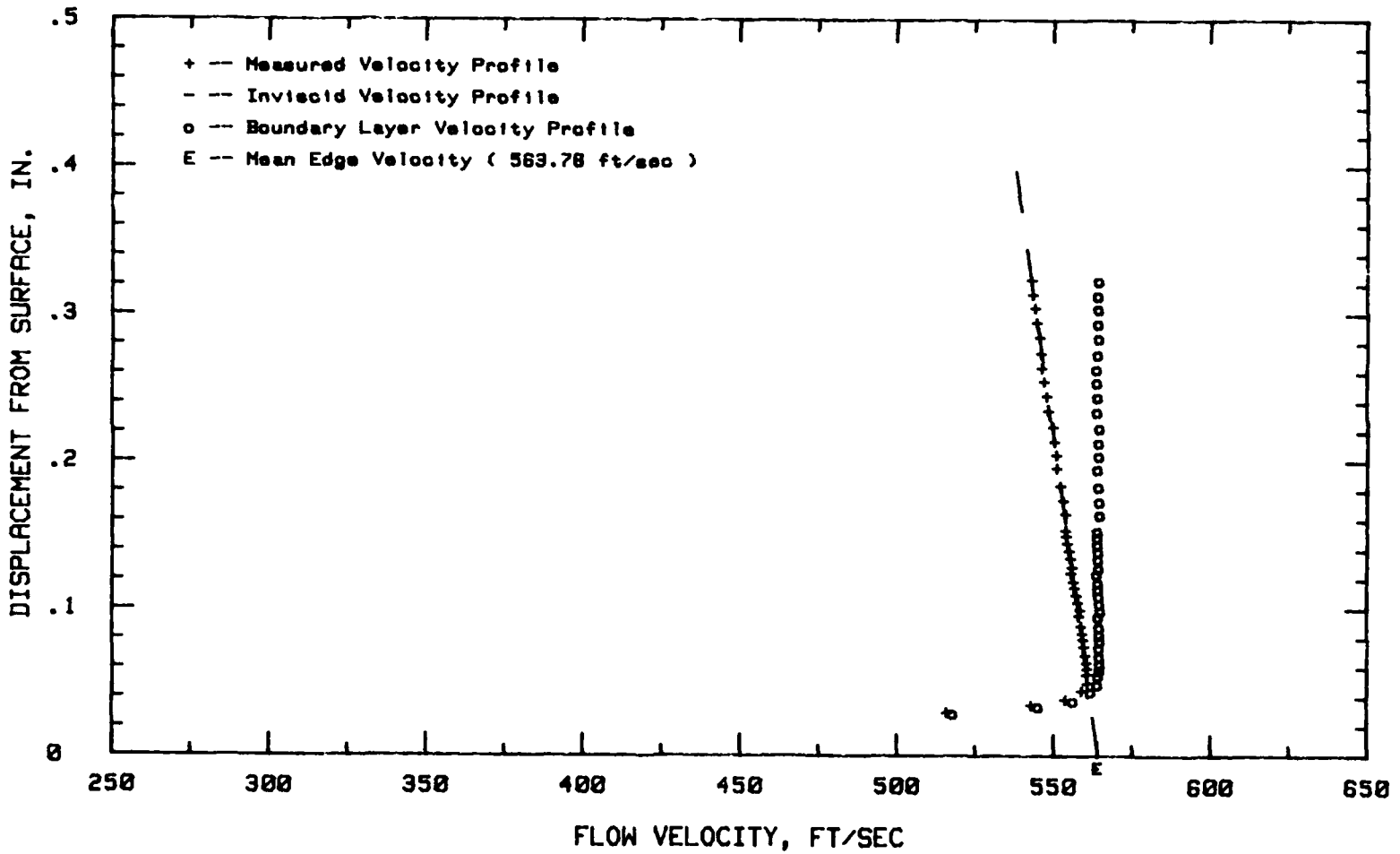

Fig. 56. Boundary Layer Velocity Profiles, Conf.#3 at 29.68 % Chord

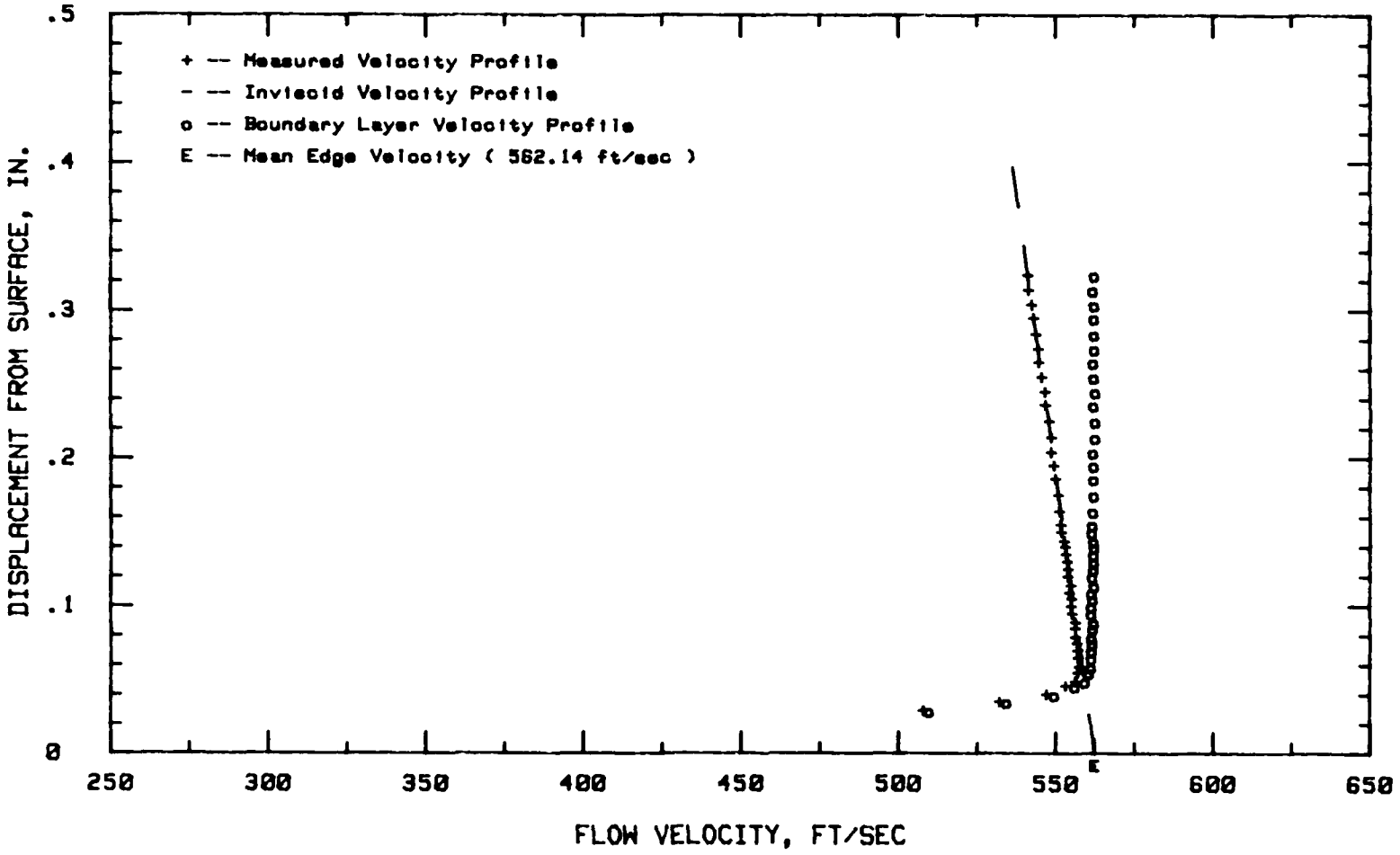

Fig. 57. Boundary Layer Velocity Profiles, Conf.#3 at 34.37 % Chord

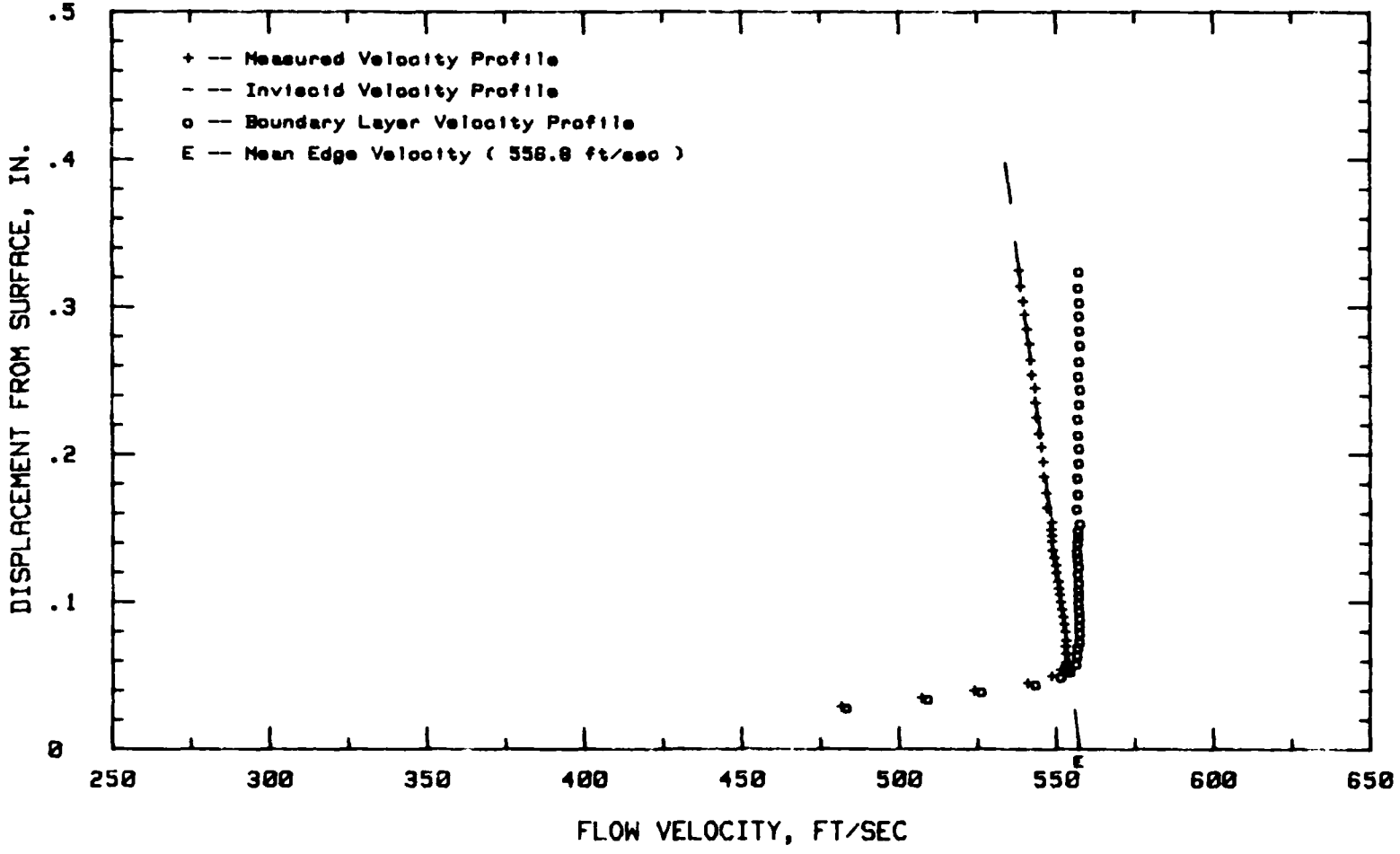

Fig. 58. Boundary Layer Velocity Profiles, Conf.#3 at 40.62 % Chord

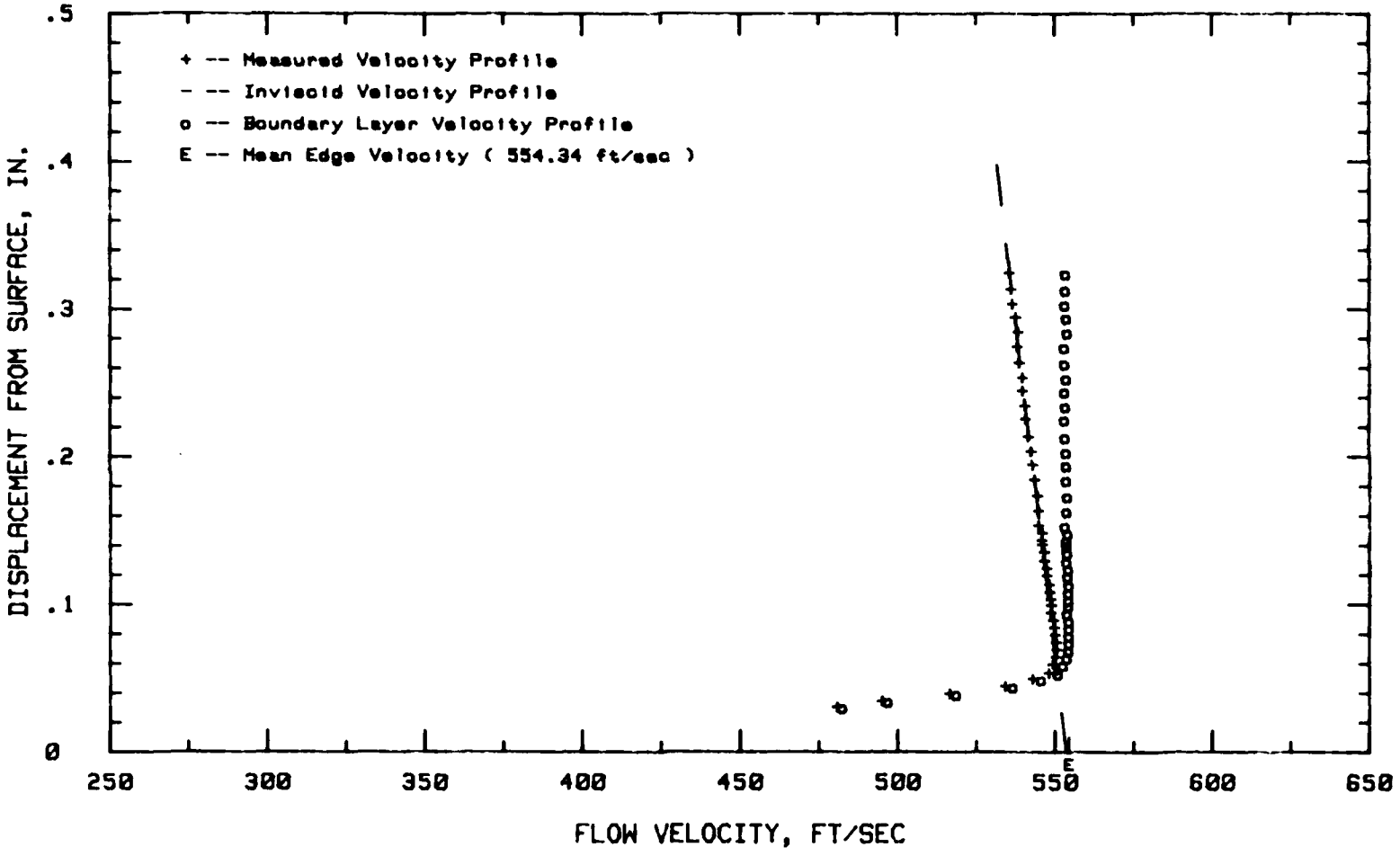

Fig. 59. Boundary Layer Velocity Profiles, Conf.#3 at 45.31 % Chord

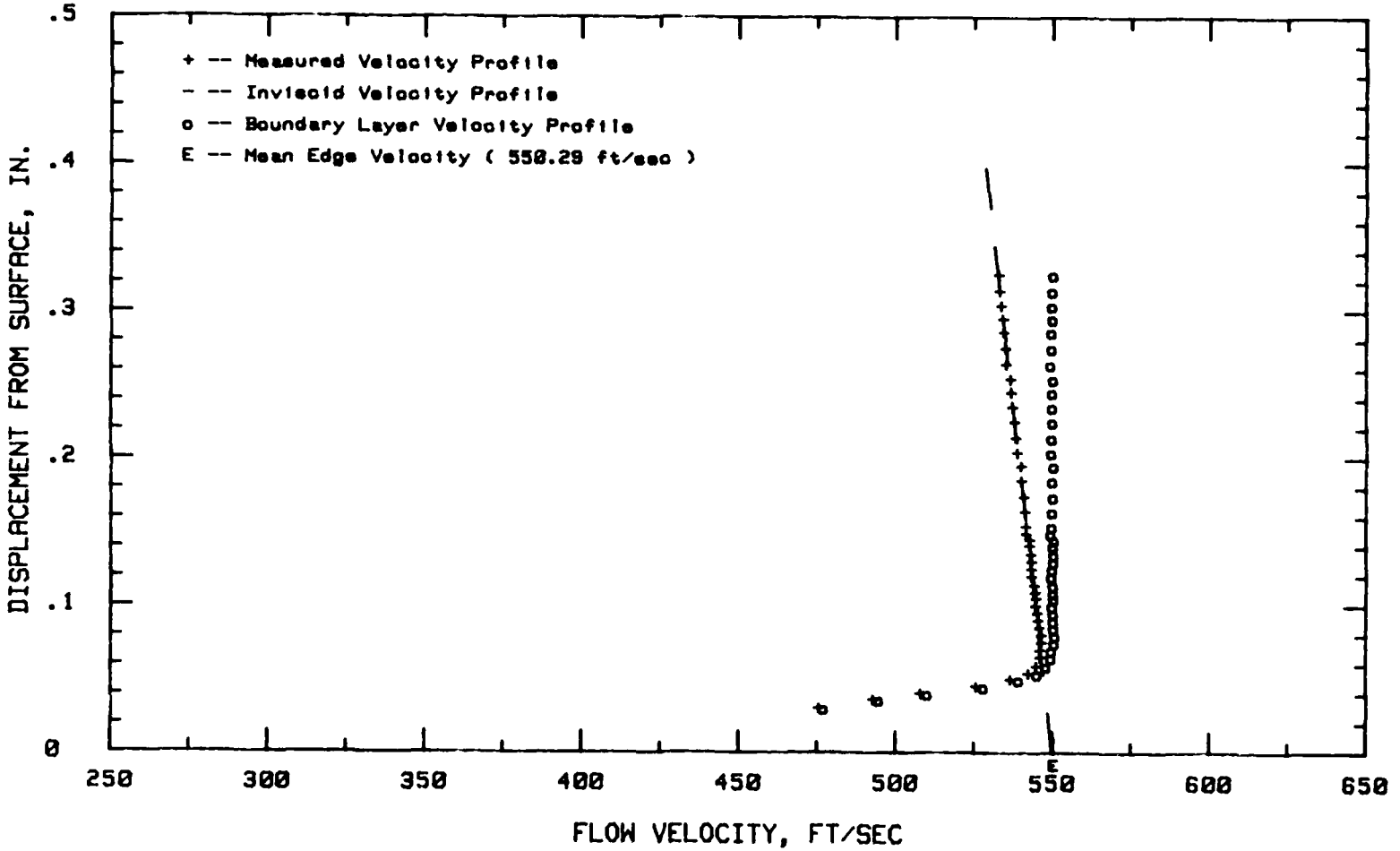

Fig. 60. Boundary Layer Velocity Profiles, Conf.#3 at 50 % Chord

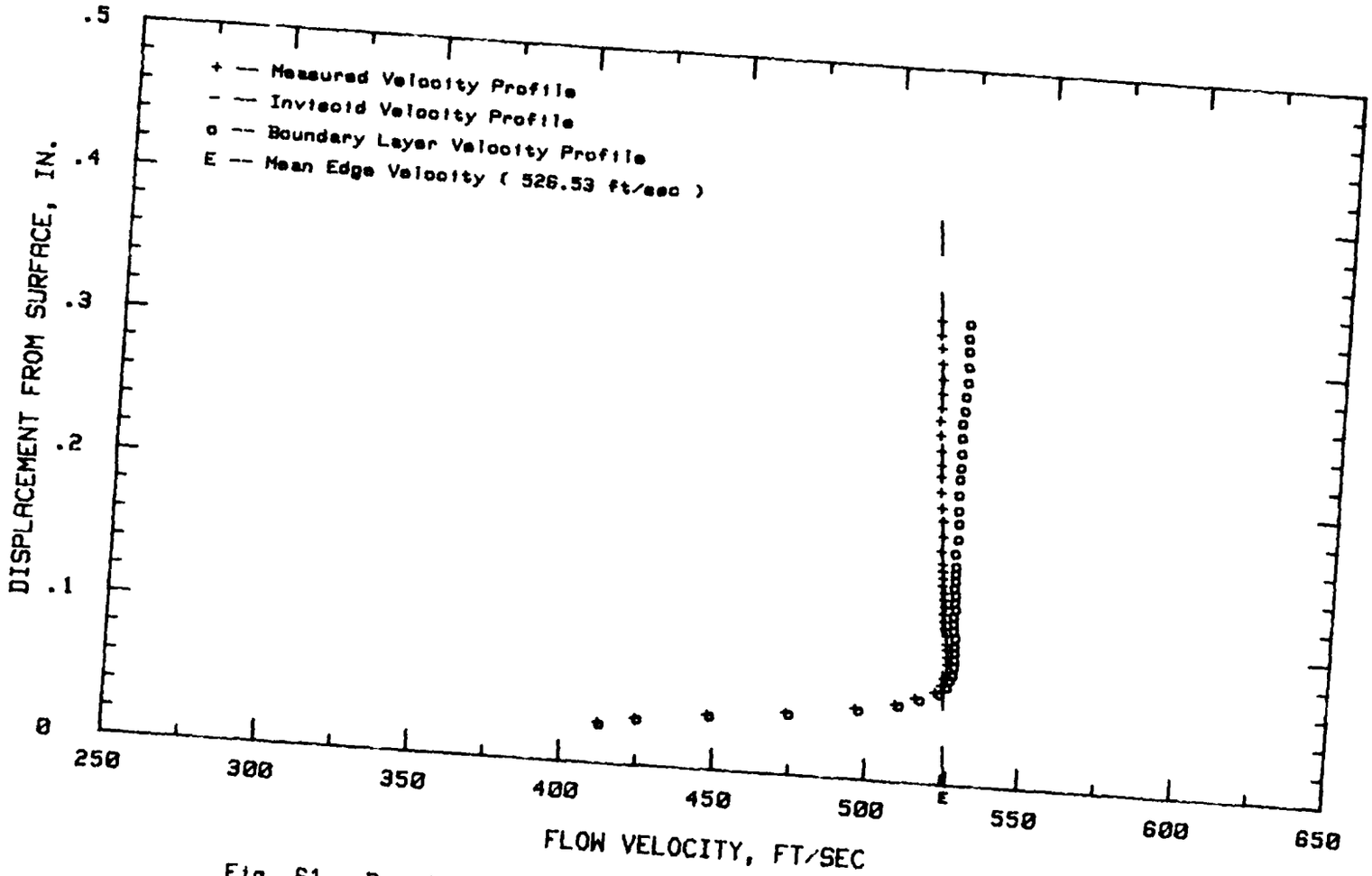

Fig. 61. Boundary Layer Velocity Profiles, Conf.#3 at 65.62 % Chord

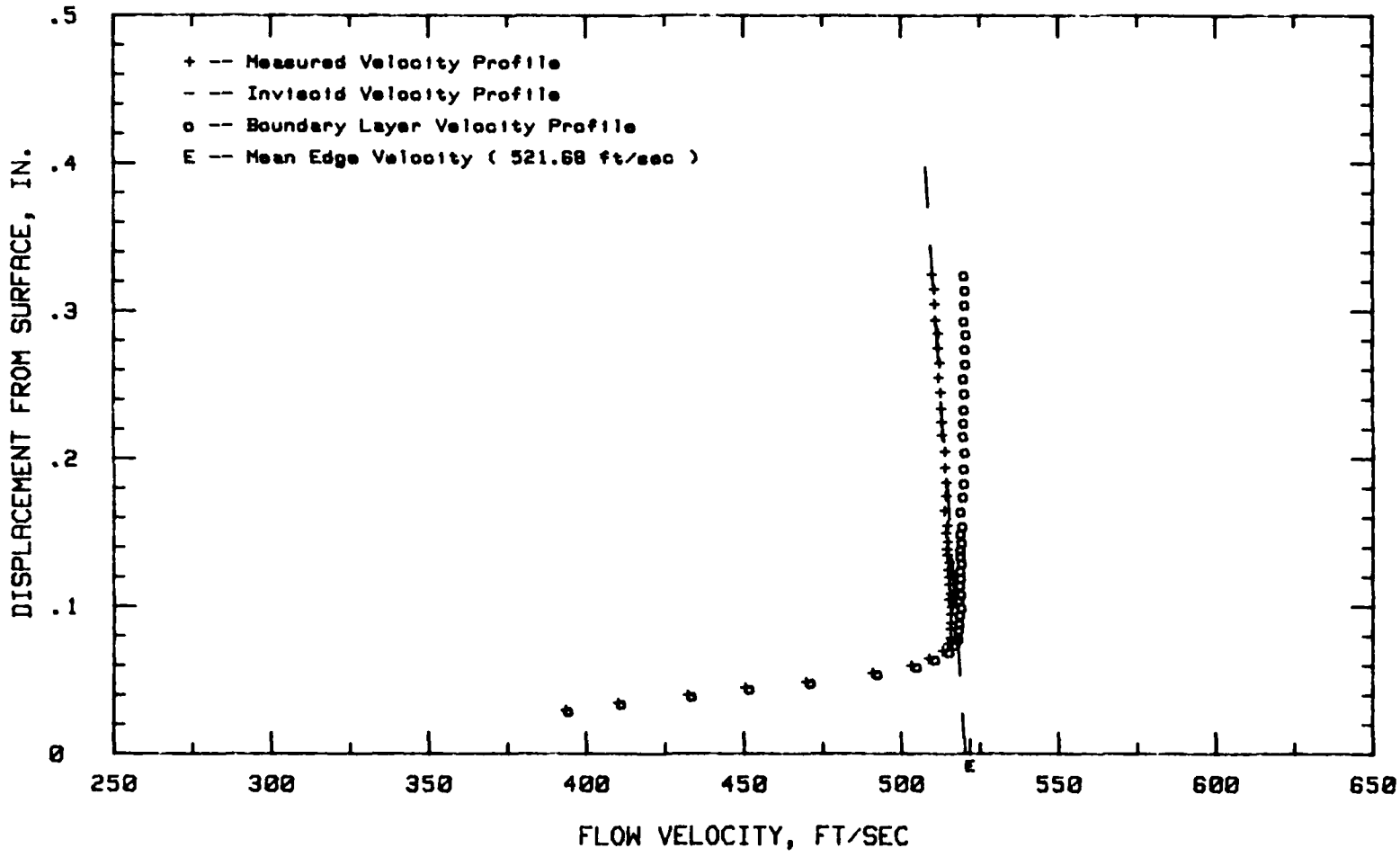

Fig. 62. Boundary Layer Velocity Profiles, Conf.#3 at 70.31 % Chord

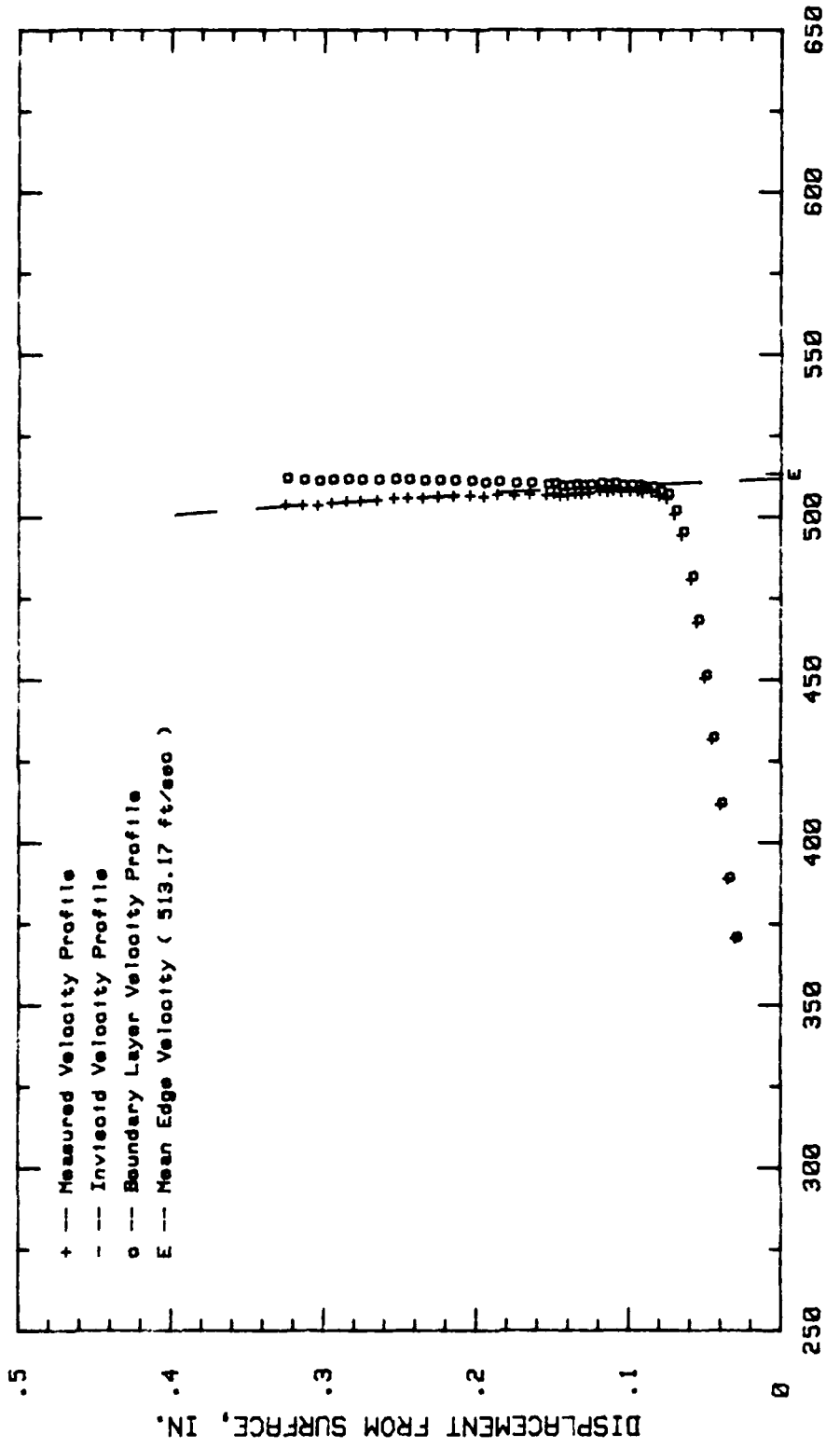

Fig. 63. Boundary Layer Velocity Profiles, Conf.#3 at 75 % Chord

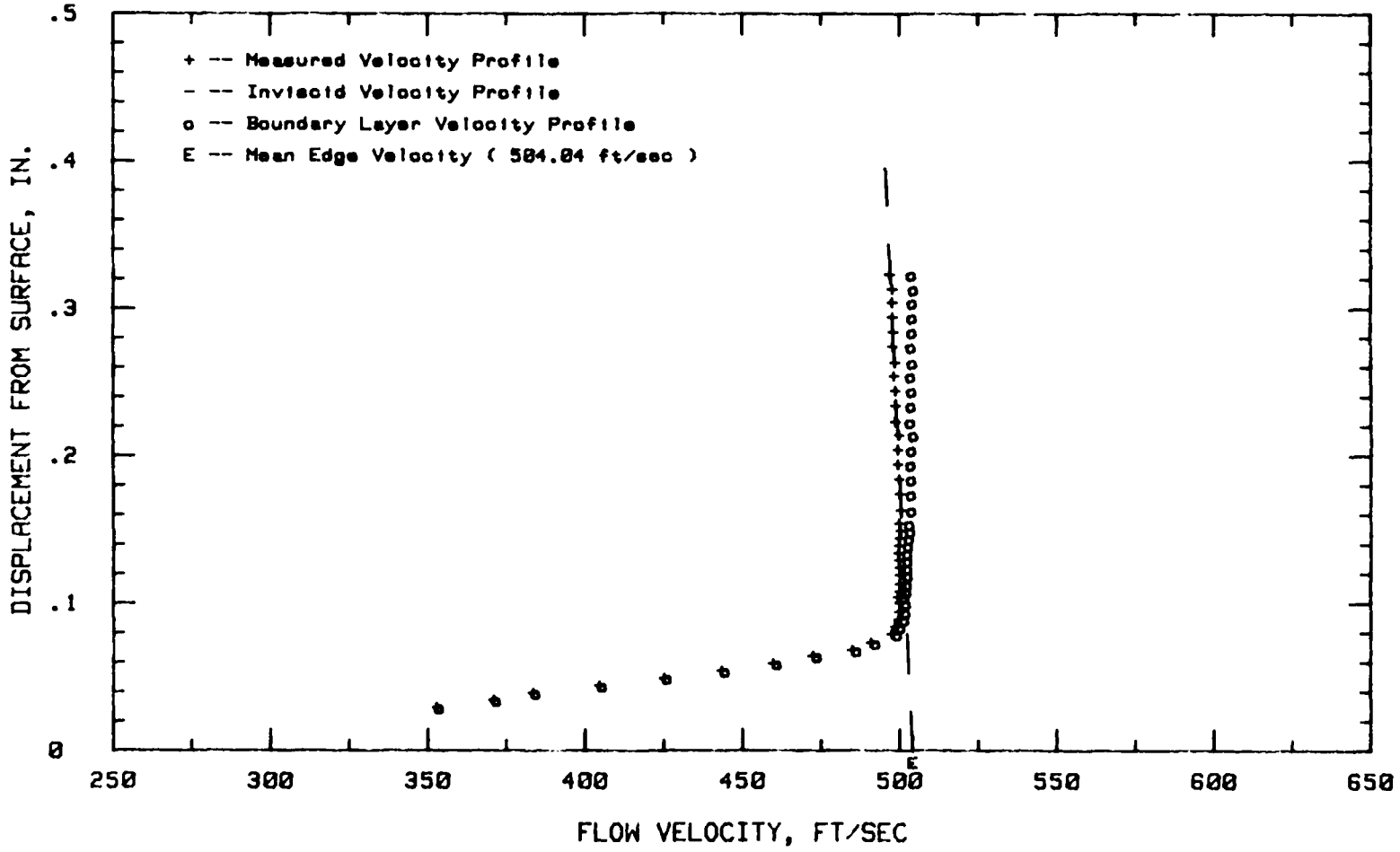

Fig. 64. Boundary Layer Velocity Profiles, Conf.#3 at 79.68 % Chord

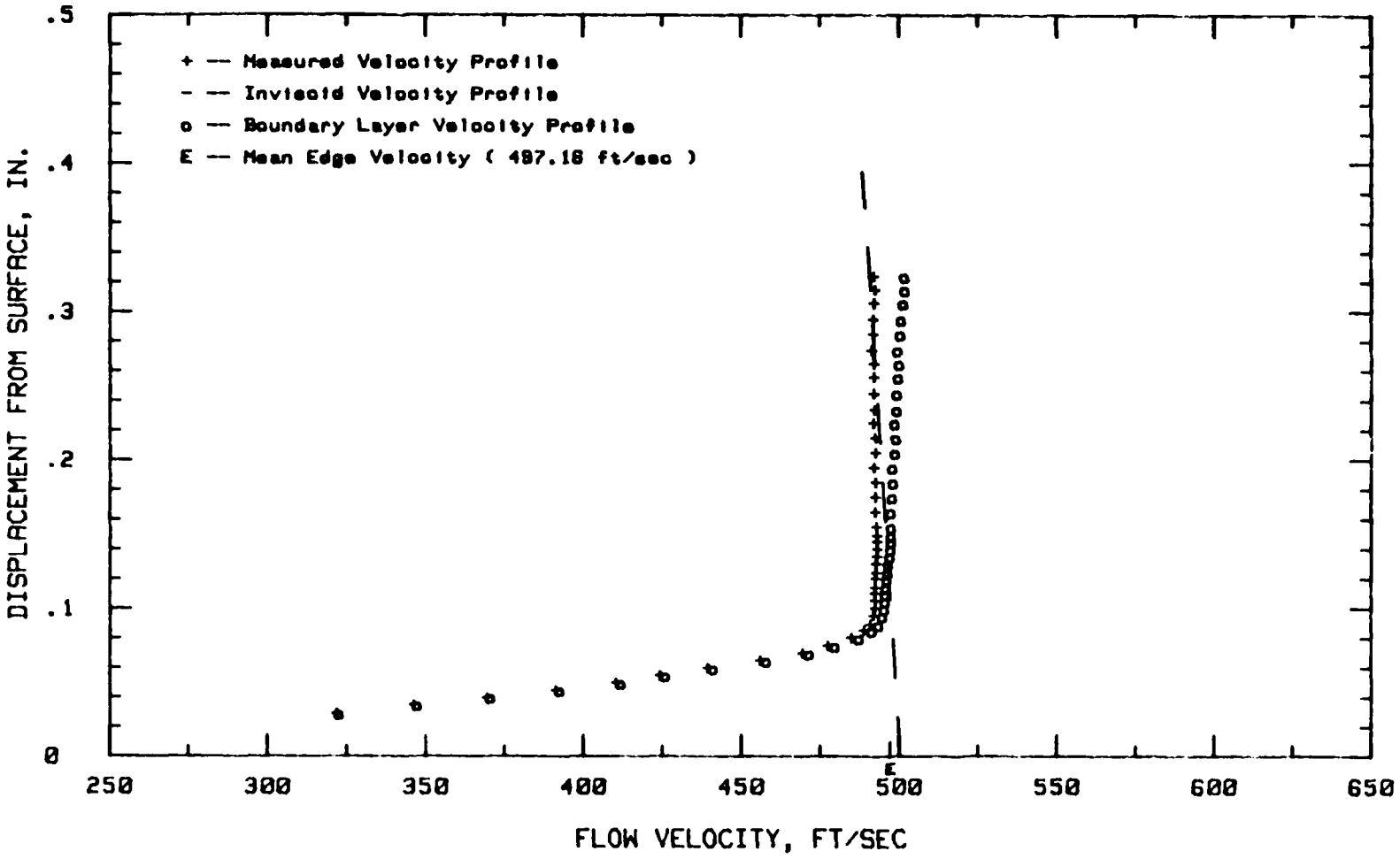

Fig. 65. Boundary Layer Velocity Profiles, Conf.#3 at 84.37 % Chord

APPENDIX G

Boundary Layer Turbulence Intensity Profiles, Configuration #1

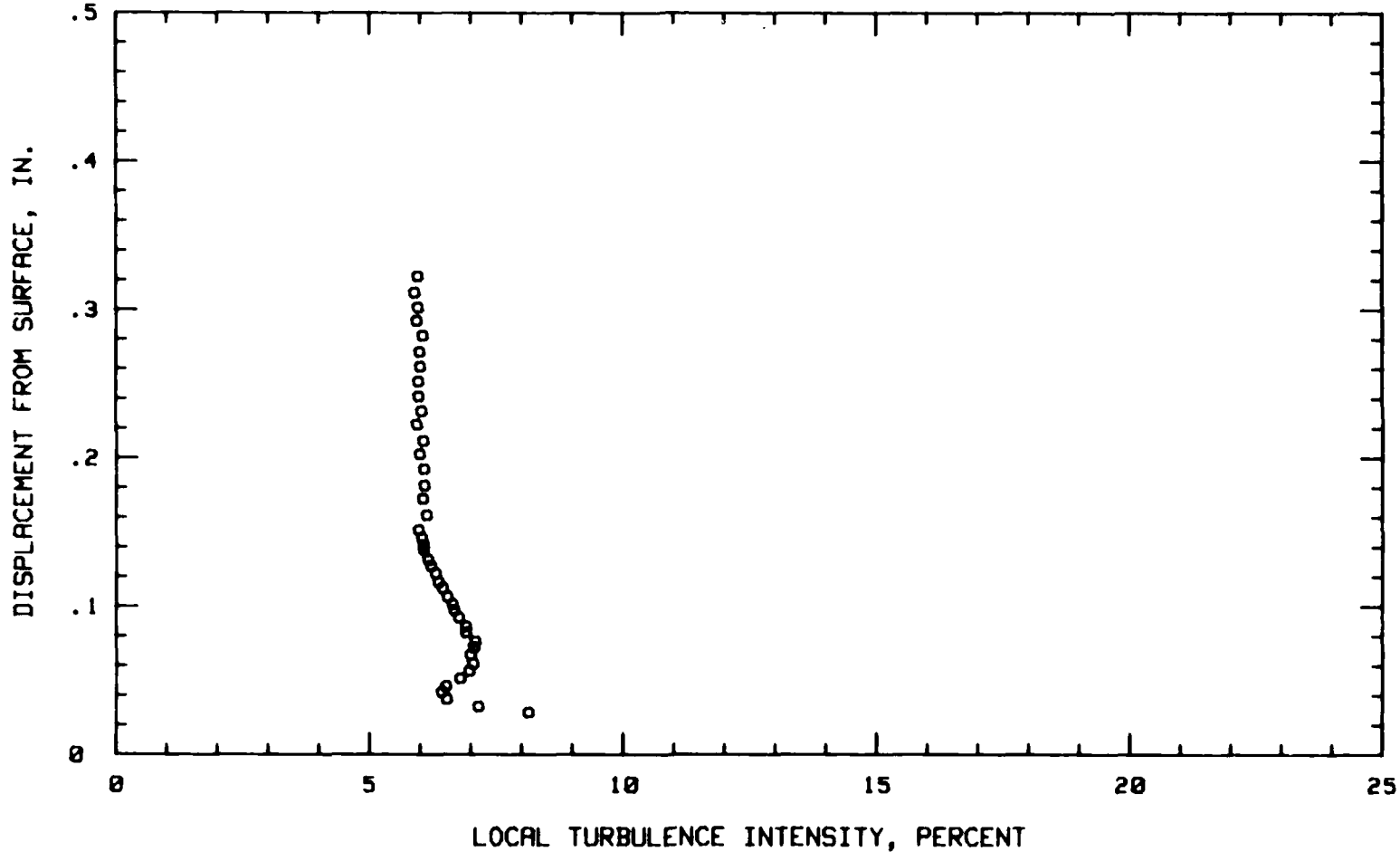

Fig. 66. Boundary Layer Turbulence Intensity Profile, Conf.#1 at 4.68 % Chord

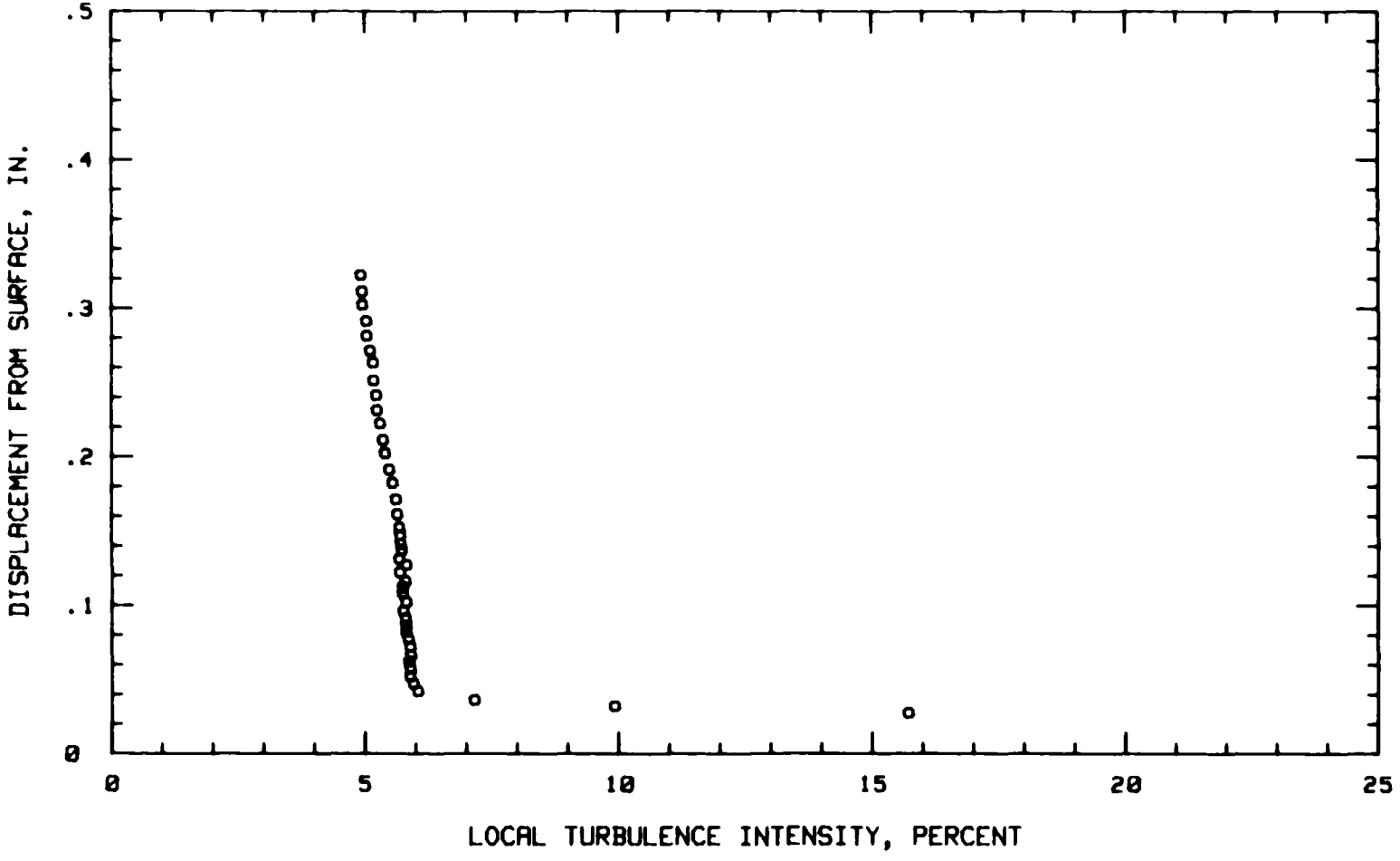

Fig. 67. Boundary Layer Turbulence Intensity Profile, Conf.#1 at 9.37 % Chord

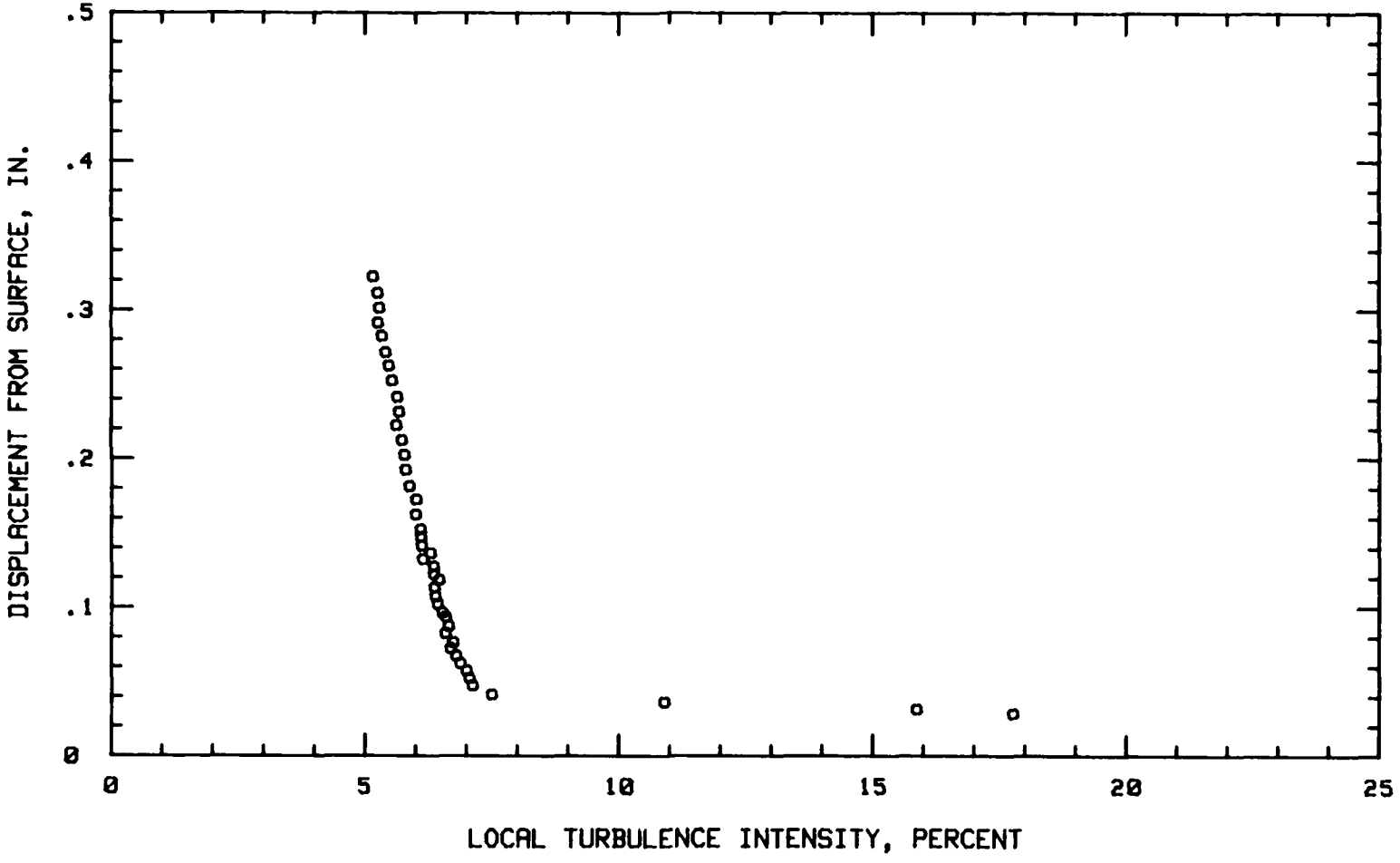

Fig. 68. Boundary Layer Turbulence Intensity Profile, Conf.#1 at 25 % Chord

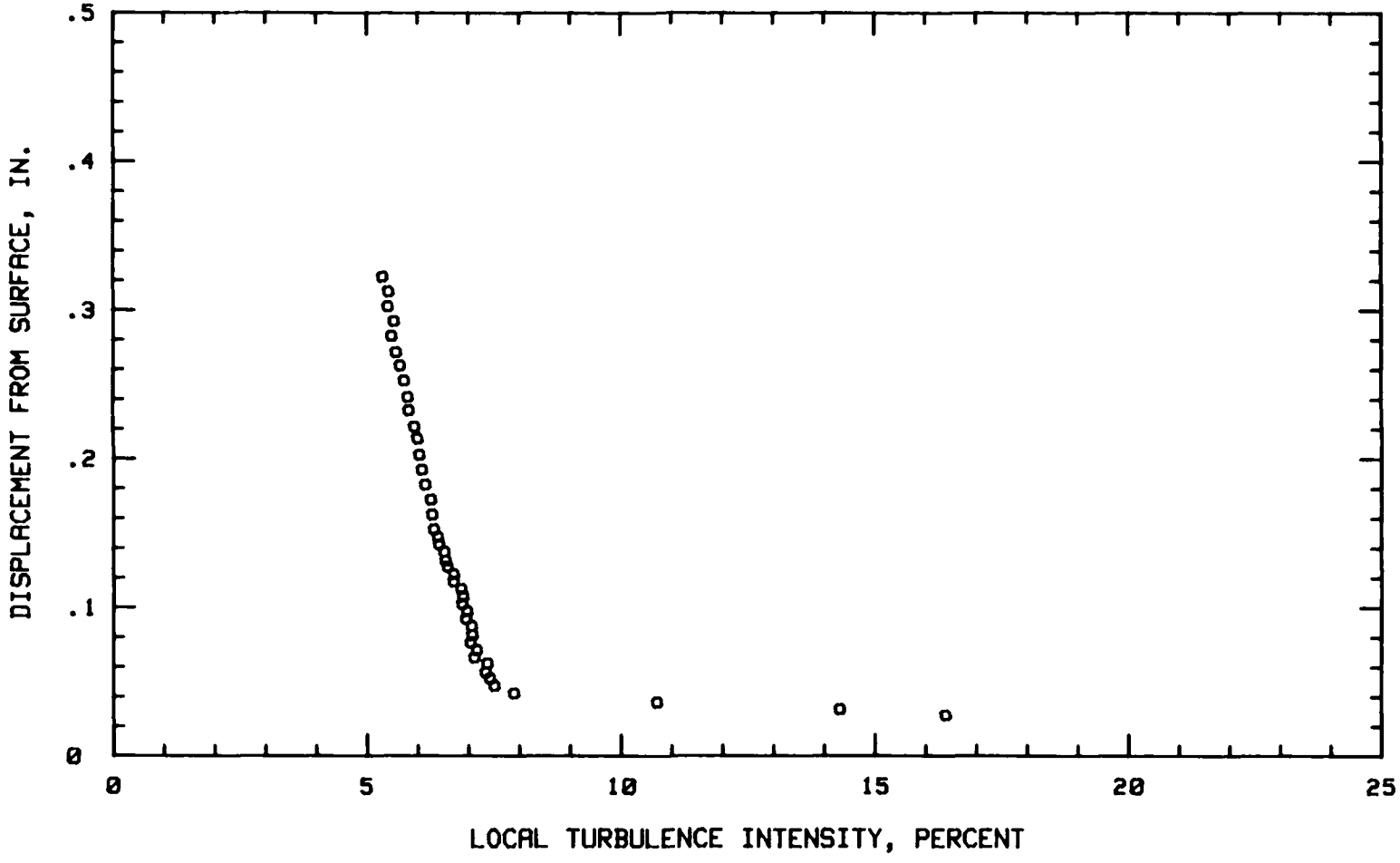

Fig. 69. Boundary Layer Turbulence Intensity Profile, Conf.#1 at 29.68 % Chord

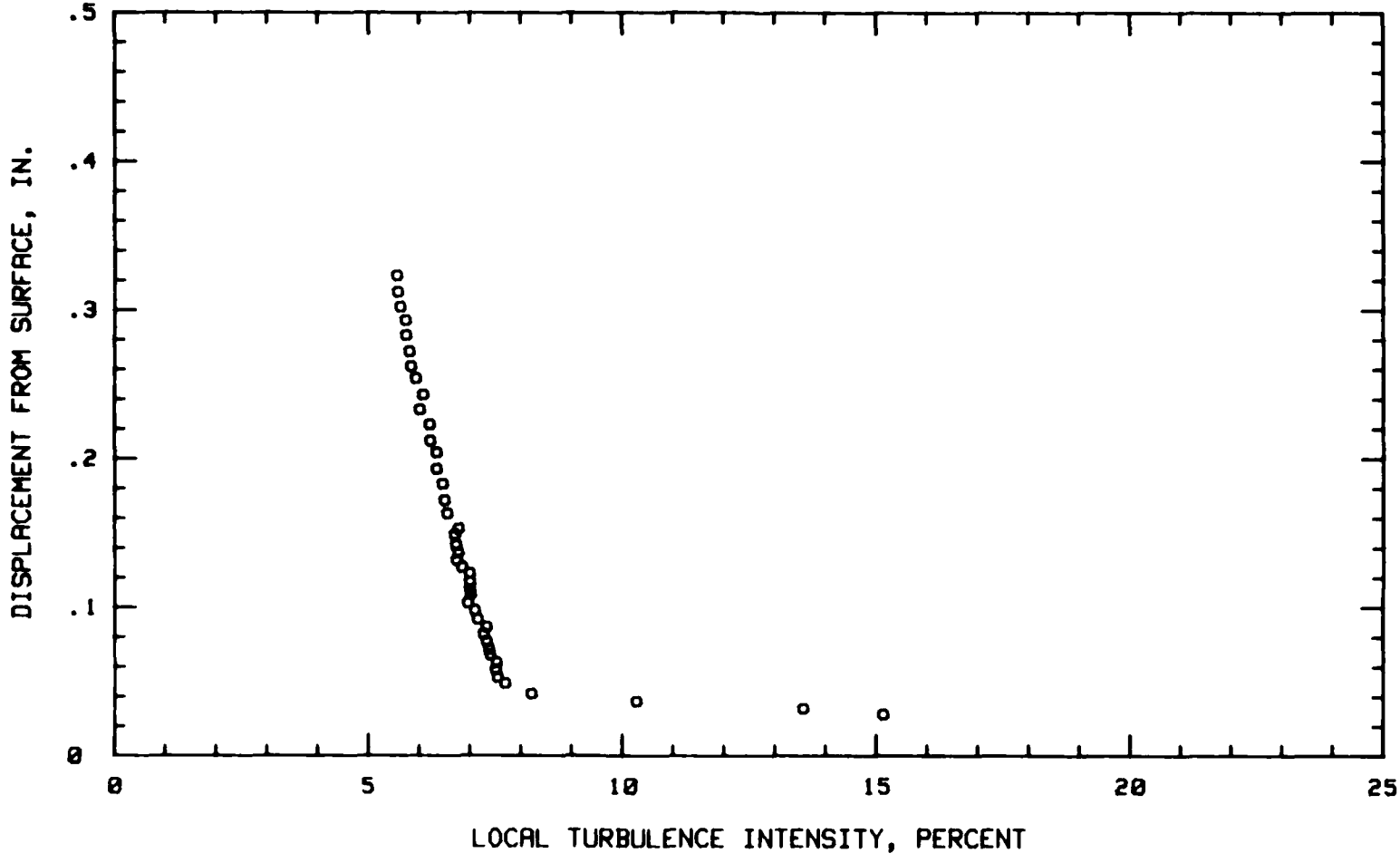

Fig. 70. Boundary Layer Turbulence Intensity Profile, Conf.#1 at 34.37 % Chord

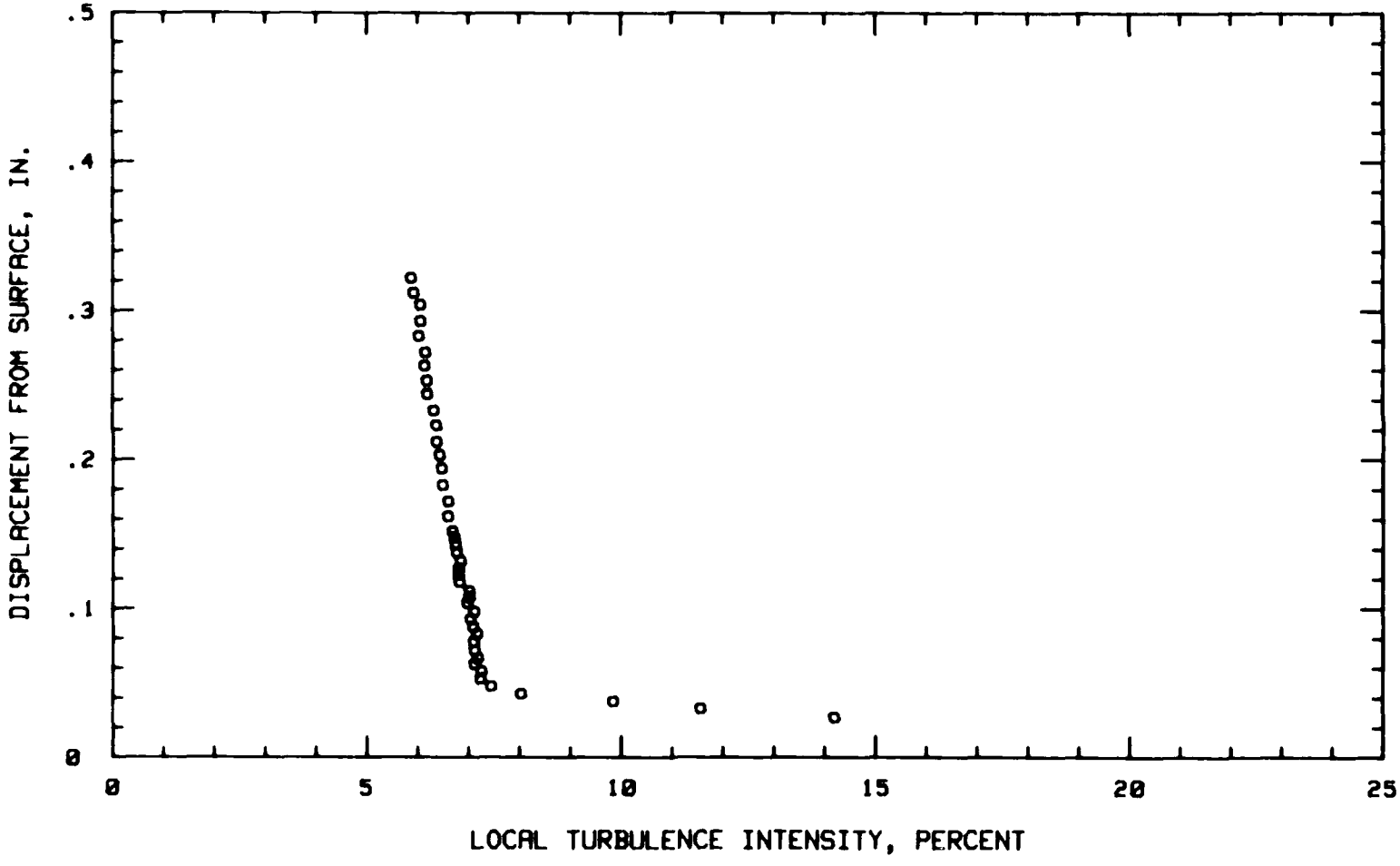

Fig. 71. Boundary Layer Turbulence Intensity Profile, Conf.#1 at 40.62 % Chord

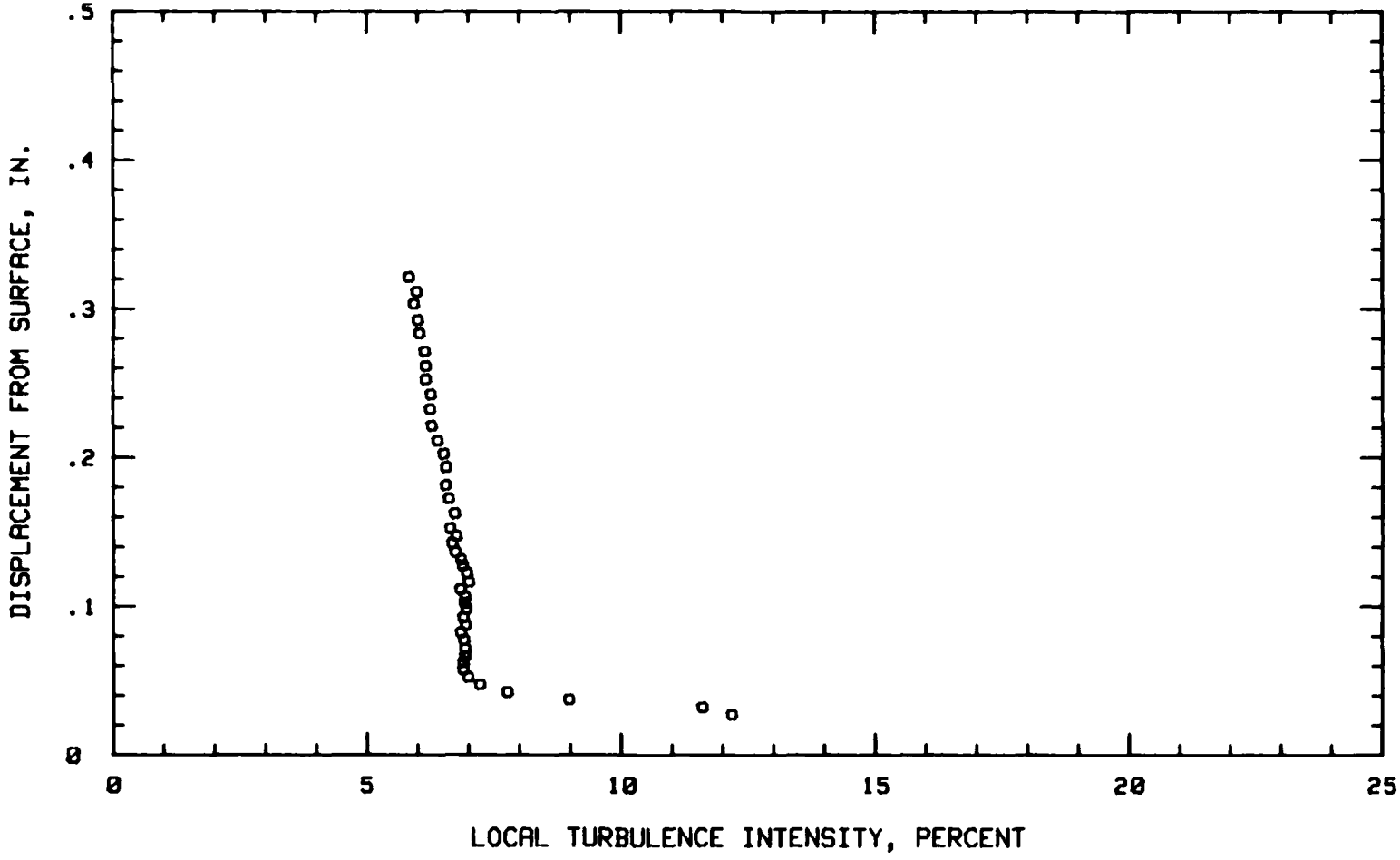

Fig. 72. Boundary Layer Turbulence Intensity Profile, Conf.#1 at 45.31 % Chord

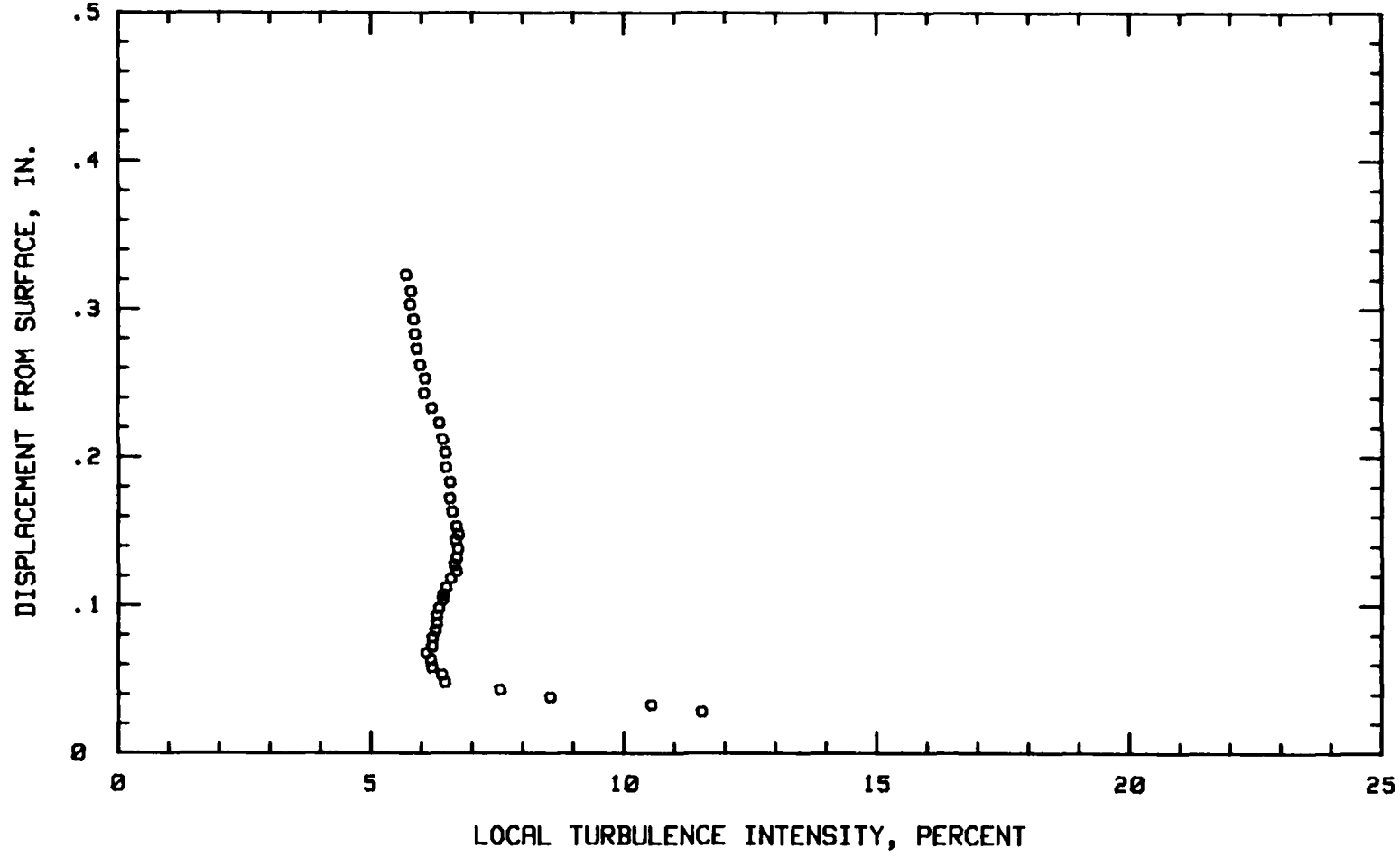

Fig. 73. Boundary Layer Turbulence Intensity Profile, Conf.#1 at 50 % Chord

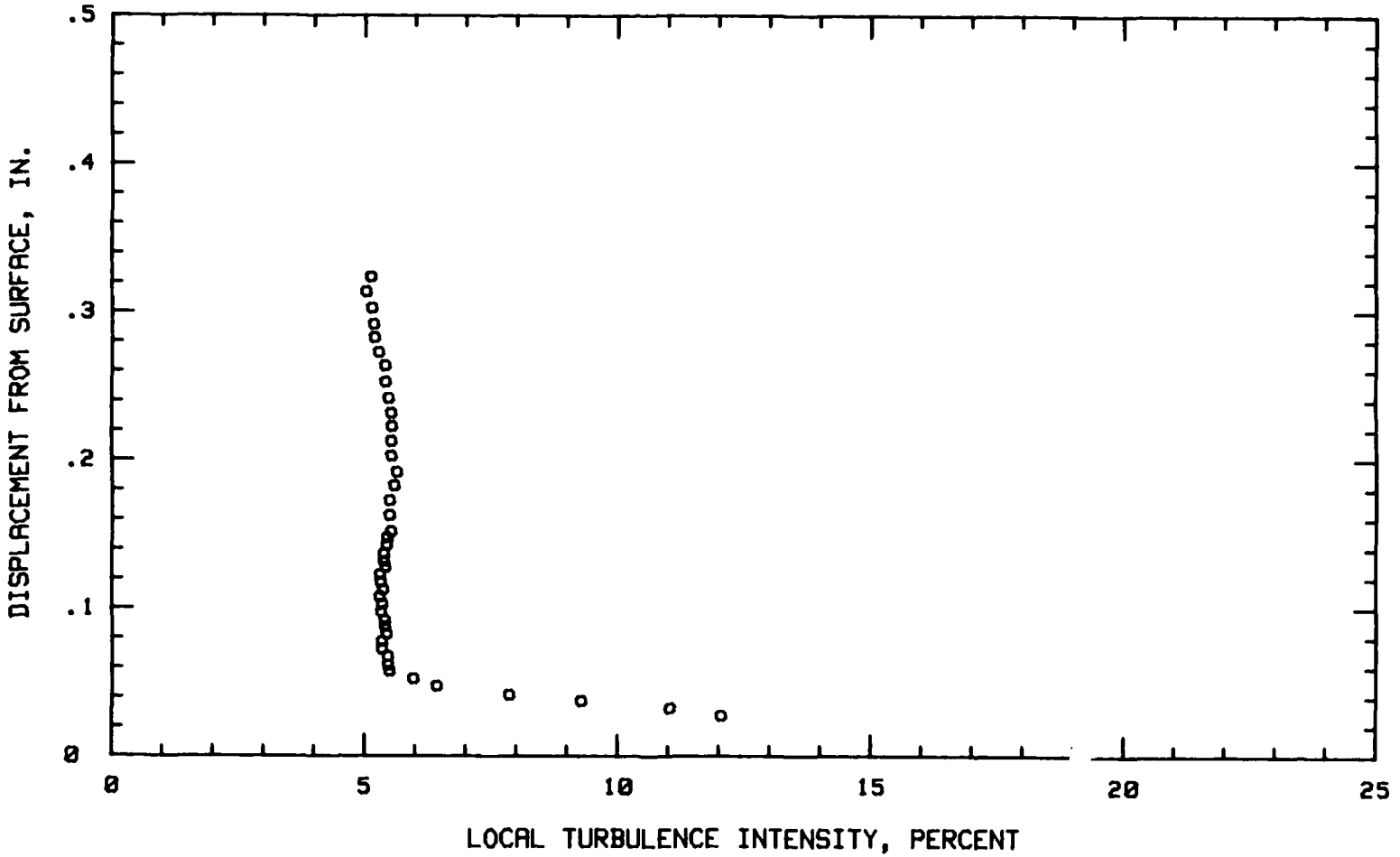

Fig. 74. Boundary Layer Turbulence Intensity Profile, Conf.#1 at 65.62 % Chord

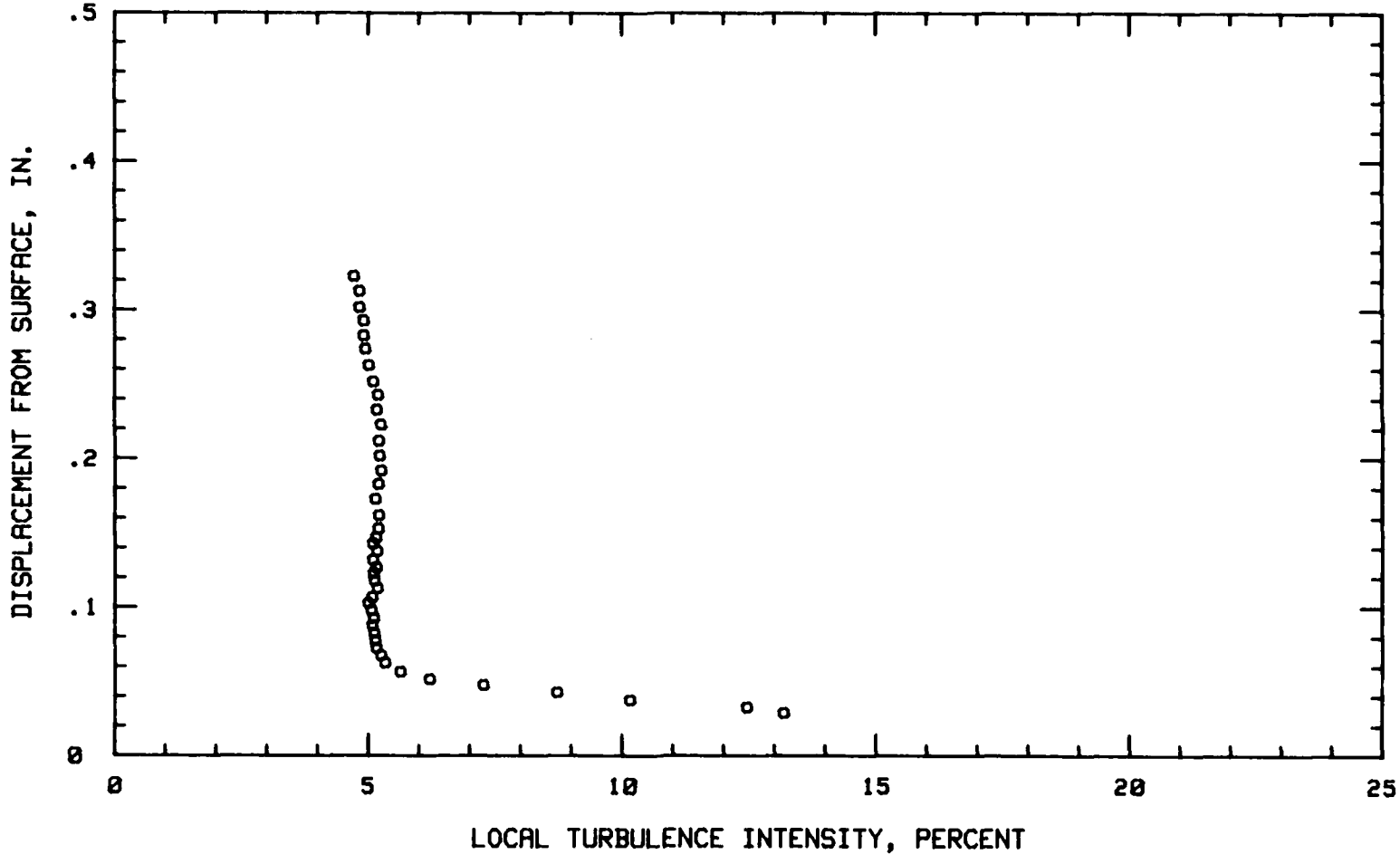

Fig. 75. Boundary Layer Turbulence Intensity Profile, Conf.#1 at 70.31 % Chord

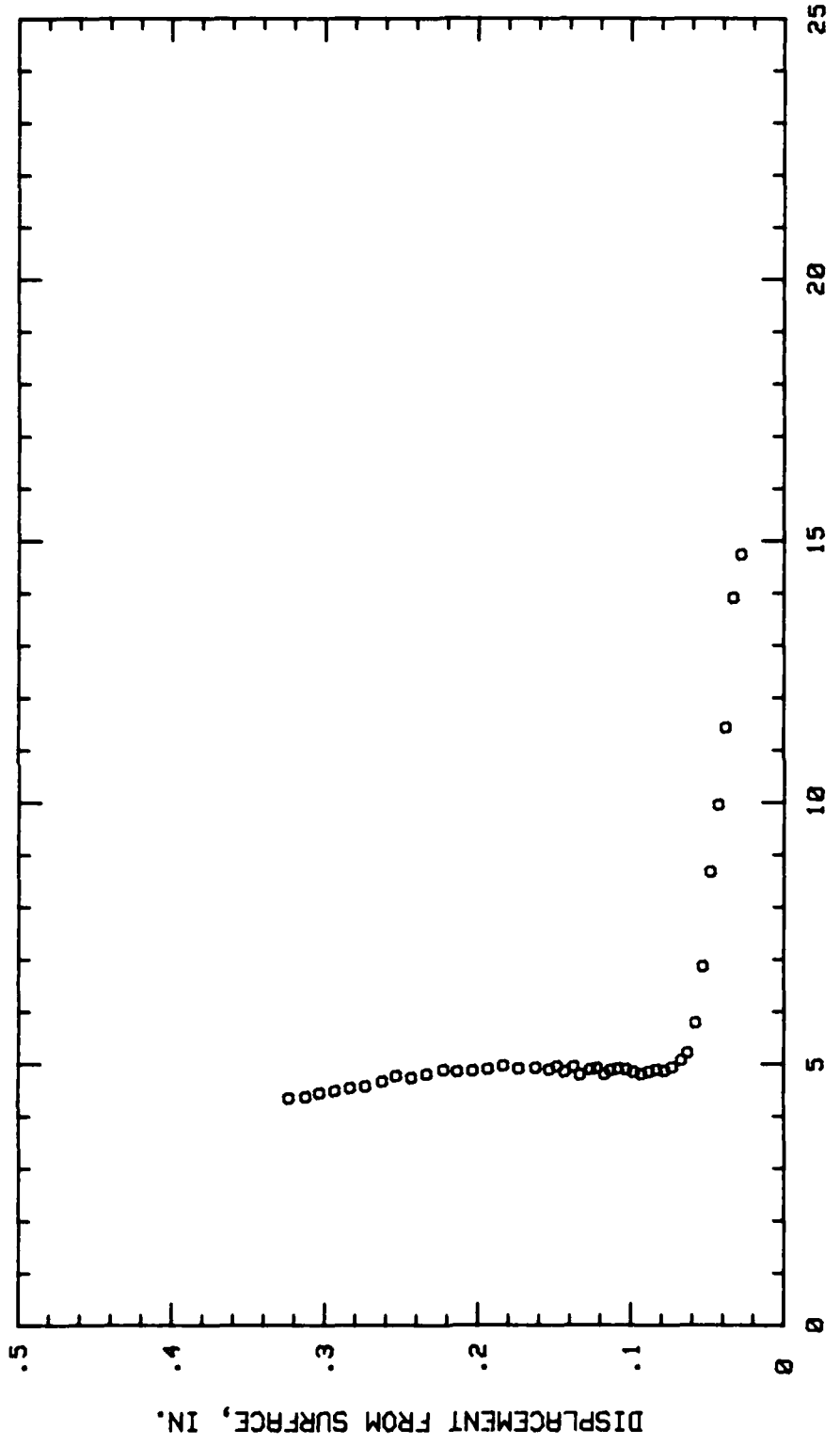

Fig. 76. Boundary Layer Turbulence Intensity Profile, Conf.#1 at 75 % Chord

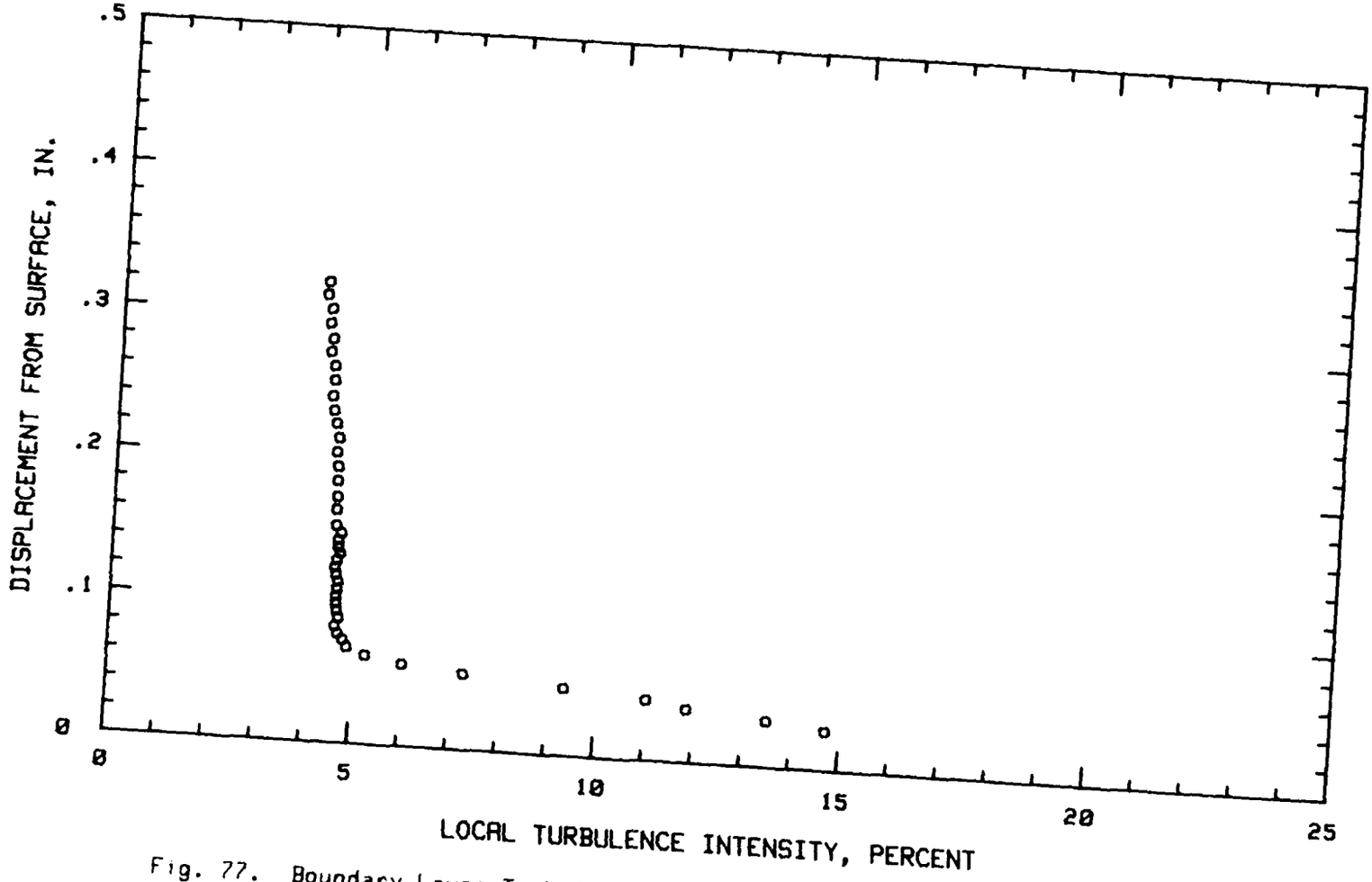

Fig. 77. Boundary Layer Turbulence Intensity Profile, Conf.#1 at 79.68 % Chord

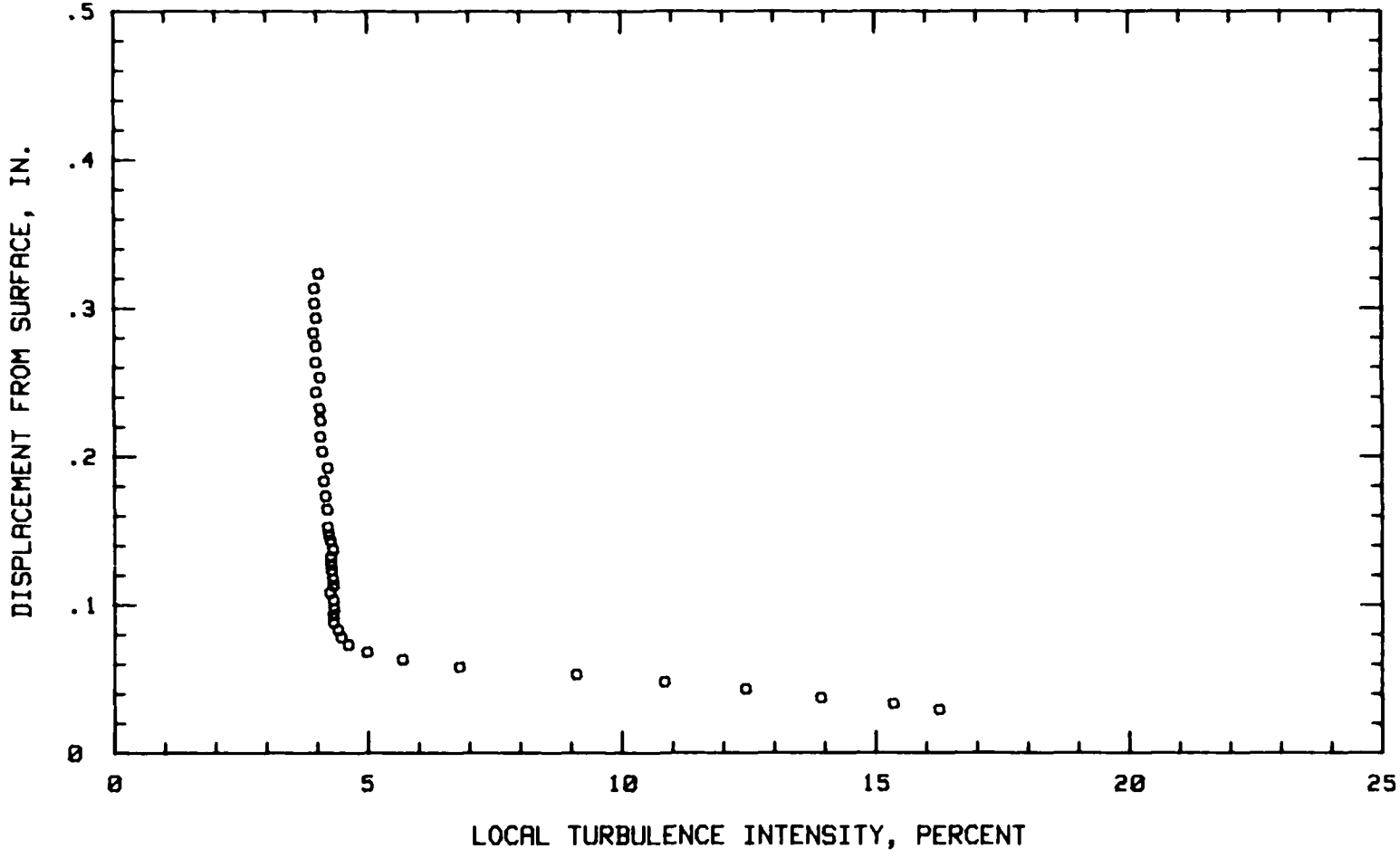

Fig. 78. Boundary Layer Turbulence Intensity Profile, Conf.#1 at 84.37 % Chord

APPENDIX H

Boundary Layer Turbulence Intensity Profiles, Configuration #2

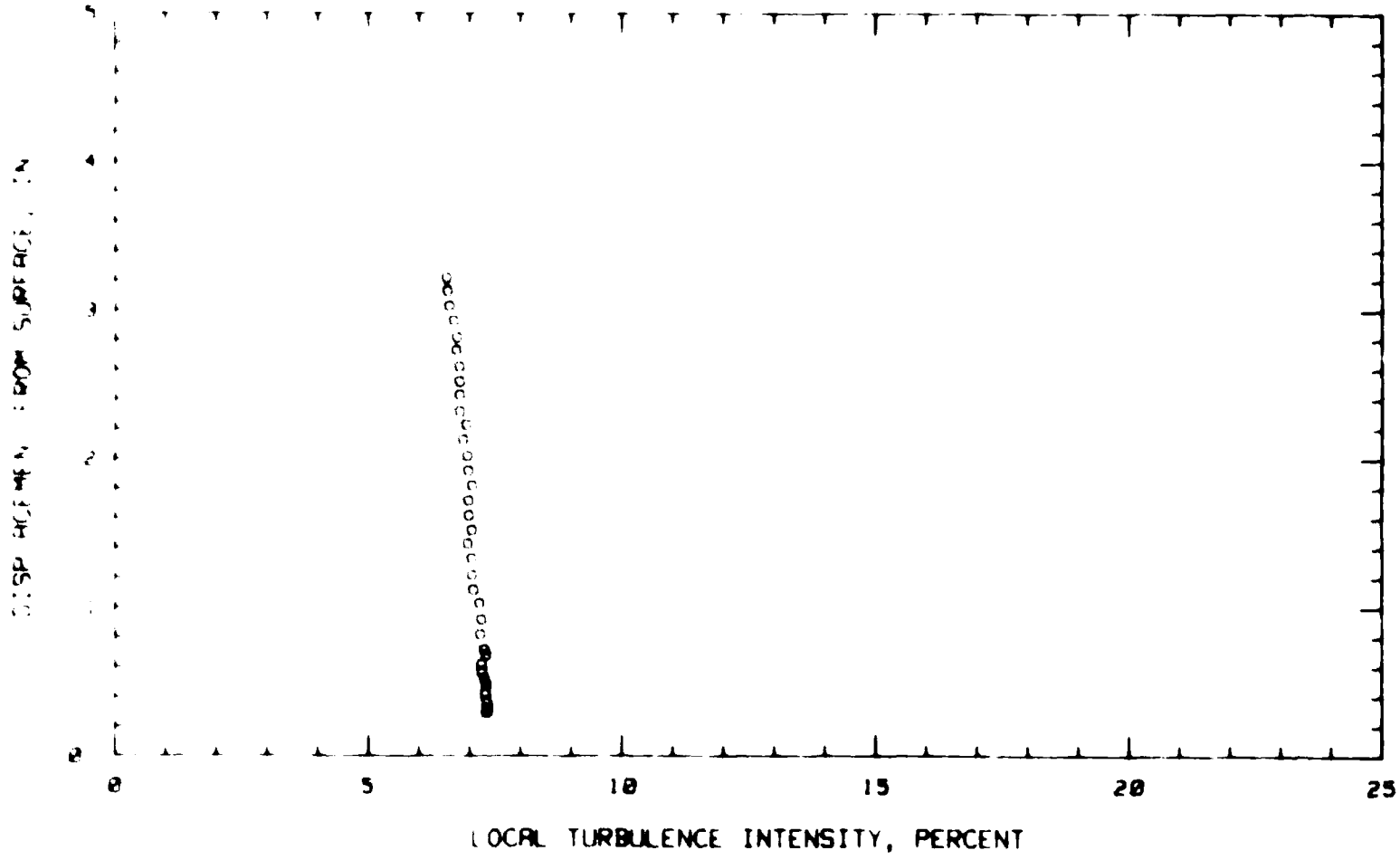

Fig. 19. Boundary Layer Turbulence Intensity Profile, Conf.02 at 4.68 % Chord

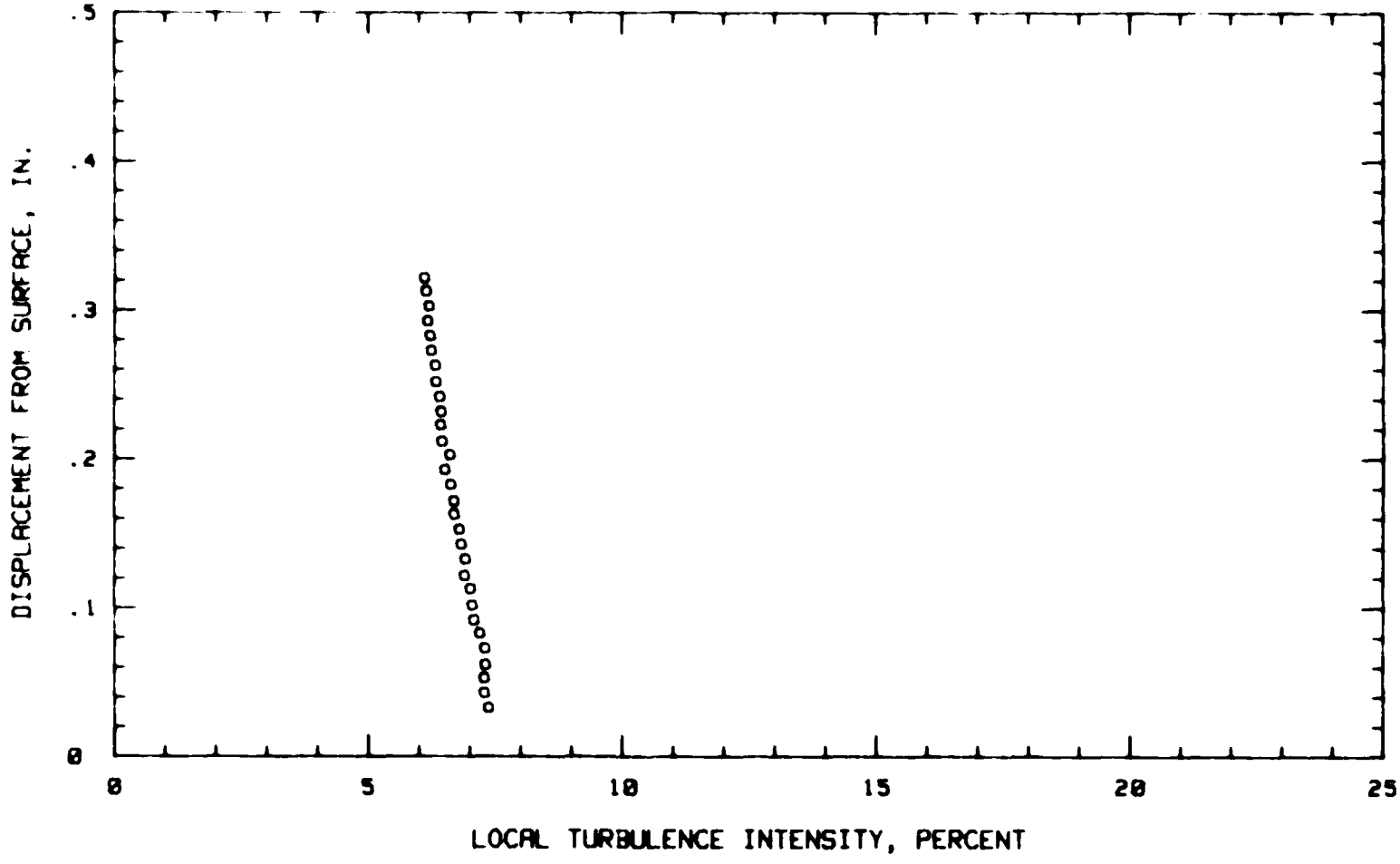

Fig. 80. Boundary Layer Turbulence Intensity Profile, Conf.#2 at 9.37 % Chord

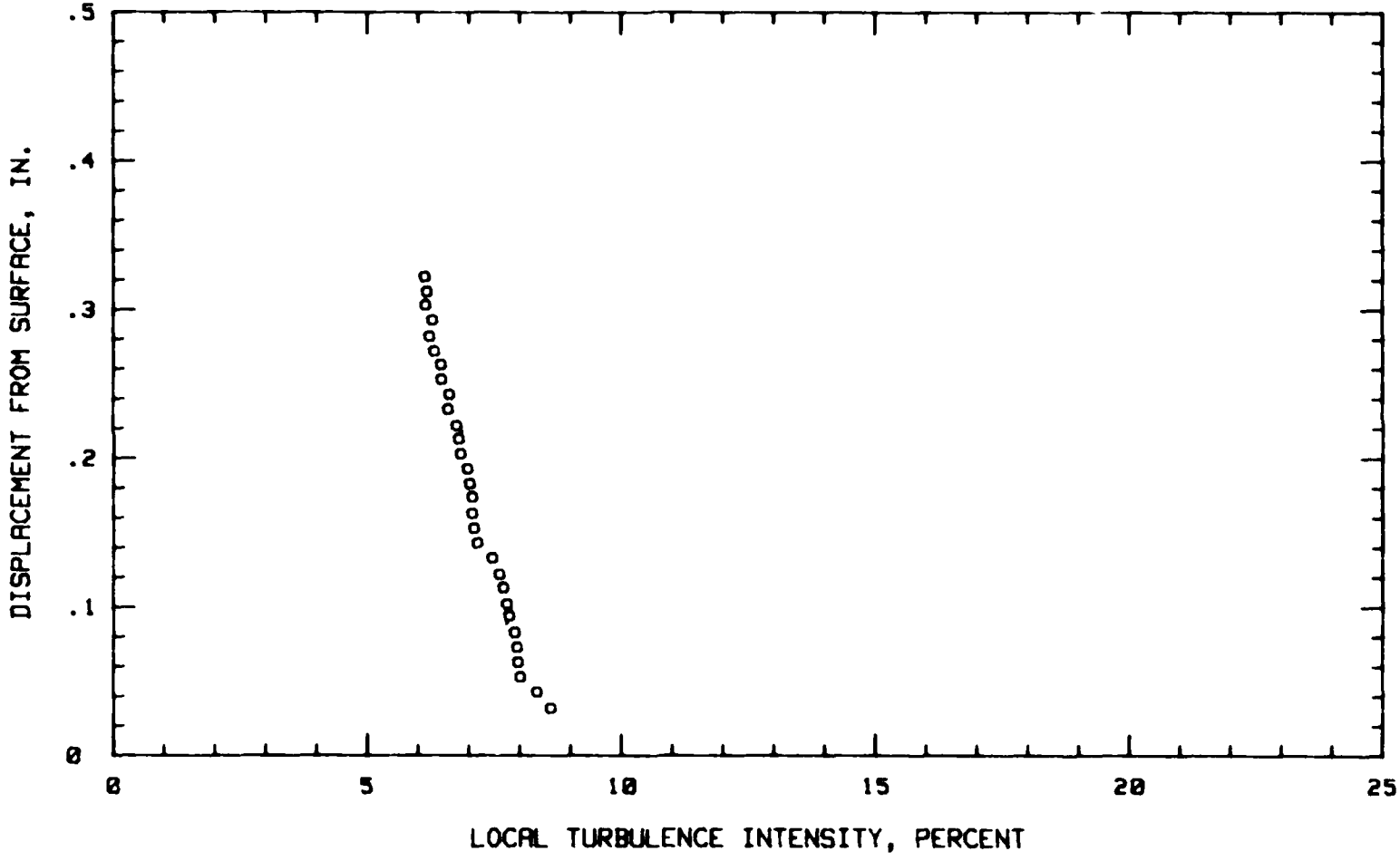

Fig. 81. Boundary Layer Turbulence Intensity Profile, Conf.#2 at 25 % Chord

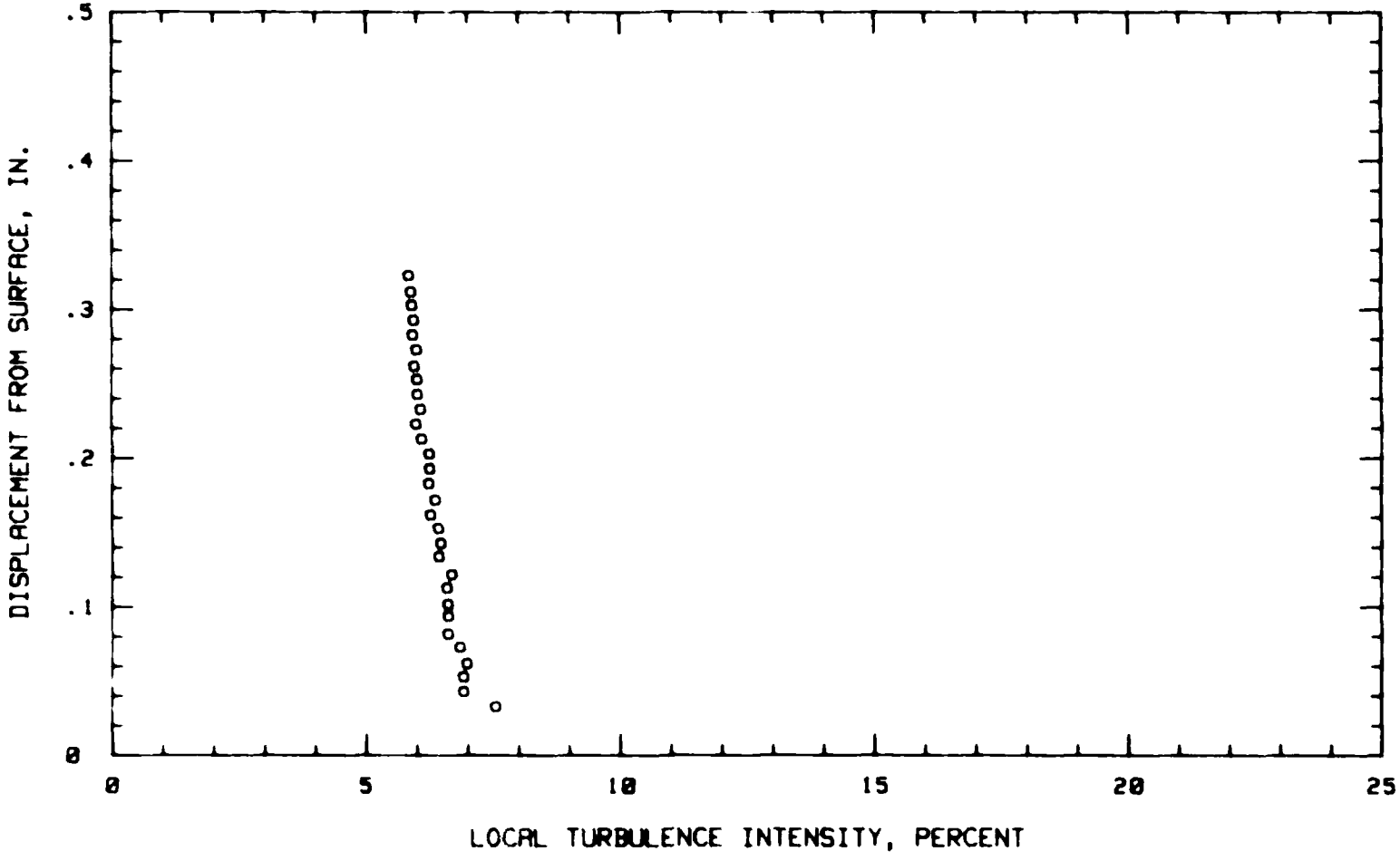

Fig. 82. Boundary Layer Turbulence Intensity Profile, Conf.#2 at 29.68 % Chord

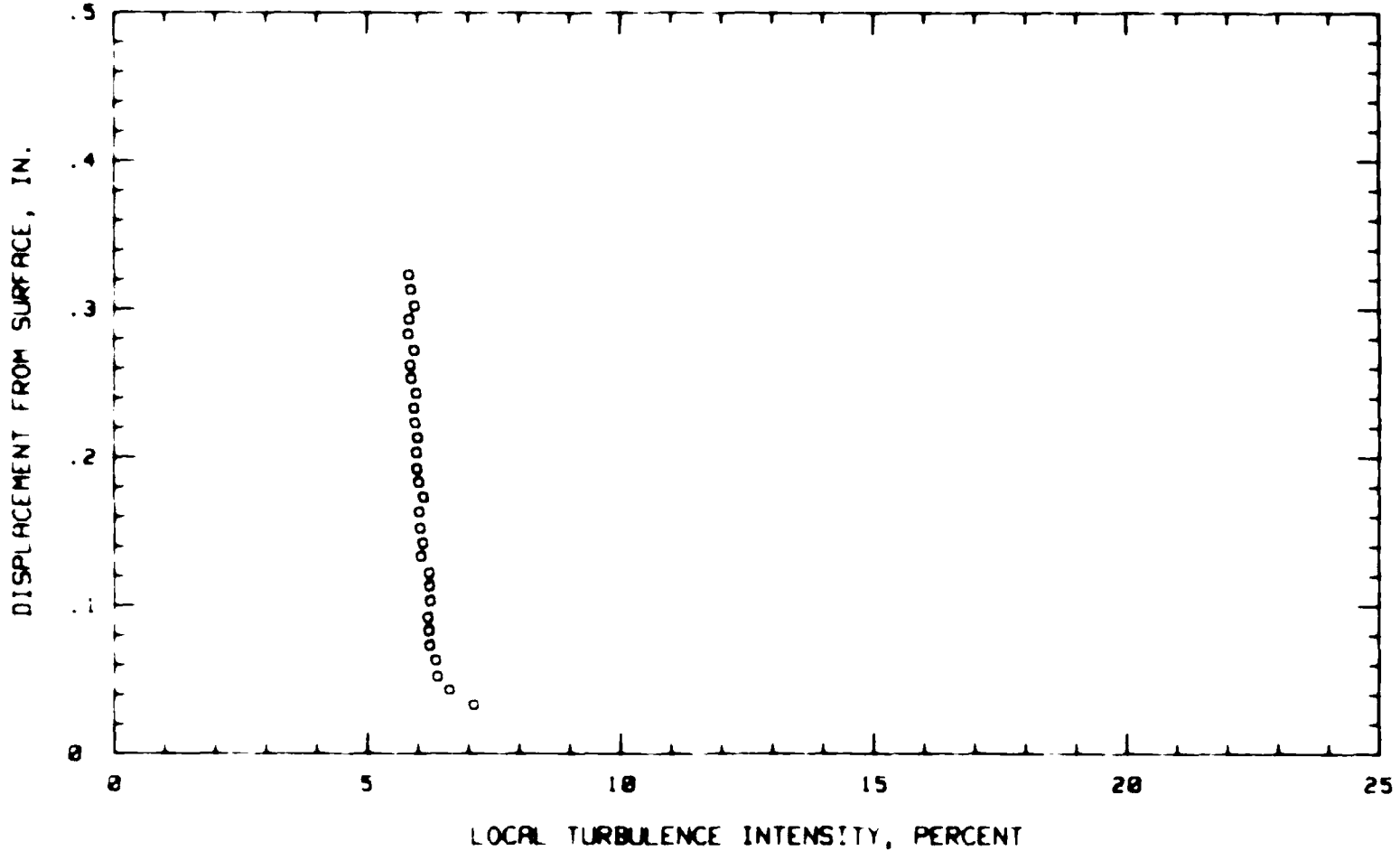

Fig. 83. Boundary Layer Turbulence Intensity Profile, Conf. 02 at 34.37 % Chord

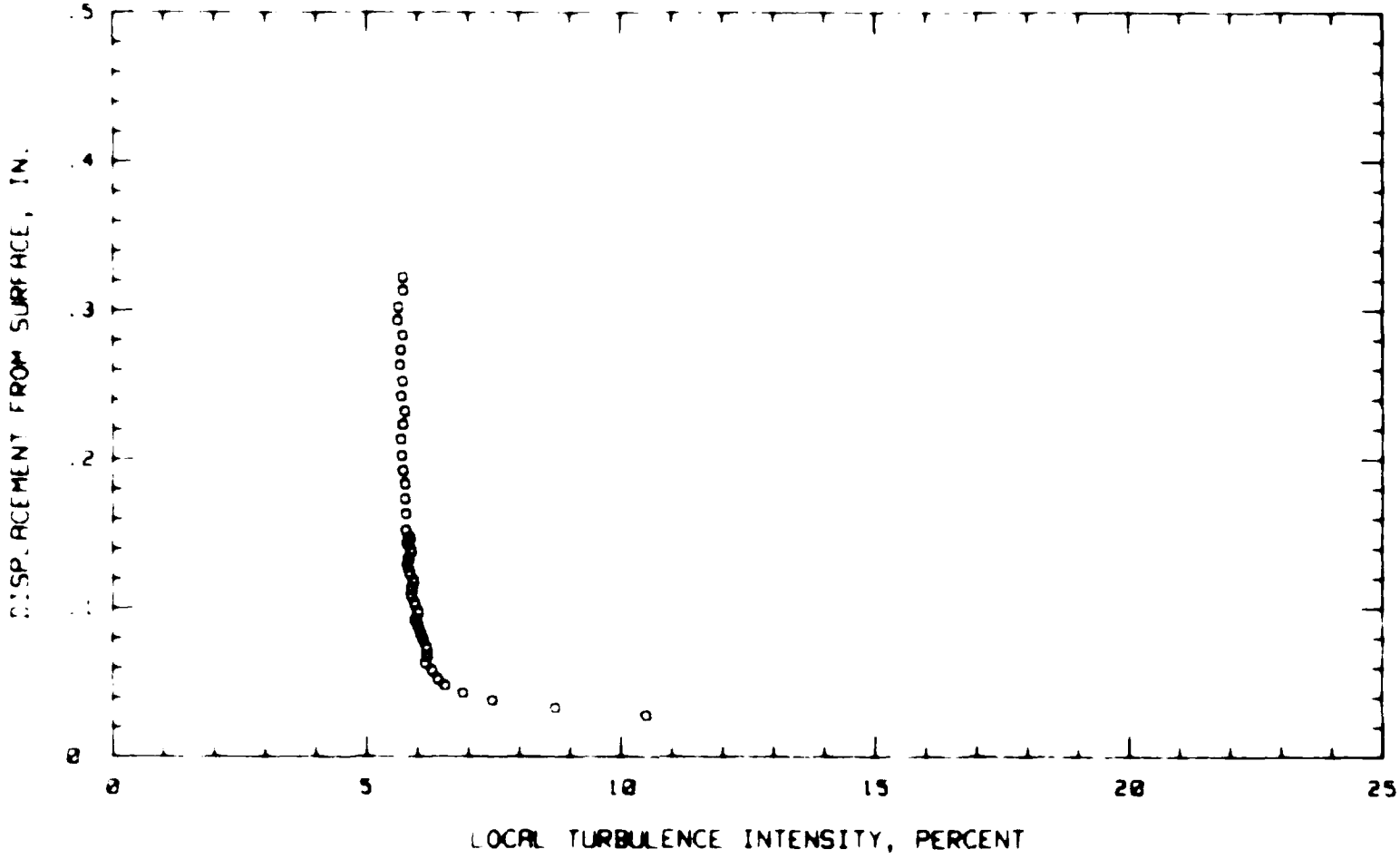

Fig. 84 Boundary Layer Turbulence Intensity Profile, Conf.02 at 40.62 % Chord

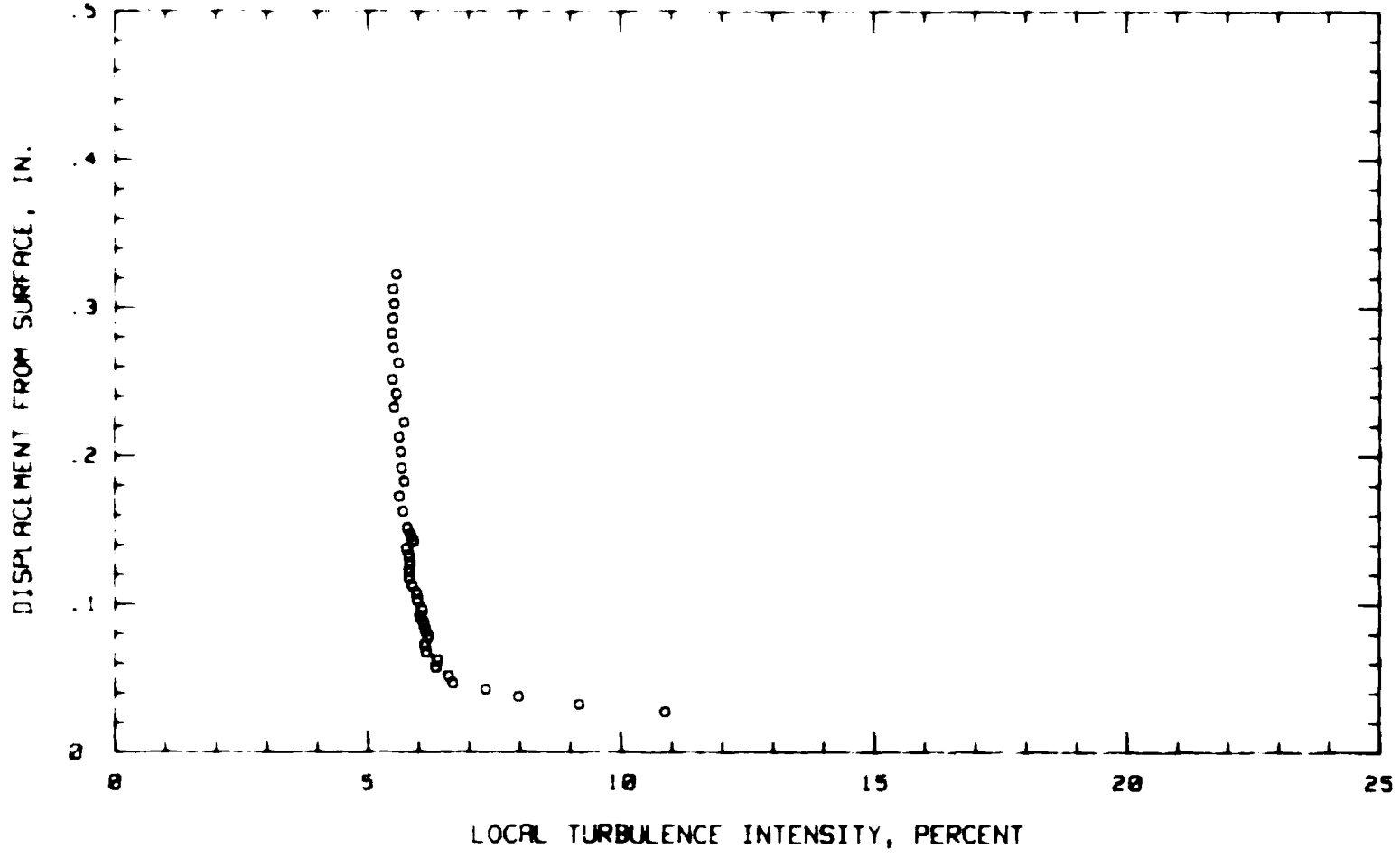

Fig. 85. Boundary Layer Turbulence Intensity Profile, Conf.#2 at 45.31 % Chord

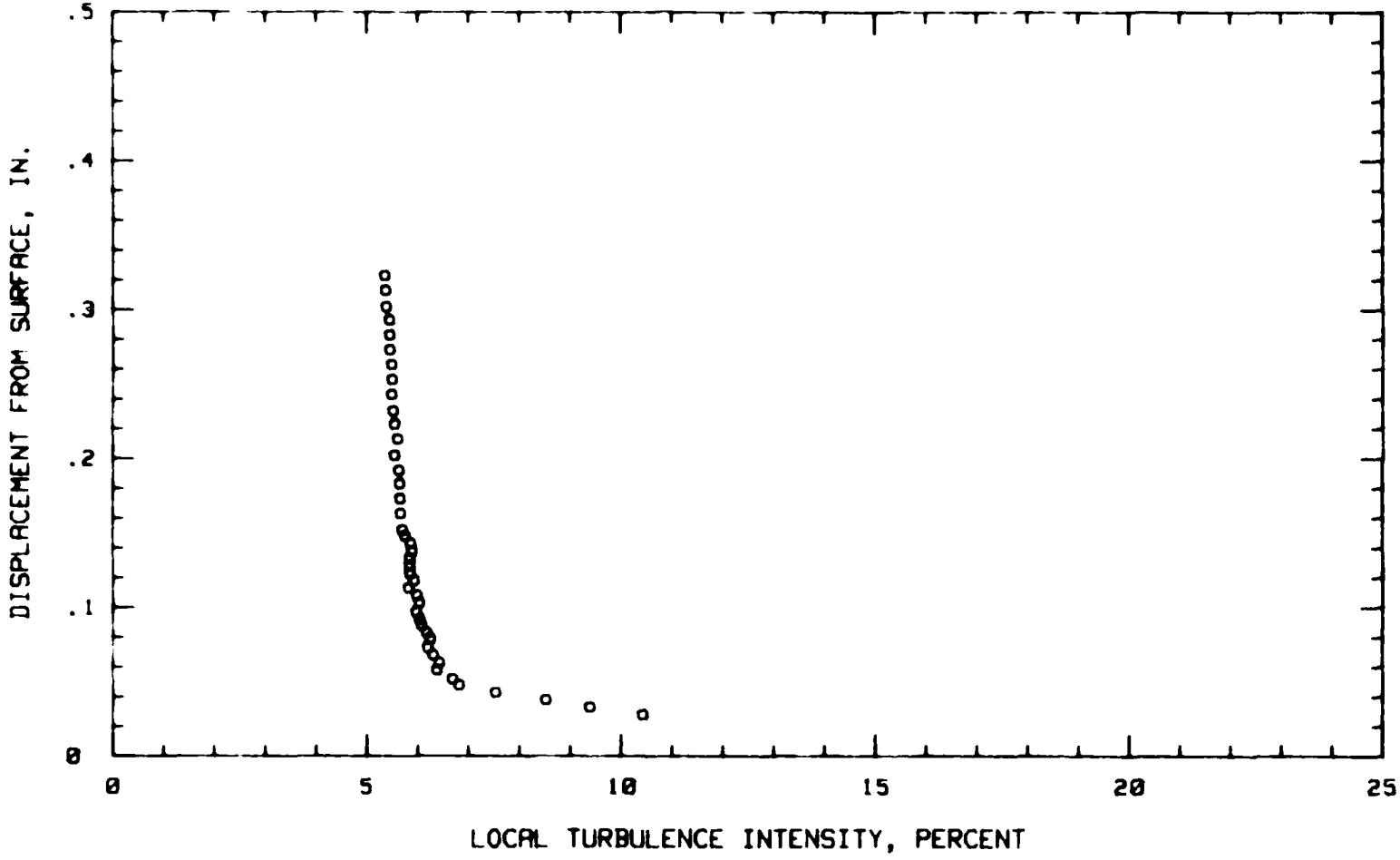

Fig. 86. Boundary Layer Turbulence Intensity Profile, Conf.#2 at 50 % Chord

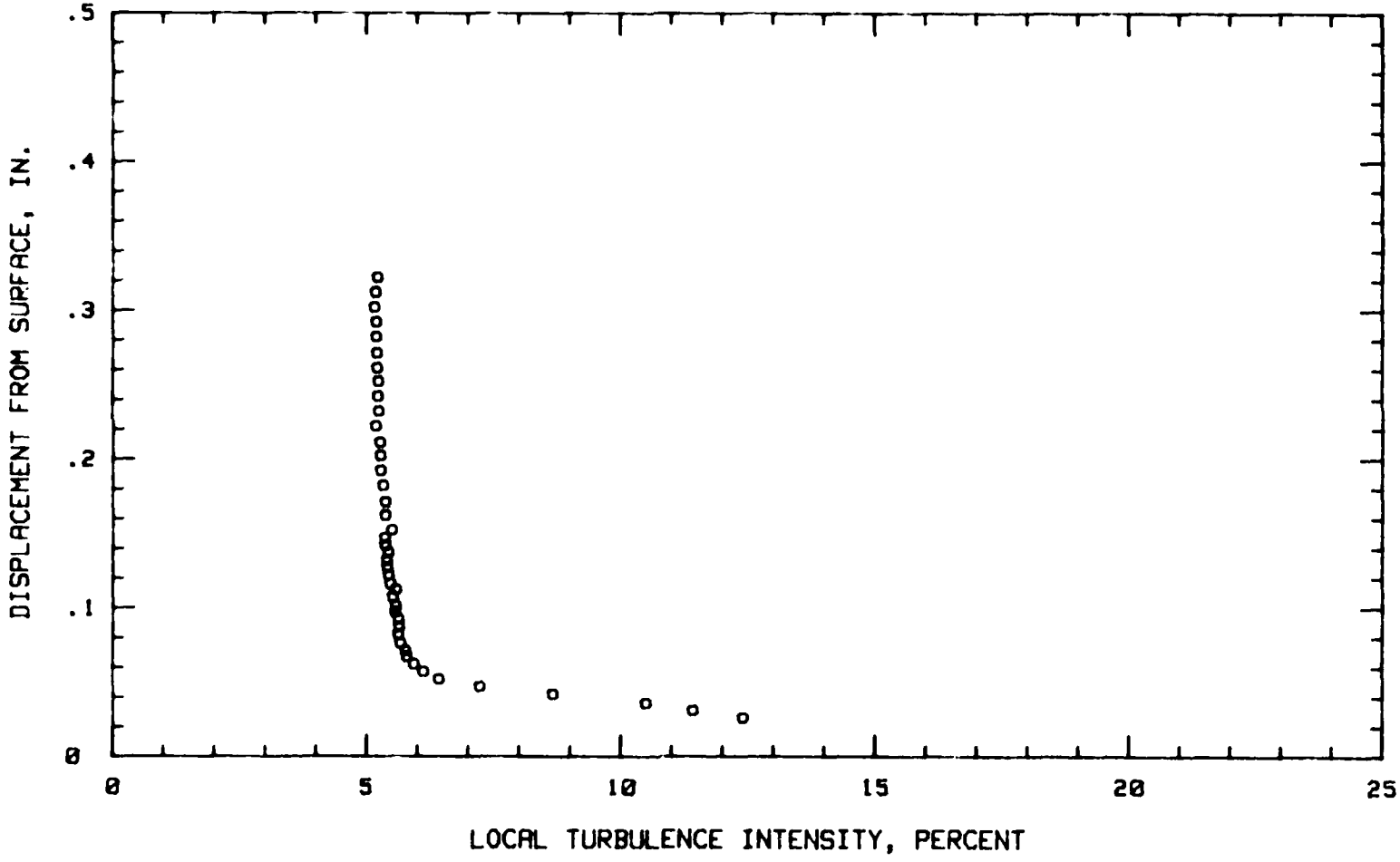

Fig. 87. Boundary Layer Turbulence Intensity Profile, Conf.#2 at 65.62 % Chord

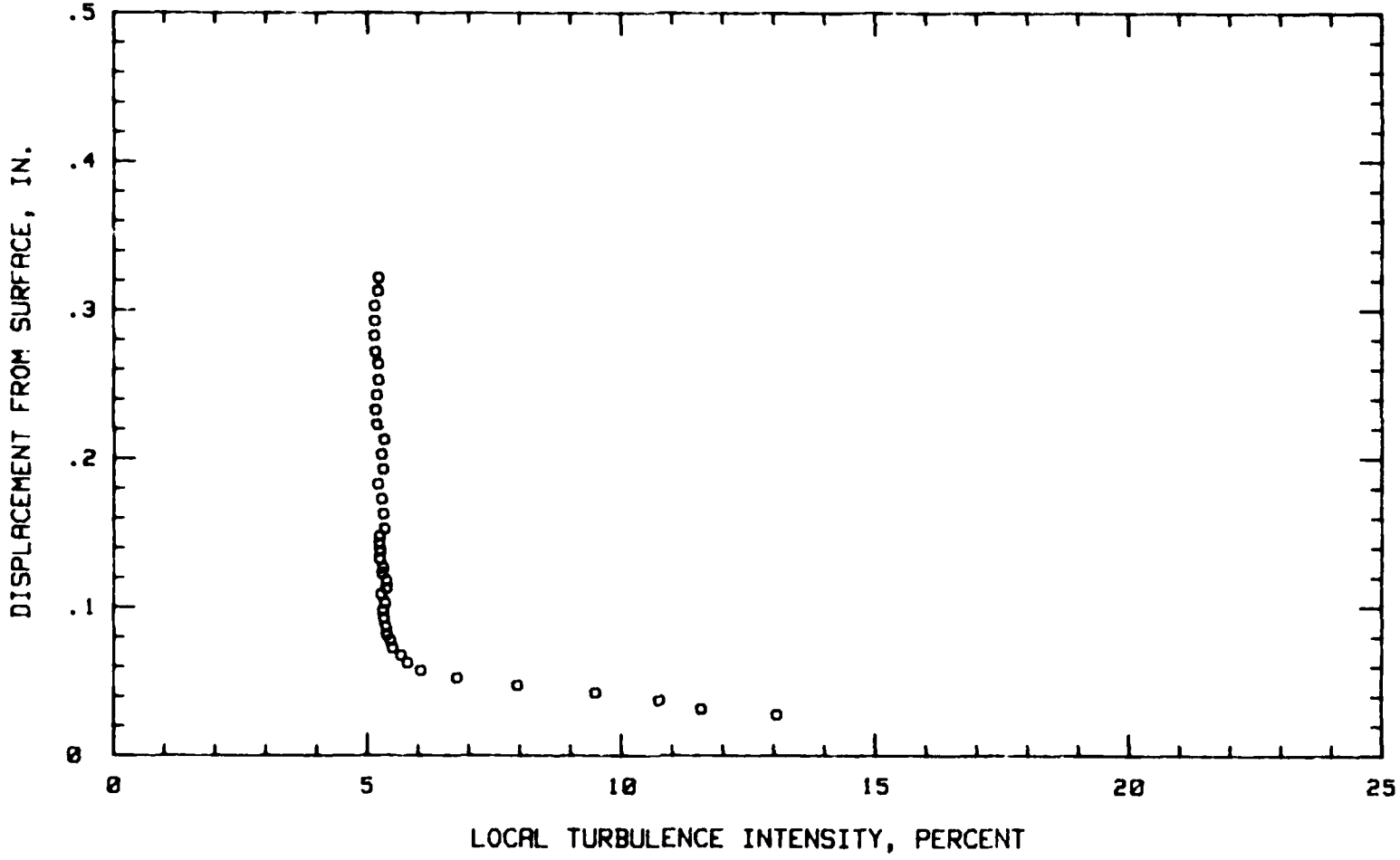

Fig. 88. Boundary Layer Turbulence Intensity Profile, Conf.#2 at 70.31 % Chord

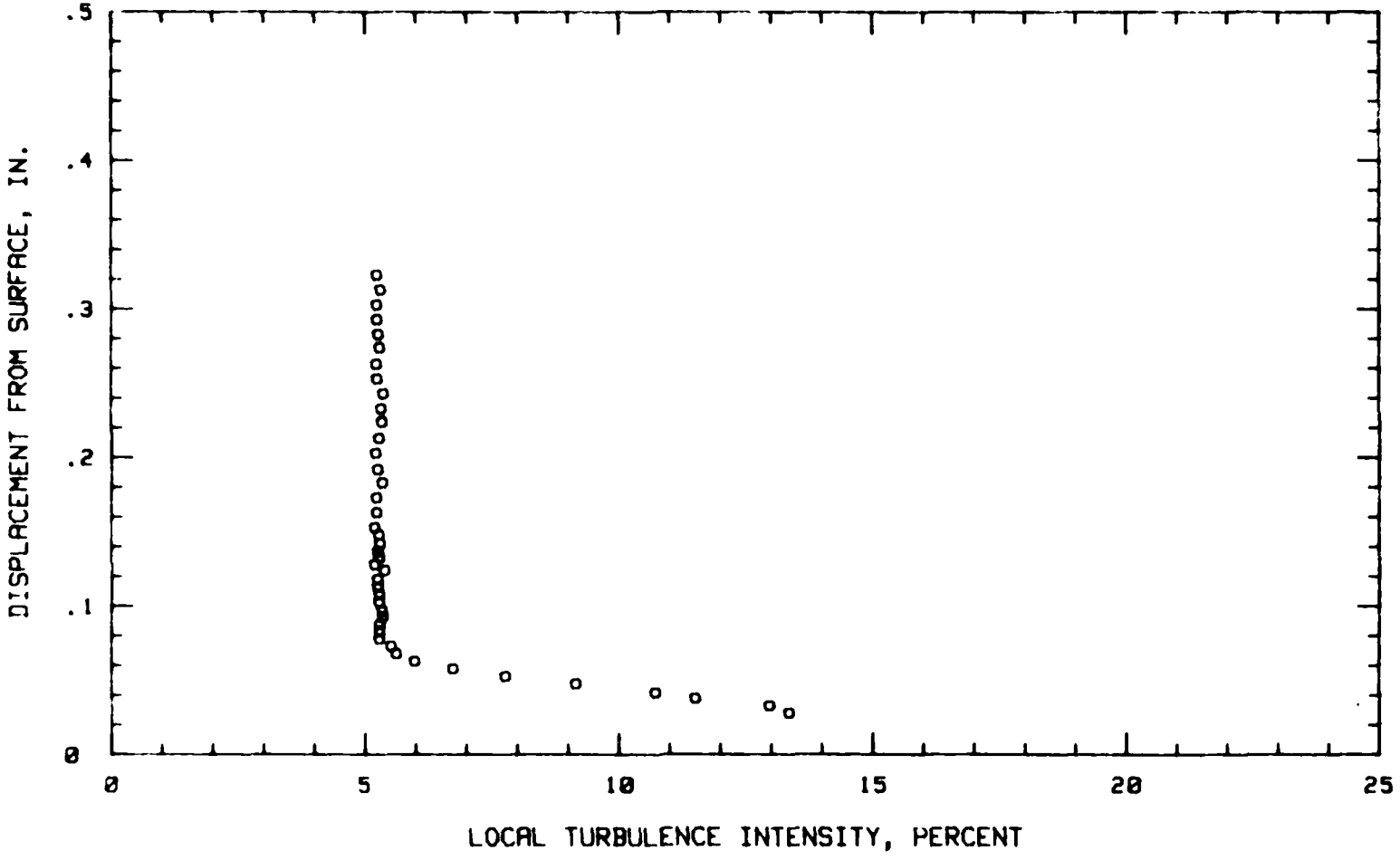

Fig. 89. Boundary Layer Turbulence Intensity Profile, Conf.#2 at 75 % Chord

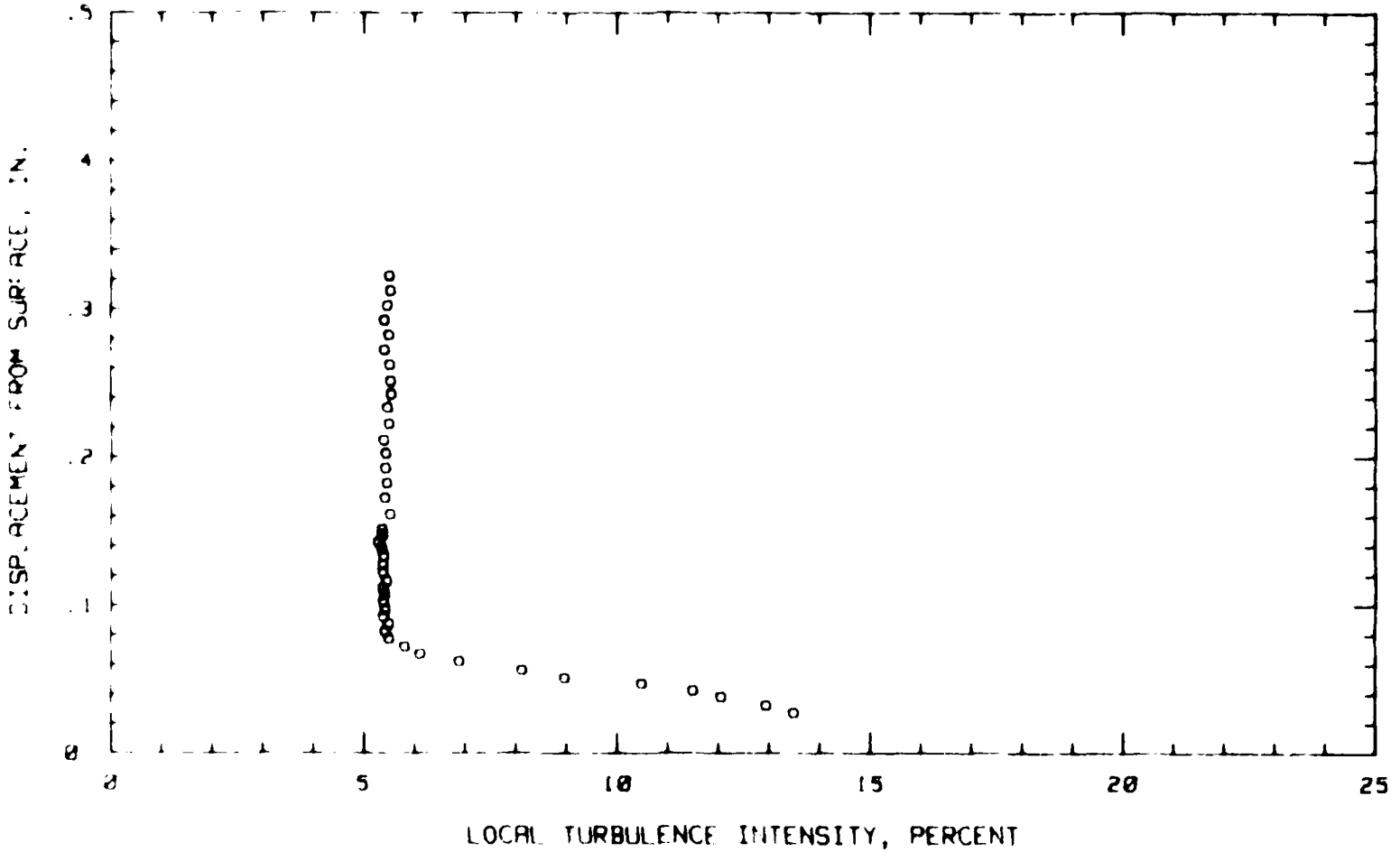

Fig. 90. Boundary Layer Turbulence Intensity Profile, Conf.02 at 79.68 % Chord

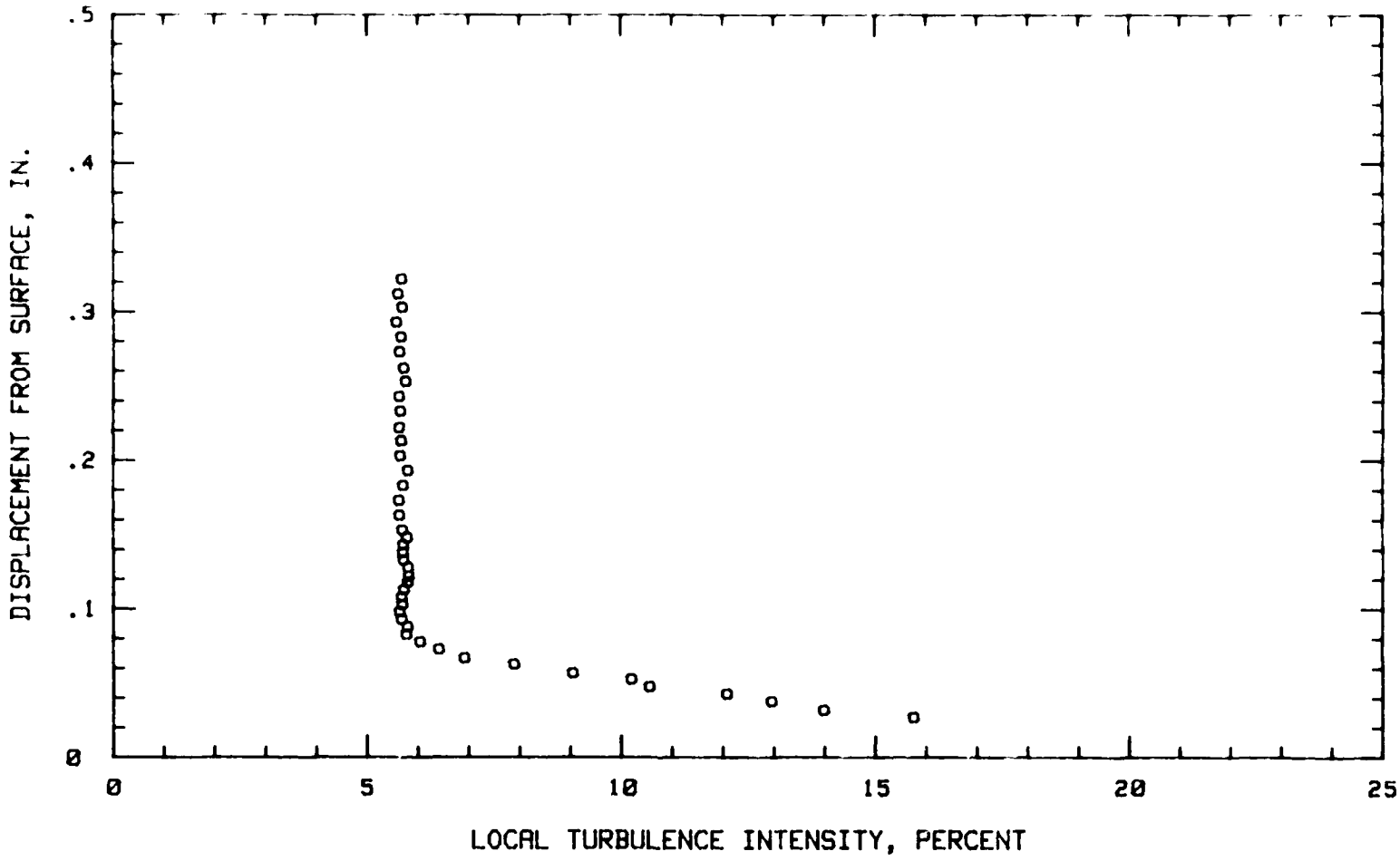

Fig. 91. Boundary Layer Turbulence Intensity Profile, Conf.#2 at 84.37 % Chord

APPENDIX I

Boundary Layer Turbulence Intensity Profiles, Configuration #3

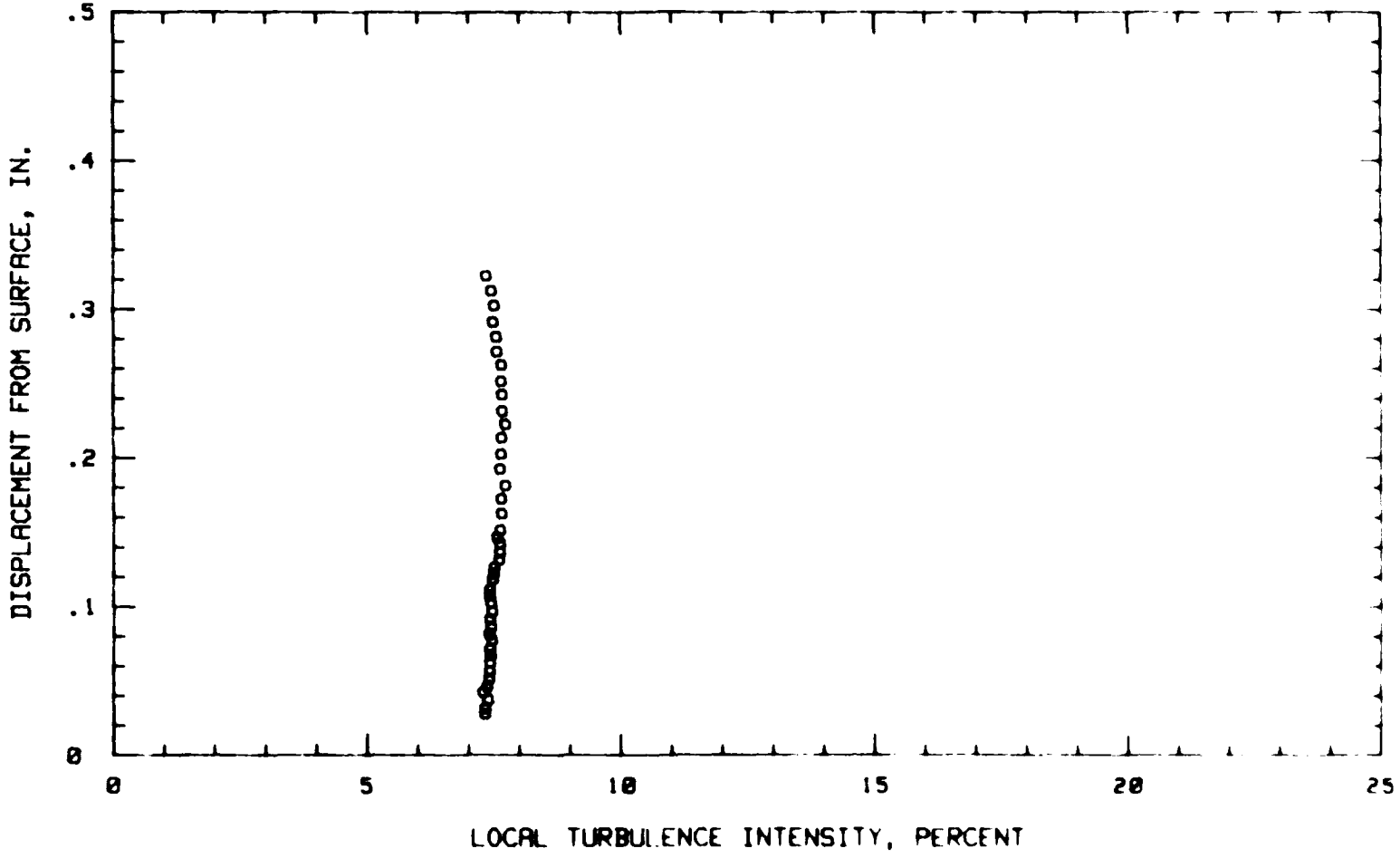

Fig. 92. Boundary Layer Turbulence Intensity Profile, Conf.#3 at 4.68 % Chord

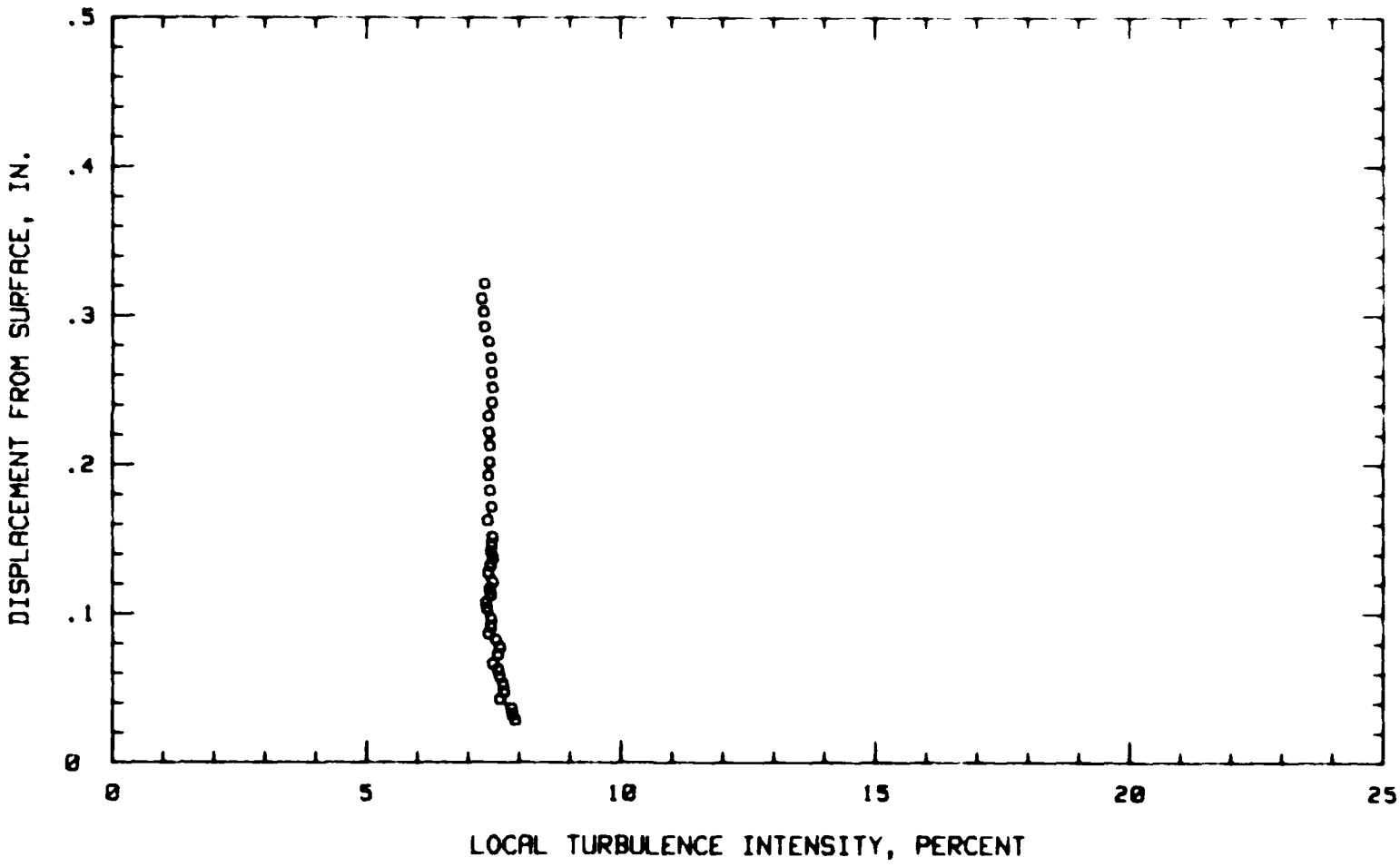

Fig. 93. Boundary Layer Turbulence Intensity Profile, Conf.#3 at 9.37 % Chord

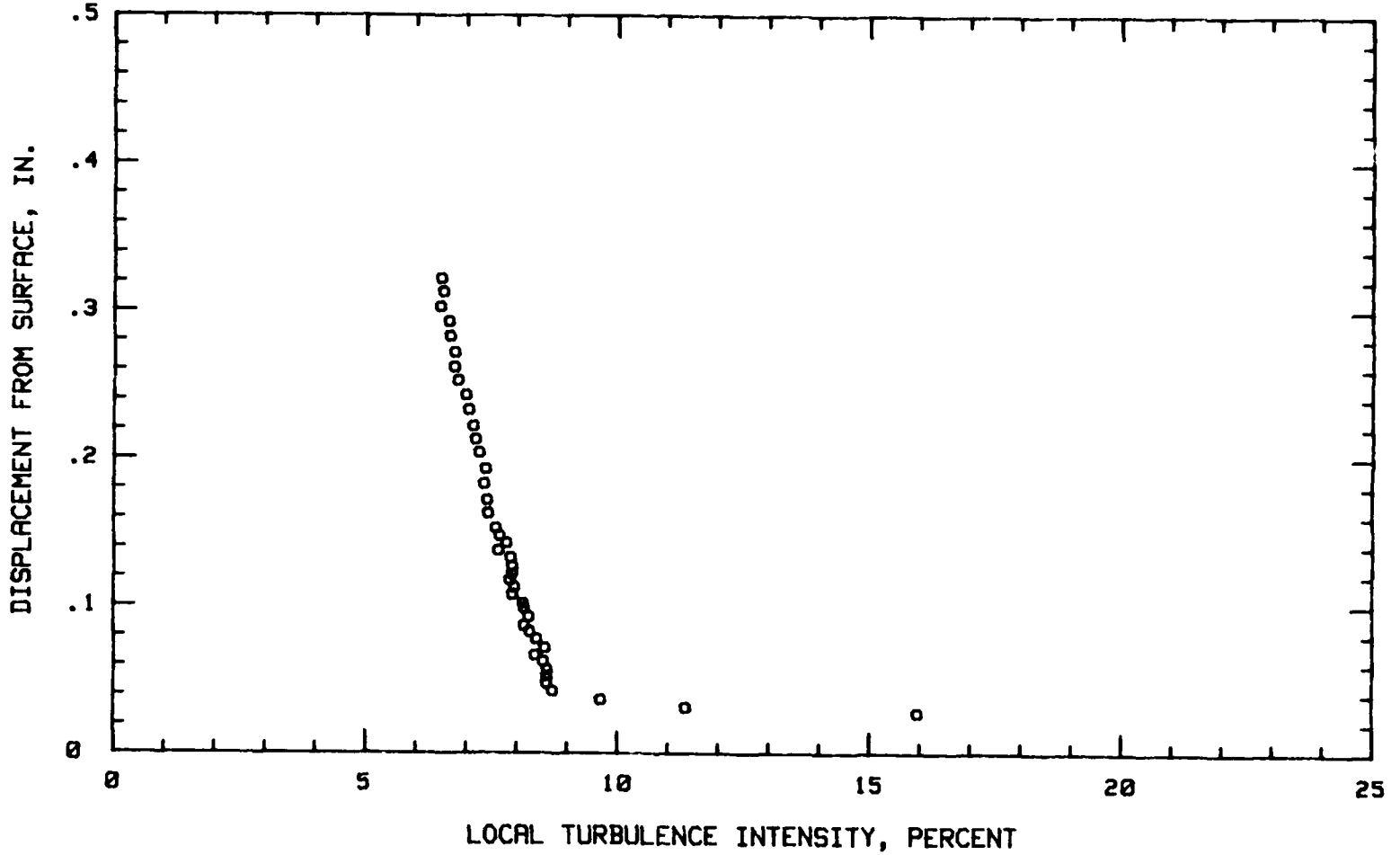

Fig. 94. Boundary Layer Turbulence Intensity Profile, Conf.#3 at 25 % Chord

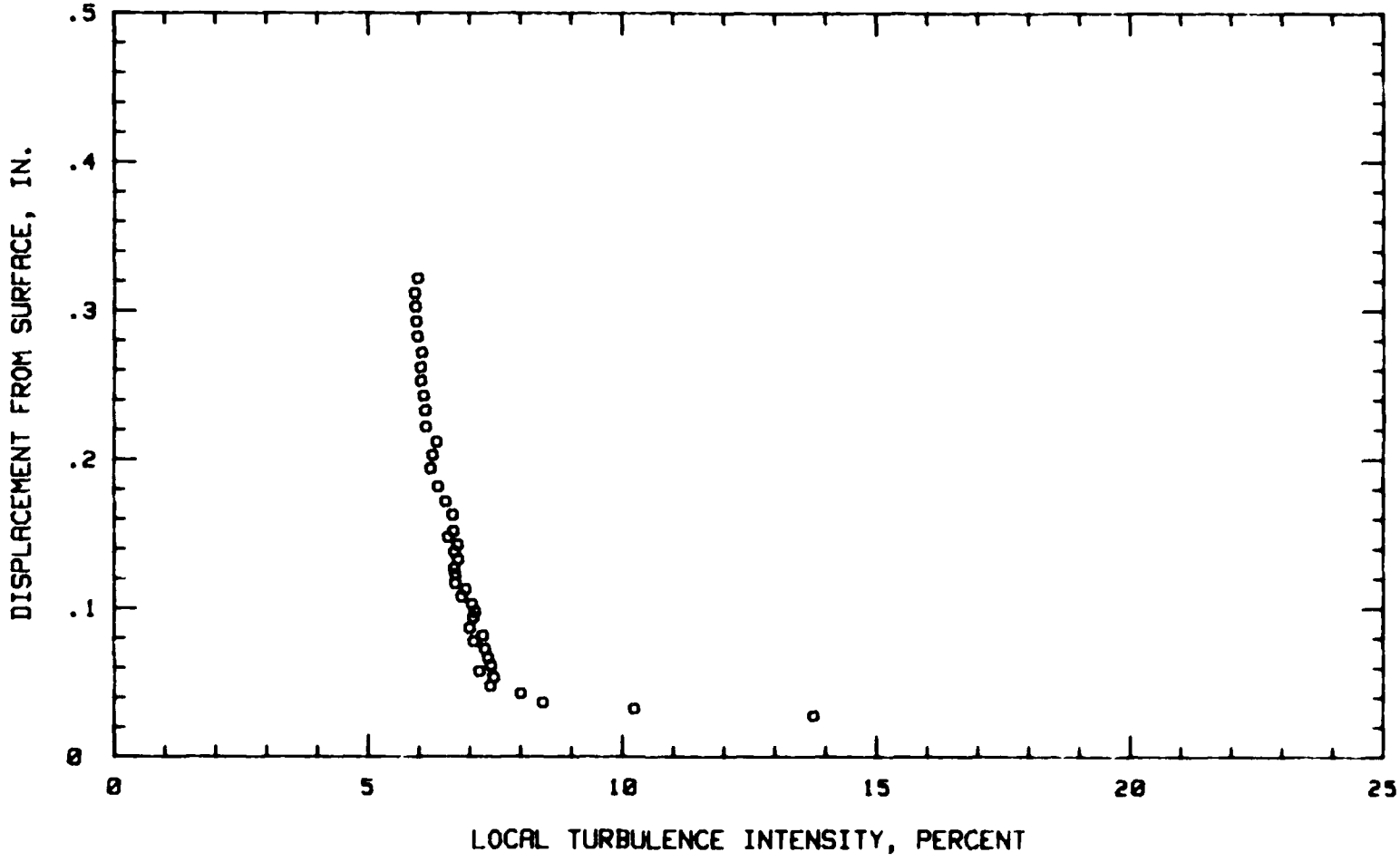

Fig. 95. Boundary Layer Turbulence Intensity Profile, Conf.#3 at 29.68 % Chord

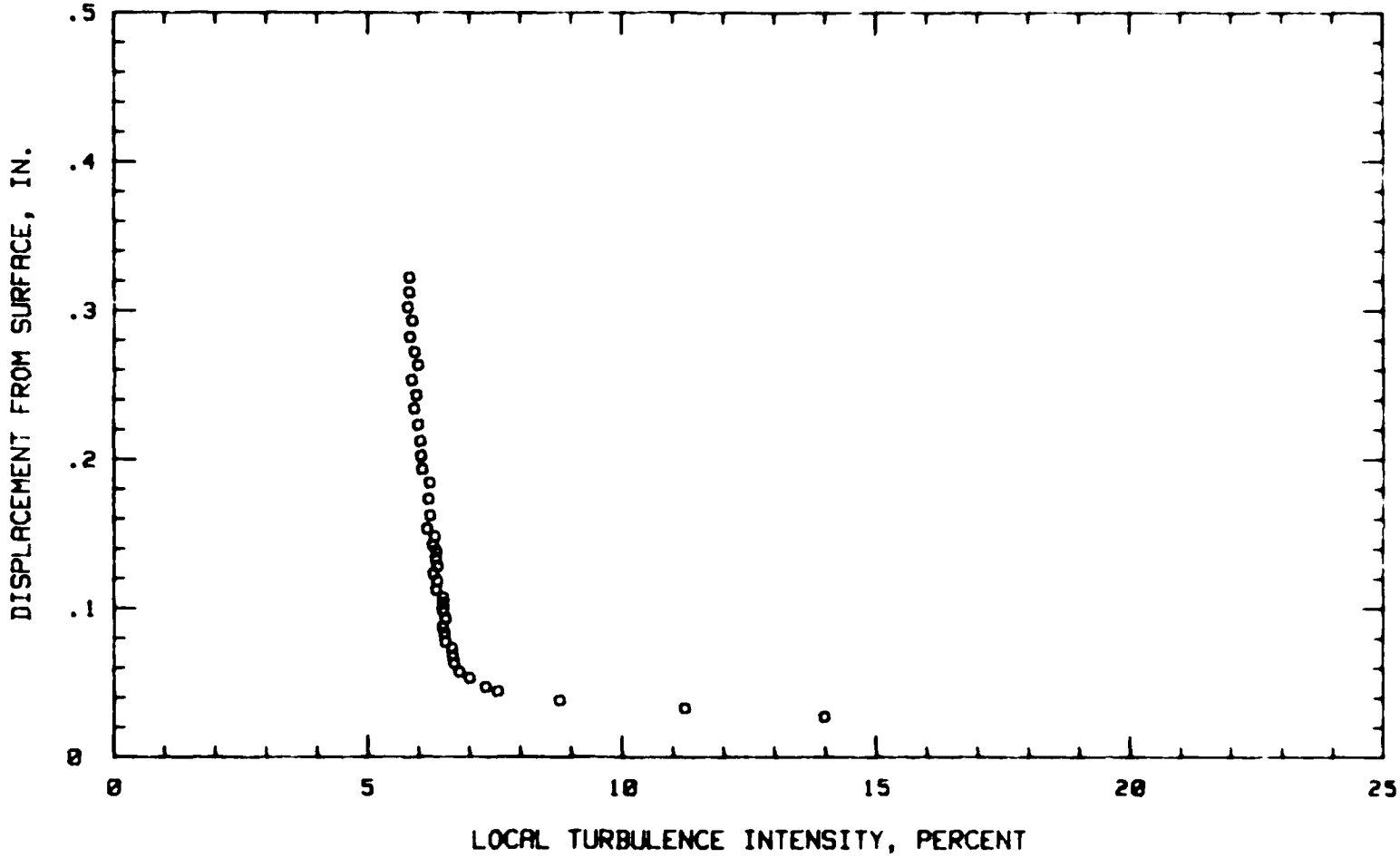

Fig. 96. Boundary Layer Turbulence Intensity Profile, Conf.#3 at 34.37 % Chord

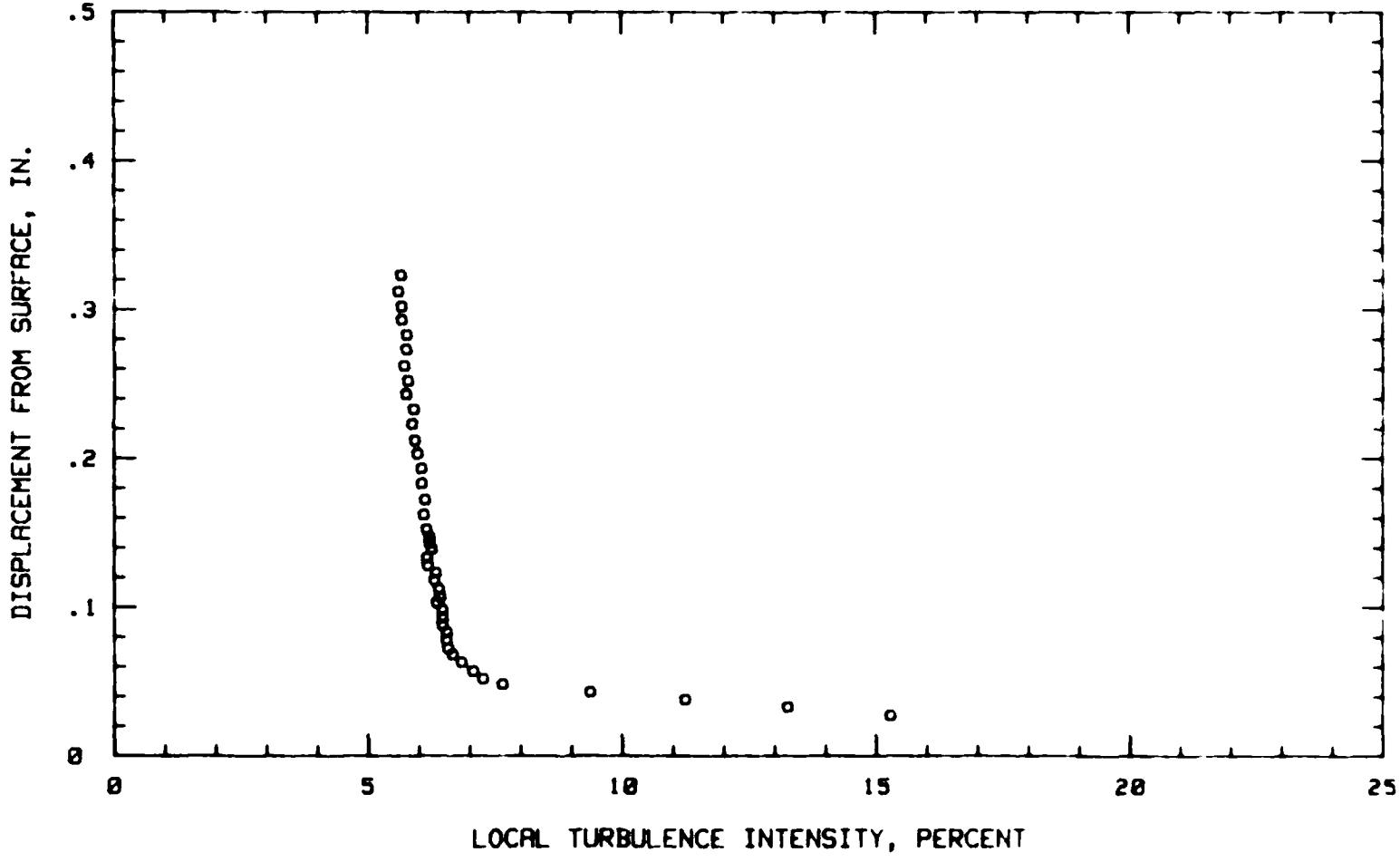

Fig. 97. Boundary Layer Turbulence Intensity Profile, Conf.#3 at 40.62 % Chord

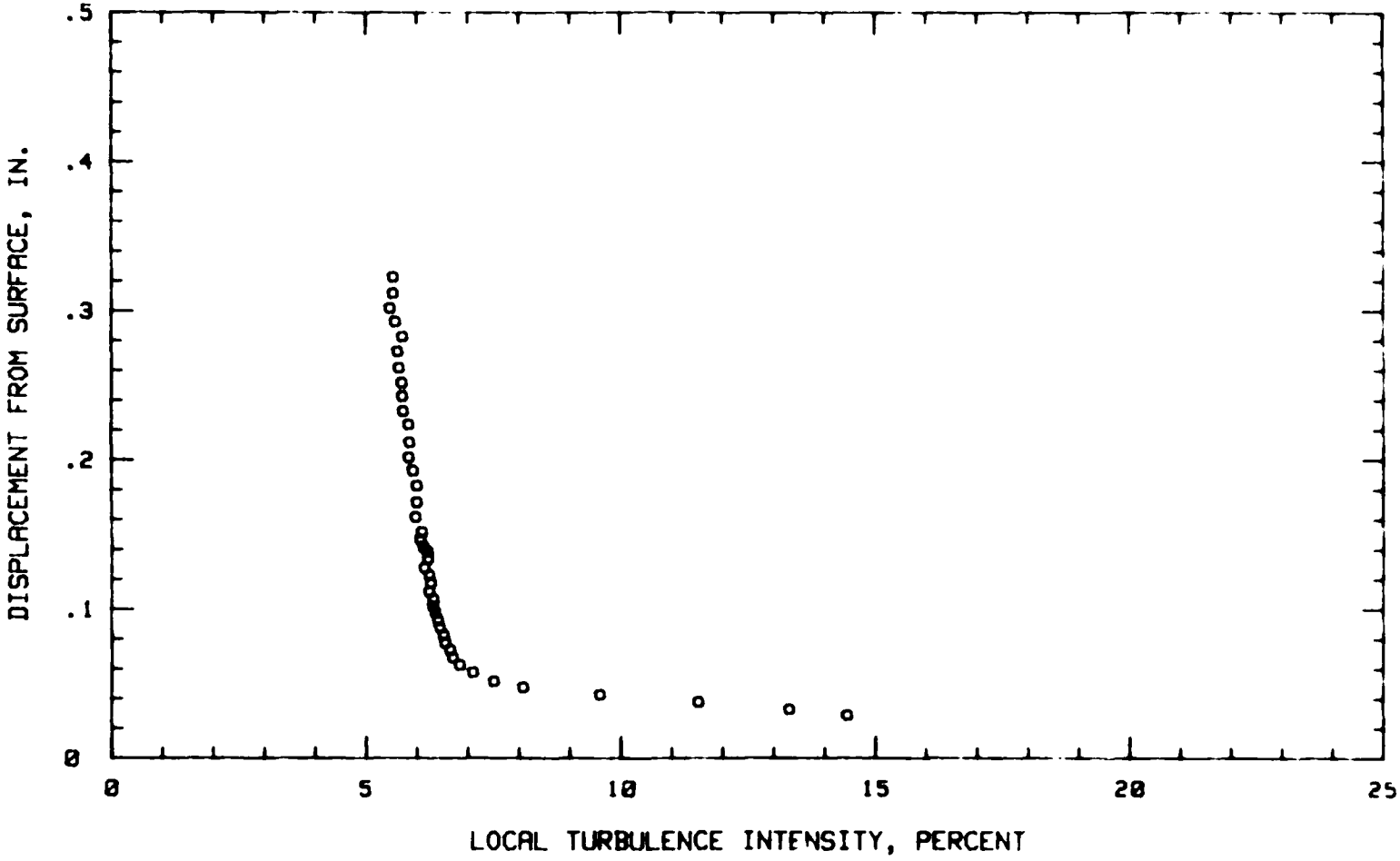

Fig. 98. Boundary Layer Turbulence Intensity Profile, Conf.#3 at 45.31 % Chord

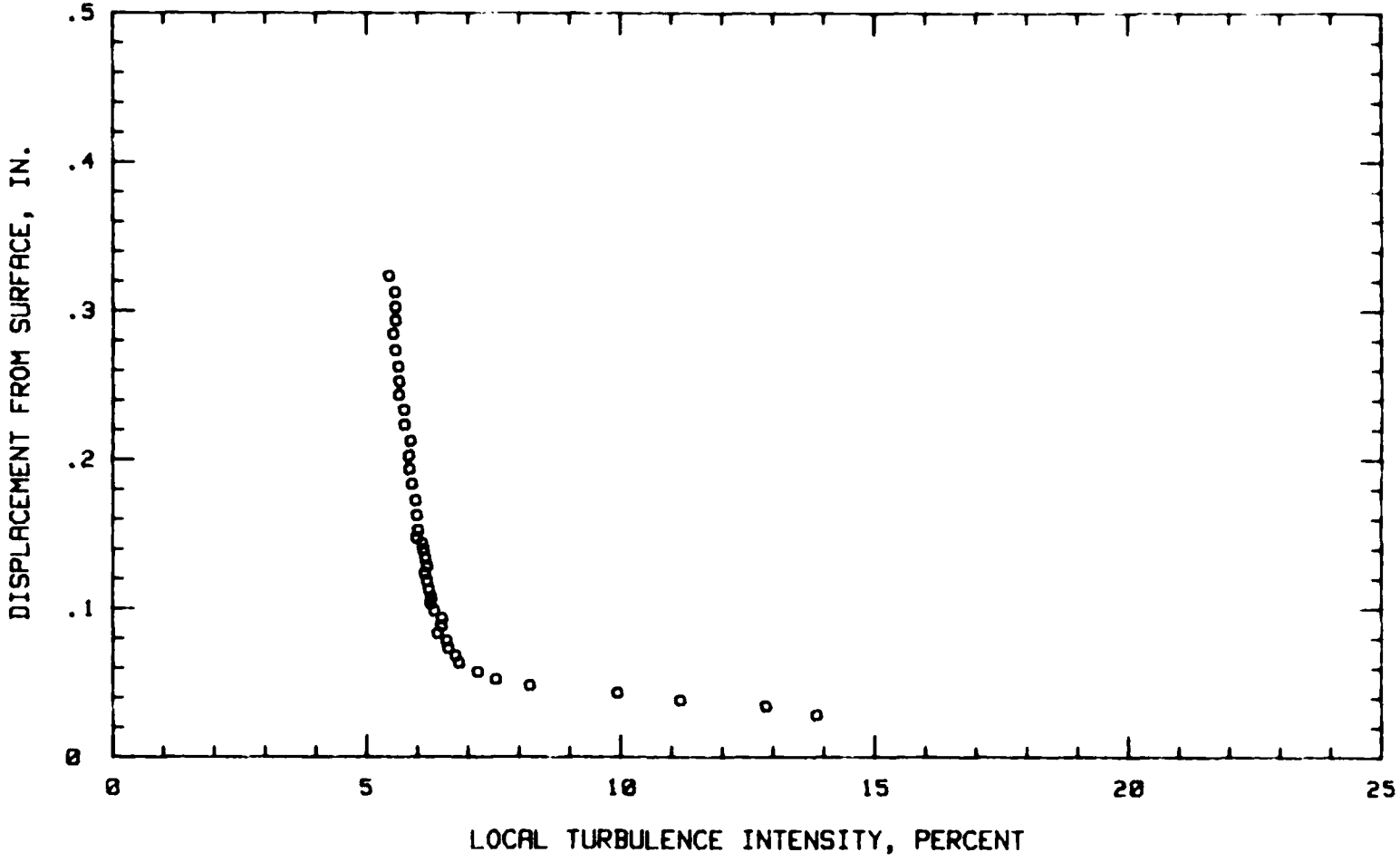

Fig. 99. Boundary Layer Turbulence Intensity Profile, Conf.#3 at 50 % Chord

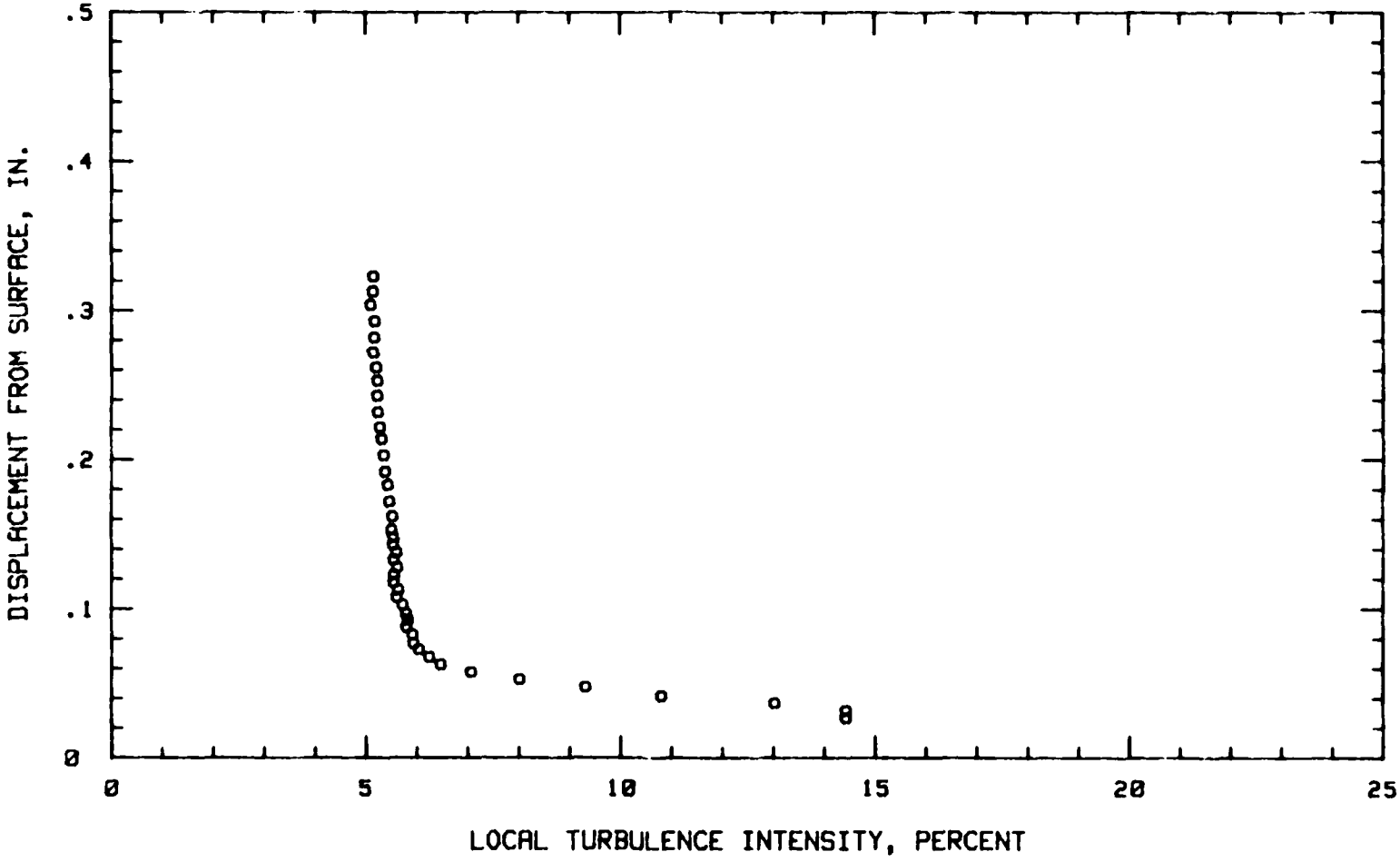

Fig. 100. Boundary Layer Turbulence Intensity Profile, Conf.#3 at 65.62 % Chord

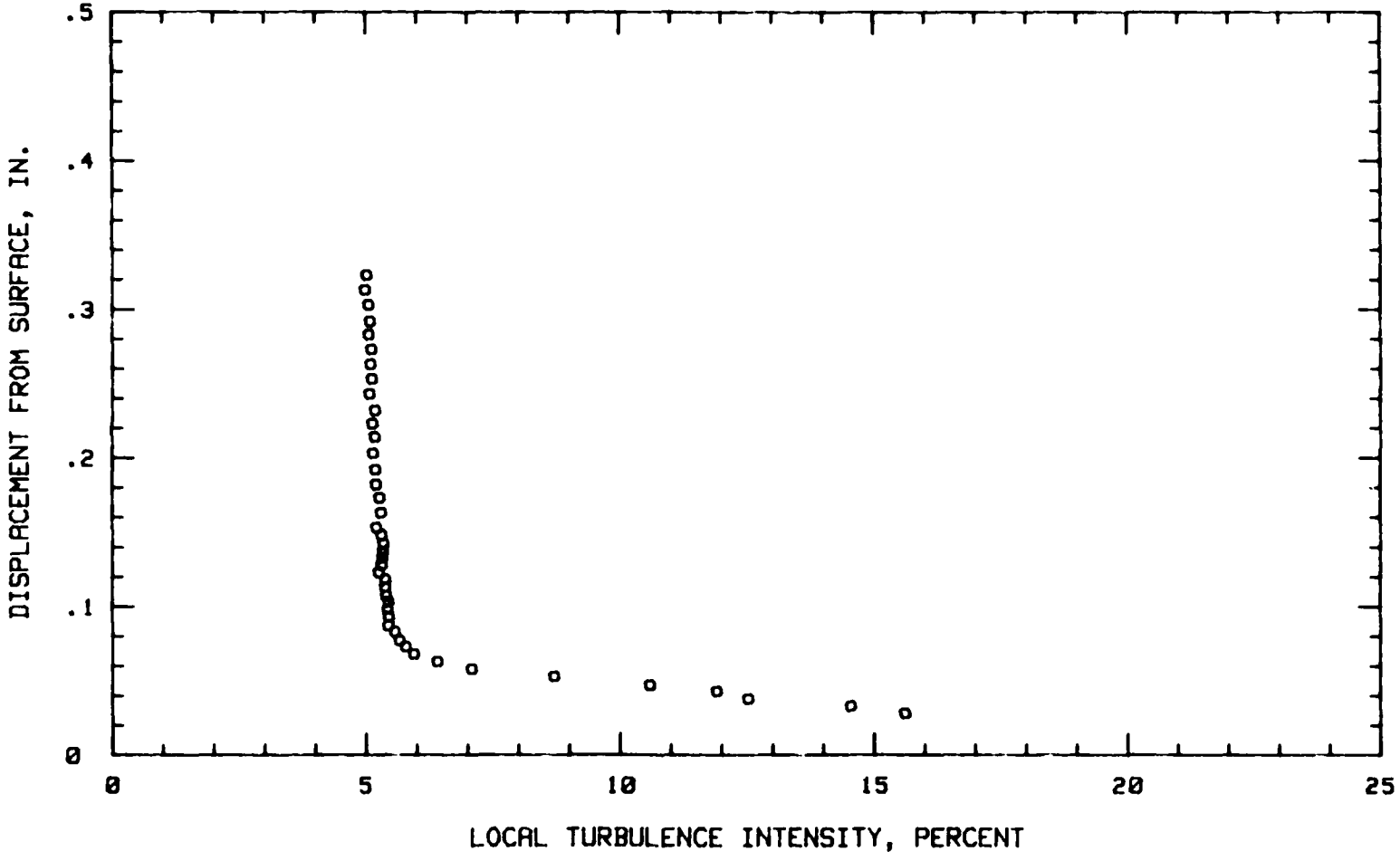

Fig. 101. Boundary Layer Turbulence Intensity Profile, Conf.#3 at 70.31 % Chord

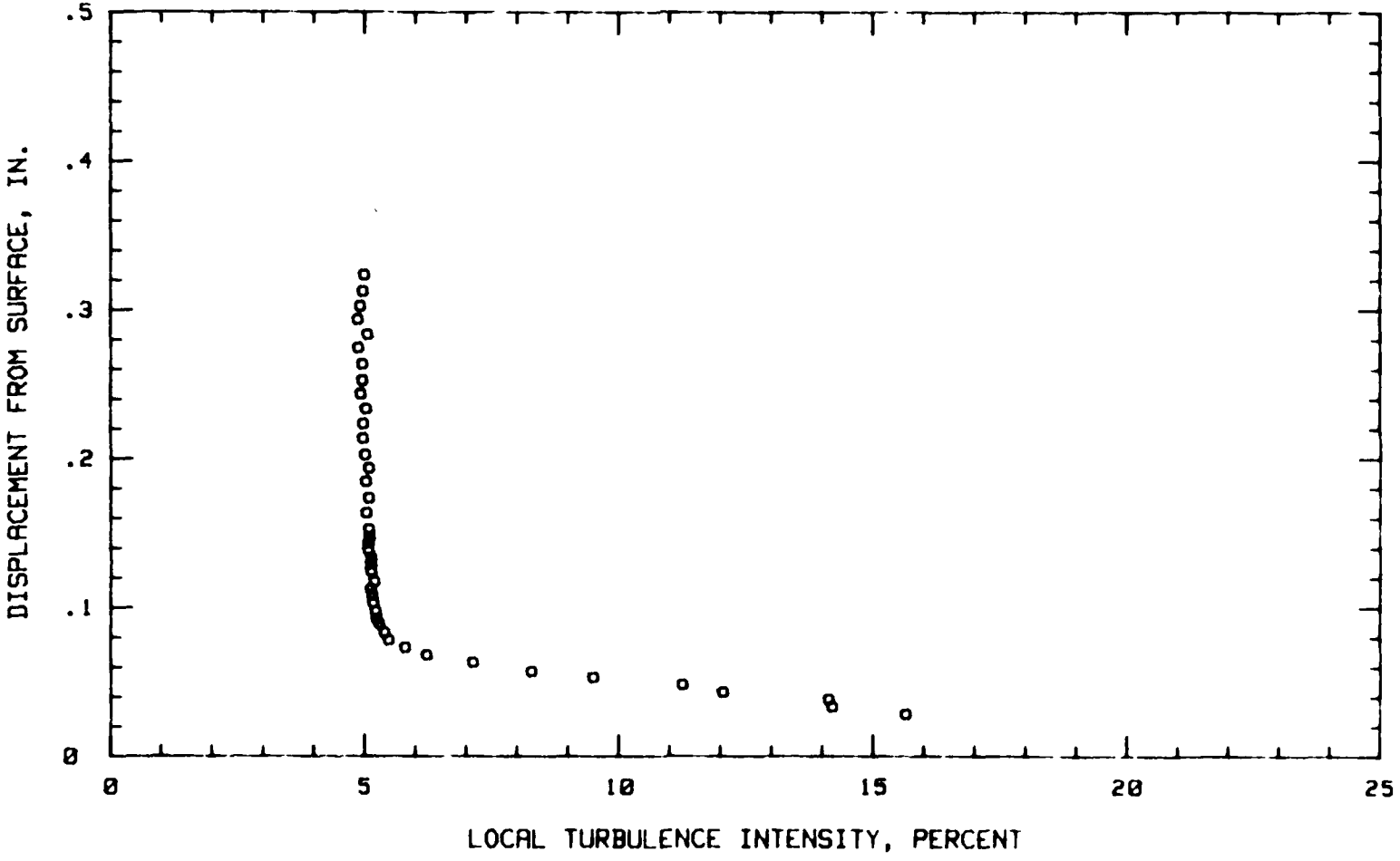

Fig. 102. Boundary Layer Turbulence Intensity Profile, Conf.#3 at 75 % Chord

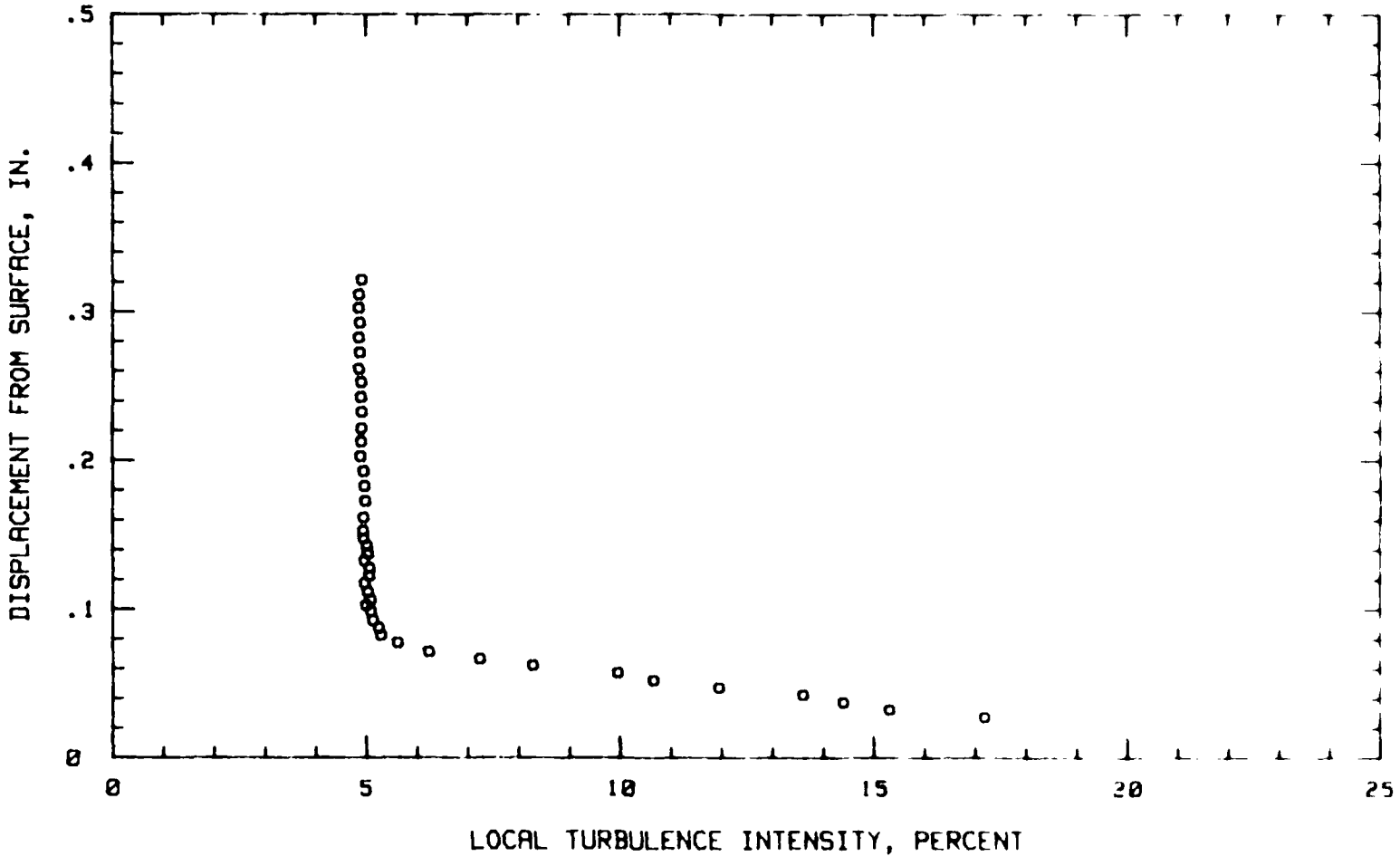

Fig. 103. Boundary Layer Turbulence Intensity Profile, Conf.03 at 79.68 % Chord

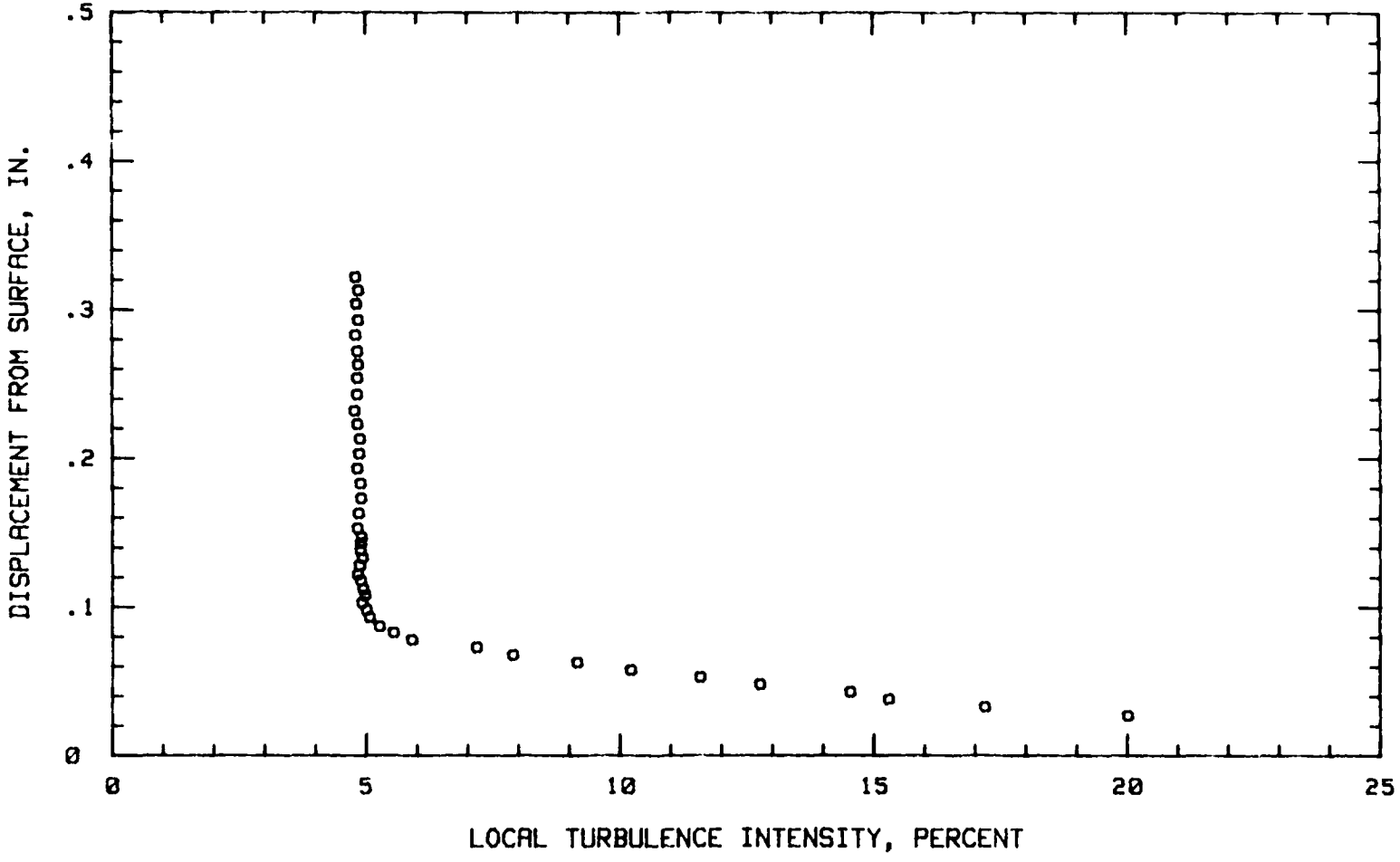

Fig. 104. Boundary Layer Turbulence Intensity Profile, Conf.#3 at 84.37 % Chord

AD-A179 506 SURFACE ROUGHNESS: ITS EFFECTS ON THE PERFORMANCE OF A 3/3
TWO-DIMENSIONAL CO (U) AIR FORCE INST OF TECH
WRIGHT-PATTERSON AFB OH SCHOOL OF ENGI J R POULIN
UNCLASSIFIED DEC 86 AFIT/GAE/AA/86D-13 F/G 20/4 NN

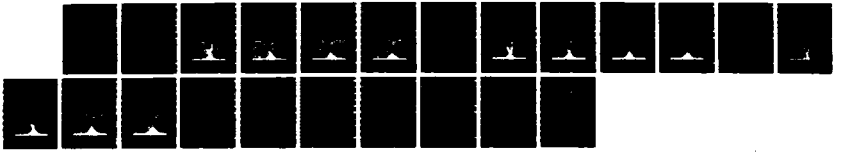

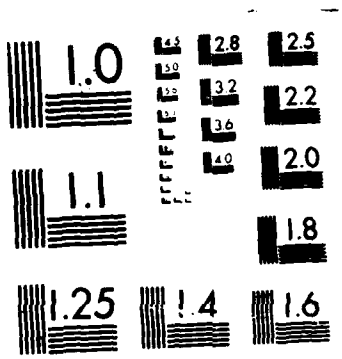

APPENDIX J

Wake Velocity and Turbulence Intensity Profiles, Conf. #1

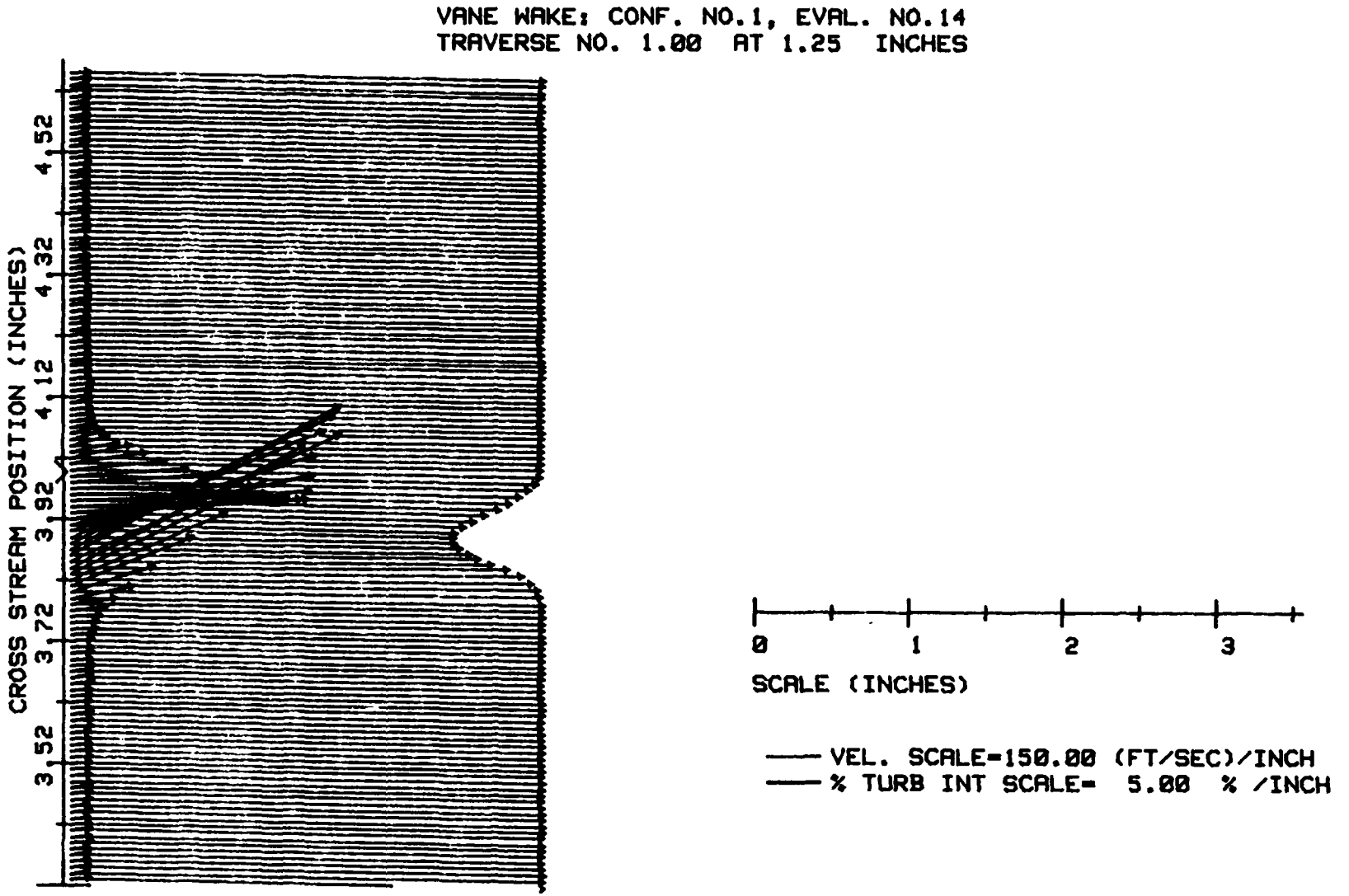

Fig. 105. Wake Velocity and Turbulence Intensity Profiles, Conf. #1, x/c = .625

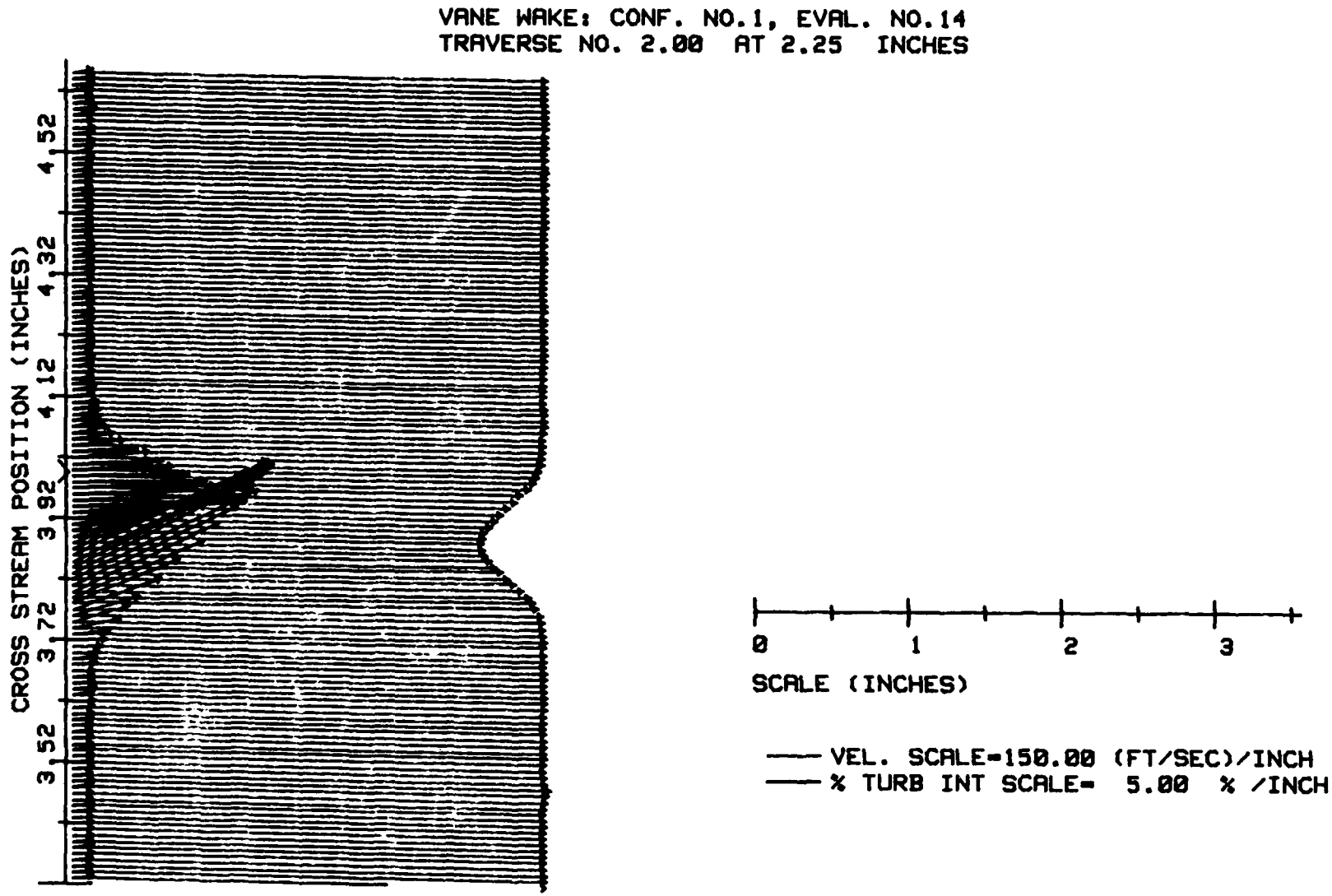

Fig. 106. Wake Velocity and Turbulence Intensity Profiles, Conf. #1, x/c = 1.125

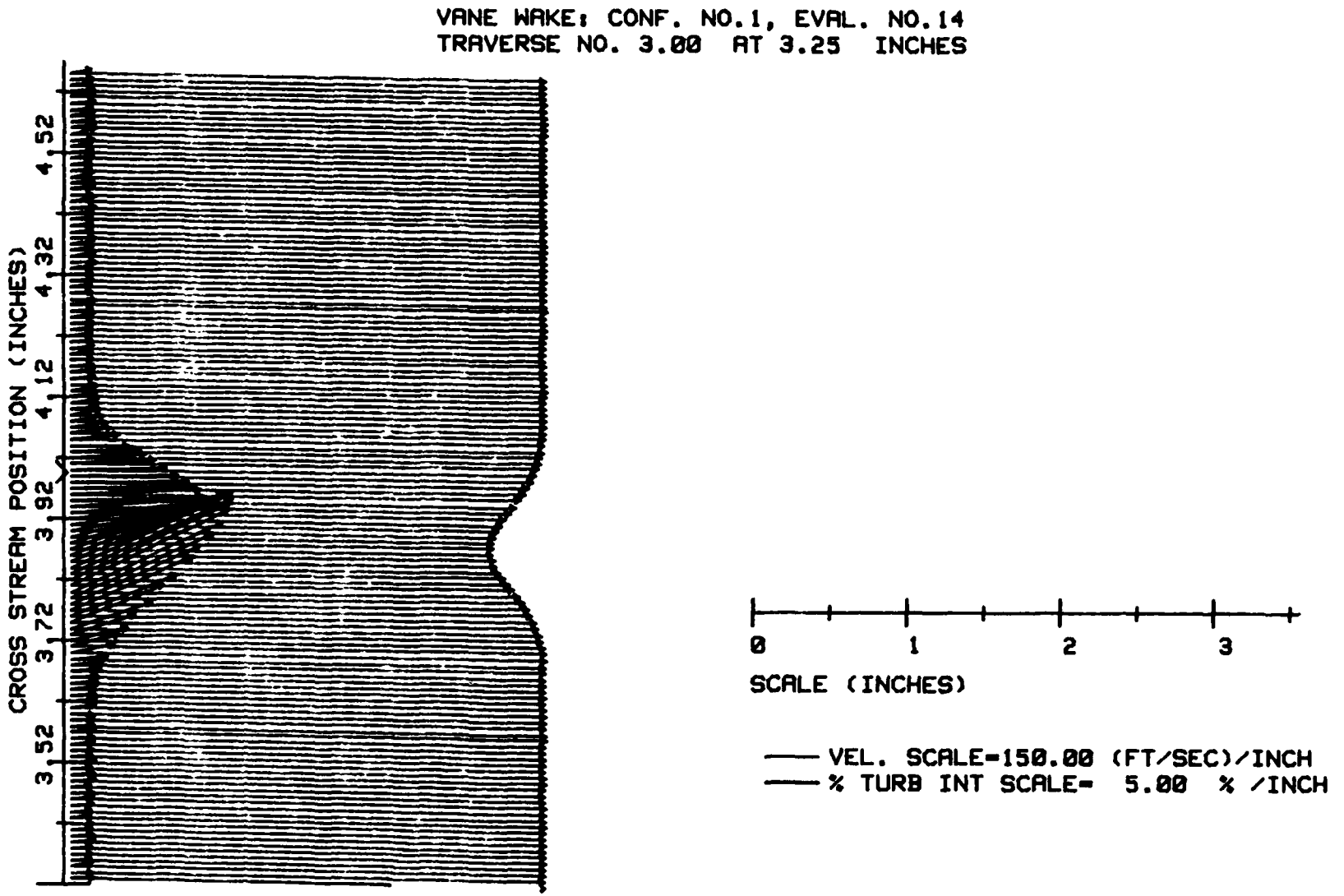

Fig. 107. Wake Velocity and Turbulence Intensity Profiles, Conf. #1, x/c = 1.625

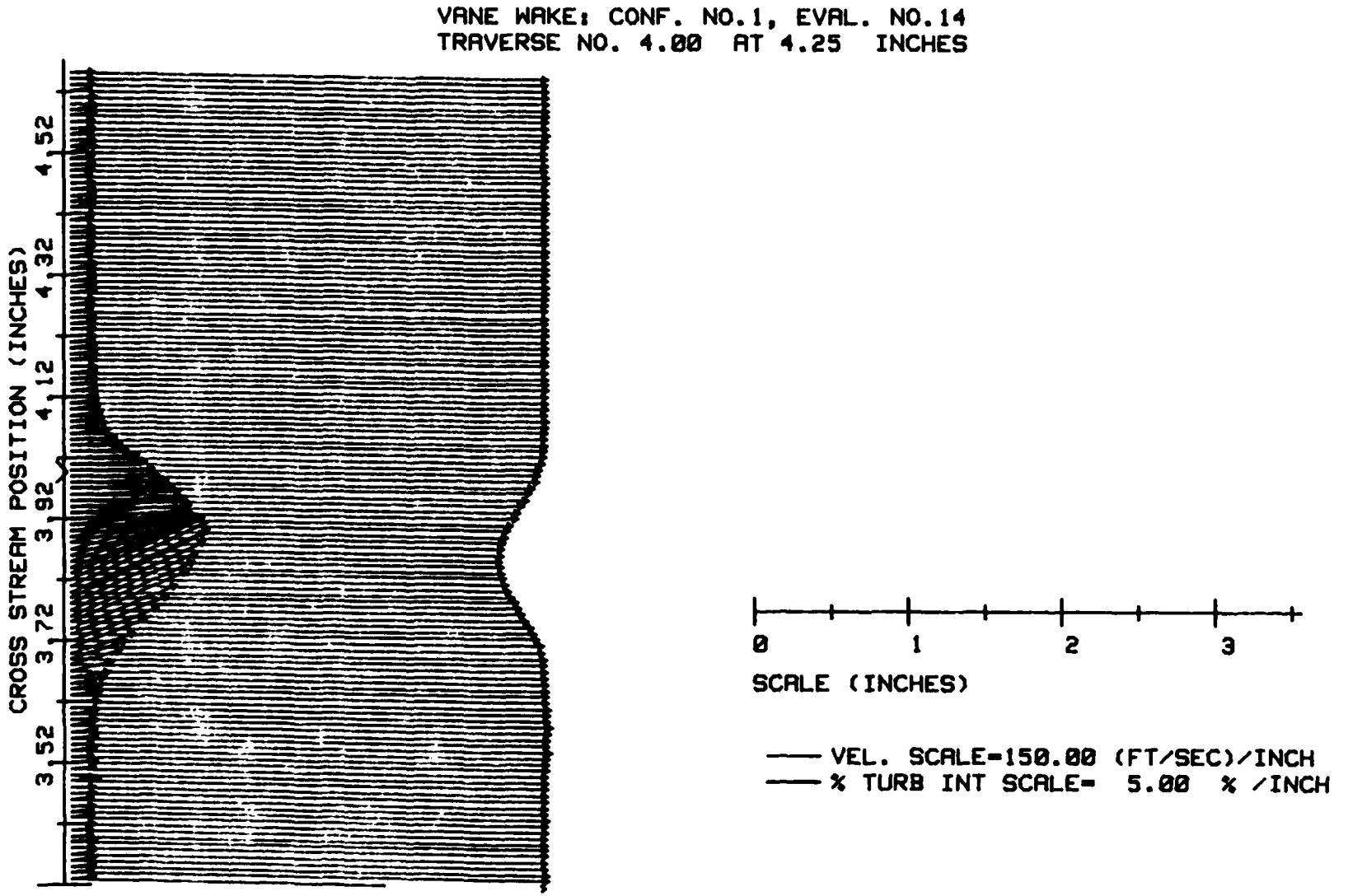

Fig. 108. Wake Velocity and Turbulence Intensity Profiles, Conf. #1, x/c = 2.125

APPENDIX K

Wake Velocity and Turbulence Intensity Profiles, Conf. #2

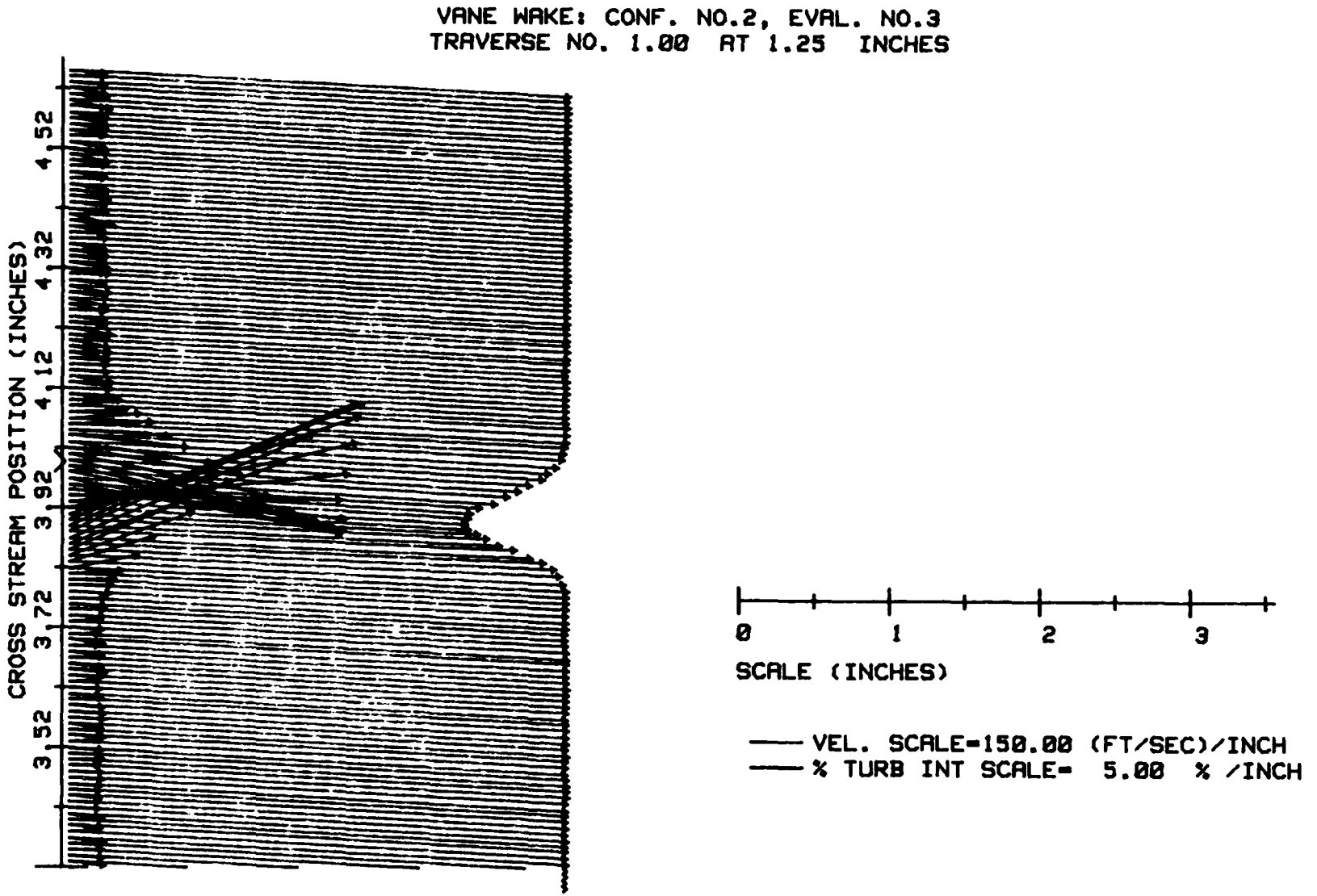

Fig. 109. Wake Velocity and Turbulence Intensity Prcfiles, Conf. #2, x/c = .625

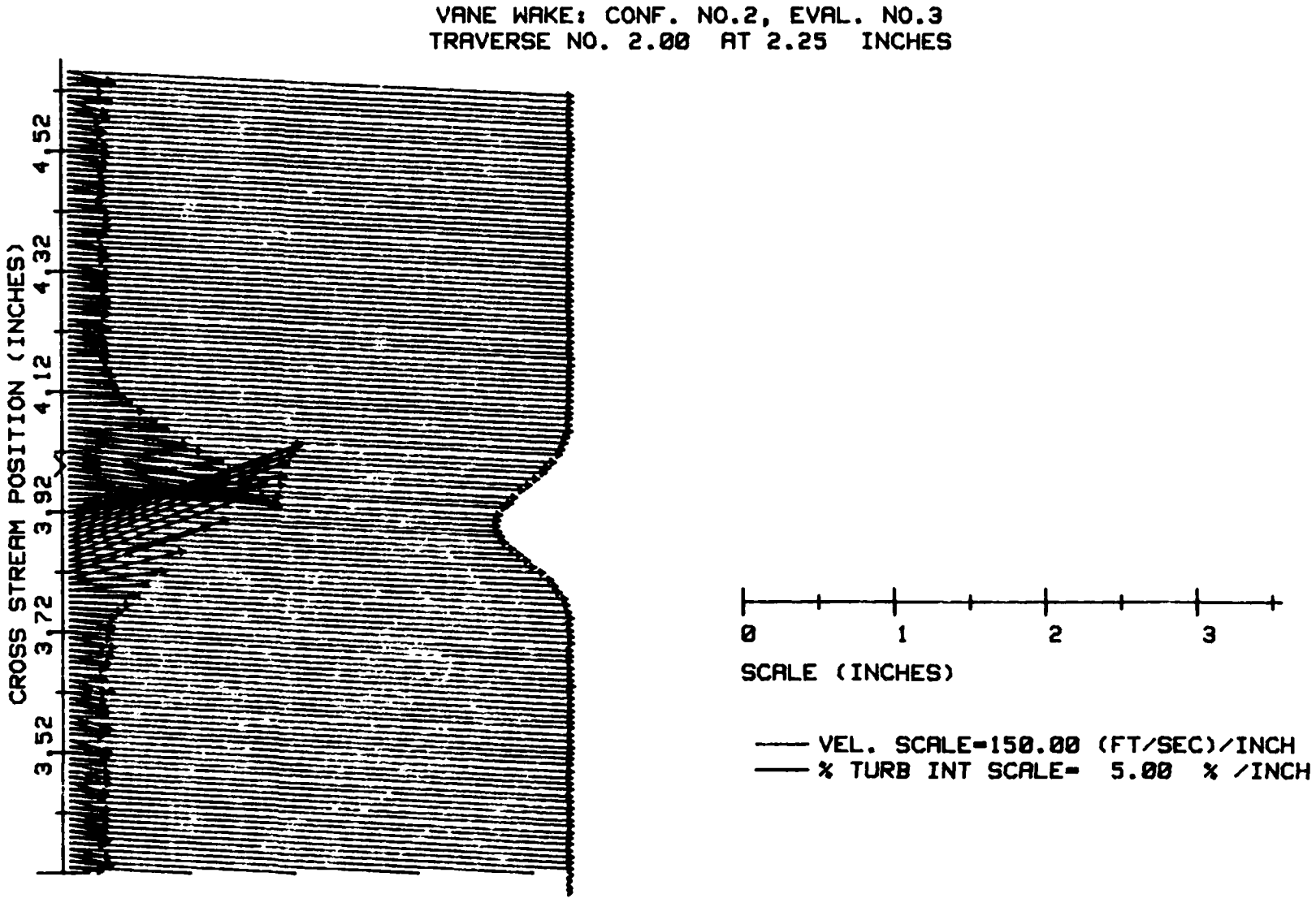

Fig. 110. Wake Velocity and Turbulence Intensity Profiles, Conf. #2, x/c = 1.125

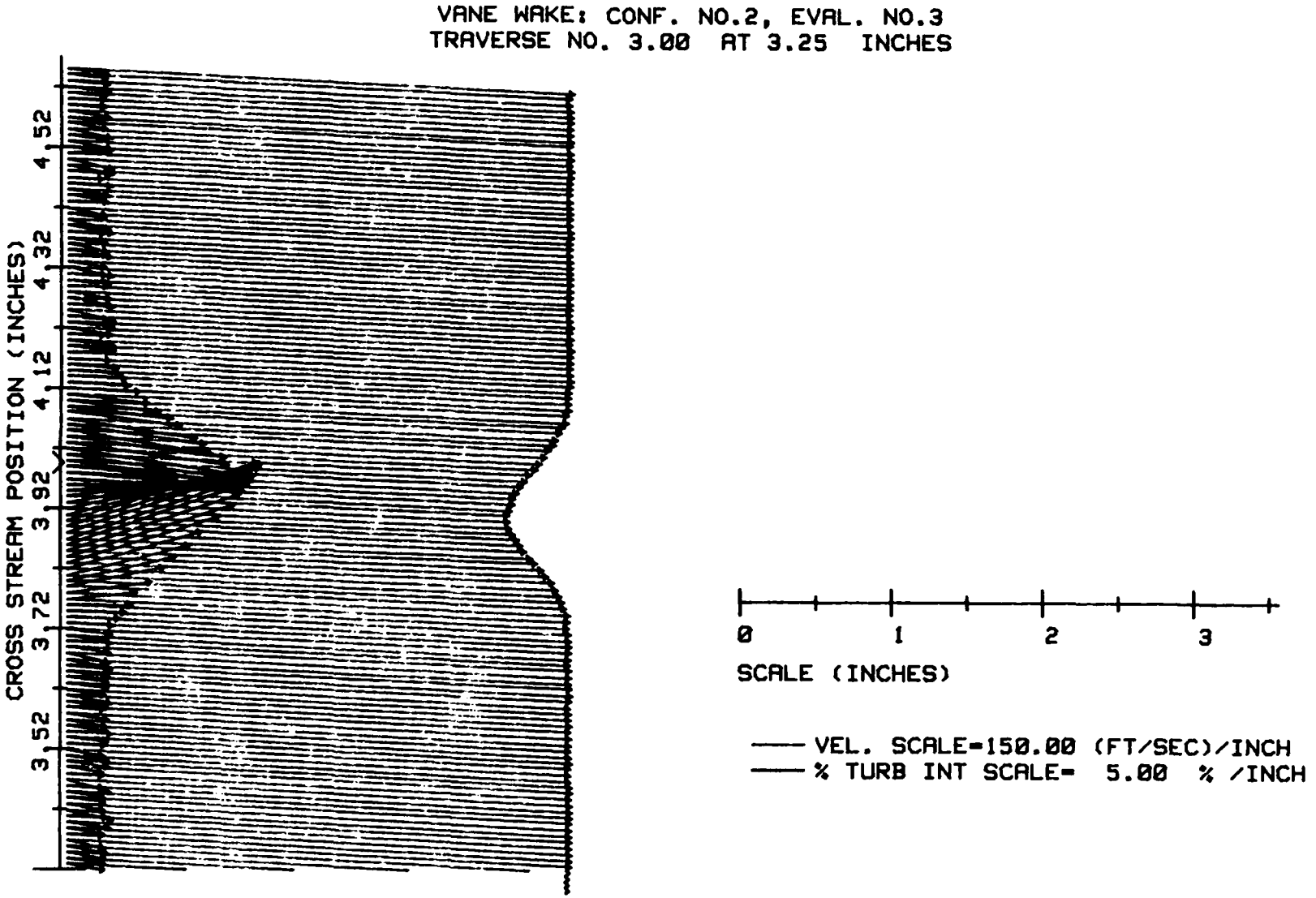

Fig. 111. Wake Velocity and Turbulence Intensity Profiles, Conf. #2, x/c = 1.625

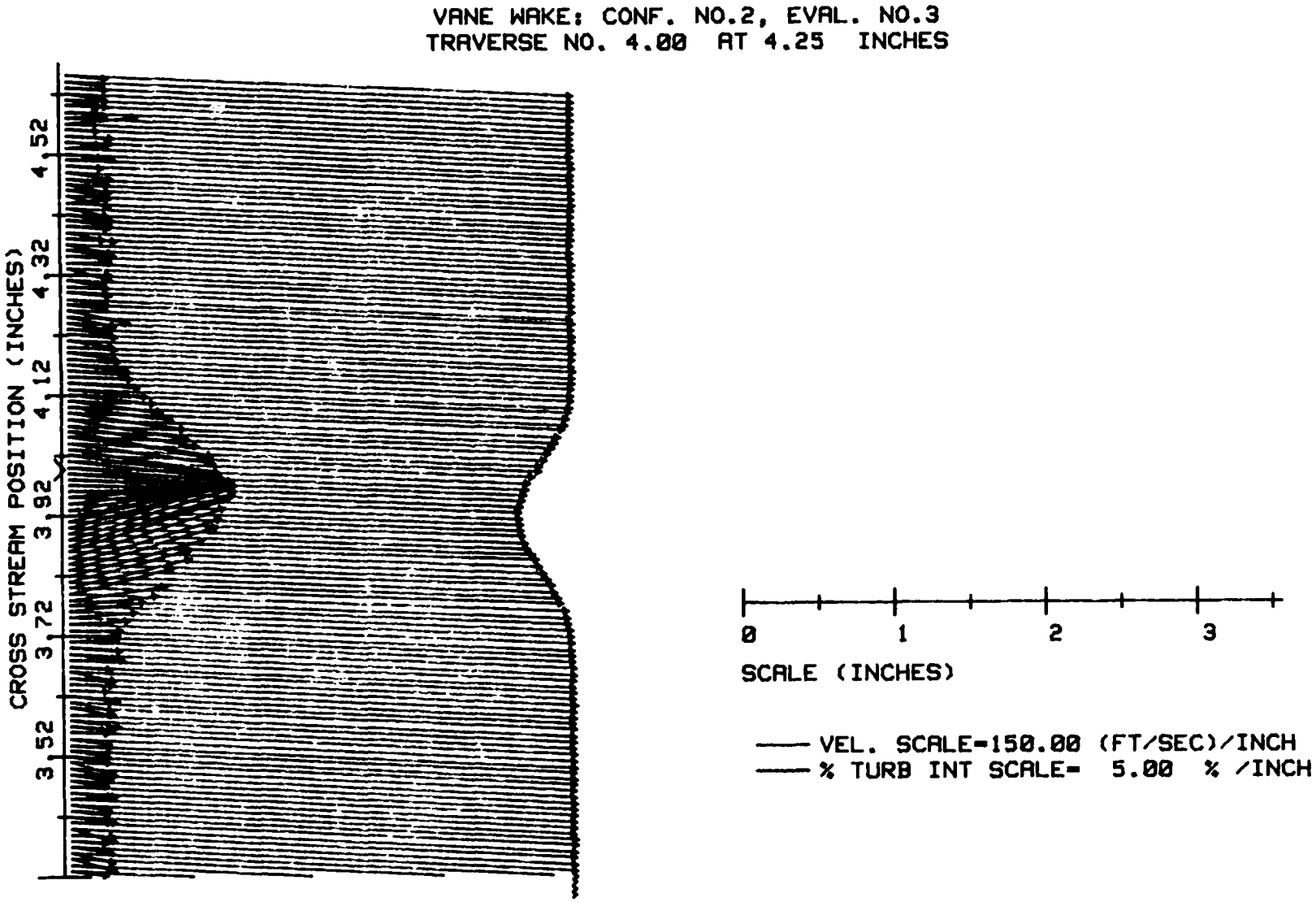

Fig. 112. Wake Velocity and Turbulence Intensity Profiles, Conf. #2, x/c = 2.125

APPENDIX L

Wake Velocity and Turbulence Intensity Profiles, Conf. #3

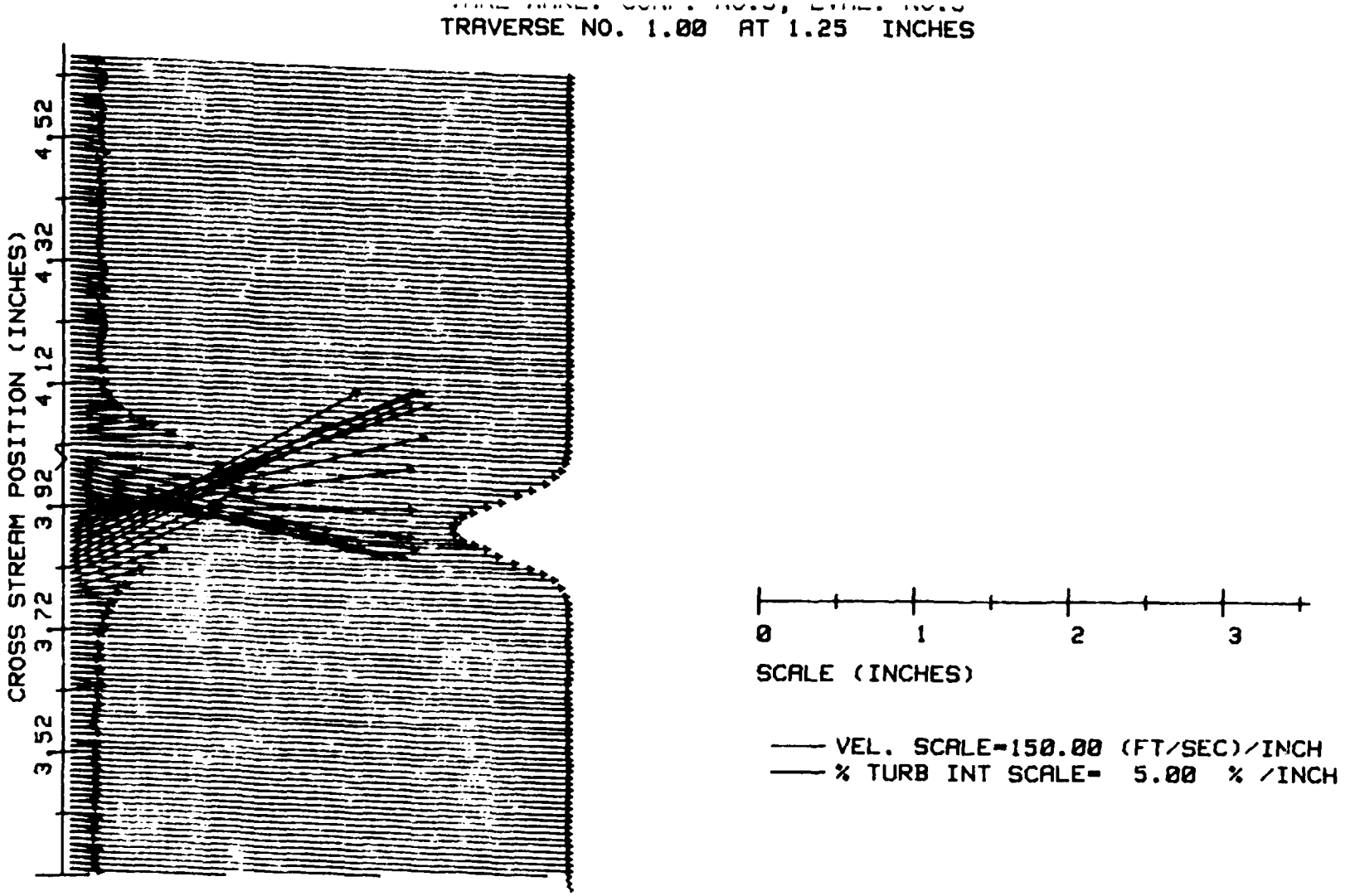

Fig. 113. Wake Velocity and Turbulence Intensity Profiles, Conf. #3, x/c = .625

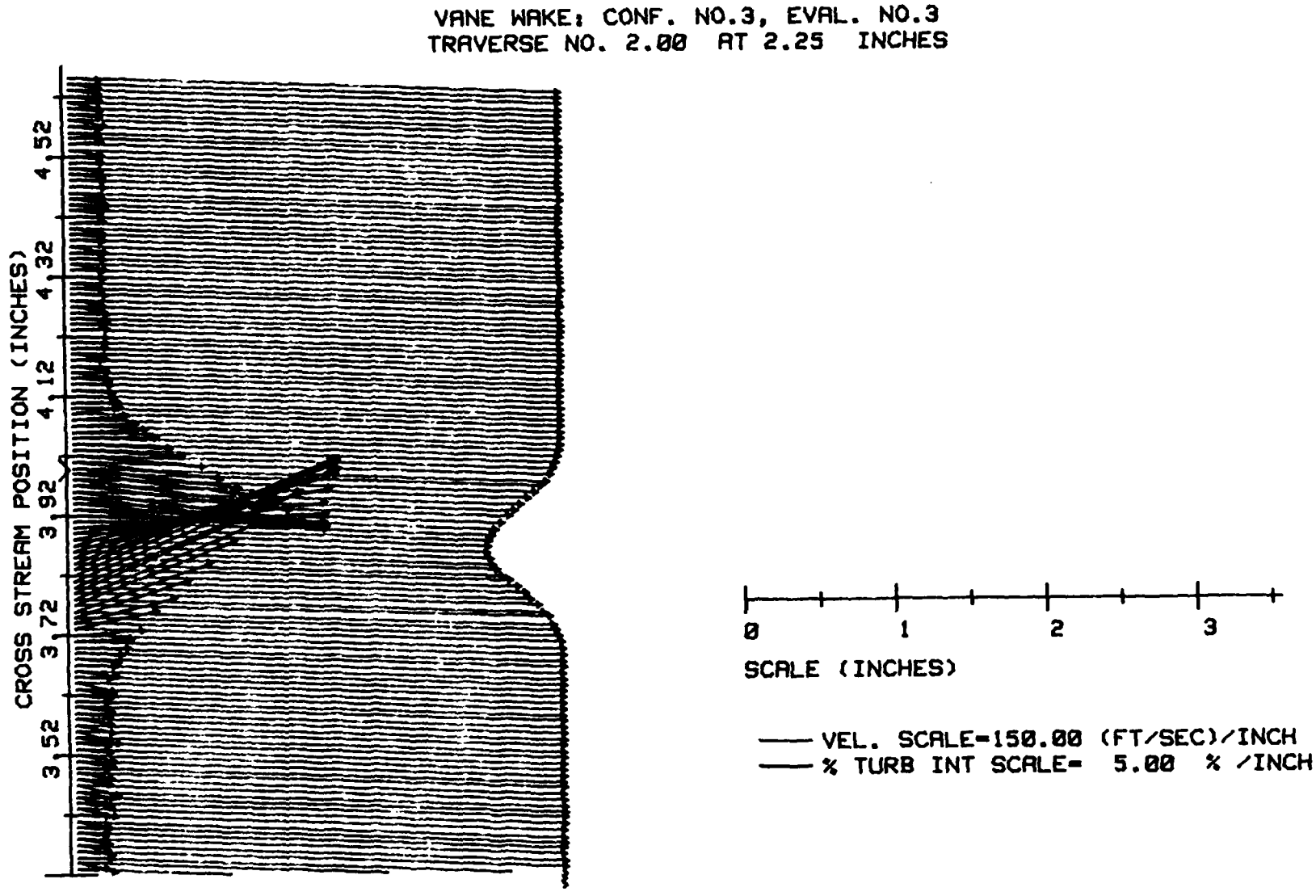

Fig. 114. Wake Velocity and Turbulence Intensity Profiles, Conf. #3, x/c = 1.125

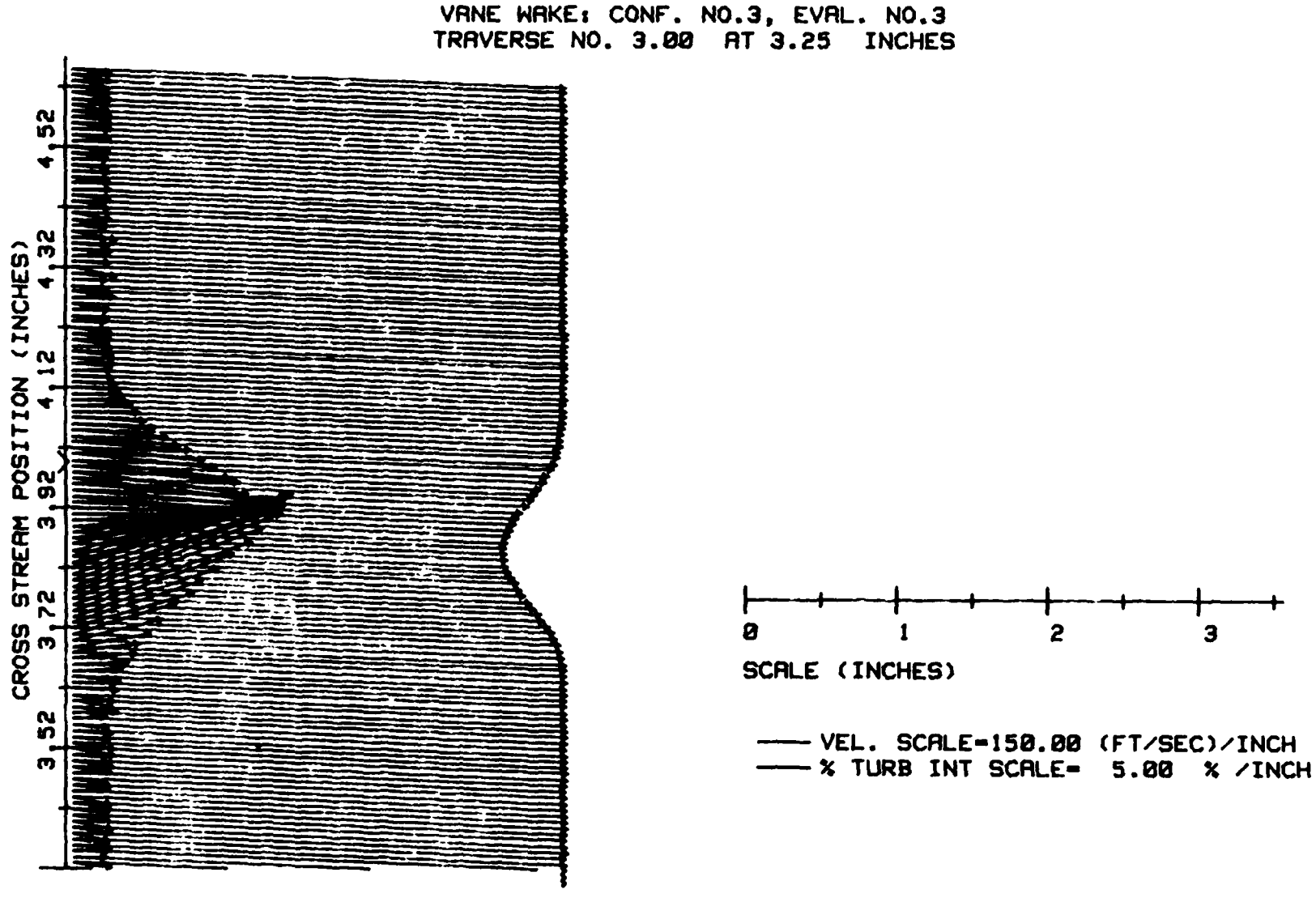

Fig. 115. Wake Velocity and Turbulence Intensity Profiles, Conf. #3, x/c = 1.625

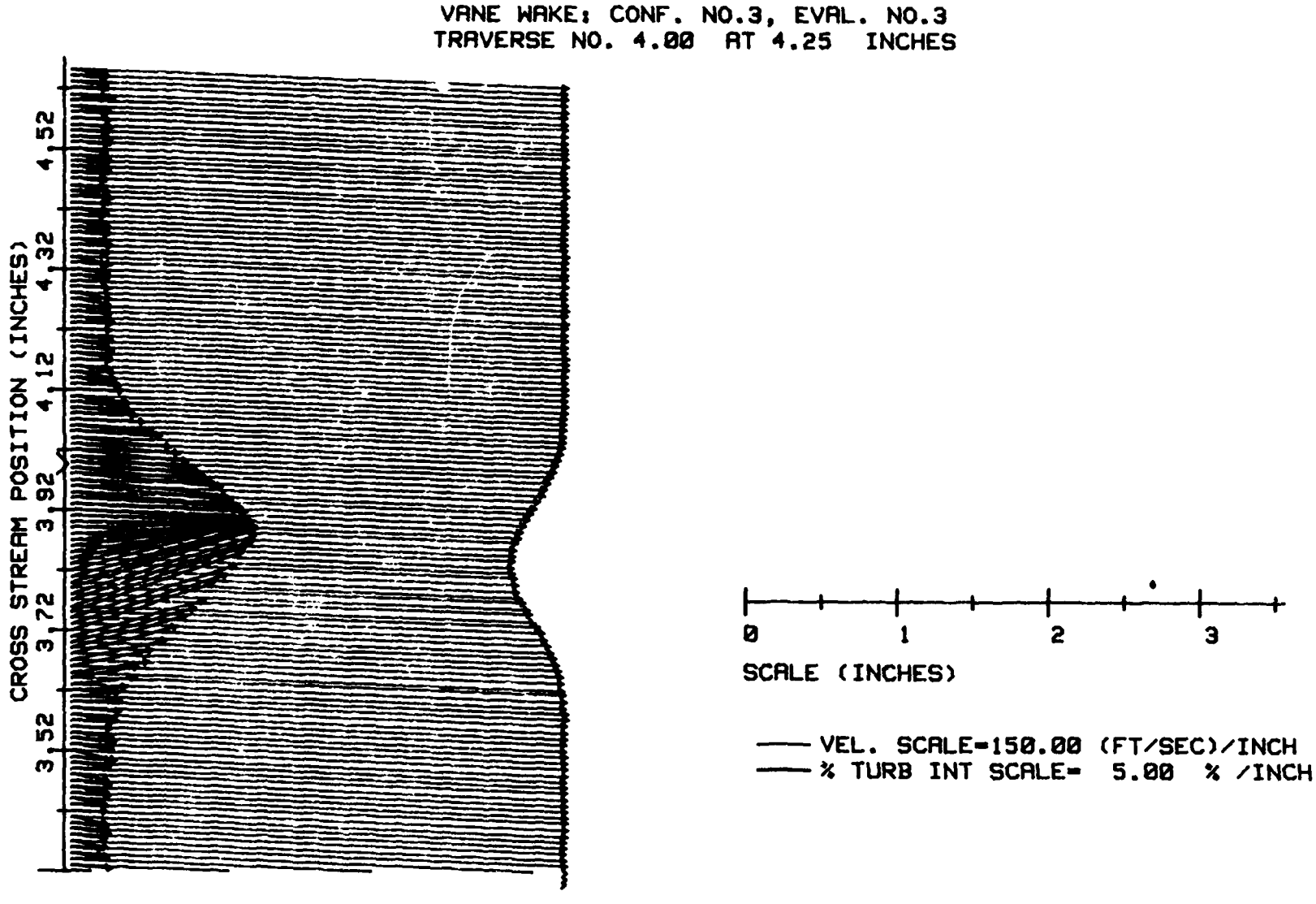

Fig. 116. Wake Velocity and Turbulence Intensity Profiles, Conf. #3, x/c = 2.125

Bibliography

1. Allison, Dennis M. Design and Evaluation of a Cascade Test Facility. MS Thesis GAE/AA/81D-2. School of Engineering, Air Force Institute of Technology (AU), Wright-Patterson AFB OH, June 1982.

2. Ball, Calvin L. and others. End-Wall Boundary Layer Measurements in a Two-Stage Fan. Technical Memorandum 83409, National Aeronautics and Space Administration, June 1983.

3. Bammert, K. and G. U. Woelk. "The Influence of the Blading Surface Roughness on the Aerodynamic Behavior and Characteristics of an Axial Compressor," ASME Journal of Engineering for Power, 102:283-287 (April 1980).

4. Bammert, K. and H. Sandstede. "Influences of Manufacturing Tolerances and Surface Roughness of Blades on the Performance of Turbines," ASME Journal of Engineering Power, :29-36 (January 1976).

5. Bradshaw, P. An Introduction to Turbulence and its Measurement. Oxford: Pergamon Press, 1971.

6. Collis, D. C. and M. J. Williams. "Two-Dimensional Convection from Heated Wires at Low Reynolds Numbers," Journal of Fluid Mechanics, 6:357-384 (1959).

7. Deutsch, A. and N. Zierke. The Boundary Layer on Compressor Cascade Blades, NASA-CR-173514: Semi-Annual Status Report, 1 December 1983 - 1 June 1984.

8. Evans, R. L. "Boundary-Layer Development on an Axial-Flow Compressor Stator Blade", ASME Journal of Engineering Power, 100: 287-293 (April 1978).

9. Helms, Vernon T., III. Measurement of Flow Angle and Mass Flow Rate in an Unknown Flow Field Using Hot Film and Hot Wire Probes, NASA 78-794: 175-184, undated.

10. Hewlett-Packard. 3052A Automatic Data Acquisition System Operating Instructions. Vol 1A, undated.

11. Kays, W. M. and M. E. Crawford. Convective Heat and Mass Transfer (Second Edition). New York: McGraw-Hill Book Company, 1980.

12. Koch, C. C. and L. H. Smith, Jr. "Loss Sources and Magnitudes in Axial-Flow Compressors," ASME Journal of

Engineering for Power, 411-424 (July 1976).

13. Lieblein, Seymour. "Experimental Flow in Two-Dimensional Cascades," Aerodynamic Design of Axial Flow Compressors (Revised), edited by Irving Johnson and Robert O. Bullock. Washington: NASA, 1965.

14. Lieblein, Seymour and William H. Roudebush. Low Speed Wake Characteristics of Two-Dimensional Cascade and Isolated Airfoil Sections. Technical Note 3771, National Advisory Committee for Aeronautics, October 1956.

15. Lieblein, Seymour and William H. Roudebush. Theoretical Loss Relations for Low Speed Two-Dimensional Cascade Flow. Technical Note 3662, National Advisory Committee for Aeronautics.

16. Mellor, G. L. and G. M. Wood. "An Axial Compressor End-Wall Boundary Layer Theory," Trans. of Basic Engr., Journal of Basic Engr. (June 1971).

17. Moe, Capt Gary P. Influence of Surface Roughness on Compressor Blades at High Reynolds Number in a Two-Dimensional Cascade. MS Thesis GAE/AA/84D-19. School of Engineering, Air Force Institute of Technology (AU), Wright-Patterson AFB OH, December 1984.

18. Mueller, Thomas J. The Structure of Separated Flow Regions Occurring Near the Leading Edge of Airfoils - Including Transition. NASA-CR-175670: Semi-Annual Status Report, November 1984-April 1985.

19. Oka, S. and Z. Kostic. "Influence of Wall Proximity on Hot-Wire Velocity Measurement," DISA Information, 13: 29-33 (May 1972).

20. Rank Taylor Hobson. Surtronic 3 Operating Instructions. Leichester, England, undated.

21. Roudebush, William H. and Seymour Lieblein. "Viscous Flow in Two-Dimensional Cascades," Aerodynamic Design of Axial Flow Compressors (Revised), edited by Irving Johnson and Robert O. Bullock. Washington: NASA, 1965.

22. Schäffler, A. "Experimental and Analytical Investigation of the Effects of Reynolds Number and Blade Surface Roughness on Multistage Axial Flow Compressors," ASME Journal of Engineering for Power, 102: 5-12 (January 1980).

23. Schlichting, Hermann. Boundary Layer Theory (Seventh Edition). New York: McGraw-Hill Book Company, 1979.

24. Scholz, Norbert. Aerodynamics of Cascades, AG220. Neuilly sur Seine, France: AGARD, 1977.

25. Tanis, 2Lt Frederick J. Jr. Roughness Effects on Compressor Blade Performance in Cascade at High Reynolds Number. MS Thesis GAE/AA/81D-2. School of Engineering, Air Force Institute of Technology (AU), Wright-Patterson AFB OH, November 1983.

26. TSI. General System Information for 1050 Series Anemometry. St. Paul, Minnesota, undated.

27. TSI. Hot Film and Hot Wire Anemometry. Theory and Application Bulletin TB5. St. Paul, Minnesota, undated.

28. Van Dyke, Milton. Perturbation Methods in Fluid Mechanics. New York: Academic Press, 1964.

29. Vonada, John A. School of Engineering, Air Force Institute of Technology. Personal Notes. Wright-Patterson AFB OH, 12 March 1982.

30. Williams, Capt Larry D. Effects of Surface Roughness on Pressure Distribution and Boundary Layer over Compressor Blades at High Reynolds Number in a Two-Dimensional Cascade. MS Thesis GAE/AA/85D-17. School of Engineering, Air Force Institute of Technology (AU), Wright-Patterson AFB OH, December 1985.

VITA

Captain J. Rémy Poulin was born on 8 October 1959 in St. Georges de Beauce, Province de Québec, Canada. In 1977, he graduated from high school in Burlington, Ontario and enrolled in the Canadian Armed Forces. He attended Royal Roads Military College in Victoria, British Columbia and the Royal Military College in Kingston, Ontario, receiving his degree of Bachelor of Engineering in Mechanical Engineering in 1981. Upon graduation, he received his commission and began one year of additional training as an Aerospace Engineer. In 1982, he was posted to 407 Maritime Patrol Squadron at CFB Comox, British Columbia, where he served first as the Squadron Armament Officer and then the Aircraft Servicing Officer. He applied and was accepted for post-graduate training in 1985, and entered the School of Engineering, Air Force Institute of Technology, in June of that year.

Permanent address: 1503-2055 Upper Middle Rd
Burlington, Ontario
CANADA
L7P 3P4

REPORT DOCUMENTATION PAGE

Form Approved
OMB No. 0704-0188

1a. REPORT SECURITY CLASSIFICATION	1b. RESTRICTIVE MARKINGS
2a. SECURITY CLASSIFICATION AUTHORITY	3. DISTRIBUTION/AVAILABILITY OF REPORT: Approved for public release; distribution unlimited.
2b. DECLASSIFICATION/DOWNGRADING SCHEDULE	
4. PERFORMING ORGANIZATION REPORT NUMBER(S): AFIT/GAE/AA/86D-13	5. MONITORING ORGANIZATION REPORT NUMBER(S)
6a. NAME OF PERFORMING ORGANIZATION: School of Engineering; 6b. OFFICE SYMBOL (If applicable): AFIT/AA	7a. NAME OF MONITORING ORGANIZATION
6c. ADDRESS (City, State, and ZIP Code): Air Force Institute of Technology, Wright-Patterson AFB, Ohio 45433	7b. ADDRESS (City, State, and ZIP Code)
8a. NAME OF FUNDING/SPONSORING ORGANIZATION; 8b. OFFICE SYMBOL (If applicable)	9 PROCUREMENT INSTRUMENT IDENTIFICATION NUMBER
8c. ADDRESS (City, State, and ZIP Code)	10. SOURCE OF FUNDING NUMBERS: PROGRAM ELEMENT NO. / PROJECT NO. / TASK NO / WORK UNIT ACCESSION NO

11. TITLE (Include Security Classification): See Box 19

12. PERSONAL AUTHOR(S): J. Remy Poulin, BEng, Capt, Canadian Armed Forces

13a. TYPE OF REPORT	13b. TIME COVERED	14. DATE OF REPORT (Year, Month, Day)	15. PAGE COUNT
MS Thesis	FROM _____ TO _____	1986 December	213

16. SUPPLEMENTARY NOTATION

17. COSATI CODES			18. SUBJECT TERMS (Continue on reverse if necessary and identify by block number)
FIELD	GROUP	SUB-GROUP	Cascade Testing, Surface Roughness, Compressor Blade Pressure Distribution, Boundary Layer
21	05		

19 ABSTRACT (Continue on reverse if necessary and identify by block number)

Title: SURFACE ROUGHNESS: ITS EFFECTS ON THE PERFORMANCE OF A TWO-DIMENSIONAL COMPRESSOR CASCADE

Thesis Chairman: Dr. William C. Elrod
Associate Professor of Aerospace Engineering

Approved for public release: IAW AFR 190-1.
13 Mar 87
Dean for Research and Professional Development
Air Force Institute of Technology (AU)
Wright-Patterson AFB OH 45433

20 DISTRIBUTION/AVAILABILITY OF ABSTRACT	21 ABSTRACT SECURITY CLASSIFICATION
☒ UNCLASSIFIED/UNLIMITED ☐ SAME AS RPT ☐ DTIC USERS	UNCLASSIFIED

22a NAME OF RESPONSIBLE INDIVIDUAL	22b TELEPHONE (Include Area Code)	22c OFFICE SYMBOL
Dr. William C. Elrod	513-255-3517	AFIT/AA

DD Form 1473, JUN 86 — Previous editions are obsolete — SECURITY CLASSIFICATION OF THIS PAGE

An experimental investigation was conducted into the effects of surface roughness on the losses in the flow through a two-dimensional compressor cascade. The cascade consisted of seven NACA 65-A506 airfoils with two inch chords and aspect ratios of one. The blades were mounted with a stagger angle of 16 degrees, an angle of attack of 15 degrees and a solidity of 1.5. The Reynolds number per foot was in excess of two million. Three blade configurations were evaluated: one smooth and two with different degrees of roughness applied to the first quarter chord. Hot wire/film anemometers were used to measure velocities and turbulence intensities both in the wake and along the suction surface of the center blade. Pressure distributions were obtained from taps drilled along the suction surface.

Surface roughness is shown to increase both boundary layer edge velocities and boundary layer thickness towards the trailing edge while advancing the transition point towards the leading edge. It is also shown to increase wake full thickness, momentum thickness, form factor, and total pressure loss coefficient while decreasing the velocity recovery immediately downstream of the trailing edge. The wake characteristics are most sensitive to an initial increase in roughness, but regardless of the roughness level, the majority of the changes occur within the first half a chord length distance downstream.

END

6-87

DTIC